DISS. ETH No. 19863

# Modeling of Cell Suspensions and Biological Tissue for Computational Electromagnetics

A dissertation submitted to the

ETH ZURICH

for the degree of

Doctor of Sciences

presented by

SONJA HUCLOVA

Master of Science in Chemistry
University of Bern, Switzerland

born January 5, 1980

citizen of Worb (BE)

accepted on the recommendation of

Prof. Dr. Ch. Hafner, examiner
Prof. Dr. D. Erni, co-examiner
Dr. J. Fröhlich, co-examiner

2011

“Life is what happens while you are busy making other plans.”
John Lennon (1940 – 1980)

To my parents

Viera, Milan and Marlène

# Abstract

Dielectric spectroscopy is a technique for non-invasive probing of materials, e.g. biological tissue. Especially in case of biological tissue many physical and physiological parameters influence the dielectric properties so the unique relation between variations in properties of the bulk material and the origin of a specific change becomes difficult to assess. In order to better understand and investigate the effective dielectric properties and certain mechanisms influencing them computational models of the material exposed to the electric field might provide a deeper insight. However, biological material is inhomogeneous, anisotropic and dispersive. In addition, large aspect ratios occurring on the cellular as well as on the macroscopic level often lead to a high computational demand in numerical simulations. Consequently, modeling of the effective dielectric properties is rather challenging. The aim of this work is to overcome the mentioned challenges and to enable the computational reproduction of the dielectric behaviour of cell suspensions and tissues.

First, the most important spectral features are identified using semi-analytical mixing formulas. Cell suspensions and tissues are assumed having a quasi-periodic microstructure with a three-phase unit cell consisting of a shelled particle (cytoplasm and cell membrane) embedded in extracellular medium. Then, more advanced models including a versatile parametrization method of the cell shape are implemented using the Finite Element Method. Additionally, thin geometrical domains are successfully replaced by boundary conditions leading to a significant computational speedup. Focusing on the microsctrucure it is shown that for frequecies up to at least $10 - 100$ MHz shape and volume fraction of cells strongly influence the dielectric spectra of biological bulk material. Above the center frequency of the $\beta$-dispersion caused by the shorting of the cell membrane, shape and volume fraction lose their importance and the principal characteristic in effective properties of the cell model is determined by the volume fractions of the different constituents only. Consequently, for dielectric modeling of biological tissue below 100 MHz cell shape and cellular volume fraction have to be accurately taken into account in the model. Mixing formulas can serve as a first approximation, but for more realistic scenarios only numerical simulations offer the required flexiblity and accuracy. Furthermore, as some tissues exhibit a layered substructure on the macro- or submacroscopic scale semi-analytical and numerical models of multilayer structures are developed. Since non-invasiveness often involves the use of coplanar electrodes the multilayer structures are exposed to an inhomogeneous electric field, an additional challenge for a potential reconstruction. The uniqueness as well as the sensitivity and selectivity of the effective properties to parameter changes are investigated using the mentioned models. Generally, the reconstruction is an ill-posed problem. However, it is shown that if the number of unknowns is sufficiently small one can potentially assign the origin of a change

in the effective parameters to a specific varying parameter. The needed information is obtained from the difference spectra of permittivity and conductivity and their first and second derivative assuming a certain parameter oscillating around a referece value. Combining the findings a versatile and flexible computational framework is implemented. For the first time a dielectric multiscale model of biological tissue in the MHz range is established, fully based on material composition and morphological parameters of the micro- and macrostructure. Finally, the approach is successfully validated with measurements on human skin.

The presented framework is extendable and can be used for identification of mechanisms causing dielectric changes as well as for optimization of sensing devices. The use of the basic approach is not limited to biological tissue but suitable for the modeling of dielectric properties of composite materials with a similar substructure in general.

# Zusammenfassung

Dielektrische Spektroskopie ist eine Methode für nicht-invasive Untersuchungen an Materialien, wie zum Beispiel an biologischem Gewebe. Vor allem im Falle von biologischem Gewebe existieren viele physikalische und physiologische Parameter, welche die dielektrischen Eigenschaften beeinflussen. Somit gestaltet sich eine eindeutige Zuordnung zwischen Variationen der Eigenschaften des Bulkmaterials und einer spezifischen Änderung eher schwierig. Eine Möglichkeit um die effektiven dielektrischen Eigenschaften eines Materials zu untersuchen und etwaige Änderungen besser zu verstehen stellen rechnergestützte Modelle dar. Allerdings ist biologisches Material inhomogen, anisotrop und dispersiv. Zusätzlich führen grosse Längenverhältnisse sowohl auf der mikro- als auch auf der makroskopischen Skala häufig zu einem grossen rechnerischen Aufwand in numerischen Simulationen. Das Ziel der vorliegenden Arbeit besteht darin, die erwähnten Herausforderungen zu überwinden und die computergestützte Berechnung vom dielektrischen Verhalten von Zellsuspensionen und biologischem Gewebe zu ermöglichen.

Zuerst werden die wichtigsten spektralen Besonderheiten mittels semi-analytischen Mischformeln identifiziert. Dabei wird angenommen, dass Zellsuspensionen und Gewebe eine quasi-periodische Struktur aufweisen. Die Einheitszelle besteht aus einem Einschluss, dem Zytoplasma umhüllt von einer Zellmebran, eingebettet im extracellulären Medium. Anschliessend werden erweiterte Modelle mit Hilfe der Methode der Finiten Elemente unter Verwendung einer vielseitigen Oberflächenparametrisierungsmethode implementiert. Dabei können dünne geometrische Domänen durch Grenzbedingungen ersetzt werden, was zu einer signifikanten Verkürzung der Rechenzeit führt. Es wird gezeigt, dass sowohl Zellform als auch der Volumenbruch, welchen die (biologische) Zelle in der Einheitszelle annimmt, das Frequenzspektrum der effektiven Materialparameter bis $10 - 100$ MHz stark beeinflussen. Über der Relaxationsfrequenz der $\beta$-Dispersion, verursacht durch den Kurzschluss der Zellmembran verlieren Zellform und Volumenbruch weitgehend ihre Bedeutung und die effektiven Eigenschaften werden hauptsächlich durch die Volumenbrüche der einzelnen Konstituenten bestimmt. Daraus folgt, dass in dielektrischen Modellen von Zellen und Geweben für Frequenzen unter 100 MHz Zellform und Volumenbruch angemessen Rechnung getragen werden muss. Mischformeln können hierfür als Approximation dienen, allerdings bieten nur numerische Simulationen die nötige Flexibiliät und Genauigkeit.
Im Weiteren werden semi-analytische und numerische Modelle von Mehrschichtensystemen erstellt, da einige Gewebearten auf der makroskopischen oder submakroskopischen Skala geschichtete Unterstrukturen aufweisen. Da bei nicht-invasiven Messanordnungen häufig koplanare Elektroden zum Einsatz kommen, ist das Mehrschichtensystem einem inhomogenen elektrischen Feld ausgesetzt, also einer zusätzlichen Herausforderung für eine potentielle Rekonstruktion. Mit den erwähnten Modellen wird sowohl Eindeutigkeit

der effektiven Eigenschaften als auch Sensitivität und Selektivität bezüglich Parameteränderungen untersucht. Im Allgemeinen ist die Rekonstruktion ein schlecht konditioniertes Problem. Es wird allerdings gezeigt, dass der Ursprung einer Änderung in den effektiven Parametern einem spezifischen, variierdenen Parameter zugeordnet werden kann, wenn die Anzahl Unbekannter klein genug ist. Die nötige Information wird aus den Differenzspektren von Permittivität und Leitfähigkeit sowie deren erster und zweiter Ableitung erhalten.
Anschliessend werden die Erkenntnisse kombiniert und es wird eine vielseitige und flexible Berechnungsprozedur implementiert. Das erste Mal überhaupt wird ein dielektrisches Multiskalen-Modell für biologisches Gewebe in der MHz-Region erstellt, welches auf Materialzusammensetzung und Morphologie der Mikro- und Makrostruktur basiert. Schliesslich wird der Ansatz erfolgreich mit Messungen auf der menschlichen Haut validiert.

Die vorgestellte Berechnungsprozedur ist erweiterbar und kann sowohl für die Identifikation von Mechanismen, welche Änderungen in effektiven dielektrischen Eigenschaften zur Folge haben, als auch für die Optimierung von Messanordungen und Sensoren verwendet werden. Der grundlegende Ansatz beschränkt sich nicht nur auf biologisches Gewebe, sondern eignet sich auch für Modellierung von Materialgemischen mit ähnlicher Substruktur im Allgemeinen.

# Contents

# List of Figures

# List of Tables

# List of Acronyms and Abbreviations

## Electromagnetics terminology

TEM ..... transverse electromagnetic

TM ..... transverse magnetic

## Dielectric and measurement terminology

BR ..... Bruggeman formula

HB ..... Hanai-Bruggeman formula

LLL ..... Landau-Lifshitz-Looyenga formula

MG ..... Maxwell-Garnett formula

VNA ..... vector network analyzer

## Numerical modeling terminology

DOF ..... degrees of freedom

FDM ..... Finite-Differenc Method

FEM ..... Finite-Element Method

FIT ..... Finite-Integration Technique

HBA ..... Hanai-Bruggeman anisotropic model

LOI ..... Landau-Lifshitz-Looyenga isotropic model

MGW ..... Maxwell-Garnett water content model

MGI ..... Maxwell-Garnett isotropic model

MGA ..... Maxwell-Garnett anisotropic model

NUM ..... model with numerically calculated dielectric parameters

PEC ..... perfect electric conductor

PMC ..... perfect magnetic conductor

## Mathematics and solid-state analysis teminology

BCC ..... body centered cubic

FCC ..... face centered cubic

HCP ..... hexagonal close packed

SCU ..... simple cubic

SF ..... superformula

## Medical terminology

D ..... dermis

DVP ..... deeper vessel plexus

E ..... epidermis

E/D ..... epidermis and dermis

HYP ..... hypodermis

M ..... muscle

MRI ..... magnetic resonance imaging

OCT ..... optical coherence tomography

PD ..... papillary dermis

RBC ..... red blood cell

RD ..... reticular dermis

SC ..... stratum corneum

SAR ..... specific absorpiton rate

SL ..... supply layer

UVP ..... upper vessel plexus

## Miscellaneous

CPU ..... central processing unit

RAM ..... random-access memory

# 1 Introduction

## 1.1 Motivation

Dielectric spectroscopy allows for monitoring changes in material properties of regions within the material under test which are not in direct contact with the electrode. Therefore, it offers the potential of non-invasive monitoring, a notion that gained increased attention in daily clinical routine as well as in material testing. Applications for the latter of non-invasive dielectric spectroscopy range from moisture measurement in food, pharmaceutical products, paper pulp to cure state monitoring in the resin transfer molding process [1] or the reconstruction of sample thicknesses e.g. of keratinocyte stem cells grown on an array of coplanar electrodes [2].
The dielectric properties of biological tissue strongly depend on frequency over a broad range of the electromagnetic spectrum and are a target for monitoring as well. In the field of medical applications dielectric spectroscopy and electric impedance spectroscopy is already used for inspection of cervical squamous tissue since the cell shape is subsequently modified with advancing precancerous stage [3], skin cancer [4], skin irritations [5], non-invasive glucose monitoring [6], ischemia detection [7], measurement of oedema in irritant-exposed skin [8], monitoring of *in vitro* tissue engineering [9] or tumor characterization [10]. On the microscopic scale specific techniques based on dielectric spectroscopy such as microfluidic cytometry, dielectrophoresis and electrorotation [11], [12], [13], [14], [15] and [16] are employed for the investigation of single cells.
However, dielectric spectroscopy did not manage the area-wide breakthrough in daily clinical use so far. Despite the mentioned applications most types of biological tissues exhibit very similar characteristics and small changes ocurring in measured effective dielectric properties cannot easily be correlated to specific changes. In living cells there is no dominant mechanism causing large variations, rather the opposite is the case: Since the effective dielectric properties depend on many factors such as the structural, physical and physiological state small variations mask each other and cumulate to a sort of a 'noise'. Therefore, it is difficult to assign an observed change in the measured signal to the underlying mechanism. Consequently, the question arises under which circumstances dielectric spectroscopy can actually be applied in patient monitoring.
One possibility in order to find out the relation between a signal change and the specific parameter variation would be to establish a model containing all features and mechanisms responsible for dielectric changes. Up to some years ago dielectric models were either rather simple or when reached for an appropriate complexity the computational demand would simply have exploded due to large aspect ratios within a cell as well as between cells and environment, as e.g. electrodes.

The goal of this work is to establish an efficient and flexible computational framework in

order to be able to model the effective dielectric properties of biological tissue, mainly in the MHz range and explicitly without the *a priori* use of fitting algorithms. In terms of explanatory power such a framework would clearly outperform a black-box model. Even though the availability of computational resources is constantly increasing it is aimed for an additional strategy for the transfer of information across several spatial scales. An advantage of such a modular build-up would enable to fine-tune the overall model complexity as e.g. the inclusion of physiological parameters.
Several research fields would certainly benefit from such a dielectric tissue model. Besides optimizations of sensing instruments, setups and configurations arising in biomedical research achievable measurement accuracy and the interactions between various mechanisms could be studied. Furthermore, such a model would substantially improve the quality of security assessements for passive exposure to electromagnetic fields (specific absorpiton rate (SAR) calculations, dosimetry).

## 1.2 Outline

The fundamentals of dielectric spectroscopy and the underlying mechanisms with the focus on biological tissues are presented in Chapter 2. Besides the introduction of dielectric relaxation, an overview of the dielectric behaviour and the underlying mechanisms of tissue over a wide frequency range is given. Measurement techniques as well as a review on existing models for effective dielectric properties are also introduced. However, the description of existing models is intentionally kept rather short since details for some models will follow throughout this work.

The first step towards modeling of dielectric properties is the application of the quasi-static approximation and field averaging on the microscopic scale. Cells are described as (shelled) spheres or ellipsoids exposed to a homogeneous electric field and the effective dielectric properties are calculated using different mixing formulas introduced by Maxwell-Garnett, Hanai-Bruggeman and Landau-Lifshitz-Looyenga. The focus of the Chapter 3 lies first, on a flexible implementation of the formulas allowing for a parametrization which is as flexible as possible and second, on initial studies concerning shape, volume fraction and some material parameter variation and their impact on the effective dielectric spectra. Simultaneously, the implementation of the formulas is validated using existing models from literature.

In a next step the concept of considering cell suspensions and tissues as a quasi-periodic structure from Chapter 3 is transferred to Chapter 4. A unit cell and its effective properties are numerically simulated as Finite-Element Method (FEM) models. The use of a very flexible shape parametrization method allows for the analytical generation of a wide variety of shapes and therefore volume fractions. Additionally, a body centered unit cell packing is also introduced. Since the implementation of the numerical model is not trivial due to large aspect ratios in the geometry some details on how to overcome numerical problems are mentioned. The numerical models are checked against mixing formulas from Chapter 3, also quantifying the influence of deviations from spherical and

ellipsoidal shapes and other simplifications.

In order to overcome problems with computational memory while still being able to include information from the microscopic in the macroscopic scale a multiscale approach is introduced. The main idea consists of the representation of the material as a quasi-periodic structure not only on one but on several scales. One starts at the smallest scale, calculates the effective dielectric tensor (numerically or analyticallly) and passes it to the next-higher scale under the assumption that the external field can be considered as more or less uniform. However, in the final step the field can be inhomogeneous, which is the topic of Chapter 6. Some issues concerning scaling, such as the replacement of a compartement of a cell (e.g. cytoplasm and nucleus) by its effective properties and the comparison to the actual geometrical inclusion or the required size of a cell array in presence of statistical variations in cell orientation are investigated.

In non-invasive applications or material testing the electrodes are often coplanar. As such configuration generates inhomogeneous fringing fields and tissue like human skin − usually the 'interface' to deeper-lying body tissue when the latter are sensed − often consists of layers this class of problems is tackeled in Chapter 6. Besides the adaption of a known analytical technique for arbitrary number of layers, sensitivity and specificity of effective dielectric parameters with respect to parameter changes in layers not in contact with the electrodes for diffferent probe geometries are assessed using numerical models.

Finally, in Chapter 7 the findings from Chapters 3 to 6 are condensed and applied to a multiscale dielectric model of the human skin probed by a fringing field sensor. Models with different degrees of complexity are evaluated and discussed.

# 2 Dielectric spectroscopy of biological tissue

Some parts of the contents of this chapter, especially Section 2.1 is adapted from [17] and [18].

## 2.1 Fundamentals

The interaction of electromagnetic fields with matter is described by macroscopic Maxwell's equations, given in their derivative form in Equations 2.1 to 2.4.

$$\nabla \times \mathbf{E} = -\frac{\partial \mathbf{B}}{\partial t} \tag{2.1}$$

$$\nabla \times \mathbf{H} = \mathbf{J} + \frac{\partial \mathbf{D}}{\partial t} \tag{2.2}$$

$$\nabla \cdot \mathbf{D} = \varrho \tag{2.3}$$

$$\nabla \cdot \mathbf{B} = 0 \tag{2.4}$$

$\mathbf{D}$ is the electric flux density, $\mathbf{E}$ the electric field, $\mathbf{B}$ the magnetic flux density, $\mathbf{H}$ the magnetic field, $\mathbf{J}$ the current density and $\varrho$ the charge density. For a region containing a source (charge or current) which is small compared to the wavelength $\lambda$ and only the fields in the immediate vicinity of the source are considered, they are called quasi-static. The fields still vary with time, but the frequency is sufficiently low so that propagation effects are not important for the range of interest. In other words the sources the electromagnetic field vary so slowly with time that the electric and magnetic fields are at every instant the same as they were generated by stationary sources and the terms containing $\frac{\partial}{\partial t}$ can be neglected.

For small electric field strenghts the electric flux density $\mathbf{D}$ can be expressed as

$$\mathbf{D} = \varepsilon(\mathbf{E} + \mathbf{P}) = \varepsilon^* \varepsilon_0 \mathbf{E} \tag{2.5}$$

where the polarization $\mathbf{P}$ designates the induced dipole moment per unit volume of the material with relative complex dielectric permittivity $\varepsilon^*$ and the dielectric permittivity of vacuum $\varepsilon_0$. In general $\varepsilon^*$ is a tensor, given by Equation 2.6.

$$\varepsilon^* = \bar{\varepsilon}^* = \begin{pmatrix} \varepsilon^*_{xx} & \varepsilon^*_{xy} & \varepsilon^*_{xz} \\ \varepsilon^*_{yx} & \varepsilon^*_{yy} & \varepsilon^*_{yz} \\ \varepsilon^*_{zx} & \varepsilon^*_{zy} & \varepsilon^*_{zz} \end{pmatrix} \tag{2.6}$$

In non-magnetic materials $\bar{\varepsilon}^*$ is a diagonal matrix. 'True' off-diagonal elements are only introduced in case of induced currents in magnetic materials with appropriate symmetry, as e.g. given in [19]. The relation between the polarization $\mathbf{P}$ and $\varepsilon^*$ is given by

$$\mathbf{P} = \mathbf{D} - \mathbf{D}_0 = (\varepsilon^* - 1)\varepsilon_0 \mathbf{E} \tag{2.7}$$

with $\mathbf{D}_0$ being the electric flux density of vacuum. The microscopic dipole moments can be either permanent or induced. In the latter case a previously equilibrated charge distribution is distorted by an external electric field, forming a dipole moment

$$\mathbf{p} = \alpha \mathbf{E}_{\mathrm{loc}}. \tag{2.8}$$

with the local electric field $\mathbf{E}_{\mathrm{loc}}$. The polarizability $\alpha$ is a measure for the displacement of positive and negative charges. Since it is not possible to polarize molecules isotropically $\alpha$ is a tensor. In molecules the induced dipole moment $\mathbf{p}$ is formed by the displacement of the electron cloud relative to the positively charged nucleus. In Figure 2.2 the term **electronic polarization** refers to charge displacement in single atoms, e.g. in noble gases. **Atomic polarization** occurs in originally apolar molecules. This displacement polarization $\mathbf{P}_{\mathrm{ind}}$ in a volume $\delta V$ is given by

$$\mathbf{P}_{\mathrm{ind}} = \frac{1}{\delta V} \sum \mathbf{p}. \tag{2.9}$$

In addition to the described displacement polarization polar molecules with permanent dipole moments are subject to **orientational polarization** due to their alignment with respect to the external electric field. Molecules (or particles) have a permanent dipole moment if the electric centres of gravity of positive and negative charges do not match. For any distribution of charges $\varrho_e(\mathbf{r})$ the dipole moment can be expressed as

$$\boldsymbol{\mu} = \int_V \mathbf{r} \varrho_e(\mathbf{r}) d^3 r. \tag{2.10}$$

Permanent dipole moments $\boldsymbol{\mu}$ are generally orders of magnitude larger than induced dipoles $\mathbf{p}$. The most prominent example of a permanent dipole is the $H_2O$-molecule. The total orientational polarization $\mathbf{P}_{\mathrm{or}}$, related to microscopic dipole moments $\mu$ of the molecules or particles within a volume $V$ and is given by

$$\mathbf{P}_{\mathrm{or}} = \frac{1}{\delta V} \sum_1^N \boldsymbol{\mu} = \frac{N}{\delta V} \langle \boldsymbol{\mu} \rangle \tag{2.11}$$

where $N$ denotes the number of dipoles in the system and $\langle \mu \rangle$ the mean dipole moment. $\mathbf{P}_{\mathrm{ind}}$ is practically temperature-independent and follows the external field up to high frequencies due to the smaller inertia of the displacement, whereas the temperature and frequency dependency of $\mathbf{P}_{\mathrm{or}}$ is strongly determined by the dynamics of the intermolecular (or interparticle) interactions. Due to thermal fluctuations not all dipoles are aligned with the applied electric field but the orientation has a statistical distribution.

Under the simplifying assumption that the dipoles do not interact with each other and if $\boldsymbol{\mu}\mathbf{E} \ll k_B T$, a mean permanent dipole moment $\langle \boldsymbol{\mu} \rangle$ is given by Equation 2.12

$$\langle \boldsymbol{\mu} \rangle = \frac{\boldsymbol{\mu}^2}{3k_B T}\mathbf{E} \tag{2.12}$$

by applying Boltzmann statistics. $k_B$ denotes the Boltzmann constant and $T$ the absolute temperature.

One of the most important polarization mechanisms in biological tissue is the **interfacial polarization**. It occurs at material interfaces due to the build-up of surface charge densities in each material. Consequently, materials containing conducting particles can be polarized due to charge transfer, not only on molecular or sub-molecular but also on meso- or even macroscale which is of great importance in biological tissue.
Finally, at low frequencies and in presence of such mobile charge carriers the charge density at the electrode rises and an electrical double-layer is formed, acting as a thin isolating barrier. This phenomenon is called **electrode polarization** and manifestates itself by a steep rise of $\varepsilon_r'$. Electrode polarization is usually unwanted, since it masks other effects potentially occurring in the material under investigation.

According to Equations 2.1 to 2.2 $\varepsilon^*$ is time (or frequency) dependent if time-dependent processes take place within a material region with the dimensions $\delta$. In general, time dependent processes within a material lead to a difference of the time dependencies of the outer electric field $\mathbf{E}(t)$ and the resulting dielectric displacement $\mathbf{D}(t)$. For a periodic electric field $\mathbf{E}(t) = \mathbf{E}_0 e^{-j\omega t}$, with the angular frequency $\omega = 2\pi f$ and the imaginary unit $j = \sqrt{-1}$ the complex dielectric function $\varepsilon^*$ is defined by

$$\varepsilon^*(\omega) = \varepsilon^{'}(\omega) - j\varepsilon^{''}(\omega). \tag{2.13}$$

The dielectric spectrum contains information on the dynamic behaviour of a material. An overview over the entire frequency region is shown in Figure 2.1. In the major part of the entire frequency spectrum relaxation phenomena occur due to various polarization mechanisms. Resonance phenomena due to molecular, atomic or electronic vibrations manifestate themselves in the IR and optical frequency range. The real part of the permittivity, $\varepsilon'$ accounts for the the internal displacement of charge systems in the material. With increasing frequency of the exciting electric field the amount of polarization induced by the field is reduced, because the system is less and less able to align with the field.
$\varepsilon''$ is a measure for dissipation in a material. It gives the rate of attenuation that is encountered by a propagating wave. In a lossy medium the electromagnetic energy is gradually converted into heat due to friction caused by the displacement of the charges in an alternating electric field. Dielectric losses are related to the displacement current of the dipoles orienting according to the time-dependent external field. Ohmic losses occur due to drift motion of mobile charge carriers (electrons, ions or charged defects), also present at zero frequency. The Ohm's law in Equation 2.14 gives the relationship between the electric field $\mathbf{E}$ and the current density $\mathbf{J}$

$$\mathbf{J} = \sigma^*\mathbf{E} \tag{2.14}$$

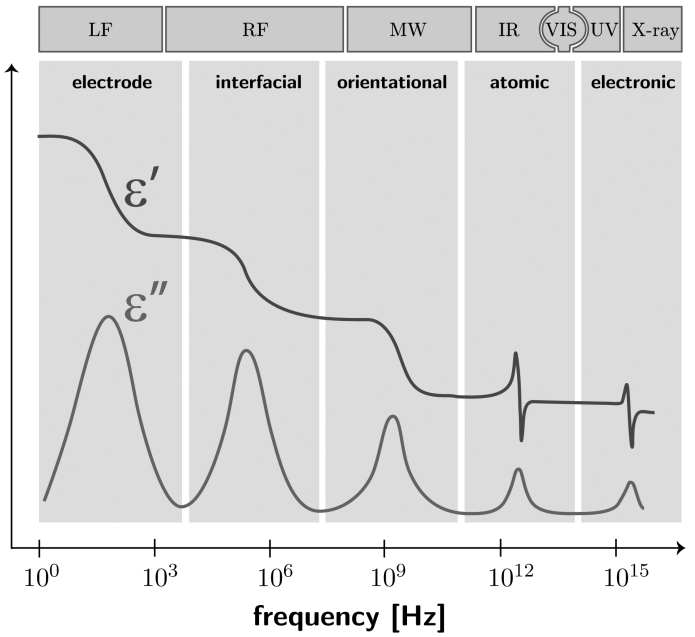


**Figure 2.1:** Frequency regions of the various polarization and resonance phenomena and the corresponding real and imaginary part of the permittivity.

where $\sigma^*$ is the complex electric conductivity $\sigma^*(\omega) = \sigma^{'}(\omega) - j\sigma^{''}(\omega)$. It is related to the permittivity by Equation 2.15.

$$\sigma^* = j\omega\varepsilon_0\varepsilon^* \tag{2.15}$$

Both, $\varepsilon'$ and $\varepsilon''$ contain the same amount of information since they can be transformed into each other with the Kramers-Kronig relations.

$$\varepsilon^{'}(\omega) = \varepsilon_\infty + \frac{1}{\pi}\oint_{-\infty}^{\infty}\frac{\varepsilon^{''}(\omega)}{\omega-\omega_0}d\omega = \varepsilon_\infty + \frac{2}{\pi}\oint_{0}^{\infty}\frac{\omega\varepsilon^{''}(\omega)}{\omega^2-\omega_0^2}d\omega \tag{2.16}$$

$$\varepsilon^{''}(\omega) = \frac{1}{\pi}\oint_{-\infty}^{\infty}\frac{\varepsilon^{'}(\omega)}{\omega-\omega_0}d\omega = \varepsilon_\infty + \frac{2}{\pi}\oint_{0}^{\infty}\frac{\omega\varepsilon^{'}(\omega)}{\omega^2-\omega_0^2}d\omega \tag{2.17}$$

If inertia effects are neglected, the time-dependent behaviour of the polarization $\mathbf{P}$ can be described by the first-order differential equation given in Equation 2.18 under the assumption that the change in polarization is proportional to its current value and $\tau_0$ being the characteristic relaxation time.

$$\frac{d\mathbf{P}(t)}{dt} = -\frac{1}{\tau_0}\mathbf{P}(t) \tag{2.18}$$

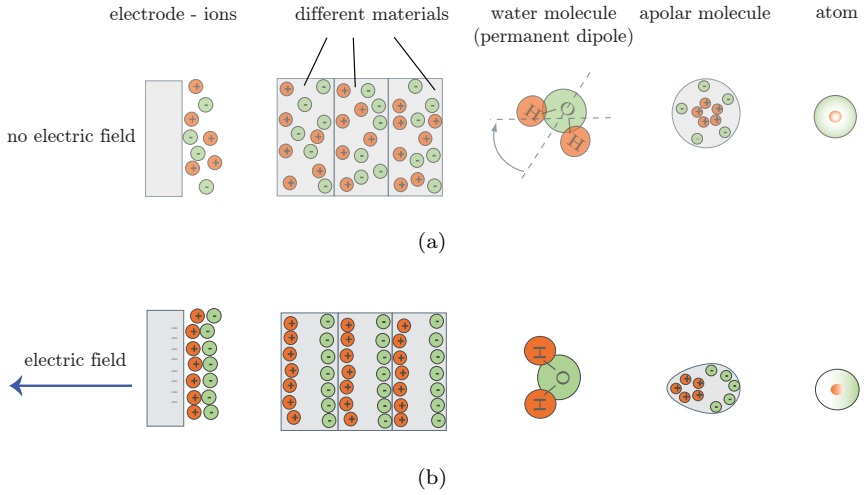


**Figure 2.2:** Polarization mechanisms causing relaxations and resonances in the dielectric spectrum displayed in Figure 2.1. Adapted and modified from [20].

The equation has the solution $F(t)$ given in Equation 2.19, which provides the difference between the polarization $\mathbf{P}(t)$ at a certain time $t$ and the limit at very long time $\mathbf{P}(t \rightarrow \infty)$.

$$F(t) = e^{-\frac{t}{\tau_0}} \tag{2.19}$$

After Fourier transformation of Equation 2.18 and the relation in Equation 2.5 one obtains the frequency-dependent permittivity for an ideal relaxation, also known as Debye-relaxation given by

$$\varepsilon^*(\omega) = \varepsilon_\infty + \frac{\varepsilon_{\text{stat}} - \varepsilon_\infty}{1 + j\omega\tau_0}. \tag{2.20}$$

However, in real, non-ideal systems relaxation processes deviate from the Debye function and exhibit a distribution of relaxation times $g(\tau)$. The mathematical decription is given by the superposition of ideal Debye relaxation processes (and the substitution $\Delta\varepsilon = \varepsilon_{\text{stat}} - \varepsilon_\infty$) in Equation 2.21.

$$\varepsilon^*(\omega) = \varepsilon_\infty + (\delta\varepsilon) \int_0^\infty \frac{g(\tau)}{1 + j\omega\tau} d\tau \tag{2.21}$$

Since $g(\tau)$ is usually not known Havriliak and Negami suggested an empirical formula to describe non-Debye relaxation processes given in Equation 2.22. The fractional shape parameters $\alpha$ and $\gamma$ describe symmetric and asymmetric broadening of the complex dielectric function at low and high frequencies.

$$\varepsilon^*(\omega) = \varepsilon_\infty + \frac{\Delta\varepsilon}{(1 + (j\omega\tau)^\alpha)^\gamma} \tag{2.22}$$

## 2.2 Dielectric properties of biological tissue

The dielectric properties of biological tissue are determined by the interaction of an electric current with the tissue at the cellular and molecular level. In biological tissues, ions are the main current carriers whereas in electrical circuits the current results from the movement of electrons. Since ions are the major charge carriers, the conductivity of biological tissue is highly dependent on factors such as concentrations, effective charge, diffusion coefficients, and the types of ions involved in the process. The linearity of the tissue properties is considered to hold as long as the current injected does not exceed a certain value [21]. A detailed non-linearity assessement of the dielectric properties of skin was performed in [22]. Higher currents and fields can also influence enzyme function or cell membrane stability [23]. A technique called electroporation is based on the latter effect: With pulsed electromagnetic fields holes are punched into the cell membrane enormously facilitating the introduction of drugs or other substances [24].

There is also a significant difference in dielectric properties of living and post mortem tissues. Post mortem tissues additionally exhibit a time-dependent characteristic. First, the conductivity drops due to depolarization and swelling of cells, but as soon as the metabolism and therefore ion channel activity breaks down and released enzymes start to degrade the cell membrane the conductivity value rises again [25].

### 2.2.1 Dispersion mechanisms

As introduced in Section 2.1 a significant change in dielectric properties can happen due to different interaction mechanisms, each governed by its own kinetics on the corresponding time scales. These changes are called dielectric dispersions by convention [26]. Dielectric dispersions directly relate to the structure, physical and physiological state of the tissue.

The **$\alpha$-dispersion** is generally considered to be associated with the properties of the cell membranes and their interactions with the intra and extra cellular media. The $\alpha$-dispersion is characterized by the very large permittivity values produced by diffusion processes of counterions at the site of the cellular membrane at very low frequencies. In other words, the low-frequency behaviour of the biological tissues can be characterised by their non-homogeneous structure and the ionic activities inside the tissues. The precise mechanism responsible for the $\alpha$-dispersion is the least well understood of the three main dispersions [26].

The **$\beta$-dispersion** occurs at radio frequencies and is mainly due to the polarization, charging and short-circuiting of cell membranes, which separate the well-conducting extracellular medium and the cytoplasm. The membrane structure blocks ion movement under an external electric field, preventing the flow of ions between the intra- and extracellular media. It is also believed that a smaller contribution to the $\beta$-dispersion is from the dipolar relaxation of proteins and other organic macromolecules in the tissue. $\beta$-dispersion can be largely affected by water content. Tissues with less water content

have more air gaps or dry components, which will also block ion passage in the same way as the membranes, thus reducing the strength of the $\beta$-dispersion significantly [26].

As the frequency increases to the GHz regions, the rotational properties of polar molecules, especially those of water become important. The relaxation of free water molecules causes the **$\gamma$-dispersion**. Since water constitutes 70-80% of the volume of most soft tissues, the $\gamma$-dispersion is of importance in the study of dielectric properties of biological tissues [26].

In addition to the three major dispersions discussed above, there is a very small dispersion, called **$\delta$-dispersion**, occurring between the $\beta$- and $\gamma$-dispersion regions. It is believed that $\delta$-dispersion originates from the relaxation of the water molecules bound to the surface of macromolecules and relaxation of small dipolar segments of biomolecules (e.g. proteins). There is no single, dominant relaxation process for this dispersion and this lack of a single domain mechanism makes the analysis of this dispersion region in tissues rather difficult [26], [27] and [28].

### 2.2.2 Measurement techniques

Dielectric properties of materials can be measured with various techniques either in time- or frequency domain. In any specific range of frequency a suitable technique for that range must be used. Generally, dielectric properties are obtained by using transmission line theory applied on a circuit in which the sample of interest is a linear and time invariant component. At low frequency regions ($< 100\,\mathrm{MHz}$), common circuit elements may be used to measure the dielectric constant and conductivity of materials. These kinds of techniques employ a parallel plate capacitor, which serves as a sample holder. The impedance (capacitance and conductance) of the assembly is measured with and without the sample by using sensitive bridges, vector impedance analyzer or other similar instrumentation. The change in the impedance introduced by the sample is a measure of its dielectric properties. Although the parallel plate configuration is very common, coaxial and other capacitor designs are also used [26]. At frequencies above 100 MHz, transmission lines are employed. In this case the sample is incorporated in a transmission line assembly and the experimental set-up is organized to measure one or more of its $S$-parameters. The setup must contain a source to provide an incident signal, a sample holder, a detection system (such as a network analyzer) to measure the response of the sample to the signal, and finally transmission line components to guide the electromagnetic signal from one point to another. As mentioned, in these techniques, the reflection and/or transmission coefficients of the sample are determined. These parameters are both functions of the dielectric properties of the sample. The different measurement techniques are usually distinguished according to the design of the sample holder, which also determines the size and shape of the sample as well as the degree of sample handling required. The transmission line techniques are generally subdivided into waveguides and coaxial lines. In the waveguide technique, a sample of well-defined shape and volume is packed into a waveguide terminated by a short circuit. A slotted line is used to characterize the standing wave formed by superposition of

the incident and reflected waves. This technique is complex but it self-calibrates and can give accurate results over a narrow range of frequencies determined by the ratio of sample thickness to the propagating wavelength. Coaxial contact probes are open-ended transmission line sections terminated by an impedance matched lossless window. The sample is placed in contact with the probe and a network analyzer or equivalent instrumentation measures its admittance or reflection coefficient. Such techniques are broadband, non-destructive and require minimal sample handling. The success of this technique depends on the theoretical model, which relates the measured quantity to the dielectric properties of the sample, as well as on the calibration procedure [26].

### 2.2.3 Uncertainty and sources of error

The uncertainties in the measurements of complex relative permittivity depend on the uncertainty in the measured reflection coefficients from which it is calculated. In other words, it depends on the sensitivity of the admittance model used, which is a function of electrode surface roughness, sample properties, dimensions of the sensor and the measurement frequency This seems to be rather a complex situation, and there are different approaches to evaluate these uncertainties [26], [29], [30] and [31]. Another issue is the aforementioned electrode polarization occuring at frequencies up to 100 kHz. The electrode polarization obscures the dielectric properties of the sample by masking the $\alpha$-dispersion to a large extent and the $\beta$-dispersion partially. The electrode polarization can be reduced using certain probe geometries (four-point-measurements) or the effect can be accounted for by numerical correction of the measured data. However, for the latter either the relaxation function for the effective dielectric dispersion and a function modeling the electrode polarization have to be known. The electrode polarization is often described by a constant phase angle element in series with the sample admittance [32].

## 2.3 Modeling approaches

The major part of this work deals with modeling of dielectric properties of biological tissue. As in the case of measurements the choice of the modeling method is purpose- and frequency dependent. Besides the modeling techniques summarized in this Section and increasingly, also statistical approaches are being applied in order to correlate dielectric parameters to structural, compositional or physiological aspects of biological material [27]. Particularly, this is the case if the physical mechanism generating the observed change is not elucidated or masked by noise.

The electrical behaviour of biological tissue is often described as an equivalent circuit containing concentrated elements. Then, Cole-Cole or Havriliak-Negami parameters introduced in Equation 2.22 are fitted to dielectric data extracted from measurements. An example of such an equivalent circuit is shown in Figure 2.3.
The resistances of the extracellular medium and cytoplasm are denoted by $R_{\text{ext}}$ and $R_{\text{cytoplasm}}$, the membrane capacitance as $C_{\text{membrane}}$. $C_{\text{membrane}}$ is a pseudo-capacitance, a so-called constant phase element. The electrode-electrolyte (extracellular medium)

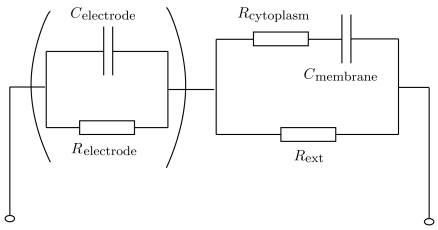


**Figure 2.3:** Half-cell equivalent circuit of a cell suspension or biological tissue. The parallel circuit in brackets denotes the electrode-electrolyte (extracellular medium) interface.

interface is denoted by a parallel circuit of the double-layer capacitance at the electrode $C_{\text{electrode}}$ and the electrode resistance $R_{\text{electrode}}$ in series with the cell circuit. At high frequencies the resistance of the tissue can be defined as the parallel combination of $R_{\text{ext}}$ and $R_{\text{cytoplasm}}$ and is denoted as $R_\infty$. $R_0$ denotes the resistance at $f = 0\,\text{Hz}$. Without taking the electrode-electrolyte interface (in brackets in Figure 2.3) into account the impedance can be written based on Equation 2.22 with $\gamma = 1$ as

$$Z = R_\infty + \frac{R_0 - R_\infty}{1 + (1 + j\omega\tau)^\alpha}. \tag{2.23}$$

This approach presented e.g. in [13], [32], [33], [34], [35], [36], [37], [38], [39] and [40] [41], [42] and [43] enabels a computationally relatively inexpensive reproduction of the dielectric spectra since it only involves least-square fitting or an optimization for $\varepsilon_{\text{eff}}$ and $\sigma_{\text{eff}}$. However, using this kind of representation the assignment of spectral features to specific tissue microstructure parameters is difficult, if not impossible, even in presence of pronounced differences among tissue types. Very different combinations of dielectric and geometric parameters can generate the same spectra of the effective dielectric parameters, therefore the models have a rather descriptive character. Nevertheless, equivalent circuit models can serve as placeholders as long as no better models are available. This is e. g. the case in Chapter 6.

The use of semi-analytical mixing formulas signifies a first step towards the incorporation of material properties and partly also microstructure of tissue or cell suspensions. Chapter 3 provides a deeper insight into the description of cells and tissue by mixing formulas as well as the implementation of the latter.
Finally, the dielectric properties of tissue on microscale can also be numerically calculated. The geometry setting corresponds to the one employed for mixing formulas but offers far more flexibility in terms of the cell's geometry variations.

## 2.4 Conclusion

To date no general procedure for the modeling of biological tissue, especially in the MHz region exists. If a model has to refer to the physical and physiological state a certain degree of complexity will be indispensable. Mixing formulas can provide first estimations,

but presumably only numerical techniques will offer the largest flexibility. However, solutions how to overcome problems with model size and large aspect ratios have to be found.
In order to do so the procedure will be as follows: First, small volumes with large complexity are considered and the relevant parameters are identified. After identification of the relevant parameters the model complexity is reduced if possible. Then, a modeling approach for larger volumes is introduced. Finally, the findings from the dielectric representation of small and large volumes are combined in a multiscale procedure providing a tissue model.

# 3 Modeling of tissue as a composite material

The main idea of effective medium or mixing theory in general consists of somehow obtaining a homogeneous replacement, effective or bulk material for a morphologically complex, highly structured multiphase material − such as biological tissue − with the same behaviour when exposed to an electric field. The simplest example is the calculation of the effective dielectric properties of a layered structure whereby the applied electric field is parallel or perpendicular to the layer boundaries.

Biological tissue is first of all built up from cells as e.g. in Figure 3.1 embedded in extracellular medium. The very first step towards a dielectric model consists of considering cell suspensions and tissues being quasi-periodically built up from unit cells containing a single biological cell. Simplifying this scenario to the consideration of a spherical or ellipsoidal inclusion in a host material exposed to a homogeneous external electric field, the two having homogeneous but different dielectric properties one arrives at one of the fundamental scenarios for effective medium theory, the calculation of the polarizability of this sphere generating an electric dipole. The result is an average electric field and flux density. In this chapter three different mixing formulas for ellipsoidal and

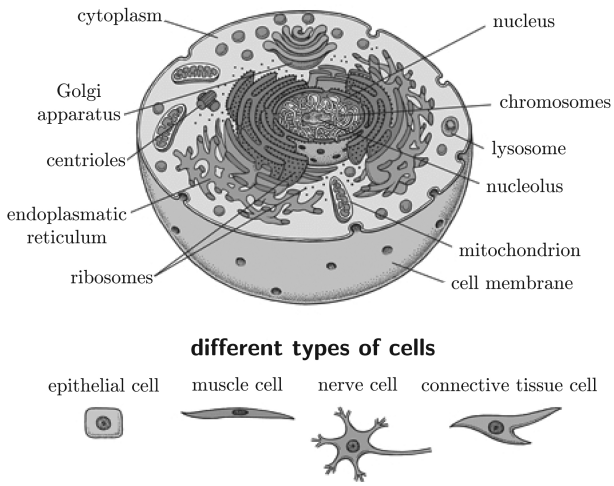


**Figure 3.1:** Eukaryotic cell with its components. Adapted from [44].

unstructured inclusions are investigated focusing on shape and inclusion volume fraction. An intensive study on those and other mixing formulas and their validity bounds are given in [45] and [46].

As concentric spheres and confocal ellipsoids belong to the group of calculable shapes simple single-shelled spherical cell models were introduced e.g. in [12], [15], [47], [48], [49] and [50] to name only a few. The advantage of confocal ellipsoidal shapes is that dielectric spectra can be calculated analytically. The Maxwell-Garnett formula (MG) formula provides a good approximation for dilute solutions, meaning for an inclusion volume fraction limit of $\varphi \leq 0.1$ [51], [47], [52] and [53]. Other single shelled sphere models are presented in [12], [15], [49] and [50]. Double-shelled [54], [55] and multishelled models including bound water to the cell membrane and including the nucleus [56] have also been investigated.
For higher volume fractions as usually occurring in tissue the MG formula is less accurate since interparticle interactions are neglected. The Hanai-Bruggeman formula (HB) formula, taking mutual particle interactions into account was shown to provide good agreement with measurements for $\varphi < 0.8$ [47]. The HB formula for multi-shelled ellipsoids was e.g. employed for modeling of the dielectric parameters of the *e. Coli* bacterium [57], [58] or rat liver tissue [59].
In [60] the Landau-Lifshitz-Looyenga formula (LLL) formula provides the effective dielectric parameters for two different types of lymphocyte models at two different volume fractions.

## 3.1 General description

If a material with a certain microstructre is exposed to an electric field oscillating with the frequency $f$ and the corresponding wavelength $\lambda$ is much larger than the size of the microstructure $\delta$ the quasi-static regime can be applied and the composite behaves as a homogeneous material with effective material properties $\varepsilon_{\text{eff}}$. On the microscale the electric field strength $\mathbf{E}$ and the electric flux density $\mathbf{D}$ both fields are related by Equation 2.5. On the microscale the fields oscillate rapidly, while on macroscopic level the fields are averaged over a volume much larger than $\delta$, oscillations smooth out and only retain slow variations. The averaged fields $\langle \mathbf{D} \rangle$ and $\langle \mathbf{E} \rangle$ are related via the effective permittivity matrix $\varepsilon_{\text{eff}}$

$$\langle \mathbf{D} \rangle = \langle \varepsilon \mathbf{E} \rangle = \varepsilon_{\text{eff}} \langle \mathbf{E} \rangle. \tag{3.1}$$

The complex effective permittivity tensor $\bar{\varepsilon}^*_{\text{eff}}$ has form given by Equation 2.6.

## 3.2 Mixing formulas

One way how to obtain the effective dielectric properties for the scenario is to solve the Laplace equation in spherical coordinates with respect to a single particle. The approach can be generalized for ellipsoids and cylinders and even inhomogeneous particles of the mentioned shapes as long as the variation of the dielectric contrast happens along the

$r$-coordinate in spherical and $\xi$-coordinate in ellipsoidal coordinate systems. This requirement has to be fulfilled because the Laplace equation has to be separable within the various regions of the problem in order to obtain an analytical solution [46].
Strictly speaking, the solutions given in Subsection 3.2.1, 3.2.2 and Section 3.3 would only be analytical when considering the entire infinite sum of Legendre polynomials. Here, only the first-order term is taken into account.

### 3.2.1 Maxwell-Garnett formula

The electric field distribution after a spherical particle (inclusion) with a permittivity of $\varepsilon_1$ is introduced into a host material with the permittivity $\varepsilon_\mathrm{h}$ exposed to a previously homogeneous electric field can be described analytically. The effective permittivity of the inclusion/host system, the inclusion occupying a volume fraction $\varphi$ is then given by the Maxwell-Garnett (MG) formula.

$$\frac{\varepsilon_\mathrm{eff} - \varepsilon_\mathrm{h}}{\varepsilon_\mathrm{eff} - 2\varepsilon_\mathrm{h}} = \varphi \frac{\varepsilon_1 - \varepsilon_\mathrm{h}}{\varepsilon_1 + 2\varepsilon_\mathrm{h}} \tag{3.2}$$

If the particles are far enough from eachother (low volume fraction, $\varphi < 0.1$), then these effective parameters hold for the entire medium. The concept can be extended for a confocal multishelled ellipsoidal and even cylindrical inclusion, since the entire particle can always be replaced by a homogeneous one with an effective permittivity. As long as the coordinate system is such that the Laplace equation $\nabla^2\varphi(\mathbf{r}) = 0$ is separable in the various regions of the problem the general form of the MG formula provides an exact solution for the effective permittivity [46].
The $\varepsilon_\mathrm{eff}$ of a spherical particle is constant for all orientations relative to the applied field due to symmetry. For ellipsoids this is not the case anymore. The shape dependence of the polarizability of an ellipsoid is a function of its principal axes lengths (or ratios, respectively) $a_x, a_y$ and $a_z$ and is expressed with the depolarization factor $L_j$, $j$ indicating the spatial direction. The depolarization factor is related to the shape factor with $u = \frac{1-L_j}{L_j}$.

$$L_j = \frac{a_x a_y a_z}{2} \int_0^\infty \frac{1}{(s + a_j^2)\sqrt{(s + a_x^2)(s + a_y^2)(s + a_z^2)}} ds \qquad j = x, y, z \tag{3.3}$$

The depolarization factor of a sphere is $L = \frac{1}{3}$, the shape factor $u = 2$ contained in Equation 3.2. The depolarization factors of a cylinder with an ellipsoidal cross-section and the axis parallel to the $z$-axis are $L_x$, $L_y = 1 - L_y$ and $L_z = 0$. Knowing the depolarization factors $L_j$ and the volumes of all $k \leq n$ ellipsoids $V_k = \frac{4\pi}{3} a_{k,x} a_{k,y} a_{k,z}$, while $V_k$ is the volume of the ellipsoid inside the boundary between permittivities $\varepsilon_{k-1}$ and $\varepsilon_k$, $\varepsilon_\mathrm{eff}$ of arbitrary ellipsoidal or cylindrical $n$-shelled particles can be calculated according to Equations 3.4 to 3.7 via the polarizability component in $j$-th direction $\alpha_j$ [61].

$$\frac{\alpha_j}{\varepsilon_\mathrm{h}} = \varphi \frac{X}{Y} \tag{3.4}$$

$$X = (\varepsilon_1 - \varepsilon_\mathrm{h}) + [\varepsilon_1 + L_{j,1}(\varepsilon_\mathrm{h} - \varepsilon_1)] \cdot \frac{(\varepsilon_2 - \varepsilon_1)\frac{V_2}{V_1} + [\varepsilon_2 + L_{j,2}(\varepsilon_1 - \varepsilon_2)]\frac{(\varepsilon_3 - \varepsilon_2)\frac{V_3}{V_1} + \ldots}{[\varepsilon_2 + L_{j,3}(\varepsilon_3 - \varepsilon_2)] + \ldots}}{\varepsilon_1 + L_{j,2}(\varepsilon_2 - \varepsilon_1) + L_{j,2}(1 - L_{j,2})(\varepsilon_2 - \varepsilon_1)\frac{(\varepsilon_3 - \varepsilon_2)\frac{V_3}{V_2} + \ldots}{[\varepsilon_2 + L_{j,3}(\varepsilon_3 - \varepsilon_2)] + \ldots}} \tag{3.5}$$

$$Y = [\varepsilon_\mathrm{h} + L_{j,1}(\varepsilon_1 - \varepsilon_\mathrm{h})] + L_{j,1}(1 - L_{j,1})(\varepsilon_1 - \varepsilon_\mathrm{h}) \cdot \frac{(\varepsilon_2 - \varepsilon_1)\frac{V_2}{V_1} + [\varepsilon_2 + L_{k,2}(\varepsilon_1 - \varepsilon_2)]\frac{(\varepsilon_3 - \varepsilon_2)\frac{V_3}{V_1} + \ldots}{[\varepsilon_2 + L_{j,3}(\varepsilon_3 - \varepsilon_2)] + \ldots}}{\varepsilon_1 + L_{j,2}(\varepsilon_2 - \varepsilon_1) + L_{j,2}(1 - L_{j,2})(\varepsilon_2 - \varepsilon_1)\frac{(\varepsilon_3 - \varepsilon_2)\frac{V_3}{V_2} + \ldots}{[\varepsilon_2 + L_{j,3}(\varepsilon_3 - \varepsilon_2)] + \ldots}} \tag{3.6}$$

$$\varepsilon_{\mathrm{eff},j} = \varepsilon_\mathrm{h} + \frac{\alpha_j}{1 - L_{j,1}\frac{\alpha_j}{\varepsilon_\mathrm{h}}} \tag{3.7}$$

In case of randomly oriented ellipsoidal particles the effective permittivity reduces to a scalar and is given by

$$\varepsilon_\mathrm{eff} = \varepsilon_\mathrm{h} + \frac{\frac{1}{3}\sum_{j=x,y,z}\alpha_j}{1 - \frac{1}{3}\sum_{j=x,y,z} L_{j,1}\frac{\alpha_j}{\varepsilon_\mathrm{h}}}. \tag{3.8}$$

Since the MG formula does not take interparticle interactions into account the validity of the analytical expression is reported to be limited up to a particle volume fraction of $\varphi < 0.1$. The MG formula also provides the exact solution for the effective permittivity of Hashin's structure, the space-filling coated spheres. The size distribution of the spheres ranges to infinitely small.

### 3.2.2 Hanai-Bruggeman formula

Another description of the effective properties of a two-phase mixture is given by Equation 3.9, the Bruggeman formula (BR) [62].

$$\varphi_1 \frac{\varepsilon_\mathrm{i} - \varepsilon_\mathrm{eff}}{\varepsilon_\mathrm{i} + 2\varepsilon_\mathrm{eff}} = \varphi_\mathrm{h} \frac{\varepsilon_\mathrm{h} - \varepsilon_\mathrm{eff}}{\varepsilon_\mathrm{h} + 2\varepsilon_\mathrm{eff}} \tag{3.9}$$

with $\varphi_\mathrm{h}$ and $\varphi_\mathrm{i}$ being the volume fractions of host and inclusion, respectively. If one has to deal with concentrated particle suspensions or systems the interactions between induced dipoles of particles have to be taken into account. Bruggeman approached this rather difficult task with his effective medium theory. The initially low volume fraction is gradually increased by an infinitesimal addition of particles [63]. When a small amount of particles of $\varepsilon_\mathrm{i}$ is added to the particle suspension which is regarded as an effective medium of $\varepsilon_\mathrm{eff}$, Equation 3.10 known as the Hanai-Bruggeman (HB) formula delivers an expression for $\varepsilon_\mathrm{eff}$ of randomly oriented inclusions. In case of $n$-shelled ellipsoids $\varepsilon_{\mathrm{eff},i(k)}$ of the $k$-th core particle consisting of the core ($n$-th material) and $n - k - 1$ shells is given by Equation 3.11.

$$-\int_0^\varphi \frac{d\varphi'}{1 - \varphi'} = \int_{\varepsilon_\mathrm{h}}^{\varepsilon_\mathrm{eff}} \frac{3}{\varepsilon_\mathrm{eff}} \left[ \sum_{j=x,y,z} \frac{\varepsilon_\mathrm{eff} - \varepsilon_\mathrm{i}}{\varepsilon_\mathrm{eff} + (\varepsilon_\mathrm{i} - \varepsilon_\mathrm{eff})L_j} \right]^{-1} d\varepsilon_\mathrm{eff} \tag{3.10}$$

$$\varepsilon_{\mathrm{eff,i}(k)} = \varepsilon_k \left( 1 + \frac{\frac{a_{x,k+1}a_{y,k+1}a_{z,k+1}}{a_{x,k}a_{y,k}a_{z,k}}(\varepsilon_{k+1} - \varepsilon_k)}{\varepsilon_k + (\varepsilon_{k+1} - \varepsilon_k)L_{k+1} - \frac{a_{x,k+1}a_{y,k+1}a_{z,k+1}}{a_{x,k}a_{y,k}a_{z,k}}(\varepsilon_{k+1} - \varepsilon_k)L_k} \right) \tag{3.11}$$

The $j$-th component ($j = x, y, z$) of effective permittivity of ellipsoids aligned to the electric field is given by Equation 3.12.

$$1 - \varphi = \left( \frac{\varepsilon_{\mathrm{eff},j} - \varepsilon_{\mathrm{i},j}}{\varepsilon_{\mathrm{h},j} - \varepsilon_{\mathrm{i},j}} \right) \left( \frac{\varepsilon_{\mathrm{h},j}}{\varepsilon_{\mathrm{eff},j}} \right)^{L_j} \tag{3.12}$$

The HB formula, for two phases is said to provide excellent agreement with experiments for volume fractions up to $\varphi < 0.8$ for colloidal suspensions containing homogeneous spherical particles [47].

### 3.2.3 Landau-Lifshitz-Looyenga formula

The Landau-Lifshitz-Looyenga formula (LLL) was independently developed by Landau and Lifshitz [64] and Looyenga [65], respecitvely using different approaches. In contrary to the MG or HB, the LLL formula does not take the geometry of the inclusion into account. In case of multiphase particles (e.g. shelled ellipsoids) the effective permittivity of the particle is calculated according to the MG or HB formulas (Equation 3.11). LLL is a special case of Lichtenecker's formula [46] with $m = 1/3$. For an isotropic inclusion results

$$\varepsilon_{\mathrm{eff}} = \left( \varphi_{\mathrm{i}} \sqrt[3]{\varepsilon_{\mathrm{i}}} + (1 - \varphi_{\mathrm{i}}) \sqrt[3]{\varepsilon_{\mathrm{h}}} \right)^3 \tag{3.13}$$

and for an anisotropic one

$$\varepsilon_{\mathrm{eff}} = \left( \frac{1}{3} \sum_{j=x,y,z} \varphi_{\mathrm{i}} \sqrt[3]{\varepsilon_{\mathrm{i},j}} + (1 - \varphi_{\mathrm{i}}) \sqrt[3]{\varepsilon_{\mathrm{h}}} \right)^3 . \tag{3.14}$$

Similarly to the MG, the LLL formula does not take any interparticle interactions into account, therefore one would expect a validity limit around $\varphi < 0.1$. However, it was shown in experiments that for certain biphasic mixtures with statistically distributed particle size the LLL formula provides good agreement for almost any particle volume fraction [66].

### 3.2.4 Spectral density function approach

Another analytical method for modeling various kinds of shapes is the spectral decomposition method or spectral density function approach developed in [45] This method is based on the separation of geometry and material properties. The general formulation is given by Equation 3.15 with $g(x)$ the spectral density function (topological or geometrical term) and $p(x) = (s + x)^{-1}$ (dielectric term). Additionally, $\int_0^1 g(x)dx = 1$ and $\int_0^1 xg(x)dx = (1 - \varphi)/d$, while $d$ denotes the dimension. It can be noted, that Equation

3.15, similarly to Equation 2.21 refers to the distribution of relaxation times [67].

$$\varepsilon_{\text{eff}} = \varepsilon_0 \left( 1 + \varphi \int_0^1 g(x)p(x)dx \right) \tag{3.15}$$

The spectral density method is relatively fast, since it does not require a discretization of the geometry. However, it was shown that one can separate the geometrical contributions from the pure dielectric response of a composite if and only if the dielectric properties of the constituents are known [67]. In practice experimental data ($\frac{\Delta\varepsilon_1}{\Delta\varepsilon_2}$ in [68]) is used to determine the spectral density function. This procedure belongs to the class of the so-called ill-posed problems and a correct solution is possible only with the use of stabilization techniques [69]. Mention may be also made of the work based on an expansion of the modified spectral density function in terms of Legendre polynomials, the reconstruction of the spectral density function using Padé approximation derived from a constrained minimization problem as well as the approach based on the Monte Carlo integration and constrained least-squares algorithm [70]. The spectral density approach has been applied to the calculation of effective dielectric properties of cells in e.g. [53], [68], [69] and [71]). Depending on the choice/determination of $g(x)$ it is possible to extract a binary mixture equation, as e.g. the MG [72] or the LLL formula [67].
An important drawback of the approach is the fact, that the analytical description gets very cumbersome with increasing complexity of the shape of the inclusion [73] and number of phases − a situation clearly occuring in biological tissue.

## 3.3 Percolation

The two-phase MG formula and the Bruggeman formula provide exact solutions for the Hashin and Milton structure, respectively shown in Figure 3.2.
The Hashin structure consists of space-filling shelled spheres which are identical up to their sizes, having a constant shell thickness/outer radius ratio. The cores of the spheres and host/background are from the same, but different from the shell material. The size distribution of the spheres filling the entire space ranges from a certain maximal size to infinitesimally small.
The Milton structure consists again of space-filling homogeneous spheres of two different materials which are well-separated on a specific length scale, embedded in a host consisting of much smaller well-separated spheres of the two materials, and so on [74]. For the following purpose the MG and BR formulas are written in terms of complex conductivites instead of complex permittivities. According to the Kramers-Kroning-relations the two expressions are interchangeable. Consequently, the MG and BR formulas for conductivities are given by

$$\frac{\sigma_{\text{eff}} - \sigma_1}{\sigma_{\text{eff}} - 2\sigma_1} = \varphi_2 \frac{\sigma_2 - \sigma_1}{\sigma_2 + 2\sigma_1} \tag{3.16}$$

and

$$\varphi_1 \frac{\sigma_1 - \sigma_{\text{eff}}}{\sigma_1 + 2\sigma_{\text{eff}}} = \varphi_2 \frac{\sigma_2 - \sigma_{\text{eff}}}{\sigma_2 + 2\sigma_{\text{eff}}}. \tag{3.17}$$

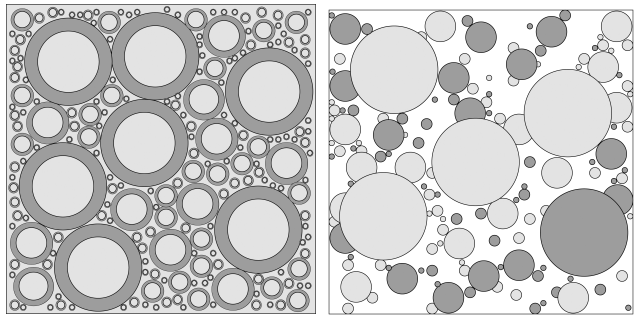

(a) (b)

**Figure 3.2:** The Hashin (a) and the Milton structure (b), adapted from [74].

Looking at the form of the MG and BR formulas a fundamental difference can be observed: The MG formula is unsymmetric with respect to material 1 and material 2, meaning an interchange would result in two different effective permittivities, whereas the BR formula is symmetric. With the two described structures in mind, the volume fraction limits of both formulas can be explained from a toplogical point of view: The materials in the Hashin structure always stay separated, meaning they do not form connected paths and the MG formula is suitable for dilute suspensions with well-separated particles. In contrast, above a critical volume fraction of material 2 ($\varphi_2 = 1/3$) the materials in the Milton structure form connected paths, a phenomenon called *percolation*. As a consequence above this volume fraction limit the BR mixture is conductive for the case $\sigma_1 = 0$ and $\sigma_2 \neq 0$ while the MG formula, where the effective material exhibits a non-zero conductivity only if $\varphi_2 = 1$ at $f = 0$ Hz. Composites exhibit a drastic change in dielectric properties if the inclusion exceeds the percolation limit yielding the formation of connected regions [46].

Percolation [75], [76] is of certain importance when it comes to biological tissue since cells are not always well-separated from each other but connected via gap junctions. A similar situation also occurs during mitosis. Tissue types, such as liver tissue have already been modeled as a porous medium using percolation theory [77]. Since other physical properties of tissue often relate to dielectric properties description of e.g. viscoelastic properties of collagen and mesenchymal tissue [78] or in-vitro capillary growth [79] within the percolation theory are worth to be mentioned.

## 3.4 Analysis, results and discussion

The main focus of this chapter consisted in the implementation of three mixing formulas in MATLAB® while being able to vary any available parameter (including consequent as well as simultaneous variation of more than one parameter). For further information and codes see Appendix B.1. Besides the implementation of the mixing formulas a

**Table 3.1:** Geometrical and material parameters of spherical and ellipsoidal cell models.

| System | | $(d_x\ d_y\ d_z)$ [$\mu$m] | $\rho_m$ [nm] | $\varepsilon_\mathrm{h}$ | $\sigma_\mathrm{DC,h}$ [S/m] | $\varepsilon_1$ | $\sigma_\mathrm{DC,1}$ [S/m] | $\varepsilon_2$ | $\sigma_\mathrm{DC,2}$ [S/m] |
|---|---|---|---|---|---|---|---|---|---|
| Sphere | S1 | (10 10 10) | | 80 | 1.2 | 9.04 | $10^{-6}$ | | |
| Shelled sphere 1 | SS1 | (0.075 0.075 0.075) | 5.5 | 80 | 1.2 | 9.04 | $10^{-6}$ | 50 | 0.5 |
| Shelled sphere 2 | SS2 | (10 10 10) | 7 | 80 | 1.2 | 9.04 | $10^{-6}$ | 50 | 0.5 |
| Ellipsoid | E1 | (0.075 0.075 0.1) | | 80 | 1.2 | 9.04 | $10^{-6}$ | | |
| Shelled ellipsoid 1 | ES1 | (5 15 50) | 7 | 80 | 1.2 | 9.04 | $10^{-6}$ | 50 | 0.5 |
| Shelled ellipsoid 2 | ES2 | (0.075 0.075 0.1) | 5.5 | 80 | 1.2 | 9.04 | $10^{-6}$ | 50 | 0.5 |
| Cylinder | C | (0.5 0.5 $\infty$) | | 80 | 1.2 | 9.04 | $10^{-6}$ | | |

first analysis of the obtained spectra with respect to parameter variations relevant for biological tissue can already be made. The focus lies on the comparison of the three formulas, especially the difference between MG and HB formula for different volume fractions: $\varphi = 0.1$ limit of MG, $\varphi = 0.5$ above the MG limit, $\varphi = \pi/6$, the maximal volume fraction of an ellipsoidal inclusion in a simple cubic unit cell and $\varphi = 0.8$, the validity limit of the HB formula. Further parameter variations are performed for the shape, the particle inhomogeneity (number of shells) and finally for material parameters of the shell in an specific particle. The material and dielectric parameters of all models are listed in Table 3.1 unless the specific reference papers are mentioned.

Here, the most important spectral feature is the $\beta$-dispersion around 1 MHz which is caused by the combination of dimensions and dielectric contrast and therefore contained in the model. The frequency range was chosen to be relatively broad between 1 kHz and 1 GHz bearing in mind, that at the lower and higher end of the spectrum other dispersion mechanisms which are not modeled take place as well.

### 3.4.1 Spherical inclusions

First, a simple single-shelled sphere model is introduced. Single-shelled models were e.g. presented in [12],[15], [49] and [50]. Figure 3.3 shows a comparison between the three different mixing formulas at three different volume fractions. It can be seen that the largest variations occur for low frequencies and high volume fractions. Especially the LLL formula deviates from the MG and HB formula. This clearly indicates the significance of the shape of the inclusion.

Whereas the permittivity of the cell membrane will not alter very much since the phospholipid bilayer structure itself is very stable and inert to physiological and non-pathological changes, the conductivity can vary mainly depending on the ion channel density and activity as well as on the state of the cell membrane. The translation these physiological facts into parameters of a dielectric model is subject of the next scenario: The membrane conductivity is varied over several orders of magnitude while keeping the membrane permittivity constant. The dielectric spectra in Figure 3.4 also exhibit varia-

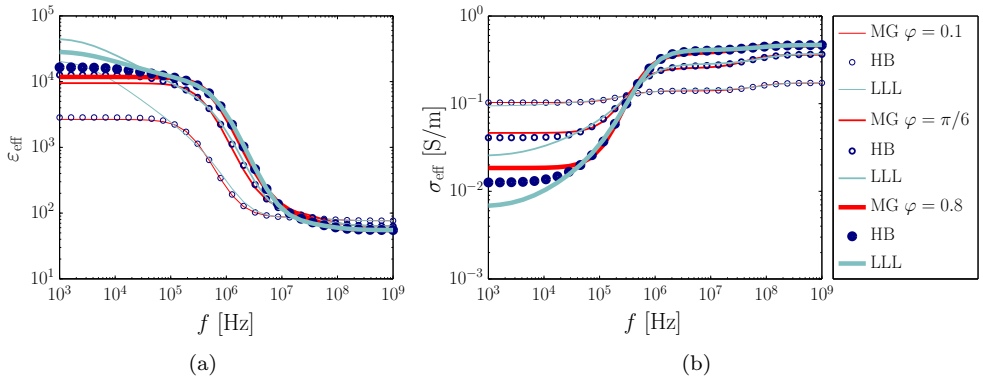


**Figure 3.3:** Effective permittivity (a) and conductivity (b) of a shelled spherical inclusion SS1 (for parameters see Table 3.1). The effective properties were calculated using the MG, HB and LLL formulas at three different volume fractions.

tions over several orders of magnitude at low and high frequencies. The center frequency of the dispersion shifts as well. This can be explained with the drastic variation of the dielectric contrast between cytoplasm, membrane and extracellular medium. The larger the contrast between the thin membrane the larger the capacitive charging responsible for the dispersion. The effect is even more pronounced at high volume fractions. The case with the highest constrast, the distinction between living and dead cells has been performed in [25].

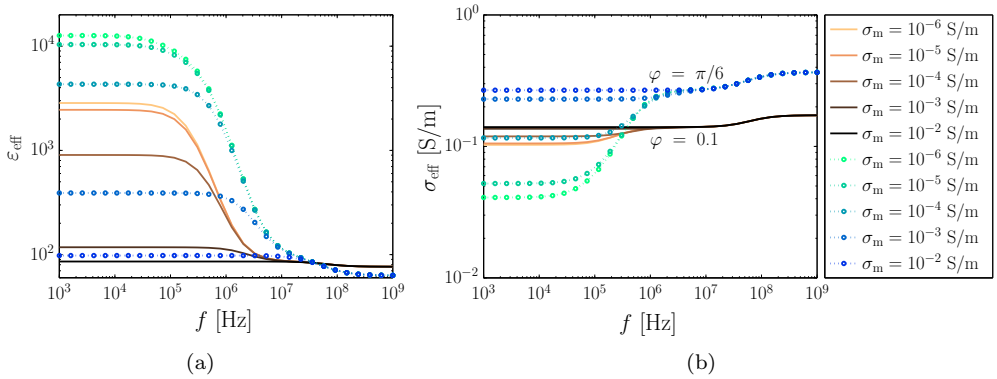


**Figure 3.4:** Effective permittivity (a) and conductivity (b) of a shelled spherical inclusion SS1 (for parameters see Table 3.1) calculated with the HB formula. Variation of the membrane conductivity $\sigma_{\text{m}}$ for two different volume fractions.

However, smaller changes caused by varying ion channel activity are a possible target for monitoring. However, in that case the impactof only small variations of ± 10 % would have to be investigated.

Double-shelled spherical inclusions were already used in order to model lymphocytes [54] and other cells [55]. In [56] a five-shelled model with a bound water layer of 0.5 nm at the cytosolic and extracellular site of the cell membrane as well as a seven-shelled model including bound water within the cell membrane as well. Here, the starting point is given by the reference single-shelled sphere. The effect of the bound water, nucleus and both is shown in Figure 3.5 for two different volume fractions. The geometrical and material parameters for the nuclear membrane and nucleus were taken from [80], the parameters for the bound water from [81]. The spectra for the effective dielectric parameters are given in Figure 3.5, the relative deviations with respect to the single-shelled spherical model in Figure 3.6. At $\varphi = 0.1$ almost no effect occurs but at $\varphi = \pi/6$ significant deviations of up to 40% with respect to the reference sphere can be observed. The three models exhibit very similar behaviour, the variations among them being under 5% in the chosen frequency range. Surprisingly, the model including nucleus and bound water deviates only by a fraction of a percent from the model only containing the bound water layers.

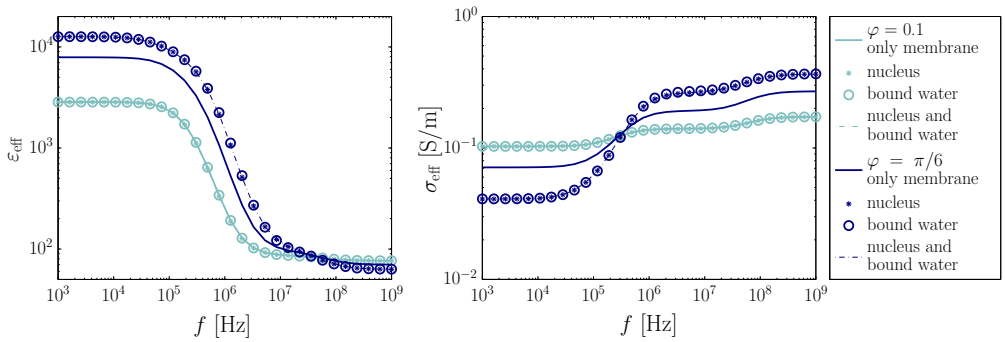


**Figure 3.5:** Effective permittivity (a) and conductivity (b) for the shelled spherical inclusion SS1 (for parameters see Table 3.1), triple-shelled sphere (SS1 including nuclear membrane and nucleus), triple-shelled sphere (SS1 including a bound water layer on each side of the cell membrane) and five-shelled sphere (reference sphere with nucleus and bound water to cell membrane) for two different volume fractions.

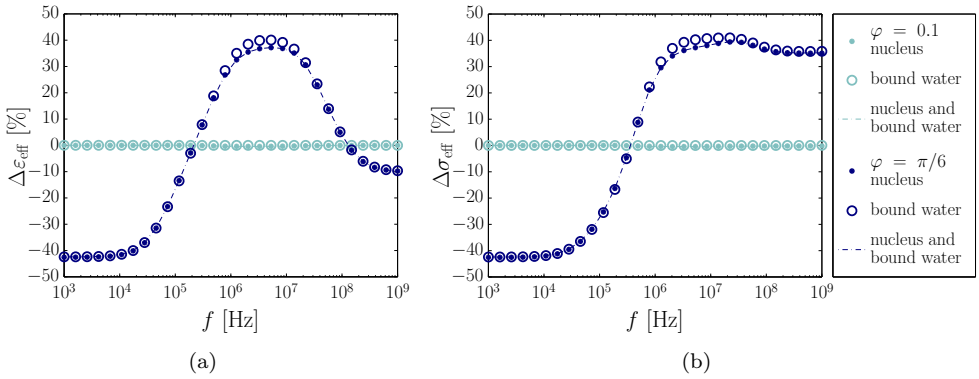


**Figure 3.6:** Relative deviations of the effective permittivity (a) and conductivity (b) of multi-shelled spherical inclusions from Figure 3.5 with respect to the values for the reference sphere SS1.

### 3.4.2 Ellipsoidal inclusions

In order to see the impact of anisotropy all calculable effective properties of an arbitrary ellipsoid with $a \neq b \neq c$ (parameters given in Table 3.1) for $\varphi = 0.1$ are given in Figure 3.7. The spectra are obtained with the MG formula. Displayed are the different cases where the external field is applied in $x$-direction (parallel to the principal axis of the ellipsoid $a_x$; case '$xx$'), $y$- and $z$-direction, respectively (cases '$yy$' and '$zz$'). Those three cases $\varepsilon^*_{xx}$, $\varepsilon^*_{yy}$ and $\varepsilon^*_{zz}$ provide the diagonal dielectric tensor $\bar{\varepsilon}^*$ of the ellipsoidal inclusion

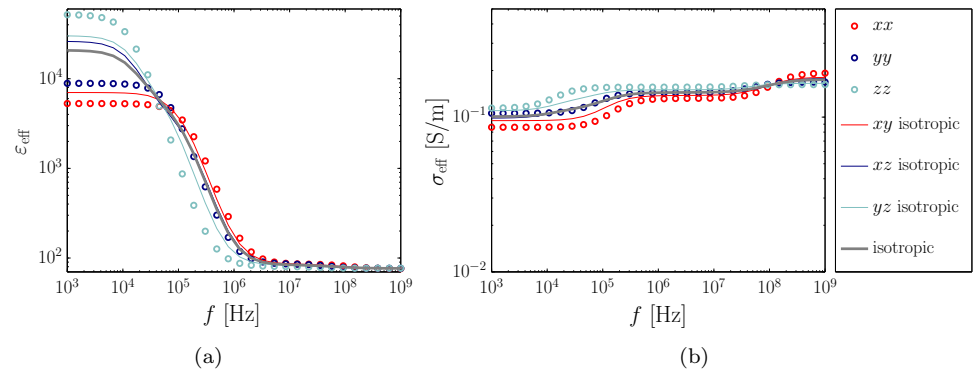


**Figure 3.7:** Effective permittivity (a) and conductivity (b) of a shelled ellipsoidal inclusion ES1 (for parameters see Table 3.1) at $\varphi = 0.1$ calculated with the MG formula. Shown are different orientations of the particle with respect to the external electric field.

(a) (b)

**Figure 3.8:** Confocal (a) and concentric (b) ellipsoid.

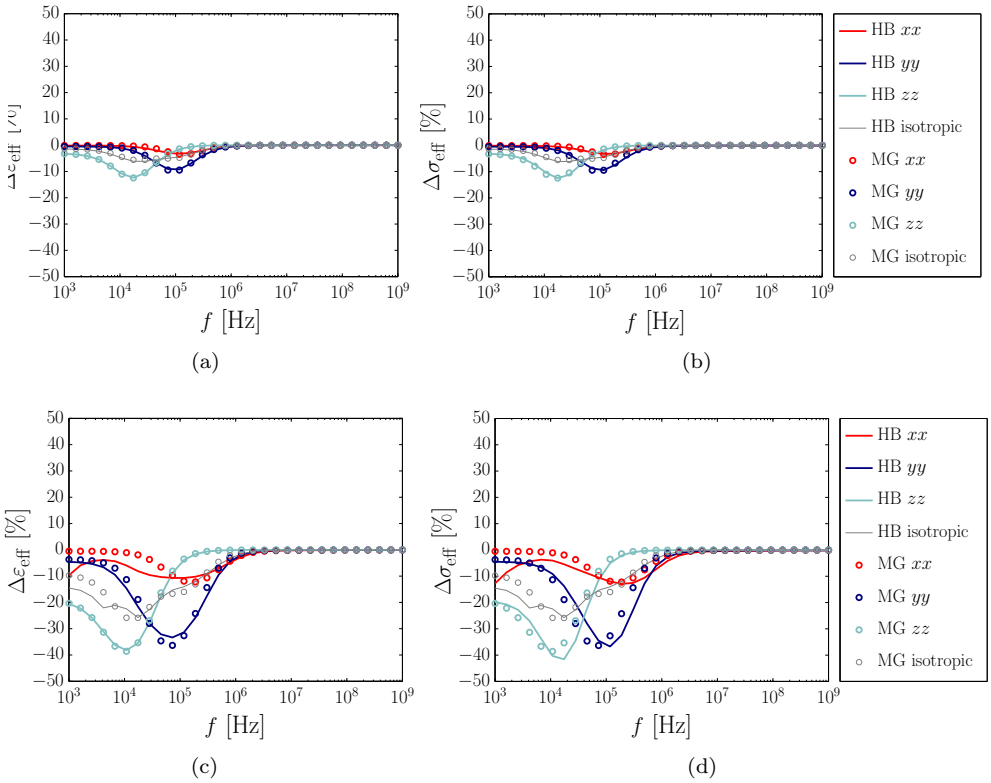


**Figure 3.9:** Relative deviations of effective dielectric parameters between a concentric and confocal ellipsoidal inclusion ES1 (for parameters see Table 3.1) calculated with the HB and MG formulas. In the concentric case the membrane thickness corresponds to the membrane thickness in $x$-direction of the confocal model. Shown are the volume fractions $\varphi = 0.1$ in (a) and (b) and $\varphi = 0.5$ in (c) and (d).

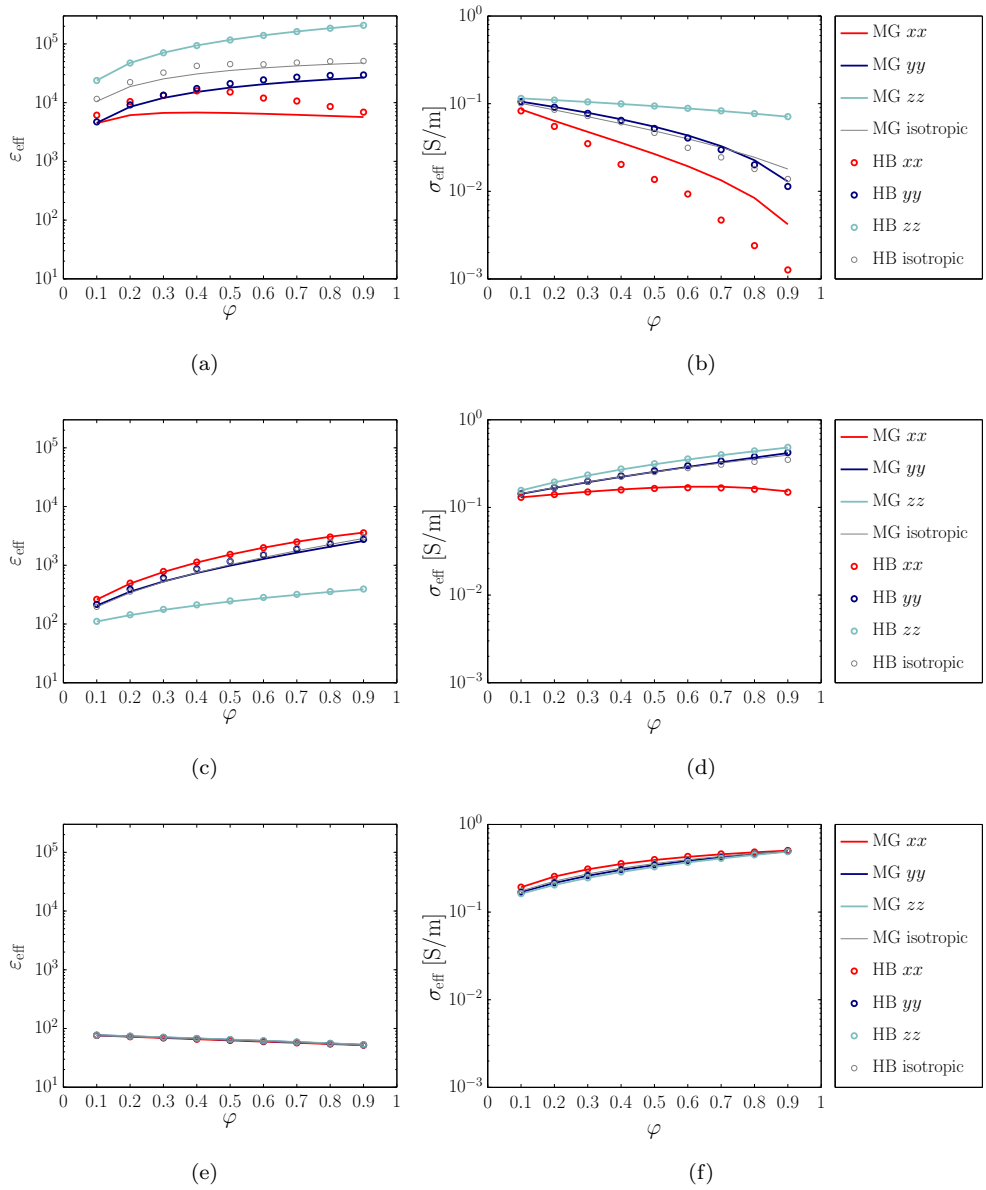


**Figure 3.10:** Effective permittivity ((a), (c) and (e)) and conductivity ((b), (d) and (f)) of a shelled ellipsoidal inclusion (concentric approximation) ES1 calculated with the MG and HB formula as a function of volume fraction $\varphi$ at three different frequencies.

embedded in the host medium. In the '$xy$-isotropic' case the ellipsoids are randomly oriented in the $x-y$-plane while the field is oriented in $x$- (or $y$-) direction. The cases '$xz$-isotropic' and '$yz$-isotropic' are set up correspondingly. In the 'isotropic' case the ellipsoids are randomly oriented in all three space directions. Another interesting aspect is the difference between the exact solution for shelled confocal ellipsoids and the concentric approximation for an arbitrary ellipsoid with $a \neq b \neq c$. The two shapes are shown in Figure 3.8. The approximation seems feasible due to the small thickness of the cell membrane. Obviously, again the influence of the geometry manifests itself at the lower end of the considered frequency range. However, it is difficult to judge the error of the approximation, i.e. how much the values differ from those of the 'real' concentric structure without having an exact, numerical simulation. This comparison will be provided in the Chapter 4.
Relative deviations between the exact solution of the MG and HB formulas for confocal ellipsoids and the concentric approximation where the overall shell thickness corresponds to the shell thickness in $x$-direction from the confocal case are displayed in Figure 3.9. Significant variations are limited to frequencies $< 100$ kHz. However, the error largely increases with increasing volume fraction. The variations for different volume fractions is again frequency dependent exhibiting the largest variations for low frequencies again as shown in Figure 3.10. The vanishing influence of the geometry can be nicely seen in Figure 3.10(e) and 3.10(f).

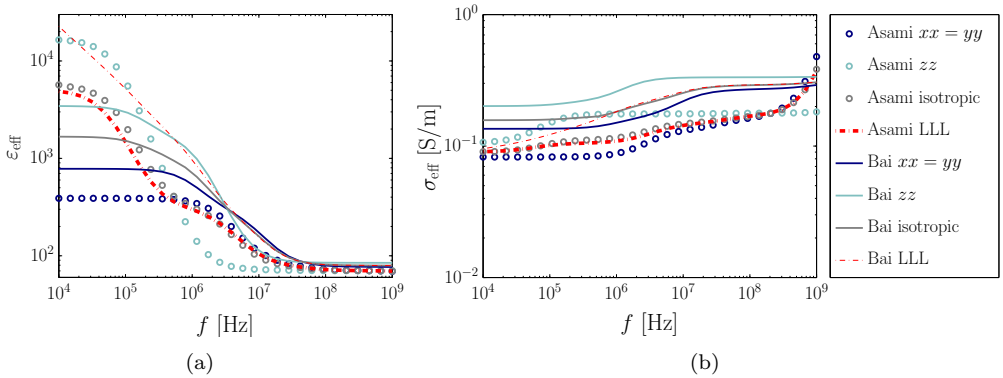


**Figure 3.11:** Effective permittivity (a) and conductivity (b) of the double-shell [51] (Asami) and triple-shell [58] (Bai) elllipsoidal model of the *E. coli* bacterium at $\varphi = 0.4$ calculated with the HB formula (concentric approximation) and LLL formula.

A popular case for modeling by mixing formulas is the *E. coli* bacterium and red blood cell, the erythrocyte. In Figure 3.11 and 3.12 spectra of three-shelled and single shelled ellipsoids from [51], [58] and [82] are reproduced. The model in [58] has an inner and outer membrane additional to the cell membrane, with dielectric parameters in between those of the membrane and cytoplasm/extracellular medium. Especially the triple-shell model

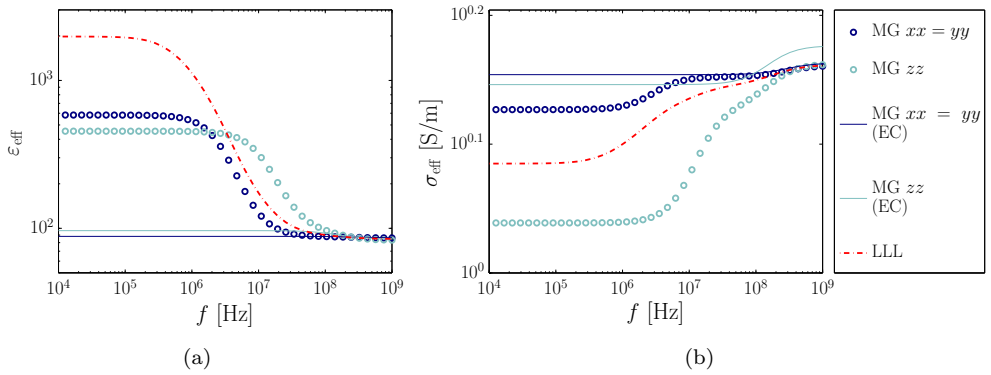


**Figure 3.12:** Effective permittivity (a) and conductivity (b) of the erythrocyte model from [82]. EC denotes the biphasic mixture without membrane (only cytoplasm and extracellular medium).

shows a decrease in the permittivity increment due to the reduced dielectric contrast.

### 3.4.3 Cylindrical inclusions

Finally, the dielectric spectra for homogeneous cylindrical inclusions with an ellipsoidal cross-section and the axis in $z$-direction for a volume fraction of $\varphi = 0.3$ and parameters given in Table 3.1 calculated with both, the MG and HB formula are given in Figure 3.13. This geometrical case is e.g. related to structures occuring in tissue on a larger scale, such as blood vessels. Since the particle is homogeneous the capacitive charging

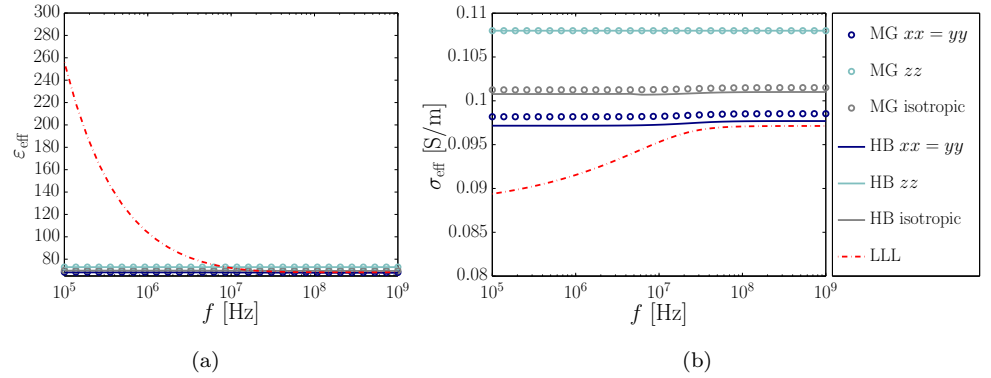


**Figure 3.13:** Effective permittivity (a) and conductivity (b) of a homogeneous cylindrical inclusion with a circular cross-section calculated with three different mixture formulas.

does not happen on such a small scale as in the case of shelled particles. Therefore, the dispersion is only very weak. Again, the influence of interparticle interactions and the consequent difference between spectra obtained from the MG and HB formulas is obvious for the dielectric parameters in $x$- and $y$-direction.

## 3.5 Conclusion

The fact that an initial approximation of such a complex system as a biological cell by a shelled spherical particle without any other features leads to the correct track is not completely self-evident, but turns out to be reasonable in the end. The Maxwell-Garnett, Hanai-Bruggeman and Landau-Lifshitz-Looyenga formulas allowing for arbitrary parameter variations such as arbitrary numbers of shells were successfully implemented. Analytical approximations provide a good start for modeling of composites with microscopic shelled particles since the main feature of spectra of biological cell models in the MHz range, the capacitive charging of an insulating shell with good conducting high-permittivity media in- and outside is part of the model. The MG is an efficient way to calculate effective dielectric properties at small volume fractions for spherical, ellipsoidal and cylindrical inclusions. For volume fractions larger than 0.1 the HB formula is more appropriate.

The case of cell membrane conductivity variation has to be investigated further. An extension of the presented simple model by the inclusion of ion channels might be required. However, it is possible that the ion channel activity exhibits large variations and oscillations but the time scale is such that the effects average out in the bulk material.

Overall it can be stated the effective properties for cell-like structures below the center frequency of the $\beta$-dispersion are sensitive to geometrical variations and volume fraction. The question to which extent the MG and HB formulas can be used in order to approximate concentric ellipsoidal inclusions in an environment, and also other questions have to be clarified with the help of numerical models. But it can be stated, that within a certain defined parameter range mixing formulas can serve as a basis for assessing the necessary degree of complexity. Those findings are not only relevant for biological cells but all similar types of comopsites such as e.g. soils [83].

# 4 Numerical modeling of composite materials

Although being computationally inexpensive the mixing formulas imply restrictions on shape and volume fraction of cells in tissue or suspensions. A way how to overcome those limitations are numerical models. However, the major issue when modeling cells numerically is the large aspect ratio between the size of the entire cell (few $\mu$m) and the dimensions of the cell membrane (few nm). Since it is required to accurately solve the electric potential in regions with a large gradient − up to the short-circuit frequency this is the case near the cell membrane this region has to be sufficiently discretized. Often, the system matrix of such models will contain several millions of elements. Due to the increased availability of computational resources even the solution of large problems becomes realisitic. Unfortunately, large aspect ratios are a challenge not only in terms of computational power but also for numerical precision in geometry generation and discretization. Therefore, workarounds have to be found in order to reduce the sensitivity towards numerical errors in geometry and mesh generation besides the reduction of the matrix size and the choice of efficient solvers. Numerical models are e.g. provided in [82], [3], [52], [53], [84], [85], [86], [87] and [88].

Mixing formulas are a useful tool in order to calculate the effective dielectric properties of cell suspensions but restricted in terms of shape and volume fraction. As the shape of inclusion shows a clear impact on the dielectric spectrum in the MHz region numerical models of realistically shaped biological cells are needed in order to assess the range of observable deviations due to certain changes in cellular geometry. Besides the development of an efficient and flexible modeling framework, the main target of this chapter is the quantification of changes in the geometric properties such as cellular volume fraction and cell shape. The investigations are carried out in order to estimate how, at which frequencies and with which magnitude the dielectric spectra depend on shape variations only. Before realizing a measurement setup this knowledge is advantageous in order to optimize it or to answer the question if an effect is measurable at all. Especially for the development of instrumentation for single-cell monitoring also the probe geometry and the specific measurement configuration become relevant.

## 4.1 Concept

As introduced in Chapter 2 and demonstrated in Chapter 3 the dominating feature in dielectric spectra of biological cell suspensions and tissues in the MHz range is the $\beta$-dispersion caused by interfacial polarization of the cell membrane. However, even as the expected changes due to variations in microstructure are smaller compared to the men-

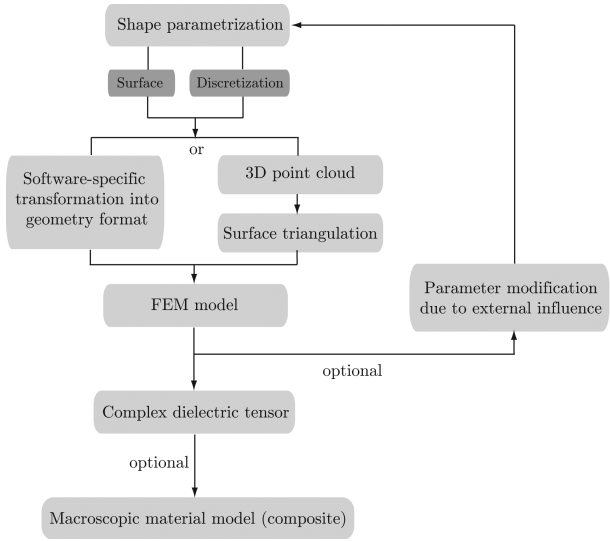


**Figure 4.1:** Flow diagram for the numerical modeling of a composite material.

tioned general characteristic variation of cellular volume fraction, dielectric properties of intra- and extracellular medium (e.g. ion concentration, presence of organelles) or cell shape still have a measurable influence on the dielectric spectrum. In order to uniquely correlate cellular features and features of the dielectric spectrum a sophisticated model of cell suspensions or tissues is required.

Besides the theoretical validity bounds in practice the spherical or ellipsoidal shapes imply an upper volume fraction limit of the inclusion. The volume fraction limit for simple cubic (SCU) packing of spheres and ellipsoids is $\varphi = \pi/6 \approx 0.5236$. A higher limit of $\varphi = \pi/\sqrt{18} \approx 0.7405$ is obtained by spheres forming lattices with hexagonal close packed (HCP), face centered cubic (FCC) or body centered cubic (BCC) unit cells. The so far known maximum of $\varphi = 0.7707$ can be reached with a specific crystal (i.e. non-random) packing of ellipsoids with certain semi-axis ratios [89]. These volume fraction limits are often exceeded in tissues since cells often do not have spherical or ellipsoidal geometry and are tightly packed. For example in the basal layer of the human epidermis the volume fraction of cells is $\varphi = 0.83$ [90].
Deviations from spherical shape clearly have an impact on the dielectric spectra. These and other shape effects were already studied in [52], [53], [84], [85], [86] and [82]. In [3] and [88] a piece of tissue was modeled as a brick-like structure.

The largest flexibility concerning shape generation provide numerical simulations. Moreover, implementation of inter-particle interactions is straight-forward: Stacking and packing of single cells enables the calculation of the dielectric tensor of cell suspensions. The first step is the generation of a geometry and a mesh. Unfortunately, the

expectiation that available computer memory will be the only limitation is not correct. In systems with large aspect ratios as presented here the occurrence of small distances can cause numerical problems potentially leading to a failure of geometry and/or mesh generation. However, once the geometry and a corresponding mesh is set up the calculation of the cell's properties is almost entirely limited by the size of the system of equations and therefore by the available computer memory.
In this work we propose a new framework in order to efficiently model cell-like structures comprising the steps depicted in Figure 4.1. The principal approach consists of implicitly representing the cell suspension as a periodic assembly of unit cells, each containing a single centered particle (biological cell). The unit cell is consecutively exposed to an external homogeneous electric field in all three spatial directions followed by the extraction of the dielectric tensor $\bar{\varepsilon}^*$ of the unit cell.

## 4.2 Numerical method

The solution of differential or partial differential equations as the introduced Maxwell equations (Equations 2.1 to 2.4) usually requires numerical methods. In the past, cells exposed to electromagnetic fields were usually modeled numerically using the Finite-Differenc Method (FDM) [91], [92], [93] or the Finite Integration Technique (Finite-Integration Technique (FIT)) [88]. Another method, not to be confused with equivalent circuit representation by Cole-Cole type material models is the equivalent circuit method. In this approach, e. g. employed in [94] for cell modeling each discretization cell is represented by an equivalent circuit and the solution is obtained without solving partial differential equations as in most other methods. The Finite-Element Method (FEM) was also employed for biological cells [14], [52] and [87] and dielectric mixtures in general [95] and [96].
Here, FEM is preferred to FDM because FEM can handle the most delicate part of the model, the cell membrane. In FEM material boundaries coincide with element boundaries and therefore each element belongs to a defined medium. No averaging or interpolation of material parameters is needed and the only error concerning this aspect is caused by the domain discretization error [97], [98]. Furthermore, FEM provides a more flexible approximation of curved boundaries by an unstructured grid, nonuniform element sizes and locally enhanced mesh densities better resolving small features [99]. Non-regular, non-cartesian grid refinement is usually not implemented in FDM software on a standard basis [100]. The mentioned issues can cause accuracy problems, especially in case of thin layers with curved boundaries, which are present in form of cell membranes. Even though FEM requires larger computational effort compared to FDM the former is preferred since it offers higher accuracy [101].

As the dimensions of the geometry are much smaller than the smallest wavelength of the electromagnetic field and the skin depth is much larger than the geometry, a quasi-static approximation of the problem can be applied and only the electric potential $V$ has to be

evaluated according to

$$-\nabla\cdot\left(\varepsilon^*\nabla\frac{\partial}{\partial t}V\right)=0. \tag{4.1}$$

For the numerical evaluation of Equation 4.1 the FEM based commercial simulation software COMSOL Multiphysics® version 3.5a with the module 'quasi-statics for electromagnetics' was used.

A cell, no matter which shape has to be placed in a unit cell filled with extracellular medium. The absolute dimensions of the (biological) cell and the desired volume fraction determine the dimensions of the unit cell. The biological cell is centered in the unit cell. In other words, the walls of the unit cell in $x$-direction are equidistant from $x_{\min}$ and $x_{\max}$ of the biological cell, the same applies for the $y$- and $z$-direction. An electric field is applied between unit cell walls placed oppositely to each other, the remaining four walls are perfect magnetic conductors (PMCs). This corresponds to the cell being in an idealized parallel plate capacitor setup. The effective dielectric properties of the biological cell in in $x$-, $y$- and $z$-direction are obtained from the admittance. The components $\varepsilon^*_{xx}$, $\varepsilon^*_{yy}$ and $\varepsilon^*_{zz}$ form the diagonal complex dielectric tensor $\bar{\varepsilon^*}$ of the single cell.
Now, the PMC boundary condition not only prevents a potentially emerging fringing of the electric field but together with the electrodes set to perfectly electric conductors (PECs) also imply a periodic structure in the plane perpendicular to the electric field. Consequently, if non-spherical cells in suspensions or tissues have a preferred orientation and the periodicity is given by mentioned unit cell, the macroscopic effective dielectric properties of such a composite material are described by the dielectric tensor $\bar{\varepsilon^*}$. Electric fields of non-invasive probes (e.g. coaxial probes [34], [33] or fringing field sensors) are usually inhomogeneous on the macroscopic scale but homogeneous on the scale of a single cell. Consequently, the measurement of the material properties of the composite can provide information on the microstructure of the material under test [102]. Vice versa, modeling of a single cell can be sufficient in order to describe macroscopic effective dielectric properties.

## 4.3 Geometry

Since the parameter space can be arbitrarily large it would be convenient to describe e.g. the cell shape with as few parameters as possible while being able to cover a wide variety of cell morphologies. Parametrization of cells (red blood cells (RBCs), fission yeast cells) from images has already been described in [103] and [104] with appropriate combinations of spherical harmonics. Another analytical parametrization of an echinocyte, a particularly shaped RBC was given in [91]. Discocytes, also a form of RBCs, were represented by rotated Jacobi elliptic functions e.g. in [93] or [87] and references therein. [84] and [85] used rotated Cassini curves in order to model RBCs and rotation of combined trigonometric functions provided pear-shaped models of cells during division. In [85] the effect of geometrical variations of the cell shape on dielectric spectra has been explicitly investigated. Except of the method in [104] the mentioned parameterizations

have rather restricted flexibility in shape variation, i.e. they offer only a small number of symmetry groups compared to the method presented in this work.

Another aspect already mentioned in Section 4.1 is the large aspect ratio between cell size and membrane thickness. Therefore, implementation issues are addressed separately in Section 4.7.

### 4.3.1 Surface parametrization

An approach to model biological structures was suggested in [105] and [106]. The presented so-called superformula (SF) is a simple geometric equation able to reproduce the morphology of many plants, flowers, animals (e.g. snail shells) generating a wide variety of surfaces that are dependent on only six parameters. The SF is a generalization of superquadrics and superellipses. Each point $\mathbf{p}(\phi, \theta) = (x, y, z)$ where $\phi \in [-\pi, \pi]$ and $\theta \in [-\pi/2, \pi/2]$ since the 2D SF can be extended to 3D using the spherical product [105]:

$$p_1 = \left| \frac{1}{a} \cos\left(m\frac{\phi}{4}\right) \right|^{n_2} + \left| \frac{1}{b} \sin\left(m\frac{\phi}{4}\right) \right|^{n_3} \tag{4.2}$$

$$p_2 = \left| \frac{1}{a} \cos\left(m\frac{\theta}{4}\right) \right|^{n_2} + \left| \frac{1}{b} \sin\left(m\frac{\theta}{4}\right) \right|^{n_3} \tag{4.3}$$

$$r_1 = \frac{1}{\sqrt[n_1]{|p_1|}} \tag{4.4}$$

$$r_2 = \frac{1}{\sqrt[n_1]{|p_2|}} \tag{4.5}$$

$$x = r_1 \cos(\phi) r_2 \cos(\theta) \tag{4.6}$$

$$y = r_1 \sin(\phi) r_2 \cos(\theta) \tag{4.7}$$

$$z = r_2 \sin(\theta) \tag{4.8}$$

The number of discretization points $d$ (see Figure 4.3) is chosen to be equal in the $\phi$- and $\theta$-intervals, therefore the distribution in the $\phi$-interval is half as dense as in the $\theta$ interval which is considered to be sufficient.
By adjusting the parameters many different cell shapes can be generated, e.g. different types of RBCs, box-shaped tissue cells, oval cells and as a special case the simple spheres or ellipsoids. Also a filling of the space beyond the mentioned limit for randomly oriented tightly packed ellipsoids can be obtained: Setting the parameters to $[a\ b\ m\ n_1\ n_2\ n_3] = [1\ 1\ 4\ n_1\ n_2\ n_3]$ the shape of a sphere ($n_1 = n_2 = n_3 = 2$) can be smoothly modified to a superellipsoid, a cube with rounded corners by increasing $n$. This shape transition can occur when e.g. applying external pressure on cell. For the parameter set $[a\ b\ m\ n_1\ n_2\ n_3] = [1\ 1\ 4\ n_1\ 4\ 4]$ the edges can be bent inwards by setting $0 < n_1 < 4$ creating an even more realistic representation of a tissue cell shown in Figure 4.4.

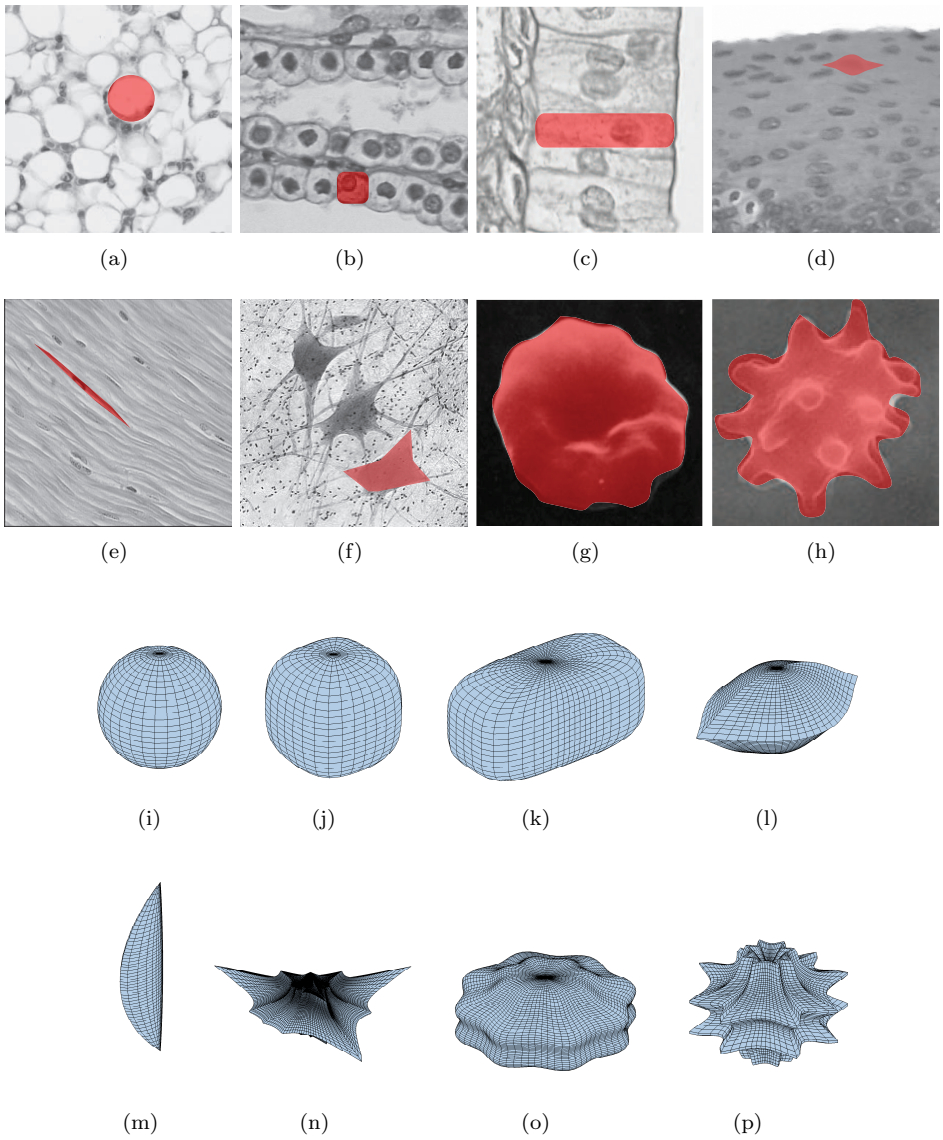


**Figure 4.2:** Various types of biological cells: (a) Adipocyte [107]. (b) Cuboidal epithelium cell in the kidney [108]. (c) Columnar epithelial cell [108]. (d) Stratified squamous epithelial cell of the tongue [108]. (e) Muscle cell [109]. (f) Neuron [110]. (g) RBC, transition state between discocyte (normal state) and echinocyte [111]. (h) RBC, echinocyte form [112]. (i) to (p) Supershape approximations of the cell types depicted in (a) to (h).

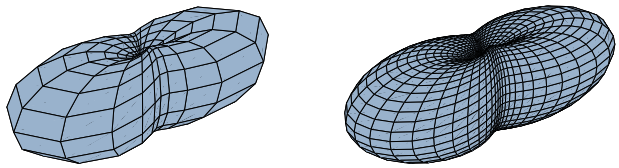

(a) (b)

**Figure 4.3:** Variation of the discretization parameter $d$: $d = 20$ in (a) and $d = 50$ in (b) for the shape $[a\ b\ m\ n_1\ n_2\ n_3] = [1\ 1\ 2\ -0.1\ 2\ 3]$.

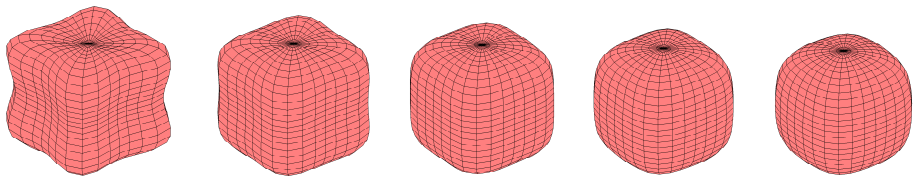

(a) (b) (c) (d) (e)

**Figure 4.4:** Variation of the shape parameter $n_1$ for the shape $[a\ b\ m\ n_1\ n_2\ n_3] = [1\ 1\ 4\ n_1\ 4\ 4]$. $n_1 = 2$ (a), $n_1 = 3$ (b), $n_1 = 4$ (c), $n_1 = 5$ (d) and $n_1 = 6$ (e).

Although the SF cannot produce fully asymmetrical shapes, if e.g. all parameters $[a\ b\ m\ n_1\ n_2\ n_3] \geq 1$ it provides surfaces with a reflection plane ($x$-$y$-plane) as the only symmetry element. Consequently, the lowest symmetry group is $C_{2v}$, compared to $D_{\infty h}$ for functions in the $x$-$y$-plane rotated around the $z$-axis [85] and [87].

### 4.3.2 Offset surface

Modeling of biological cells not only requires the generation of the principle shape but also the modeling of the cell membrane represented by an additional equidistant offset surface. The distance is given by the cell membrane thickness $\rho$. Since the cell shape is given in parametric form it is straight-forward to obtain this offset surface via shifting each point $\mathbf{p}$ of the original surface by a constant value along the normal vector $\mathbf{n}$ [93]. The parametric equation of a point $\mathbf{p}'$ of the offset surface is given by

$$\mathbf{p}'(\phi, \theta) = \mathbf{p}(\phi, \theta) + \rho \mathbf{n}(\phi, \theta) \tag{4.9}$$

where

$$\mathbf{n}(\phi, \theta) = \frac{\frac{\partial \mathbf{p}}{\partial \theta} \times \frac{\partial \mathbf{p}}{\partial \phi}}{\| \frac{\partial \mathbf{p}}{\partial \theta} \times \frac{\partial \mathbf{p}}{\partial \phi} \|}. \tag{4.10}$$

**Table 4.1:** Supershape parameters for selected cells. The parametrizations with an '*' were used in calculations.

| Cell type | Supershape parameters | | | | | | | Figure |
|---|---|---|---|---|---|---|---|---|
| | $a$ | $b$ | $m$ | $n_1$ | $n_2$ | $n_3$ | $d$ | |
| Spherical* | 1 | 1 | 2 | 2 | 2 | 2 | 32 | 4.2(i) |
| Cuboidal* | 1 | 1 | 4 | 5 | 4 | 4 | 32 | 4.2(j) |
| Columnar | 1 | 0.5 | 4 | 4 | 4 | 4 | 50 | 4.2(k) |
| Squamous | 1 | 1 | 4 | 5 | 4 | 4 | 50 | 4.2(l) |
| Muscular | 0.2 | 1 | 2 | 1 | 2 | 2 | 50 | 4.2(m) |
| Nerve | 2 | 1 | 7 | 1 | 1 | 1 | 150 | 4.2(n) |
| Pre-Echinocyte | 2 | 2 | 8 | 3 | 3 | 3 | 80 | 4.2(o) |
| Echinocyte | 1 | 1 | 8 | 8 | 20 | 6 | 80 | 4.2(p) |
| Echinocyte* | 1 | 1 | 8 | 4 | 4 | 5 | 48 | – |
| Keratinocyte* | 0.5 | 0.5 | 4 | 4 | 4 | 4 | 30 | 4.10(a) |

In order to ensure that the new surface is not self-intersecting $\rho$ has to be smaller than the distance from an arbitrary point to the medial axis (for a definition of the medial axis see [113]) illustrated in Figure 4.5 as a simplified 2D sketch. In other words, the theoretical minimal radius of curvature of such features is thus $\rho$. At the $\rho$-limit two parts of the inner membrane surface touch each other. If the radius increases the protuberance also contains a small volume of cytoplasm. If the diameter of this small volume is on the same scale as $\rho$ or even smaller, model geometry and/or mesh generation might potentially fail due to numerical problems. Although the *a priori* determination of $\rho$ from the supershape parameters is difficult, $\rho$ is about two orders of magnitude smaller than the actual cell dimensions. Most cells tend to have a flat surface and the offset surface can be easily generated by aforementioned simple linear translations. Exceptions might be cells with stellae, such as muscle cells or neurons shown in Figures 4.2(m) and (n).

After obtaining the cell's inner and outer surface this geometry has to be introduced into the FEM software. Although some FEM solvers as e.g. COMSOL Multiphysics® and HFSS™ are capable to generate parametric surfaces in 2D and 3D the "singularities", points with coordinates $(0, 0, \pm z)$, may cause problems. For the mentioned $\phi$ and $\theta$ intervals the locations $(0, 0, +z)$ and $(0, 0, -z)$ are degenerated according to the roots of sin and cos. While visual representation of the surface is straight-forward, problems with the mentioned singular points occur if the surface has to be transformed into a "water-tight" boundary or solid geometry object and used for further calculations. Since COMSOL Multiphysics® provides appropriate functions (after removal of $\pi/2$ and $-\pi/2$ from the $\theta$-interval) a valid geometry for further processing can be obtained using a procedure similar to the one suggested for generating solid models from magnetic resonance imaging (MRI) or CT scan data [114]. For further details and code see appendix B.3.

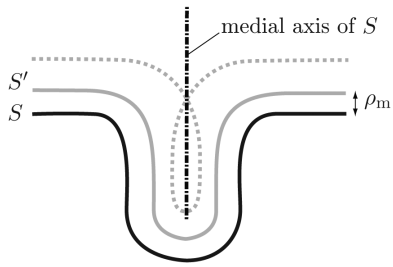


**Figure 4.5:** Original surface $S$ (black solid line) with its medial axis (also a surface in 3D, here represented by the black dot-dashed line) and a valid offset surface $S'$ (light-grey solid line) obtained from Equations 4.9 and 4.10. The dashed light-grey line represents an invalid offset surface, generated if $\rho$ is larger than the distance of a point from $S$ to the medial axis.

If the FEM software does not contain high-level geometry modeling functions a possibility is to reconstruct the shape from a surface triangulation. A very simple but efficient way to do so is presented in the next section.

It has to be mentioned that the SF allows the generation of shapes with non-spherical topology, depending on the choice of the parameters. This can e.g. happen if non-integer values are chosen. Also 'sharp' corners can be produced setting $n_1 < 1$ or $n_2, n_3 < 2$. Even though the cell shape might be appropriate to approximate a certain cell shape, e.g. a neuron depicted in Figures 4.2(f) and 4.2(n) one has to be aware of numerical problems when establishing the mesh as well as with the field solution due to bad-quality tetrahedrons.

## 4.4 Discretization

In FEM software it is often the case that the choice of geometrical elements is restricted to a few basic shapes such as ellipsoid, block or cone. A very wide variety of objects can be created using the mentioned shapes in combination with boolean and other geometrical operations as revolving, lofting, extruding, etc. However, complicated objects often require numerous steps until the final form is elaborated. Additionally, even if automatized in a script the procedure has limited flexibility with respect to the shape of the final object.
The representation of an object by an analytical formula drastically reduces the above-mentioned effort. In the case of COMSOL Multiphysics® and HFSS™ it is possible to generate parametric surfaces in 2D as well as in 3D. Extracting only the unique vertices as a list removes the singularities mentioned in Section 4.3.2 but also causes the loss of connectivity information. From this moment on the shape is purely represented by the $x$-,$y$-, and $z$-coordinate of its points.
Nevertheless, the representation of the surface as a 3D point cloud is a step towards a possible solution. Since most commercial FEM software packages are able to import

a mesh, the point cloud can be triangulated externally and then passed to the FEM software as a mesh. However, calculating a topologically correct surface triangulation of an arbitrarily-shaped closed object is a highly non-trivial task and a research field on its own [115]. In the following two triangulation algorithms are presented: A general one and a simple, effective triangulation algorithm applicable to supershapes generated with the mentioned restrictions on the input parameters.
Many triangulation methods are based on criteria concerning the input point cloud. If those criteria are met the particular procedure theoretically provides a 'correct' triangulation. Two terms have been suggested by [113] and [116] in order to quantify a 'sufficiently' dense sampling: The $r$-sample and least feature size (LFS).
A sample (point cloud) $S$ is an $r$-sample of a surface $F$ when the Euclidean distance from any point $p \in F$ to the nearest sample point is at most $r$ times the distance from $p$ to the nearest point of the medial axis of $F$.

### 4.4.1 Triangulation algorithm

In some cases numerical software packages are able to directly import tetrahedral meshes and create the corresponding geometry. An example for a triangulation algorithm for mesh generation for 3D point clouds of non-convex surfaces is e.g. given in the appendix A. However, in the case of parametric surfaces the idea from the general algorithm of obtaining 'inner' and 'outer' points and computing the Delaunay diagram of the latter and $S$ can be simplified: With supershapes calcualted under the mentioned restrictions an offset surface $S'$ replacing the 'outer' (or 'inner') poles can be generated. The more concave regions $S$ possesses the denser should be $S'$. Depending on the density of $S'$ the simple algorithm requires just one Delaunay triangulation of approximately $2n$ when $n$ is the number of points and very little postprocessing if at all. Generally, in surface triangulation algorithms the Delaunay triangulation is still the most time-consuming step [117] and [118].
The quality of the calculated tesselation depends on the distance of the offset surface for a given discretization $d$, which again depends on the complexity of the shape.
Compared to the general algorithm from appendix A or to other surface triangulations the presented simple algorithm only requires the following implementation steps:

1. Generate offset surface $S'$ (already performed in Section 4.3).
2. Compute the Delaunay triangulation of $S \cup S'$.
3. Keep only those tetrahedrons with one vertex from $S'$ and three from $S$. Remove slivers by normal filtering [113] if needed.
4. The triangles of tetrahedrons obtained in 3. whose vertices all belong to $S$ represent the final triangulation.
5. If required remove edge triangles (and repair holes) or adjust the stretching factor $\delta$ and retriangulate as long as triangulation is not edge- and hole-free (function available).

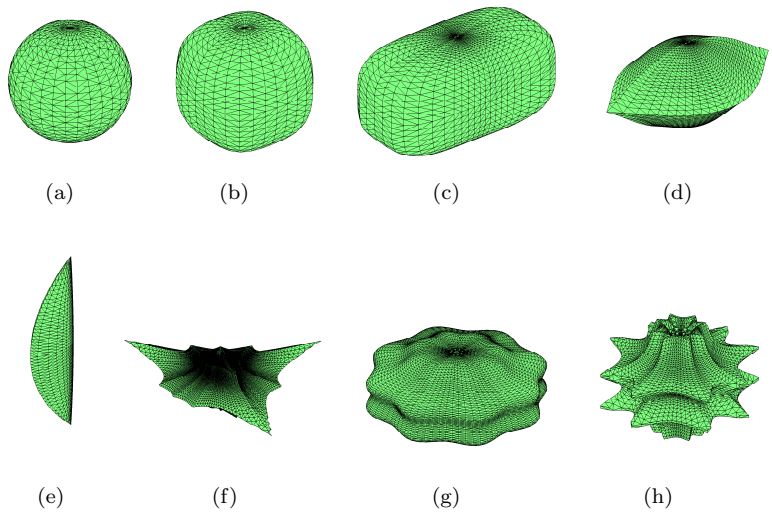


**Figure 4.6:** Surface triangulations of the parametrized biological cells from Figure 4.2 generated with the algorithm introduced in Section 4.4.1.

### 4.4.2 Meshing issues

Similar to the geometry generation also the meshing of the volume causes problems due to the large aspect ratio. In COMSOL Multiphysics® the most frequently occurring issues are failed insertion of points, generation of empty cavities, and so on. In order to resolve this rather unsatisfactory situation and to anyhow obtain an adequate mesh the following can be tried:

1. Mesh edges, boundaries and subdomains in that order
2. Define location of mesh points on edges and boundaries manually
3. Rescale mesh in a certain spatial direction in case of flat/narrow geometries
4. Start with a coarse mesh and perform one or more refinement steps
5. Perform local refinement on subdomains
6. Adaptive mesh refinement would be a good solution but takes extremely long
7. Swept mesh requires sectioning of particle into octants in order to avoid ambiguities for sweep direction

Besides software-specific meshing issues also general ones exist, such as the optimal mesh size for a problem. A too coarse mesh resolution within regions with large gradients of the solution variable (as e.g near the cell membrane in case of cell models) leads to errors. On the other hand, if the mesh is too fine in some regions again the large aspect ratio between the smallest and largest mesh element leads to a high matrix condition number responsible for numerical imprecisions in the solution.

In the case of supershapes with an offset surface close to the original one and the resulting large aspect ratios the ability of COMSOL Multiphysics® to generate a mesh also depends on the choice of the discretization parameter $d$ of the original surface. If the discretization is too coarse small features as e.g. the spicules of the echinocyte cannot be properly resolved and the resulting shape will have unwanted sharp corners. On the other hand, if the points are too dense the meshing tool of COMSOL Multiphysics® fails in some cases due to internal numerical errors, meaning a distance between two points cannot be resolved. Consequently and unfortunately, one has to try different values for $d$ 'by hand'.

## 4.5 Packing of unit cells

Depending on their sizes and electronic interactions atoms in a crystal always form an ordered assembly or packing. A selection of basic lattice structures is given in Figure 4.7. In order to overcome volume fraction limits imposed by allowing a unit cell to only contain a single particle within a unit cell one can borrow the concept for the modeling of the dielectric tensor of periodic structures introduced in Section 4.1. For the specific problem of tissue or cell suspension exposed to a homogeneous external field only the cubic packings are relevant because only those have the appropriate symmetry in order to provide the correct diagonal effective dielectric tensor $\bar{\varepsilon}^*_{\text{eff}}$.

Besides the simple cubic the body-centered cubic packing will be used in this work in order to model densely packed cells in tissue.

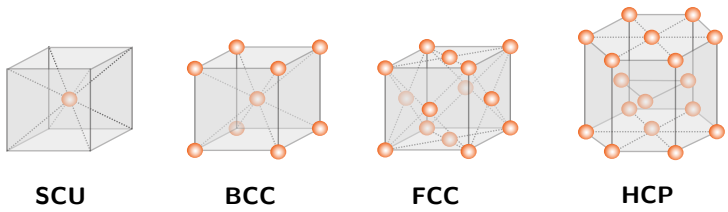


**Figure 4.7:** Lattices structures: simple cubic (SCU), body centered cubic (BCC), face centered cubic (FCC) and hexagonal close packed (HCP).

## 4.6 Analysis, results and discussion

### 4.6.1 Model validation and accuracy of analytical approximations

The numerical model was validated for a shelled ellipsoidal inclusion (for parameters see Table 3.1) at a volume fraction of $\varphi = 0.1$. The corresponding deviations of the numerical model to the MG and HB formulas are depicted in Figure 4.8.

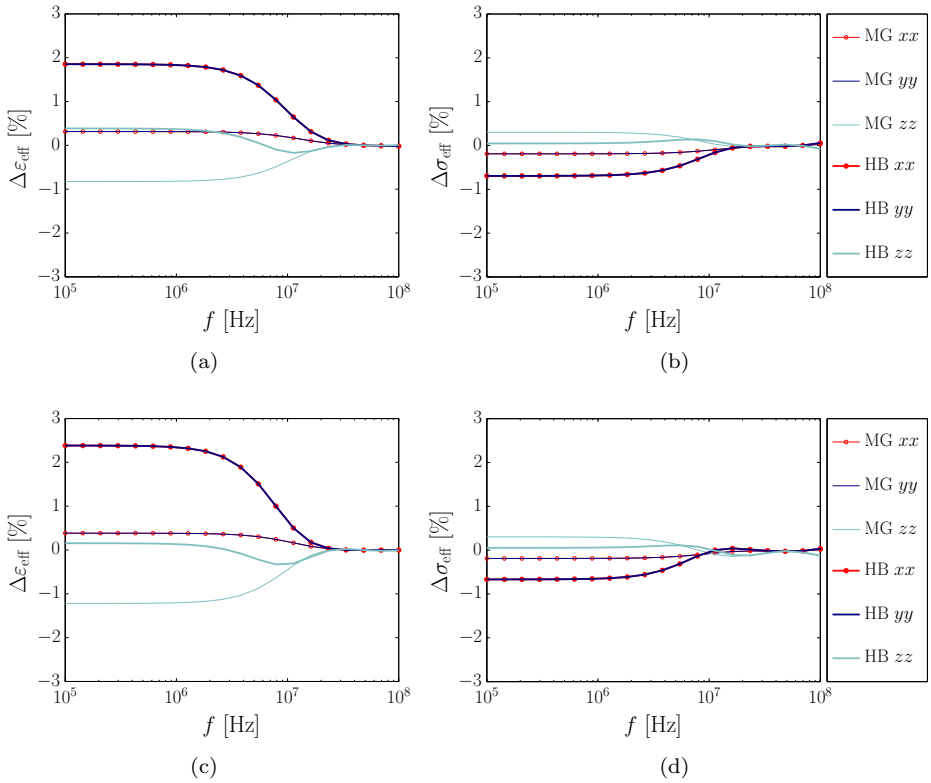


**Figure 4.8:** Deviations between numerically modeled effective dielectric parameters and those obtained by mixing formulas. Confocal ((a) and (b)) and concentric ((c) and (d)) shelled ellipsoidal inclusion ES2 (for parameters see Table 3.1) for $\varphi = 0.1$.

### 4.6.2 Sensitivity to parameter variations

Three different cell types out of the overview in Figure 4.2 are chosen in order to invesitgate the irregularity in cell shape. The first two cell types occur in the human body on a regular basis. The subcutaneous fat or adipose tissue consists of spherical or slightly deformed fat cells as shown in 4.2(a). Epithelial tissue lines almost the entire body from inside as well as from the outside. An example is the cuboidal epithelium cell in the kidney given in 4.2(b). The third example in 4.2(h) depicts a special form of an RBC, an echinocyte . Echinocytes are crenated RBCs characterized by convex rounded protrusions or spicules. The shape transformation from normal RBCs (discocytes) is e.g. induced by anionic amphipaths, high salt concentration, high pH, ATP depletion, cholesterol enrichment, and proximity to a glass surface [111]. The dielectric parameters for the phases of the cell models were assumed to be frequency independent with $\varepsilon = 80$ and $\sigma = 0.12$ [S/m] for the extracellular medium, $\varepsilon = 9.04$ and $\sigma = 1 \cdot 10^{-6}$ [S/m] for

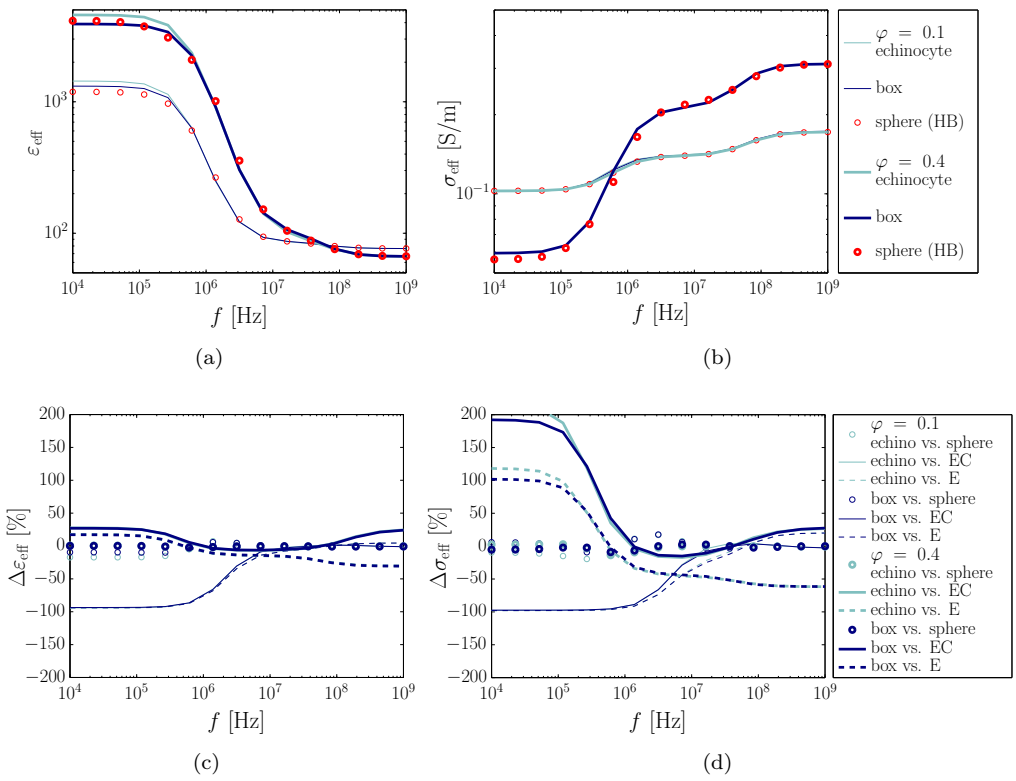


**Figure 4.9:** Echinocyte from Figure 4.2(p) and box-shaped cell from Figure 4.2(j) and their spherical approximation, approximation by a series circuit of cytoplasm and extracellular medium (EC) and extracellular medium only (E). Absolute dielectric spectra in (a) and (b) and relative deviations of the EC and E approximations with respect to the cell model in (c) and (d).

the membrane and $\varepsilon = 50$ and $\sigma = 0.53$ [S/m] for the cytoplasm [48]. The dielectric parameters were kept fixed for all models.
Simulated dielectric spectra for the box-shaped, echinocyte-like and spherical cell and the analytically calculated spectra obtained from the MG formula for the spherical cell for volume fractions $\varphi = 0.1$ and $\varphi = 0.4$ are given in Figure 4.9. The purpose of the displayed spectra is to show occurring differences on a larger scale.
In order to quantify deviations between the non-spherical shapes and the spherical cell shows the relative difference of permittivity and conductivity of the box-shaped cell and echinocyte with respect to the spherical cell. Furthermore, the error is quantified for the cases when the three-phase cell model is replaced by a simple series circuit of extracellular medium and cytoplasm and by extracellular medium only.
Another example where a supershape, a keratinocyte ocurring in the human epidermis,

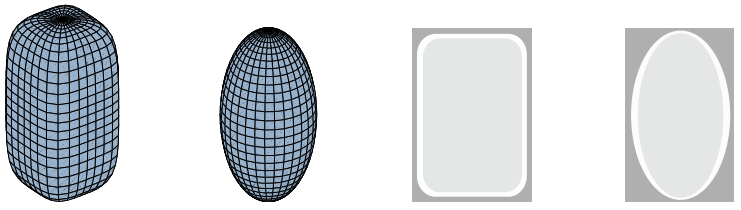

(a) (b) (c) (d)

**Figure 4.10:** Keratinocyte shape (a) and (c) and ellipsoid (b) and (d) with equal semi-axis ratios.

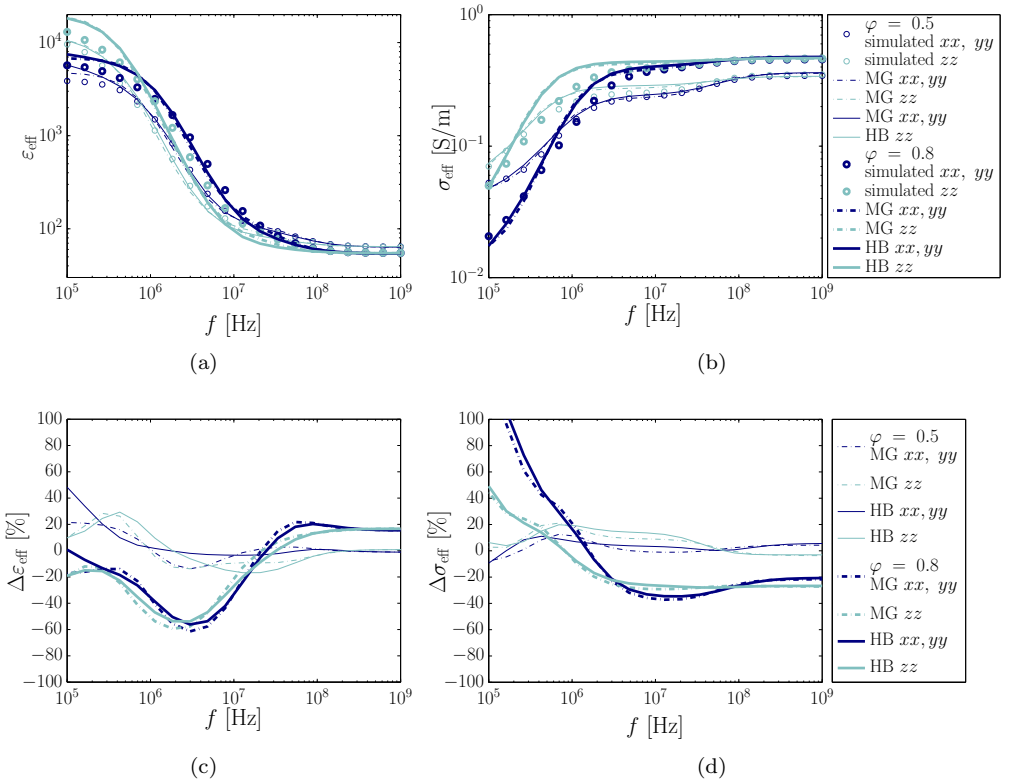


**Figure 4.11:** Keratinocyte and its ellipsoidal approximation. Absolute dielectric spectra in (a) and (b) and relative deviations of the ellipsoidal approximation with respect to the exact keratinocyte shape in (c) and (d).

is compared to its volume-fraction equivalent ellipsoid is given in Figure 4.10. The corresponding spectra, calculated using the MG and HB formulas for the ellipsoid as well as the numerical simulations of the keratinocyte are given in Figure 4.11.

### 4.6.3 Unit cell

The comparison between dielectric spectra of a particle in a SCU or BCC unit cell is given in Figure 4.12. The models with the box-shaped cell from Figure 4.4(c) were established using the replacement of the cell membrane by a boundary condition described in the next section. This was necessary since at the volume fraction of $\varphi = 0.8$ in the BCC model the center particle and the corner particle-eights are very close together causing an additional large aspect ratio. A significant difference between the values for the SCU and BCC can be seen. However, the BCC model was established using a relatively coarse mesh which is responsible for the large deviation between the parameters in $x$-direction compared to those in $y$- and $z$-direction. This should not be the case since the shape has cubic symmetry. For further use this BCC model would have to be recalculated using a finer mesh, because otherwise the differences among the spatial directions in the BCC model are even larger than between the SCU and BCC model.

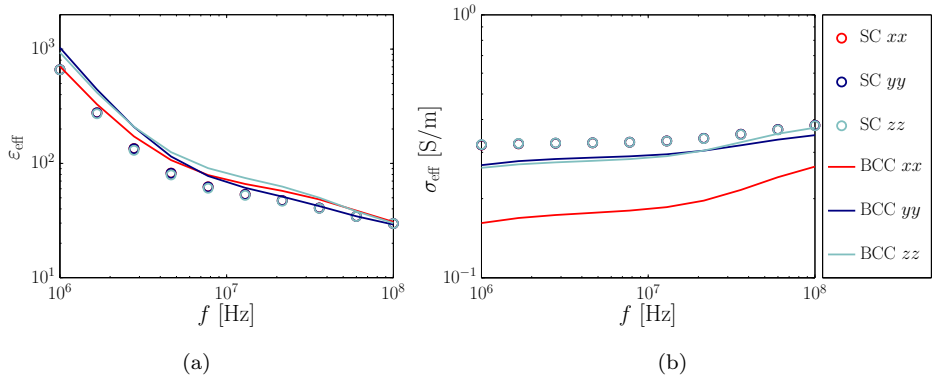


**Figure 4.12:** Box-shaped cell from Figure 4.4(c) with semi-axes lengths $d_x = d_y = d_z = 45$ $\mu$m and a membrane thickness of $\rho_{\mathrm{m}} = 7$ nm. Effective permittivity (a) and conductivity (b) of a box-shaped cell. Comparison between a SCU and BCC unit cell at $\varphi = 0.8$.

## 4.7 Replacement of the cell membrane by boundary conditions

The representation of the shelled spherical geometry as a supershape and the implementation in COMSOL Multiphysics® showed to be less prone to numerical errors during mesh generation for the thin membrane than the ellipsoidal geometry object available directrly in COMSOL Multiphysics® .

Unfortunately, it can happen that a large model cannot be solved even if the required computer memory is available. This can happen if e.g. the PARDISO solver is not able to handle the matrix anymore due to internal problems. Therefore, a way has to be found how to reduce the number of elements. One possibility is to replace the membrane with a boundary condition which allows the solution variable, the electric potential $V$ to be discontinuous across the boundary. Software-specific implementional details are given in Section B.4. An example comparing the MG and HB formulas with the numerical solution for a shelled spherical inclusion SS1 (for parameters see Table 3.1) is given Figure 4.13 for two different volume fractions of $\varphi = 1$ and $\varphi = 0.5$. The deviations are larger for the higher volume fraction. This is due to the fact that the spherical shape was created using the SF: For both volume fractions the same discretization was used and therefore the piecewise linear approximation has a larger impact in the case of the higher volume fraction. Overall it can be stated that the replacement of the membrane by a boundary condition was successful.

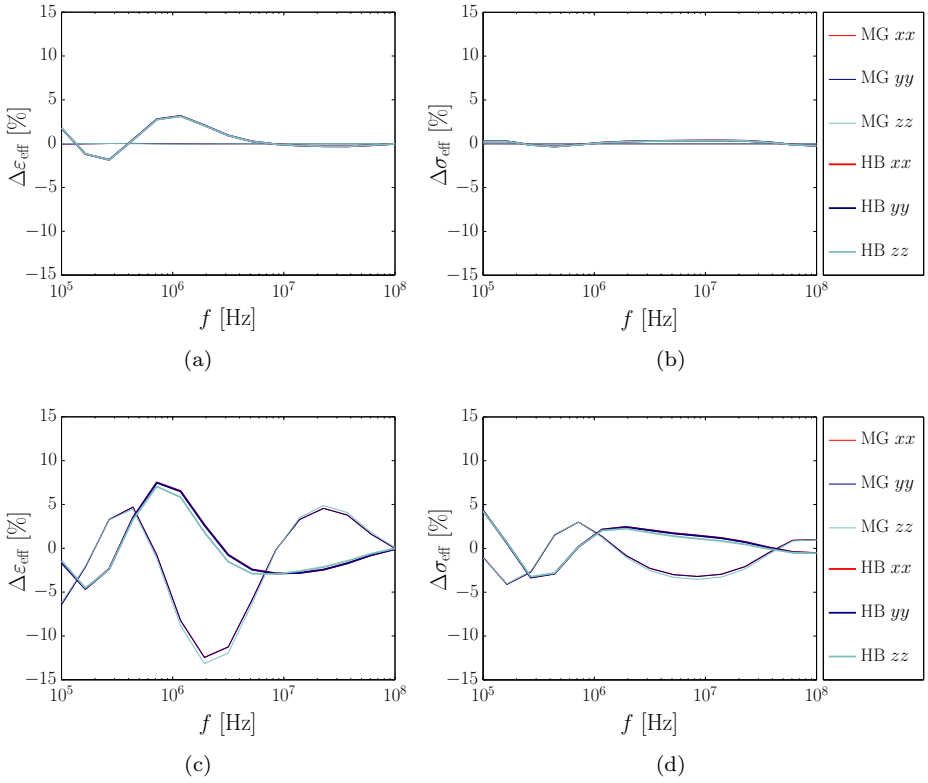


**Figure 4.13:** Shelled spherical inclusion (SS1) at $\varphi = 0.1$ in (a) and (b) and $\varphi = 0.5$ in (c) and (d). Numerical model with replacement of the membrane by a boundary and the deviations to the MG and HB formulas.

Some models presented later in Chapter 7 are only possible to establish using this replacement of the cell membrane by a boundary condititon. It leads to a reduction of the mesh size by a factor of 10.
Several examples on solving of large problems are given in [119] or for the octree multigrid solver in [120]. A rather sophisticated method is the immersed FEM used for biological systems [121].

## 4.8 Anisotropy in a shell

Due to the rotation of the hydrophilic head groups of the phospholipid bilayer the cell membrane exhibits different dielectric parameters in normal and tangential direction to its surface [48], [81]. This means that the dielectric tensor is diagonal in the local coordinate system

$$\bar{\varepsilon}^* = \begin{pmatrix} \varepsilon^*_{\perp} & 0 & 0 \\ 0 & \varepsilon^*_{||} & 0 \\ 0 & 0 & \varepsilon^*_{||} \end{pmatrix}, \tag{4.11}$$

but will contain off-diagonal elements in the global coordinate system. The tensor can be transformed from the local to the global coordinate system by multiplication with the rotation matrix $\mathbf{R}$ and its transpose $\mathbf{R}^T$ according to

$$\bar{\varepsilon}^* = \mathbf{R}\bar{\varepsilon}^*_{\text{local}}\mathbf{R}^T. \tag{4.12}$$

With the Euler angles $\phi$, $\theta$ and $\psi$ depicted in Figure 4.14 the rotation matrix is defined as

$$\mathbf{R} = \begin{pmatrix} \cos\theta\cos\psi & -\cos\phi\sin\psi + \sin\phi\sin\theta\cos\psi & \sin\phi\sin\psi + \cos\phi\sin\theta\cos\psi \\ \cos\theta\sin\psi & \cos\phi\cos\psi + \sin\phi\sin\theta\sin\psi & -\sin\phi\cos\psi + \cos\phi\sin\theta\sin\psi \\ -\sin\theta & \sin\phi\cos\theta & \cos\phi\cos\theta \end{pmatrix}. \tag{4.13}$$

The resulting $\bar{\varepsilon}^*$ contains off-diagonal elements but is symmetric. In terms of implementation for each membrane element the closest boundary element (outer or inner, but same for all membrane elements) has to be found. Then the normal vector of this boun-

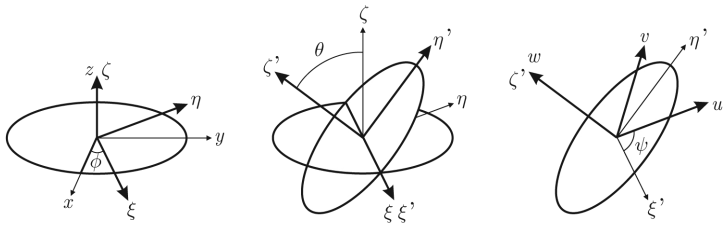


**Figure 4.14:** Euler angles.

dary triangle $ABC$, $\vec{n}_{ABC}$, e.g. $\overrightarrow{BC}$ and a second tangential vector calculated by the cross product forn a right-handed basis set for the local coordinate system. After determination of the Euler angles the application of Equation 4.12 delivers the permittivity tensor for a specific membrane element in the global coordiate system.
Parameters for an anisotropic cell membrane can be e.g. obtained from [122].

## 4.9 Conclusion

The validity of the numerical models was shown using several examples. The replacement of the cell membrane by a boundary provides a computational speedup of approx. 5-10 times with an error smaller than 5% for a volume fraction of $\varphi = 0.1$ and smaller than 15% for a volume fraction of $\varphi = 0.5$. Furthermore, the non-negligible influence of the intercellular interactions was demonstrated simulating a box-shaped cell in a SC and BCC unit cell.

The results from the numerical simulations again emphasize that shape clearly has an influence on the dielectric spectra in the lower MHz region and has to be accounted for in modeling, depending on the desired accuracy. In contrast to most other works where the shape effects are investigated in terms of quantities derived from the Cole-Cole relaxation model (such as e.g. $\Delta\varepsilon$) the presented quantitative study is more general due to its very emphasis on the actual cell geometry.
For the given overall shape and volume parameter range the presented work provides a robust and flexible method for the calculation of dielectric spectra of cells. Nevertheless, certain limitations have to be mentioned. The large aspect-ratio between cell membrane thickness and cell dimensions requires a high mesh resolution and therefore large computational power. A model incorporating the cell membrane only in terms of boundary conditions is in preparation. Another issue, advantage and limitation at the same time concerns the large parameter ranges for $a, b, m, n_1, n_2$ and $n_3$. Sharp edges and non-spherical topologies can both be easily generated. Spike-like features may occur e.g. in neurons, which are likely to cause problems in numerical simulations and eventually require some special care, such as removal of points. Certain parameter combinations lead to self-intersection or other modifications ($n_1$ and $n_3 < 0$) so the topology is not spherical anymore. Both issues can be avoided indicating a certain parameter range if modeling biological cells. Since the computational effort for the generation of a solid object with the described software-specific procedure depends on the number of points the discretization parameter $d$ should be chosen as small as possible but as large as necessary in order to properly reproduce the curvatures of the corresponding cell shape. Generally, it can be stated that the higher $m$ (while $n_1$, $n_2$ and $n_3 > 2$) the more protuberances or spikes a supershape will posess and the larger $d$ has to be chosen.
From a general point of view the few parameters required in the shape representation, the flexible discretization and robustness make the procedure suitable in shape optimization of any kind. The multi-scale modeling concept for tissues can be extended by setting up minimal-size cell arrays in order to include and control interparticle interactions.
Using the presented framework for cell shape generation, the influence of geometrical

variations as well as the cell volume fraction on dielectric spectra was investigated between 100 kHz and 1 GHz. The quantification of the cell shape's influence was introduced via the relative deviation between non-spherical and spherical spectra. Results for the different cell shapes suggest that below 1 MHz the effective dielectric properties of different cell shapes at different volume fractions significantly deviate from the spherical case. Furthermore, the three different cell shapes were compared to a simple serial connection of the involved materials with scaled thicknesses in order to demonstrate the influence of the cell membrane. The absolute values for the dielectric parameters of such equivalent circuit models are significantly larger than for the single-cell models but location and characteristics of the dispersion are comparable.
Concerning measurability it can be stated that the changes are pronounced in the high kHz-range but potentially masked by electrode polarization effects. Above the occurrence of electrode polarization, starting in the low MHz-range the magnitude of the deviations due to shape changes decrease and would therefore require a higher sensitivity of the measurement setup.
The SF turned out to be a suitable parametrization method for non-axisymmetric shaped biological cells, also applicable to test a functional dependence between environmental changes (concentration of a species, pressure, temperature, etc.) and the shape of a surface. As an example the RBC shape strongly depends on the electrolyte concentration in the blood plasma. Although completely asymmetrical shapes cannot be generated by the SF this drawback could e.g. be compensated by a an additional "deformation" function acting on the supershape. Furthermore, multiplying the SF with other functions or another SF would also extend the variety of possible shapes [106].
Followed by FEM simulations of dielectric spectra of the mentioned cell models the overall method is very flexible for single cell and tissue modeling. However, in order to establish an efficient and reliable macroscopic tissue model the influence of other aspects such as ion channels, proteins, organelles, etc. have to be investigated as well, especially for frequencies above 50 MHz.
On the microscopic scale itself the developed models can be used in order to analyze the local distribution of applied electromagnetic fields in order to investigate potential non-thermal effects.

# 5 The multiscale approach

Multiscale modeling usually contains a combination of information on several temporal and spatial scales while several physical processes may be involved [123]. Multiscale modeling is quite popular e.g. in mechanics [124] and [125]. For the calculation of dielectric properties of tissueo no general multiscale model has been presented so far, although the idea already exists for some time [126].
As already mentioned in Section 1.1 modeling of microscopical geometry details on macroscale remains challenging if not impossible: If considering a coaxial probe with outer dimensions of approximately 2 cm and a very roughly estimated penetration depth of 2 mm, if including cells with an extent of few $\mu$m not speaking of the cell membrane in the order of nm the number of degrees of freedoms (DOFs) would explode. Therefore, a way has to be found how to avoid modeling of small details while allowing for an accurate incorporation of structural information. A method for solving this problem is outlined in this chapter.

## 5.1 Concept

Although the external electric field is inhomogeneous on the macroscale its approximate homogeneity on the microscale suggests representing each tissue type by the effective permittivity of its unit cell. The idea is to consider the material as a quasi-periodic structure and to calculate average properties for a unit cell on a particular scale, pass the so-obtained effective/averaged value to the next scale. This can be considered as an $n$-step homogenization. By defining a cubic unit cell of the structure (containing one biological cell embedded in extracellular medium in the simplest case of stratum corneum (SC) packing) the complex effective dielectric tensor $\bar{\varepsilon}^*$

$$\bar{\varepsilon}^*_{\text{eff}} = \begin{pmatrix} \varepsilon_{xx,\text{eff}} & 0 & 0 \\ 0 & \varepsilon_{yy,\text{eff}} & 0 \\ 0 & 0 & \varepsilon_{zz,\text{eff}} \end{pmatrix} \tag{5.1}$$

can be calculated al already elucidated in Section 4.2. If the tissue contains quasi-periodic structures on a smaller (subcellular) or larger (mesoscopic) scale the procedure can be iteratively repeated in a sort of recursion scheme by starting at the smallest scale, calculating the effective dielectric parameters of the unit cell, building up a structure in a new unit cell on the next-higher scale with assigned material parameters from the previous scale, again calculating the effective parameters of this new unit cell, and so on. For a better understanding the general procedure is depicted in Figure 5.1.
An application of this idea will be presented in Chapter 7 [127] for the dielectric spectroscopy of the human skin in the MHz region, employing a fringing-field sensor.

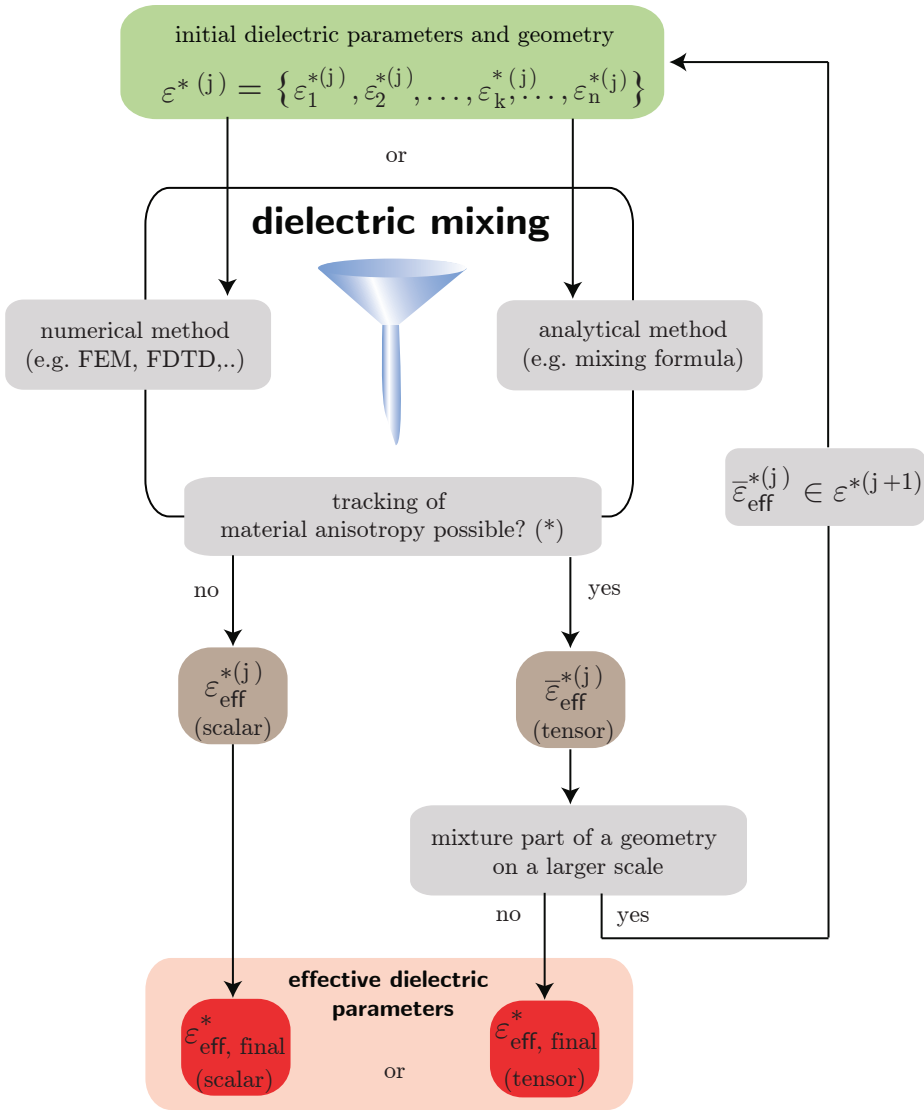


**Figure 5.1:** Scheme of the dielectric homogenization procedure for a material with (quasi-)-periodic on one or more scales. Depicted is the step for one hierarchy or scale step, $j$. (*) The tracking of the material anisotropy is only possible if the geometry consists of a cubic unit cell with walls parallel to the $xy$-, $yz$- and $xz$-planes and the electric field is applied to the $z$-, $x$- and $y$-direction, respectively in order to obtain the dielectric tensor of the material.

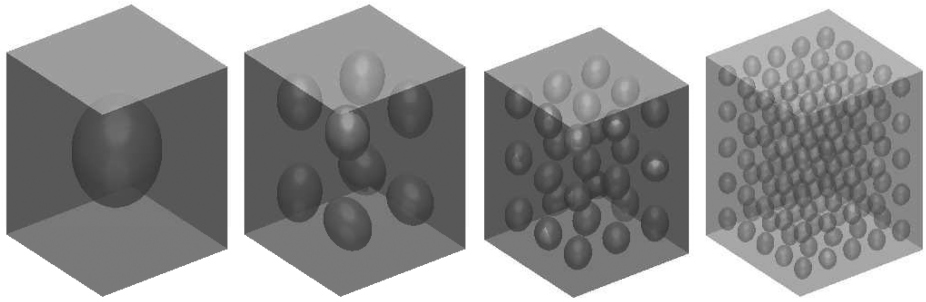


**Figure 5.2:** Arrays of tilted ellipsoidal particles with statistically distributed deviations (pseudo-normal distribution) in polar and azimuthal angles with respect to a preferred orientation. 5.2(a) Single tilted homogeneous ellipsoidal particle with $\phi = 45°$ and $\theta = 60°$[111]. 5.2(b) 5.2(c) and 5.2(d) [222]-, [333]- and [555]-arrays with tilted particles with standard deviation of $\pm$ 10 ° for $\phi$ and $\theta$ with respect to the [111]-array.

## 5.2 Statistical variations and required size of unit cell

Since cells either in suspensions or in tissue are not perfectly equal the question arises how much can a certain parameter vary in order to obtain effective dielectric parameters that vary only in a defined range or what is the smallest possible unit cell. The hypothesis is that depending on the standard deviation the error will converge as a function of array sizes. The question is what is the deviation between the effective properties of an array where the particles have a standard deviation from a certain orientation and the reference (single particle with the defined orientation). The homogeneous ellipsoidal inclusion E1 (for parameters see Table 3.1) with a volume fraction of $\varphi = 0.1$ is taken as a test structure. The investigated arrays are given in Figure 5.2. The corresponding deviations in dielectric parameters with respect to a single ellipsoidal particle rotated by the azimuthal angle $\theta = 60°$ and polar angle $\phi = 45°$, are shown in Figure 5.3. It can be seen that the deviation decreases with increasing size of the unit cell as expected. Furthermore, the deviation is practically frequency independent.
The required size of the unit cell in order stay under a certain deviation threshold with respect to a single particle is supposed to be larger with increasing volume fraction due to stronger interparticle interactions. However, this assumption would have to be verified with simulations.

## 5.3 Anisotropy propagation

In this section it is investigated how much impact does anisotropy have if it occurs in certain directions either in the host or inclusion phase of a two-phase mixture. One phase is always isotropic, In the first case the host medium can be fully or partly anisotropic, in the second case host and inclusion change roles. The isotropic-isotropic case serves

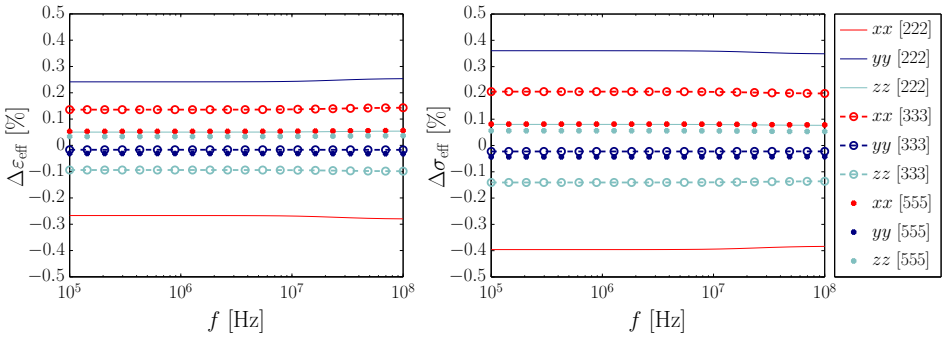


(a) (b)

**Figure 5.3:** Deviations of effective permittivity (a) and conductivity (b) of [222]-, [333]- and [555]-arrays of a tilted particles with statistically distributed variations in azimuthal and polar angles from Figures 5.2, (b) to (d) with respect to those obtained for the single particle, the [111]-array in Figure 5.2(a).

as reference for each of the two cases. All possible combination are listed on the following.

**Case 1**

- Reference: Host isotropic (isotropic parameters of fully anisotropic inclusion), inclusion isotropic
- Host anisotropic, inclusion isotropic
- Host $xy$-isotropic, inclusion isotropic
- Host $xz$-isotropic, inclusion isotropic
- Host $yz$-isotropic, inclusion isotropic

**Case 2**

- Reference: Host isotropic, inclusion isotropic (isotropic parameters of fully anisotropic inclusion)
- Host isotropic, inclusion anisotropic
- Host isotropic, inclusion $xy$-isotropic
- Host isotropic, inclusion $xz$-isotropic
- Host isotropic, inclusion $yz$-isotropic

The dielectric parameters for the anisotropic phase are always obtained from the mixture of shelled ellipsoids ES1 with a volume fraction of $\varphi = 0.1$ (for parameters see Table 3.1). The isotropic phase has a frequency-independent $\varepsilon = 80$ and $\sigma = 1.2$ [S/m] (parameters also used for the extracellular medium). The geometric structure corresponds to the homogeneous sphere S1 at a volume fraction of $\varphi = 0.1$. The results are displayed in Figure 5.4.
It can be seen that effective parameters are far more sensitive to the anisotropy in the

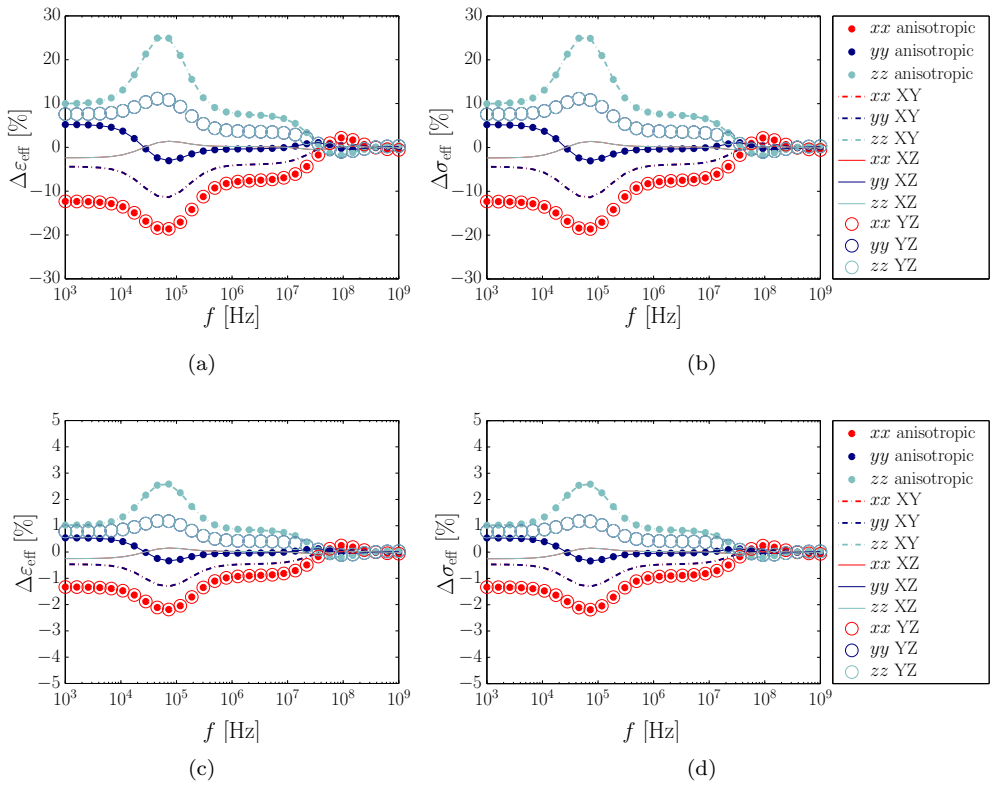


**Figure 5.4:** Single, untilted ellipsoidal inclusion E1 (for parameters see Table 3.1), [111]-array. Expression of anisotropy in all possible directions with respect to the case isotropic host/isotropic inclusion. Deviations in effective permittivity (a) and conductivity (b) for the combination anisotropic host/isotropic inclusion for isotropic host/anisotropic inclusion in (c) and (d) from the fully isotropic reference scenario.

inclusion, even though the volume fraction of the inclusion is much smaller. In the first case the absolute maximum sensitivity is around 25%, in the second case only approx. 3 %. Permittivity and sensitivity exhibit the same sensitivity spectra. Another interesting aspect is the frequency dependency of the anisotropy sensitivity. The sensitivity has a maximum below the center frequency of the main dispersion of the anisotropic phase at around 100 kHz and strongly decreases for frequencies above 50 MHz.

## 5.4 Conclusion

In this chapter a framework for modeling of the effective dielectric properties of tissue while incorporating information fromu multiple spatial scales was introduced. A question which automatically arises concerns the size limits of a scale. In other words, how large

has the unit cell to be in order to accurately approximate the bulk material? Using specific examples, the influence of statistical distribution of particle orientation was demonstrated and quantified comparing the effective dielectric properties of particle arrays of different sizes. Furthermore, the impact of anisotropy either in the host or inclusion in a two-phase system was investigated as well. The unit cell size and anisotropy impact depend on the specific structure and problem and have to be reevaluated for each specific geometry. For example in [83] a higher sensitivity for anisotropy in 2D case than in 3D ('paradox of anisotropy') is claimed which could be investigated with the presented approach.
In order to answer the question when a geometry has to be considered on two consecutive scales one could e. g. investigate a three-shelled sphere with $\varepsilon_\mathrm{h}$, $\varepsilon_1$, $\varepsilon_2$, $\varepsilon_3$ and $\varepsilon_4$. Then the minimal size of inner single-shelled sphere ($\varepsilon_3$ and $\varepsilon_4$) would be assessed from which on it is necessary to geometrically include it in the three-shelled model. This investigation could be performed for both, MG and HB formulas as well as for ellipsoids, e.g. with an oblate center particle in prolate outer particle. This would allow to decide up to which extent the dielectric properties of smaller structures can be simulated on its own scale or if a more complex model with larger aspect ratios is required.

# 6 Multilayer systems and fringing fields

Since many important physiological phenomena are reflected by changes of the dielectric properties of the human skin, i.e. in the epidermis and dermis layers, it seems to be straight forward to apply dielectric spectroscopy as a monitoring technique. Parameters of interest include glucose levels of diabetes patients, benefits of moisturizers in cosmetics or the characterization of membrane activity for drug delivery, respectively. The technique was already used to monitor pathological changes caused by diseases like cancer [128] or auto-immune disorders of the skin [129]. Applications of dielectric spectroscopy to the measurement of dielectric properties of human skin were reported in various publications [130], [131] and [132].

To some extent attempts were made to correlate physiological conditions with measured dielectric data [6] and [133]. However, there have been challenges in the unequivocal assignment of the measured signal change as well as the sensitivity. These issues have to be resolved in order to employ dielectric spectroscopy for tracking of physiological data in clinical use. The question of sensitivity and related aspects are well treated in this work, while a general uniqueness analysis is out of scope. Nevertheless, the latter issue is also fundamental: Correlating changes of certain parameters in a multi-layer system can also be described as the solution of an inverse problem, which is usually non-trivial [45]. As reported e.g. in [134] techniques based on dielectric or impedance spectroscopy of multilayer materials and their spatial reconstruction is an ill-posed problem. The solution is non-unique and as a consequence, various parameter combinations yield the same result. Already the reconstruction of a 1D profile is rather challenging as shown in an extensive study for a distribution of dielectric mechanisms and parameters in [135]. Therefore, a possibility to reduce the complexity of the inverse problem is to gather as much information as possible about the system [136]. Then a forward model is established in such a way that the number of parameters is minimized turning the problem into a well-posed one. For this reason the presented work solely focuses on the assessment of the forward problem of a dielectric skin model and potential variations of effective parameters.

In addition to the skin itself being the target system, a consistent forward model could potentially also be applied to subtract the skin's contribution from measurements of tissues located below the skin layers.

Non-invasive monitoring of changes in dielectric properties within the epidermal and dermal layers requires the design of a sensor geometry featuring maximal measurement sensitivity regarding the target quantity. In the case of human skin, non-invasive measurements allow only one-sided access and thus suggest the application of coplanar elec-

trodes. Different designs of coplanar electrode systems are available, e.g. coaxial probes [137], [138] and [139], interdigitated sensors [140], [141], [142], [143] and [144], or mesh-type sensors [145] and [146].

In this chapter effective dielectric parameters of a three-layer human skin model under different probe geometries are numerically evaluated between 100 kHz and 100 MHz. First, a coaxial probe geometry is employed in order to assess the number of necessary layers and to perform an extensive sensitivity analysis for dielectric and thickness parameter variations in the second layer. The measurement sensitivity is derived without taking noise and biological variations into account. Additionally, the dependency of the sensitivity as a function of a relative parameter change is assessed at two different frequencies. In the framework of the sensitivity analysis the importance of dispersive dielectric parameters for each layer is demonstrated. Furthermore, the specificity of changes in effective dielectric parameters is investigated by means of sign patterns obtained from the sensitivity spectra and their first and second derivatives. Then, the transferability of these results to less symmetric probe geometries is investigated. As an example of such a geometry, a multi-electrode probe in a coplanar design employed in clinical use is chosen. The effective dielectric properties obtained by this probe are compared with coaxial probes to show the transferability of the obtained results. Finally, employing the proposed sensitivity analysis technique, the efficiency of space utilization in terms of inter-electrode distance is investigated. This investigation is performed by comparing an interdigitated probe with a coaxial probe geometry.
The model applied for the investigation of sensitivity and specificity can be divided into two components. One component is the model of the probe and the other is an approximate model of the complex biological structure of skin. Three different probes are used in the numerical simulations.

## 6.1 Extraction of dielectric parameters

In this chapter the quasi-static regime applies as outlined Section 4.2. As in Chapter 4 simulations were performed using the FEM software COMSOL Multiphysics® Version 3.5a.

The solution of the numerical simulation provides the input admittance of the system consisting of a probe and material under test (i.e. the three-layer system). The effective dielectric parameters are extracted using the standard procedure of determination of the cell constants of the measurement cell [147]. In the equivalent circuit the admittances $Y = G + j\omega C$ of probe and material under test are in parallel. In order to remove the probe's contribution to the admittance cell constants of the measurement cell, $k_m$ and $k_p$ are introduced. Then, the real parts of the effective permittivity and conductivity $\varepsilon_{\mathrm{eff}}$ and $\sigma_{\mathrm{eff}}$ for a material under test are then given by

$$\varepsilon_{\mathrm{eff}} = \frac{C_{\mathrm{material}} - k_{\mathrm{p}}}{k_{\mathrm{m}}} \tag{6.1}$$

and

$$\sigma_{\text{eff}} = \frac{G_{\text{material}}\varepsilon_0}{k_{\text{m}}}. \tag{6.2}$$

The geometry characteristic is though still contained in the the electric field pattern. The cell constants can be calculated when the admittances of two materials with known dielectric parameters are determined. In this process, one material is air, the second material usually water or an aqueous electrolyte solution, as NaCl(aq) or KCl(aq)

$$Y = Y_{\text{probe}} + Y_{\text{material}}\,. \tag{6.3}$$

The cell constants are calculated according to

$$k_{\text{m}} = \frac{C_{\text{NaCl(aq)}} - C_{\text{air}}}{\varepsilon'_{\text{NaCl(aq)}} - 1} \tag{6.4}$$

and

$$k_{\text{p}} = C_{\text{air}} - k_{\text{m}}. \tag{6.5}$$

Equations (6.1) and (6.2) are used in the following in order to determine the effective dielectric parameters of the skin model.

## 6.2 Probes

The analysis of the multilayer systems was performed with different fringing-field probe geometries.

### 6.2.1 Coaxial probe

The open coaxial probe geometry is widely used for characterizing dielectrics and biological tissue. Due to the rotational symmetry, the full geometry can be represented by a 2D axial symmetric model. This simplification allows for efficient numerical calculations of many different scenarios using less computational resources and time compared to full 3D models.
The dimensions of the employed coaxial probe shown in Figure 6.1 are chosen according to [148] for measurements on human skin. The inner and outer conductor radii are $r_{\text{i}} = 1.05\,\text{mm}$ and $r_{\text{o}} = 3.5\,\text{mm}$, the flange radius is $r_{\text{flange}} = 10.5\,\text{mm}$. The material between inner and outer conductor is teflon having the dielectric parameters $\varepsilon_r = 2.09$ and $\sigma = 0$ in the operating frequency range between 100 kHz and 100 MHz.

As described e.g. in [148] and [149] the sensed volume of a coaxial probe is related to the distance between inner and outer conductor. The measured admittance value as a function of frequency is determined by the current flowing through the multi-layer structure. The amplitude and the distribution of the current density is itself dependent on the corresponding dielectric properties of the different layers.

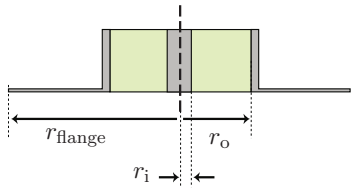


**Figure 6.1:** Geometry of the coaxial probe. The inner conductor of the coaxial probe has a radius $r_{\text{i}} = 1.05\,\text{mm}$, the outer conductor $r_{\text{o}} = 3.5\,\text{mm}$ and the flange radius is denoted with $r_{\text{flange}} = 10.5\,\text{mm}$. The dielectric of the probe is teflon ($\varepsilon_r = 2.09$ and $\sigma = 0$).

### 6.2.2 Interdigitated sensor

In the framework of the sensitivity analysis the coaxial probe is compared to an interdigitated sensor geometry. Interdigitated sensors have the advantage, that from a certain number of digits the structure and therefore the potential can be considered as quasi-periodic in $x$-direction and the only relevant dependency is the decay of the electric field strength in $z$-direction [142]. A 3D sketch of an interdigitated sensor is given in Figure 6.2(a).

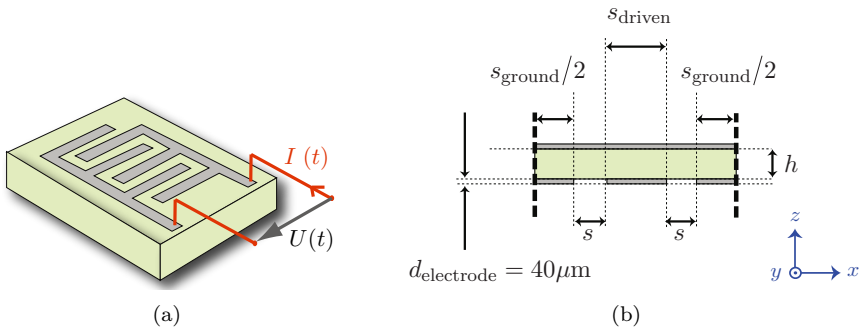


(a) (b)

**Figure 6.2:** Typical interdigitated sensor (a). Adapted from [150]. Partial 2D cross-section of an interdigitated sensor in (b). Two periods consisting of one driven and two halves of a grounded electrode. The substrate is teflon ($\varepsilon_r = 2.09$ and $\sigma = 0$).

The interdigitated sensor is approximated with a 2D model representing an infinite array ($x$-direction) of infinitely long electrodes (in $y$-direction) with alternating polarization. Figure 6.2(b) depicts one unit cell modeling the infinite array by exploiting periodic boundary conditions (bold dashed lines). This 2D model excludes edge effects such as additional fringing fields at the borders of the sensor. The interdigitated sensor has more independent spatial degrees of freedom compared to the coaxial probe. Starting from a coaxial probe as a reference geometry the length of the electrodes in $y$-direction is set to $2r_{\text{flange}}$. The normalization consists of setting the inter-electrode distances and

corresponding electrode areas equal in both probe geometries: The area of the driven electrode is chosen to be equal to the area of the inner conductor of the coaxial probe. The inter-electrode distance is chosen to be equal to $r_o - r_i$ for the corresponding coaxial probe setting. Finally, the area of the grounded electrode is consequently set equal to the area of the outer conductor of a coaxial probe. The 40$\mu$m thick interdigitated electrodes are placed on a 1.6 mm thick teflon substrate backed by a top ground plane, similar to the multi-electrode sensor.
Similar to the coaxial probe the effective dielectric properties of materials sensed by interdigitated fringing field sensors can be modeled semi-analytically by a technique based on conformal mapping [2] and [151]. Nevertheless, in this work only FEM is used.

### 6.2.3 Multi-electrode sensor

The multi-electrode fringing-field sensor[1] shown in Figure 6.3 contains three strip-like driven electrodes $E_i$ with different gap widths $s_i$ $(i = 1, 2, 3)$. The electrode widths for each electrode is equal to the corresponding gap widths: $s_1 = 4\,\text{mm}$, $s_2 = 1.5\,\text{mm}$ and $s_3 = 0.3\,\text{mm}$. The lengths of the electrodes are $l_1 = 16\,\text{mm}$, $l_2 = 18.5\,\text{mm}$ and $l_3 = 19.8\,\text{mm}$. The electrode thickness is 40 $\mu$m as shown in Figure 6.3(b). The circular patches at the electrode ends have radii equal to $s_i/2$.

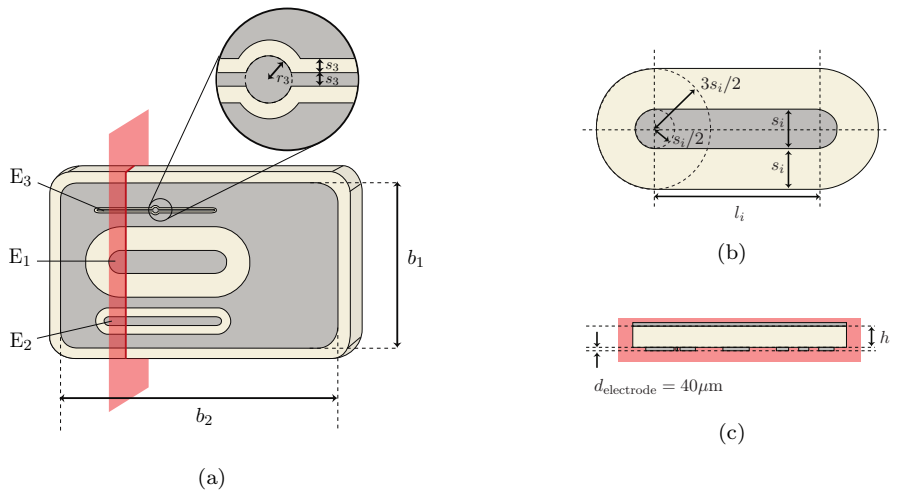


**Figure 6.3:** (a) Multi-electrode sensor with a ground plane of size $b_1 = 28\,\text{mm}$ and $b_2 = 47\,\text{mm}$. (b) Electrode and gap dimensions. The electrode widths are equal to the gap widths: $s_1 = 4\,\text{mm}$ ($E_1$), $s_2 = 1.5\,\text{mm}$ ($E_2$) and $s_3 = 0.3\,\text{mm}$ ($E_3$). The electrode lengths are $l_1 = 16\,\text{mm}$, $l_2 = 18.5\,\text{mm}$ and $l_3 = 19.8\,\text{mm}$. The circular patches at the electrode ends have radii equal to $s_i/2$. The radius of the circular patch in the center of $E_3$ is $r_3 = 0.5\,\text{mm}$. The substrate thickness $h_s$ is 1.6 mm, the material Rogers RO4350b with $\varepsilon_r = 3.48$ and $\sigma = 0$. (c) Sensor cross-section. The electrode thickness is $d_{\text{electrode}}$ is 40 $\mu$m.

[1] Solianis Monitoring AG, http://www.solianis.com

The radius of the circular patch in the center of $E_3$ is $r_3 = 0.5\,\text{mm}$. The total area of the sensor is $A_{\text{sensor}} = 1316\,\text{mm}^2$. The electrodes are printed on a Rogers RO4350b substrate with thickness $h_s = 1.6\,\text{mm}$ and $\varepsilon_r = 3.48$ ($\sigma = 0\,\text{S/m}$). The electrodes are fed by coaxial connectors on the backside of the sensor, where the inner conductors extend to vias contacting the middle of each electrode. The outer conductors of the coaxial feeds are connected to a ground plane on the back of the sensor. The ground planes on the back and on the front of the sensor are also connected through vias. Similarly to the coaxial probe the multi-electrode sensor is a capacitive probe with negligible inductance up to several 100 MHz. Above a certain frequency the sensor starts to resonate and acts as an antenna. However, according to measurements (not shown here) these resonances occur above 100 MHz for all three electrodes.

Regarding the sensed volume, a similar relation as for coaxial probes holds for the distance between driven electrode and the ground plane coplanar to the driven electrodes in the case of the presented multi-electrode sensor. Consequently, the sensed volume is different for each electrode. 2D FEM simulations and measurements of non-biological two-layer systems probed with the presented multi-electrode sensor were performed in [152].

## 6.3 Layered skin model

The human skin morphology consists of structures on several spatial scales. On the submicroscopic and microscopic level there are organelles, cells and macromolecules. On a scale in the order of a few 100 $\mu$m, blood vessels form a network. For the assessment of changes of the dielectric properties of substructures on the effective dielectric properties of skin the model has to contain certain information on the skin structure while keeping the number of model parameters as small as possible. However, the establishment of a model containing microscopic features would lead to a huge number of parameters, therefore other ways in order to include the relevant information in the model have to be found.
Although most types of cells share the same basic structure consisting of extracellular medium, phospholipid cell membrane and cytoplasm the composition (i.e. water content) of the generally aqueous extracellular medium and cytoplasm may vary and is also reflected on the macroscopic scale. As a macroscopic quantity, the water content is the target quantity in order to subdivide the skin into layers.
The topmost layer, the stratum corneum (SC), has a thickness of around 20 $\mu$m, consists of dead cells and contains approximately 20% water. Although composed of different microstructures, the epidermis (thickness of 100-200 $\mu$m) and 1-1.2 mm thick dermis exhibit a similar water content between 60 and 70% and are therefore combined to form the second layer (E/D) in the presented model. Finally, the hypodermis (HYP) consisting mainly of subcutaneous fat with a water content of approximately 20% is forming the third layer. An MR image of human skin taken at the dorsal upper left arm is depicted in Figure 7.5. A detailed description of the measurement procedure is given in Section 7.3.2. The different layers of epidermis, dermis, hypodermis and muscle are

clearly distinguishable according to [153]. It has to be mentioned that the MR image indicates compositional differences between the epidermis and dermis. Nevertheless, these two layers are gathered in a first approximation. The uppermost layer of the epidermis, the stratum corneum, lies below the resolution limit and cannot be visualized. The three-layer model which is employed in the numerical simulations in order to approximate human skin is shown in Figure 6.4(a). These three layers represent the stratum corneum, the dermis/epidermis and the hypodermis. The thicknesses of the layers are chosen to be $d_1 = 20\,\mu$m, $d_2 = 1$ mm and $d_3 = \infty$. The model is truncated with $d_3 = 2$ cm (could be in fact even smaller) and the boundary condition $\mathbf{n} \cdot \mathbf{E} = 0$, where $\mathbf{n}$ is the normal vector at the boundary. The question if muscle tissue has to be included into the model as a fourth layer will be discussed later.

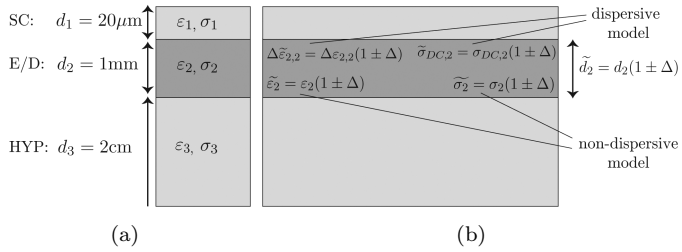


**Figure 6.4:** (a) Simplified numerical reference model of human skin and (b) the corresponding model with parameters of the second layer varied by a factor $(1 \pm \Delta)$ for the sensitivity and selectivity analysis.

Since the primary goal of this Chapter is not directly related to tissue microstructure but the assessement of sensitivity with respect to parameter changes in an entire layer of a multilayer system the use of Cole-Cole models is considered as justified. As mentionend in Section 2.3 here, the Cole-Cole models serve as placeholder. In the three layer skin model, each layer $i$ is represented by a complex permittivity $\varepsilon_i^*$ characterized by

$$\varepsilon_i^* = \varepsilon_{\infty,i} + \sum_n \frac{\Delta\varepsilon_{n,i}}{1 + (j\omega\tau_{n,i})^{(1-\alpha_{n,i})}} + \frac{\sigma_{DC,i}}{j\omega\varepsilon_0} \tag{6.6}$$

where $\varepsilon_{\infty,i}$ denotes the optical limit of the permittivity, $\sigma_{DC}$ the static conductivity, $\tau_n$ the $n$-th relaxation time, $\Delta\varepsilon_n$ the $n$-th permittivity increment, $\alpha_n$ the $n$-th broadening parameter and $n$ the number of dispersions. For the stratum corneum parameters from [130] for the 'untreated stratum corneum' case are taken. Since to the author's best knowledge there are no parameters for the isolated epidermis/dermis available, this layer is approximated by blood [34]. Blood vessels are non-uniformly distributed among the dermis and make up roughly 30% of its volume. But as a large part of the other epidermis/dermis components are cells with similar water content and dielectric characteristics as blood cells ($\beta$-dispersion) and thus the dispersive dielectric parameters of blood can be used as an approximation for these cells as well. The subcutaneous tissue,

**Table 6.1:** Cole-Cole parameters for each layer in the three-layer skin model. The values refer to 'untreated stratum corneum' from [130] for the SC, 'blood' for E/D and 'infiltrated fat' for HYP from [34].

| | $\varepsilon_\infty$ | $\sigma_{DC}$ [S/m] | $\Delta\varepsilon_1$ | $\tau_1$ [ps] | $\alpha_1$ | $\Delta\varepsilon_2$ | $\tau_2$ [ns] | $\alpha_2$ |
|---|---|---|---|---|---|---|---|---|
| SC | 4.4093 | 0.188 | 40.6 | 35 | 0 | 195 | 2.58 | 0 |
| E/D | 4 | 0.7 | 56 | 8.38 | 0.1 | 5200 | 132.6 | 0.1 |
| HYP | 2.5 | 0.035 | 9 | 79.6 | 0.2 | 35 | 15.92 | 0.1 |

| | $\Delta\varepsilon_3$ | $\tau_3$ [$\mu$s] | $\alpha_3$ | $\Delta\varepsilon_4$ | $\tau_4$ [ms] | $\alpha_4$ |
|---|---|---|---|---|---|---|
| SC | - | - | - | - | - | - |
| E/D | - | - | - | - | - | - |
| HYP | 33000 | 159 | 0.05 | $10^7$ | 15.9 | 0.01 |

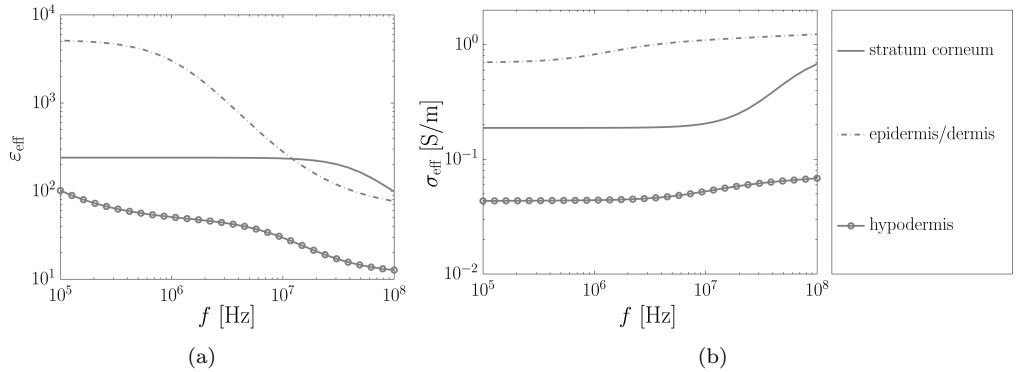


**Figure 6.5:** (a) Effective permittivity and (b) of skin layer models: The stratum corneum is modeled as 'untreated stratum corneum' from [130], the epidermis/dermis as 'blood' from [34] and the hypodermis as 'infiltrated fat' from [34]. The corresponding Cole-Cole parameters are given in Table 6.1.

the hypodermis is approximated by infiltrated fat [34]. The dispersive spectra for the single layers are shown in Figure 6.5 and the Cole-Cole parameters of each material are given in Table 6.1.

In order to determine the necessary computational volume in terms of the location of the boundary conditions and the number of layers to be modeled, the multi-layer system with and without the muscle below the hypodermis is investigated. For this purpose a fourth layer representing muscle tissue (exhibiting similar water content as epidermis and dermis and therefore also approximated with the same dielectric parameters) is included below the third layer. For the probe dimensions $r_\text{i} = 1.05\,\text{mm}$ and $r_\text{o} = 3.5\,\text{mm}$ it is found that the third layer must be thinner than $d_3 = 1\,\text{mm}$ in order to change both, the effective permittivity $\varepsilon_\text{eff}$ and conductivity $\sigma_\text{eff}$ by at least 1%. However, in most parts of the body the fat layer is much thicker than 1 mm and therewith a three-layer

approximation of the skin in combination with the probe/sensor size is sufficient. Consequently, the third layer in the model is assumed to be an infinite half space.
In the sensitivity analysis, the behaviour of the system employing dispersive as well as non-dispersive material characteristics will be investigated. The parameters for the non-dispersive case are taken at 1 MHz and 10 MHz of the Cole-Cole models as follows

- $\varepsilon_1 = 240$ (1 MHz) and 235.0460 (10 MHz)
- $\sigma_1 = 0.1882\,\mathrm{S/m}$ (1 MHz) and $0.2052\,\mathrm{S/m}$ (10 MHz)
- $\varepsilon_2 = 3026.3$ (1 MHz) and 280.0309 (10 MHz)
- $\sigma_2 = 0.8221\,\mathrm{S/m}$ (1 MHz) and $1.0967\,\mathrm{S/m}$ (10 MHz)
- $\varepsilon_3 = 50.8$ (1 MHz) and 29.5813 (10 MHz)
- $\sigma_3 = 0.0508\,\mathrm{S/m}$ (1 MHz) and $0.0526\,\mathrm{S/m}$ (10 MHz).

## 6.4 Analysis

The sensitivity and selectivity analysis is based on a 2D axial-symmetric FEM analysis of the coaxial probe introduced in Section 6.2.1. It is investigated how sensitive the system responds to changes of the dielectric parameters and thickness in the second layer of the three-layer skin model. Additionally, the effect of dispersive material characteristics versus constant dielectric parameters in each layer is demonstrated. For this purpose, the sensitivity analysis is performed both, for dispersive material parameters as well as for constant values of permittivity and conductivity. Thereafter, the specificity of the obtained sensitivity spectra is evaluated. In a next step, the transferability of these findings to other probe geometries is shown in an example where the multi-electrode sensor geometry (shown in Figure 6.3) is compared with coaxial probes. Finally, the dependence of the sensitivity on electrode distance is assessed for the coaxial and the interdigitated sensor geometry introduced in Subsection 6.2.2.

### 6.4.1 Semi-analytical solution

The effective dielectric properties of materials sensed by coaxial probes, interdigitated fringing field sensors or general coplanar electrode systems can be modeled with several techniques, as e.g. analytically by a technique based on conformal mapping [151] and [2].
For the coaxial probe, semi-analytical solutions are e.g. given in [154], [155],[156], [149] and [139]. The effective dielectric properties of a layered material under a coaxial probe as a function of capacitance, admittance or $S$-parameters are calculated with a variational method employed e.g. in [154], [157], [158], [159], [155], [160] and [156].
This method is based on a spectral domain analysis/ Hankel transform with respect to the radial coordinate. It is assumed that only the TEM mode propagates along the coaxial line, but evanescent $\mathrm{TM}_{0n}$ modes are taken into account in order to match boundary conditions at the probe-material and layer-to-layer interfaces. The theory is exact but in practice only a finite number of $\mathrm{TM}_{0n}$ modes is evaluated. Higher-order modes were included for the first time in [161], [162] and [163].
Since most publications provide the expressions for a limited number of layers and modes

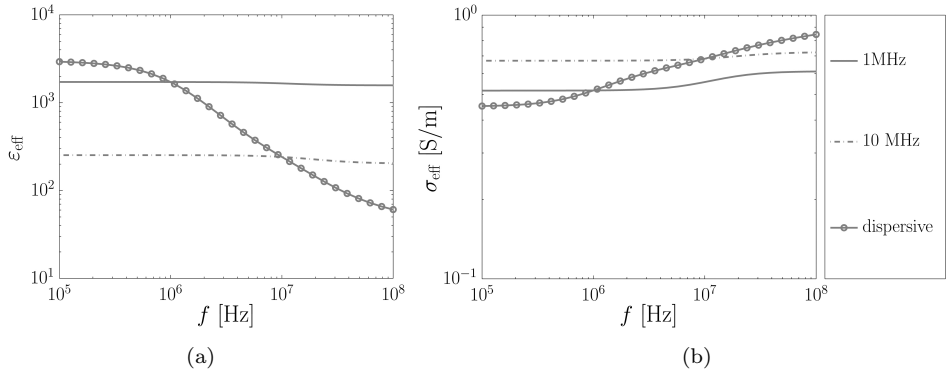


**Figure 6.6:** Effective permittivity (a) and conductivity (b) of the reference three-layer skin models (parameters extracted at 1 MHz and 10 MHz; $d_1 = 20\ \mu$m, $d_2 = 1$ mm and $d_3 \to \infty$) under a coaxial probe with $r_{\text{i}} = 1.05$ mm and $r_{\text{o}} = 3.5$ mm.

only, here, the procedure is generalized in Appendix C for $m$ layers with corresponding complex permittivities $\varepsilon_m^*$ and thicknesses $d_m$ taking $I$ evanescent $\text{TM}_{0i}$-modes into account. The procedure was implemented in MATLAB® (for code see Appendix B.5) in order to save computation time, but first of all for the accuracy assessement of the numerical model.

### 6.4.2 Sensitivity

For the sensitivity analysis the system is sensed by a coaxial probe given in Figure 6.1. The sensitivity of the system is investigated by varying the dielectric parameters as well as the thickness of the second layer by $\Delta = 0.1$. This variation is chosen because it is believed that most of the realistic changes within the skin would not exceed 10%. A relative measure for the sensitivity of the effective permittivity, $\Delta\varepsilon_{\text{eff}}$, is defined by

$$\Delta\varepsilon_{\text{eff}} = 100\frac{\varepsilon_{\text{eff}} - \varepsilon_{\text{eff,ref}}}{\varepsilon_{\text{eff,ref}}}\,. \tag{6.7}$$

where $\varepsilon_{\text{eff,ref}}$ is the reference effective permittivity (at $\Delta = 0$) of the second layer. An analogous definition to is employed for $\Delta\sigma_{\text{eff}}$.
In the case of a dispersive material model, the dielectric parameters of the three layers are given by the Cole-Cole models introduced in Section 6.3. For the sensitivity analysis, the parameters of the second layer are varied. Seven different scenarios are investigated, where either the thickness of the layer, the permittivity, the conductivity or a combination is varied by $\Delta = 0.1$ in the following way:

- $\Delta\widetilde{\varepsilon}_{2,2} = \Delta\varepsilon_{2,2}(1 \pm \Delta)$
- $\widetilde{\sigma}_2 = \sigma_{DC,2}(1 \pm \Delta)$
- $\Delta\widetilde{\varepsilon}_{2,2} = \Delta\varepsilon_{2,2}(1 + \Delta)$, $\widetilde{\sigma}_{DC,2} = \sigma_{DC,2}(1 + \Delta)$

- $\Delta\widetilde{\varepsilon}_{2,2} = \Delta\varepsilon_{2,2}(1-\Delta)$, $\widetilde{\sigma}_{DC,2} = \sigma_{DC,2}(1-\Delta)$
- $\Delta\widetilde{\varepsilon}_{2,2} = \Delta\varepsilon_{2,2}(1+\Delta)$, $\widetilde{\sigma}_{DC,2} = \sigma_{DC,2}(1-\Delta)$
- $\Delta\widetilde{\varepsilon}_{2,2} = \Delta\varepsilon_{2,2}(1-\Delta)$, $\widetilde{\sigma}_{DC,2} = \sigma_{DC,2}(1+\Delta)$
- $\widetilde{d}_2 = d_2(1 \pm \Delta)$ .

In order to assess the influence of the dispersive characteristics of tissue, the sensitivity analysis is repeated with constant dielectric parameters. In this case, the dielectric parameters of the three layers are taken at frequencies of 1 MHz and 10 MHz of the Cole-Cole models. These frequencies are chosen because the layers exhibit a high (at 1 MHz) and a lower (at 10 MHz) dielectric contrast representing two extreme cases. For the sensitivity analysis the parameters of the second layer are varied by $\Delta = 0.1$:

- $\widetilde{\varepsilon}_2 = \varepsilon_2(1 \pm \Delta)$
- $\widetilde{\sigma}_2 = \sigma_2(1 \pm \Delta)$
- $\widetilde{\varepsilon}_2 = \varepsilon_2(1+\Delta)$, $\widetilde{\sigma}_2 = \sigma_2(1+\Delta)$
- $\widetilde{\varepsilon}_2 = \varepsilon_2(1-\Delta)$, $\widetilde{\sigma}_2 = \sigma_2(1-\Delta)$
- $\widetilde{\varepsilon}_2 = \varepsilon_2(1+\Delta)$, $\widetilde{\sigma}_2 = \sigma_2(1-\Delta)$
- $\widetilde{\varepsilon}_2 = \varepsilon_2(1-\Delta)$, $\widetilde{\sigma}_2 = \sigma_2(1+\Delta)$
- $\widetilde{d}_2 = d_2(1 \pm \Delta)$

The absolute permittivity and conductivity spectra for the dispersive reference case and the non-dispersive models are given in Figure 6.6. The dielectric parameters and thicknesses of stratum corneum, epidermis/dermis and hypodermis layer are in a such relation that a layered structure generates a dispersion in the MHz region due to the thin (compared to the inter-electrode distance) and poorly conductive stratum corneum. In the non-dispersive case with the parameters taken at 1 MHz this effect is more pronounced than at 10 MHz because of a higher dielectric contrast within a small volume. Although the mechanisms are the same (interfacial polarization), this dispersion should not be confused with the $\beta$-dispersion.

The sensitivity of a system depends on the sensed volume, which strongly depends on the probe itself (as mentioned in Section 6.4.2), but also on the measured system. As an illustrative case, the electric potential and electric field lines at 1 MHz of the sensing system employing a coaxial probe are shown in Figure 6.7. Two completely different field distributions and sensing volumes can provide the same effective dielectric parameters: Figure 6.7(a) shows the field distribution in three-layer system, whereas Figure 6.7(b) displays the field distribution in a homogeneous material exhibiting the effective material properties extracted from the simulation shown in Figure 6.7(a). The plots in Figure 6.7(a) and 6.7(b) show systems exhibiting the same effective dielectric parameters $\varepsilon_{\text{eff}}$ and $\sigma_{\text{eff}}$. It can be seen, that the field distribution strongly depends on the geometry and the dielectric contrast. In the layered system the field is pushed towards the sensor by the second, relatively high-$\varepsilon$- and high-$\sigma$ layer. This leads to a significantly smaller sensing volume compared to the homogeneous case.
In [59] and [164] the penetration depth is defined as the distance between probe and sample after lift-off at which the measured value drops to 1% and 3%, respectively of

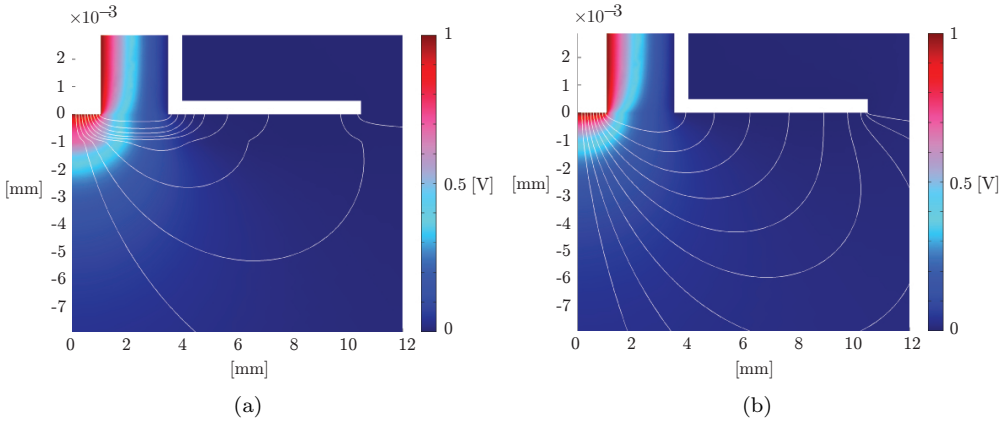


**Figure 6.7:** Plots of the electric field (lines) and electric potential (color-coded intensity plot) at 1 MHz of a coaxial probe from Figure 6.1. In (a) the material under test is composed of three layers, in (b) the material is homogeneous with the effective dielectric parameters obtained from the system in (a). Only a part of the electric field lines is displayed. In both subfigures the field lines have the same starting points on the bottom of the inner condutctor.

the original value. This is 'dangerous' since the distances will not be absolute but depend on the measured system (layering and material parameters). In other words the so-obtained distance for measurements of two different systems might be the same but the fields having in fact very different penetrations into the material.
In simulations it can be determined up to which layer a defined amount (e.g. 99%) of the total electric energy and resistive heat is contained.

### 6.4.3 Specificity

The parameter variations of the second layer cause a shift of the absolute effective dielectric spectra. This fact can be exploited in order to identify these parameter changes from the changes of the sensed effective skin parameters. The specificity of the system is investigated by establishing a characteristic spectral sign pattern from the relative effective permittivity and conductivity in Equation 6.7 as well as their first and second derivatives. This pattern is analyzed in order to investigate if and to what extent it can be used for a unique identification of a specific parameter change. In order to be able to adapt the procedure for noisy data (e.g. from measurements) an absolute threshold value for the sensitivity $t_s$, indicating the lowest detectable $\Delta\varepsilon_{\text{eff}}$ and $\Delta\sigma_{\text{eff}}$ is introduced. Additionally, as the numerical values for the derivatives can get very small relative thresholds for the first and second derivative $t_\partial = \pm\max(|\frac{\partial\Delta\varepsilon_{\text{eff}}}{\partial f}|)$ and $t_{\partial^2} = \pm\max(|\frac{\partial^2\Delta\varepsilon_{\text{eff}}}{\partial f^2}|)$ are defined. In the performed calculations the thresholds are set to $t_s = \pm 0.1$ and $t_\partial = t_{\partial^2} = \pm 0.05$.

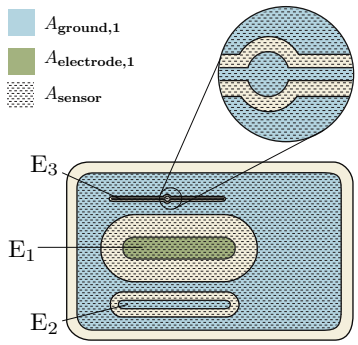


**Figure 6.8:** Graphical description for the area equivalents for the approximation of the effective properties of the multi-electrode sensor by a coaxial probe. The illustration refers to the electrode $E_1$: The area $A_{\text{electrode},1}$ corresponds to the contact area of the inner conductor, the area $A_{\text{ground},1}$ to area of the outer conductor/flange. The procedure for obtaining the area equivalents for the the other two electrodes $E_2$ and $E_3$ is the same.

### 6.4.4 Transferability to other sensor geometries

It is investigated to what extent data obtained by coaxial probes can serve as an approximation for the presented multi-electrode fringing-field sensor. As described e.g. in [149] the sensed volume of a coaxial probe is strongly related to the distance between inner and outer conductor (the electrode spacing) $r_{\text{o}} - r_{\text{i}}$. Additionally, the effective dielectric properties also depend on the electrode area. Here, this characteristics is assumed to be similar for the multi-electrode sensor. Thus, the size of the coaxial probe might be adjusted in order to mimick the properties of the fringing-field sensor. The dimensions $r_{\text{i},\,i}, r_{\text{o},\,i}$ and $r_{\text{flange},\,i}$ of the scaled coaxial geometry are given in the following. The area of the inner coaxial conductor should be the same as the one of the driven electrode of the multi-electrode sensor

$$A_{\text{electrode},i} = \pi \left(\frac{s_i}{2}\right)^2 + s_i l_i \tag{6.8}$$

and hence the radius of the inner conductor $r_{\text{i},\,i}$ can be computed from

$$r_{\text{i},\,i} = \sqrt{\frac{s_i}{l_i + s_i} \frac{A_{\text{electrode},i}}{\pi}}. \tag{6.9}$$

Here, the electrode area of the multi-electrode sensor is multiplied by an empirical correction factor $s_i/(l_i + s_i)$ in order to capture the deviation of the original electrode from a circular shape. The electrode spacing is kept constant and hence the radius of the outer conductor $r_{\text{o},\,i}$ is given by

$$r_{\text{o},\,i} = r_{\text{i},\,i} + s_i. \tag{6.10}$$

Finally, the flange radius $r_{\text{flange},\,i}$ is obtained by setting the area of the outer conductor equal to the area multi-electrode sensor ground plane plus the non-driven electrodes

$A_{\mathrm{ground},\,i}$

$$r_{\mathrm{flange},\,i} = \sqrt{\frac{A_{\mathrm{ground},\,i}}{\pi} + r_{\mathrm{o},\,i}^2} \tag{6.11}$$

with

$$A_{\mathrm{ground},\,i} = A_{\mathrm{sensor}} - \sum_i A_{\mathrm{gap},\,i} - A_{\mathrm{electrode},i} \tag{6.12}$$

and

$$A_{\mathrm{gap},\,i} = \pi \left(\frac{3}{2} s_i\right)^2 + 3 s_i l_i - A_{\mathrm{electrode},i}\,. \tag{6.13}$$

The area of the driven electrode is $A_{\mathrm{electrode},i}$ and the area of the gap is denoted with $A_{\mathrm{gap},\,i}$. A graphical description of these areas is given in Figure 6.8.

### 6.4.5 Sensitivity of different probe geometries

The influence of the spatial utilization of the probe footprint on its sensitivity is analysed by comparing the coaxial probe to an interdigitated sensor representing another type of commonly employed sensors. The spatial utilization of the coaxial probe is varied by changing the electrode distance while keeping the radius of the inner conductor $r_\mathrm{i}$ and the total size of the probe constant. This means that the radius of the outer conductor $r_\mathrm{o}$ and consequently the area of the outer electrode/conductor $A_\mathrm{o}$ are variable. The dimensions of the interdigital sensor are derived from those for the coaxial probe geometry according to Subsection 6.2.2.

### 6.4.6 Geometry simplifications

The full 3D system consisting of sensor and skin model is computationally expensive in terms of central processing unit (CPU) time and random-access memory (RAM). This is especially challenging if many simulations, e.g. for the presented sensitivity analysis have to be performed. Hence, it is desirable to reduce the computational effort of those simulations. One approach is to approximate the 3D geometry by a 2D representation as performed in this paragraph. The most important parameter of the multi-electrode sensor is the electrode spacing, whereas the length of the electrode exhibits a smaller influence. In the following, the electrodes are assumed to be infinitely long allowing for a 2D simulation. In this way, only the 2D cross section of the electrode has to be modeled, resulting in a large computational speedup. An additional simplification of the 2D cross-section can be performed by simulating each electrode as a 2D cross-section separately (see plots denoted by 'E$_i$ - single' in Figure 6.21). The driven electrode has the width $s_i$ and is again separated by $s_i$ on each side from the left and right ground electrode. The widths of the ground electrodes corrspond to half the sum of the grounded electrodes from the original 2D sensor cross-section.

## 6.5 Results and discussion

### 6.5.1 Semi-analytical vs. numerical solution

The semi-analytical solution for the coaxial probe assumes an infintely long flange, so the question is from which flange radius on will the difference between semi-analytical and numerical solution drop below a certain threshold value defined as accurate enough. The minimum length will depend on the system under test. Deviations of the numerical solution of the three-layer skin model with dispersive parameters with respect to the semi-analytical calculation is given in Figure 6.9. The semi-analytical solution involves 5 $\mathrm{TM}_{0n}$ modes. The plots provide the deviation of numerical simulations with increasing flange radii of the coaxial probe. One would expect that the absolute error converges to zero or a value near zero with increasing flange radius as the semi-analytical solution assumes an infintely long flange. Although the error is smaller than 8% for the permittivity and smaller than 3% for the conductivity in the entire frequency range the mentioned assumption only holds for $f > 10\,\mathrm{MHz}$. In order to answer that question aspects such as the sensitivity to the discretization on the side of the numerical simulations as well as the number of $\mathrm{TM}_{0n}$ modes and numerical precision of the numerical integrations in the semi-analytical solution would have to be investigated in detail.

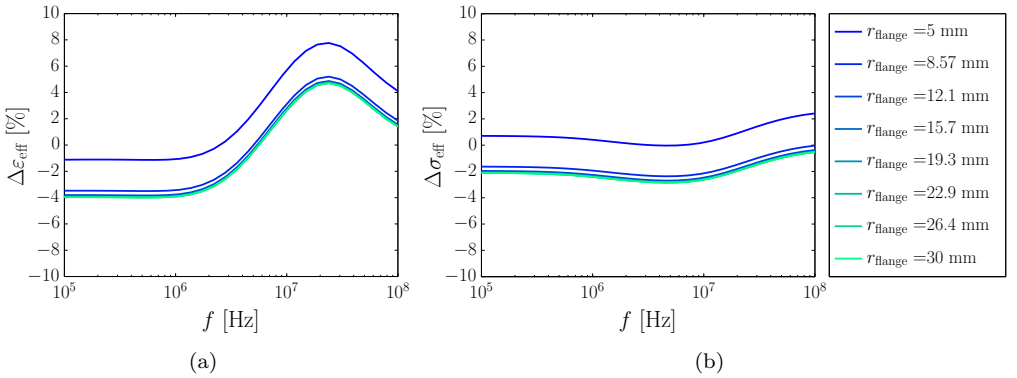


**Figure 6.9:** Relative deviations in effective permittivity (a) and conductivity (b) of a coaxial probe ($r_{\mathrm{i}} = 1.05$ mm and $r_{\mathrm{o}} = 3.5$ mm) on top of the reference three-layer system. Shown are deviations for the numerical models for different flange radii with respect to the semi-analytical solution ('infinite' flange radius).

### 6.5.2 Sensitivity

The sensitivity analysis for parameter variations with respect to the reference system ($\Delta = 0$) are plotted in Figure 6.10 for the three-layer system with dispersive material characteristics. It can be seen in the spectra that each relative variation exhibits a characteristic behaviour over the frequency. It has to be noted that a simultaneous increase

(decrease) of both dielectric parameters $\Delta\varepsilon_{2,2}$ and $\sigma_{DC,2}$ qualitatively corresponds to an increase (decrease) of the layer thickness $d_2$. However, a perfect match of the two cases could only be realized if both dielectric parameters were varied independently. It can be seen that the measured change in dielectric properties is sensitive to the kind of the parameter ($\Delta\varepsilon_{2,2}$, $\sigma_{DC,2}$ or $d_2$) and the frequency. The slight asymmetry with respect to $\Delta\varepsilon_{\text{eff}} = 0$ and $\Delta\sigma_{\text{eff}} = 0$ almost vanishes but exists. In the end the crucial quantity is the resulting dielectric contrast between the layers: Is the contrast increased a higher sensitivity can be expected, the opposite is true if the change causes a dielectric contrast reduction.

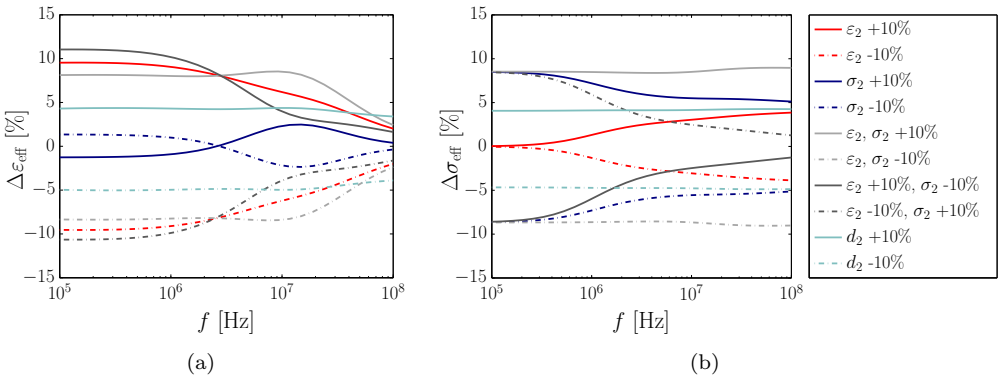


**Figure 6.10:** Relative deviations in effective permittivity (a) and conductivity (b) with respect to the reference three-layer system (dispersive dielectric parameters given in Figure 6.5 and $d_1 = 20$ $\mu$m, $d_2 = 1$ mm and $d_3 \to \infty$) under a coaxial probe with $r_\text{i} = 1.05$ mm and $r_\text{o} = 3.5$ mm.

For the non-dispersive case, Figure 6.11 shows the sensitivity analysis for dielectric parameters extracted at 1 MHz and Figure 6.12 for the dielectric parameters extracted at 10 MHz. A comparison the sensitivity spectra shows the importance of the dispersive skin layers in the model. The sensitivity spectra in the non-dispersive cases which are assumed to less accurately represent the dielectric behaviour of skin strongly differ from those for the dispersive case. Therefore, only the model with the dispersive skin layers will be further investigated.

The sensitivity behaviour as a function of parameter change $\Delta$ is investigated in the following. For this purpose, the range of parameter variation is extended to $\Delta = \pm 0.2$. The results of this analysis for a parameter change of $\Delta\widetilde{\varepsilon}_{2,2} = \Delta\varepsilon_{2,2}(1 + \Delta)$ in shown in Figure 6.13(a) for the change of effective permittivity and in (b) for the change of effective conductivity. The variation of $\widetilde{\sigma}_{DC,2} = \sigma_{DC,2}(1 + \Delta)$ in depicted in Figure 6.13(c) and (d). Variation of both, permittivity and conductivity in the same direction (same sign of $\Delta$) results in relative deviations of the effective parameters as shown in Figure 6.14(a) and (b) for $\Delta\widetilde{\varepsilon}_{2,2} = \Delta\varepsilon_{2,2}(1 + \Delta)$ and $\widetilde{\sigma}_{DC,2} = \sigma_{DC,2}(1 + \Delta)$. The relative

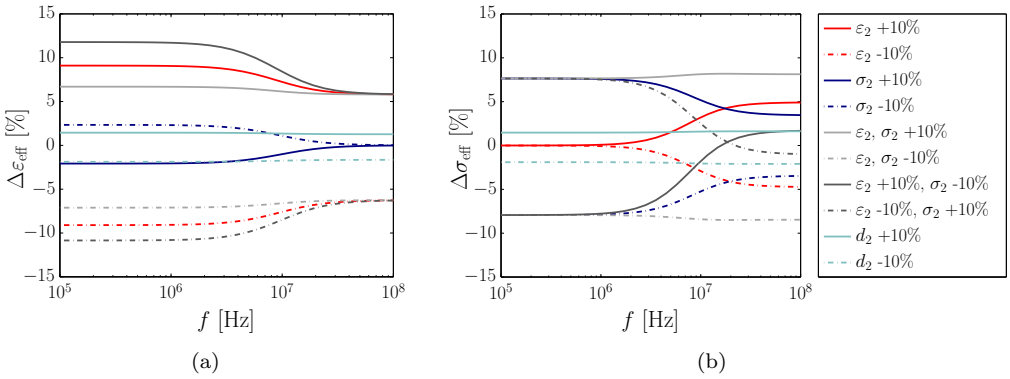


(a) (b)

**Figure 6.11:** Relative deviations in effective permittivity (a) and conductivity (b) with respect to the reference three-layer system (parameters from Figure 6.5 extracted at 1 MHz and $d_1$ = 20 $\mu$m, $d_2$ = 1 mm and $d_3 \to \infty$) under a coaxial probe with $r_\text{i}$ = 1.05 mm and $r_\text{o}$ = 3.5 mm.

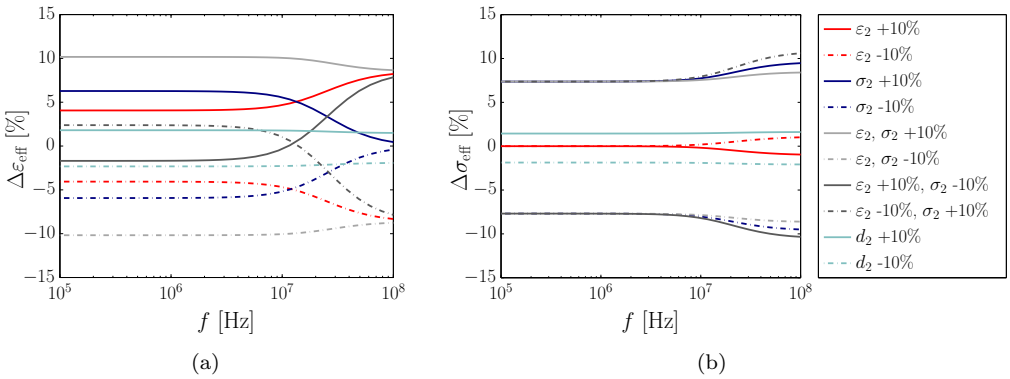


(a) (b)

**Figure 6.12:** Relative deviations in effective permittivity (a) and conductivity (b) with respect to the reference three-layer system (parameters from Figure 6.5 extracted at 10 MHz and $d_1$ = 20 $\mu$m, $d_2$ = 1 mm and $d_3 \to \infty$) under a coaxial probe with $r_\text{i}$ = 1.05 mm and $r_\text{o}$ = 3.5 mm.

deviations of the effective parameters for a simultaneous change of the dielectric parameters in opposite directions (opposite signs of $\Delta\varepsilon_{\text{eff}}$ and $\Delta\sigma_{\text{eff}}$) $\Delta\widetilde{\varepsilon}_{2,2} = \Delta\varepsilon_{2,2}(1+\Delta)$ and $\widetilde{\sigma}_{DC,2} = \sigma_{DC,2}(1-\Delta)$ are reflected in Figure 6.14(c) and (d). Overall, it can be stated that the sensitivity behaviour is linear at least up to $\Delta = 0.2$ for variations of the dielectric parameters. In the case of thickness variation shown in Figure 6.15 the dependency is approximately logarithmic. The dielectric variation and thickness variation do

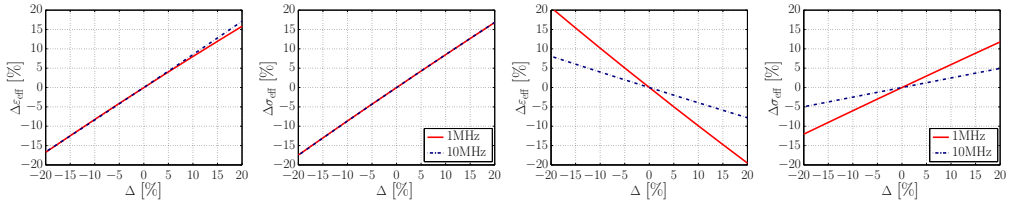


**Figure 6.14:** Relative changes in effective permittivity and conductivity of the dispersive three-layer system ($d_1 = 20$ $\mu$m, $d_2 = 1$ mm and $d_3 \to \infty$) under a coaxial probe with $r_\mathrm{i} = 1.05$ mm and $r_\mathrm{o} = 3.5$mm as a function of the variation. Variations of the following parameters of the second layer by -0.2 $\leq \Delta \leq$ 0.2 are shown: $\Delta\widetilde{\varepsilon}_{2,2} = \Delta\varepsilon_{2,2}(1+\Delta)$ and $\widetilde{\sigma}_{DC,2} = \sigma_{DC,2}(1+\Delta)$ in (a) and (b) and $\Delta\widetilde{\varepsilon}_{2,2} = \Delta\varepsilon_{2,2}(1+\Delta)$ and $\widetilde{\sigma}_{DC,2} = \sigma_{DC,2}(1-\Delta)$ in (c) and (d).

not scale in the same way as the distribution of the electric field is non-uniform within the sensing volume.

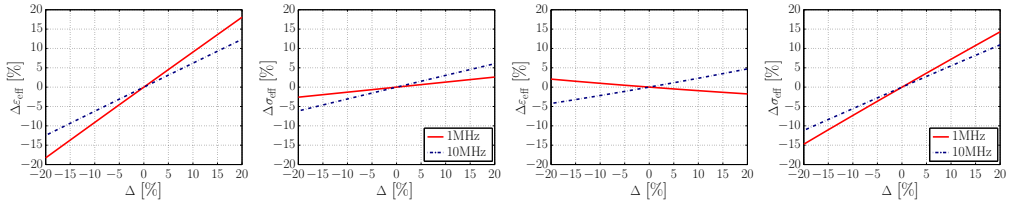


**Figure 6.13:** Relative changes in effective permittivity and conductivity of the dispersive three-layer system ($d_1 = 20$ $\mu$m, $d_2 = 1$ mm and $d_3 \to \infty$) under a coaxial probe with $r_\mathrm{i} = 1.05$ mm and $r_\mathrm{o} = 3.5$mm as a function of the variation. Variations of the following parameters of the second layer by -0.2 $\leq \Delta \leq$ 0.2 are shown: $\Delta\widetilde{\varepsilon}_{2,2} = \Delta\varepsilon_{2,2}(1+\Delta)$ in (a) and (b) and $\widetilde{\sigma}_{DC,2} = \sigma_{DC,2}(1+\Delta)$ in (c) and (d).

### 6.5.3 Specificity

The sensitivity analysis indicates that the origin of the change in the effective properties can be identified if the $\Delta\varepsilon_\mathrm{eff}$ and $\Delta\sigma_\mathrm{eff}$ spectra and their derivatives are known. As shown in Figure 6.16, analysing the $\Delta\varepsilon$ spectra and their first and second order derivatives $\partial\Delta\varepsilon_\mathrm{eff}/\partial f$ and $\partial^2\Delta\varepsilon_\mathrm{eff}/\partial f^2$ (and for $\Delta\sigma$ accordingly), each parameter variation shows a characteristic behaviour over the frequency. The signs of the sensitivity spectra and their first and second derivatives with respect to the frequency provide an characteristic pattern. These patterns are shown in Figure 6.17. In the presented setting exhibiting a significant dielectric contrast, and for the given thresholds, the sign patterns are unique

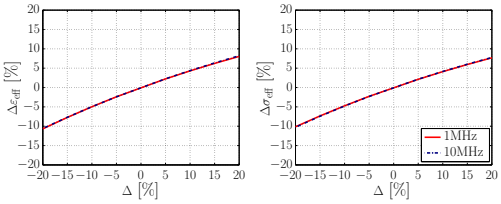


(a) (b)

**Figure 6.15:** Relative changes in effective permittivity and conductivity of the dispersive three-layer system ($d_1 = 20$ $\mu$m, $d_2 = 1$ mm and $d_3 \to \infty$) under a coaxial probe with $r_\mathrm{i} = 1.05$ mm and $r_\mathrm{o} = 3.5$mm. Variation of the second layer thickness $d_2$ by -0.2 $\leq \Delta \leq$ 0.2, $\widetilde{d_2} = d_2(1+\Delta)$ is shown for the permittivity (a) and conductivity (b).

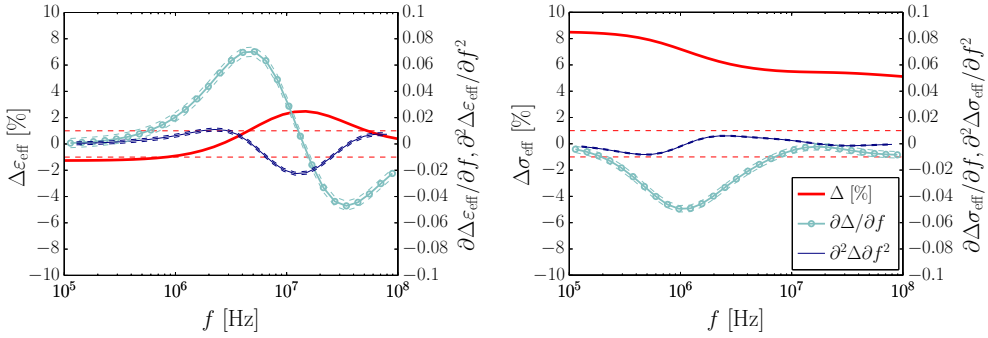


(a) (b)

**Figure 6.16:** Relative deviations in effective permittivity (a) and conductivity (b) and the derivatives for the case $\widetilde{\sigma_2} = \sigma_2(1-\Delta)$ and $\Delta = 0.1$. Reference three-layer system (dispersive dielectric parameters, $d_1 = 20$ $\mu$m, $d_2 = 1$ mm and $d_3 \to \infty$) under a coaxial probe with $r_\mathrm{i} = 1.05$ mm and $r_\mathrm{o} = 3.5$ mm. Additionally the absolute threshold bounds of $\pm$ 10 % for the sensitivity curve are shown ($t_s = \pm 0.1$) as well as the relative threshold bounds for each derivative of $\pm$ 5% of the corresponding maximal value ($t_\partial = t_{\partial^2} = \pm 0.05$). The corresponding thresholds are denoted by dashed lines.

and therefore show a specificity for parameter changes of the second layer. However, the uniqueness strongly depends on the measurement precision (signal-to-noise ratio) as well as on the numerical precision of the evaluation of the derivatives.

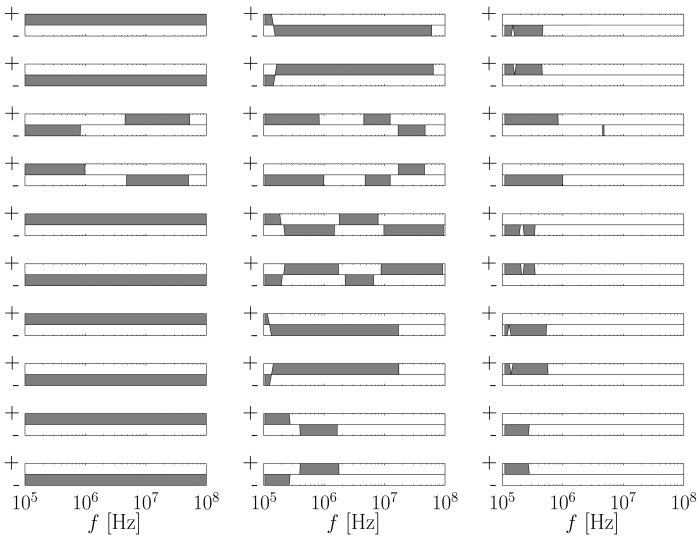


(a)

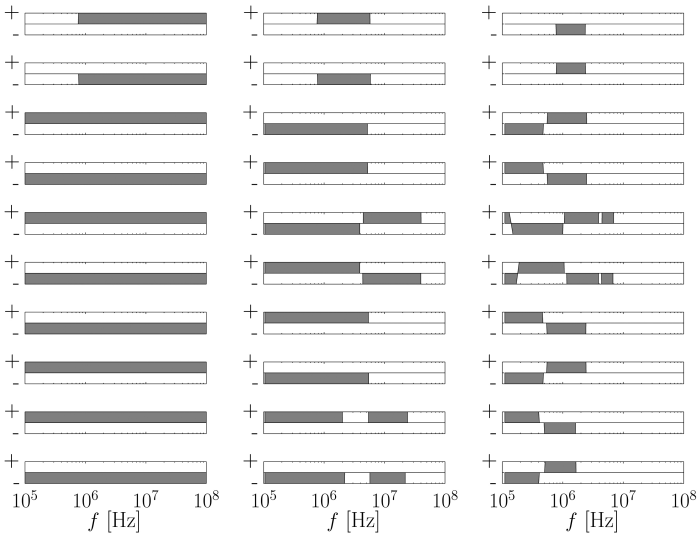


(b)

**Figure 6.17:** Sign patterns for the difference spectra and their first and second derivatives for the permittivity (a) and conductivity (b): $\Delta$ (left, absolute threshold value $t_s = \pm\ 0.1$), $\partial\Delta$ (middle, relative threshold value $t_\partial = \pm\ 0.05$) and $\partial^2\Delta$ (right, relative threshold value $t_{\partial^2} = \pm\ 0.05$).

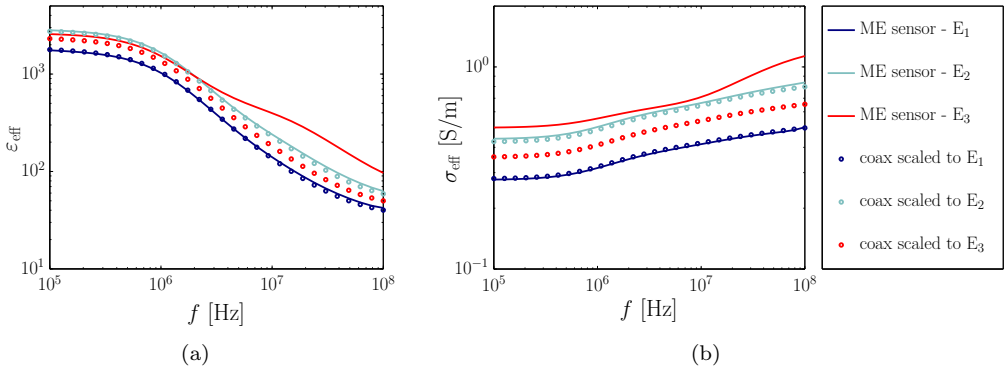


**Figure 6.18:** Effective permittivity (a) and conductivity (b) for the multi-electrode (ME) sensor displayed in Figure 6.3 and the coaxial probe geometry from Figure 6.1 with scaled inner and outer radii with respect to the electrodes of the ME sensor, $E_1$, $E_2$ and $E_3$.

.

### 6.5.4 Transferability to other probe geometries

A comparison between the dielectric spectra obtained with the multi-electrode sensor and the scaled coaxial probes is presented in Figure 6.18. It can be seen that the approximation works best for the electrode $E_1$ and to a lesser extend for $E_3$. This can be explained with the shape of the electrode, as $E_1$ has the largest ratio between electrode width and length and therefore the smallest deviation from the circular shape among all three electrodes. Overall, the general behaviour of the multi-electrode sensor can be approximated by a coaxial geometry, which means that the sensitivity analysis presented in Section 6.4.2 can be transferred also to other types of sensors.
The results also indicate that, up to a certain ratio between electrode width and length, the 2D axial symmetric analysis can be used as a quick evaluation of the sensitivity and specificity for less symmetric coplanar electrodes as well. Furthermore, the results underline the influence of the interelectrode distance on the effective properties of a layered system.

### 6.5.5 Sensitivity of different probe geometries

A sensitivity analysis of two different probe geometries (coaxial and interdigital) as a function of electrode distance is performed at 1 MHz and 10 MHz. The results of this analysis are plotted in Figure 6.19(a) and (b) for a variation of $\Delta\widetilde{\varepsilon}_{2,2} = \Delta\varepsilon_{2,2}(1 \pm \Delta)$, and $\widetilde{\sigma}_{DC,2} = \sigma_{DC,2}(1 \pm \Delta)$ in Figure 6.19(c) and (d). The simultaneous variation of $\Delta\widetilde{\varepsilon}_{2,2} = \Delta\widetilde{\varepsilon}_{2,2}(1 \pm \Delta)$ and $\widetilde{\sigma}_{DC,2} = \sigma_{DC,2}(1 \pm \Delta)$ is shown in Figure 6.20(a) and (b). Simultaneous variation of $\Delta\widetilde{\varepsilon}_{2,2} = \Delta\widetilde{\varepsilon}_{2,2}(1 \pm \Delta)$ and $\widetilde{\sigma}_{DC,2} = \sigma_{DC,2}(1 \mp \Delta)$ are plotted in Figure 6.20(c) and (d).
It can be seen that the coaxial probe is more sensitive, except for $\varepsilon_{\text{eff}}$ in case of a change in $\sigma_{DC,2}$ for electrode distances between 1 mm to 6.25 mm at 10 MHz. The field of the

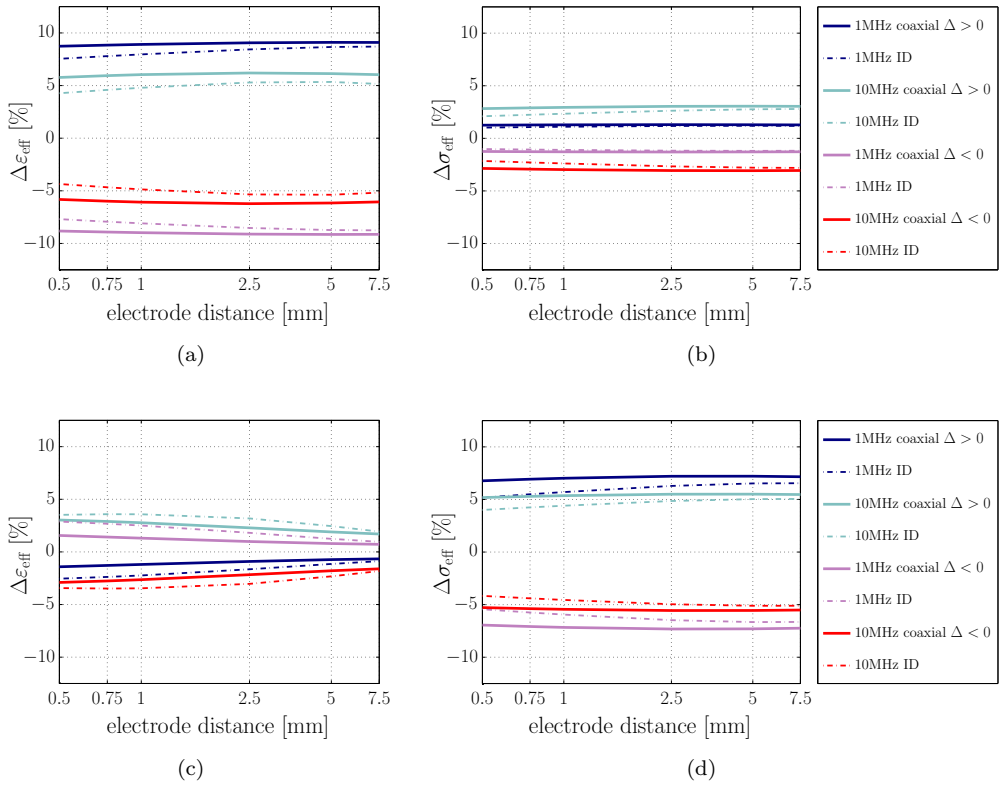


**Figure 6.19:** Comparison of relative changes in effective permittivity and conductivity of the dispersive three-layer system ($d_1 = 20\ \mu$m, $d_2 = 1$ mm and $d_3 \to \infty$) under a coaxial probe and an 2D model of an interdigitated sensor (denoted as ID in the legend) as a function of the electrode distance. Variations ($\Delta = 0.1$) of the following parameters of the second layer: $\Delta\widetilde{\varepsilon}_{2,2} = \Delta\varepsilon_{2,2}(1 \pm \Delta)$ in (a) and (b), and $\widetilde{\sigma}_{DC,2} = \sigma_{DC,2}(1 \pm \Delta)$ in (c) and (d).

coaxial probe is more concentrated close to the inner conductor as in the case of the interdigitated sensor, where the electric field decays slower in the negative $z$-direction (normal to the electrode surface, see Figure 6.2(b)) and is more uniform in $x$-direction. Except for the variation of $\sigma_{\mathrm{DC},2}$ the sensitivity is also higher for both geometries at 1 MHz.

It has to be noted that only one parameter setting for the interdigitated geometry is investigated. It is expected that its sensitivity rises as the total electrode area increases for a larger number of digits. Another possible parameter variation for a total fixed sensor area and $s_{\mathrm{ground}} = s_{\mathrm{driven}} = s$ would be to find the optimum number of digits. In any case, the interdigital geometry provides a larger number of degrees of freedom than the coaxial geometry and finding an electrode configuration providing the highest

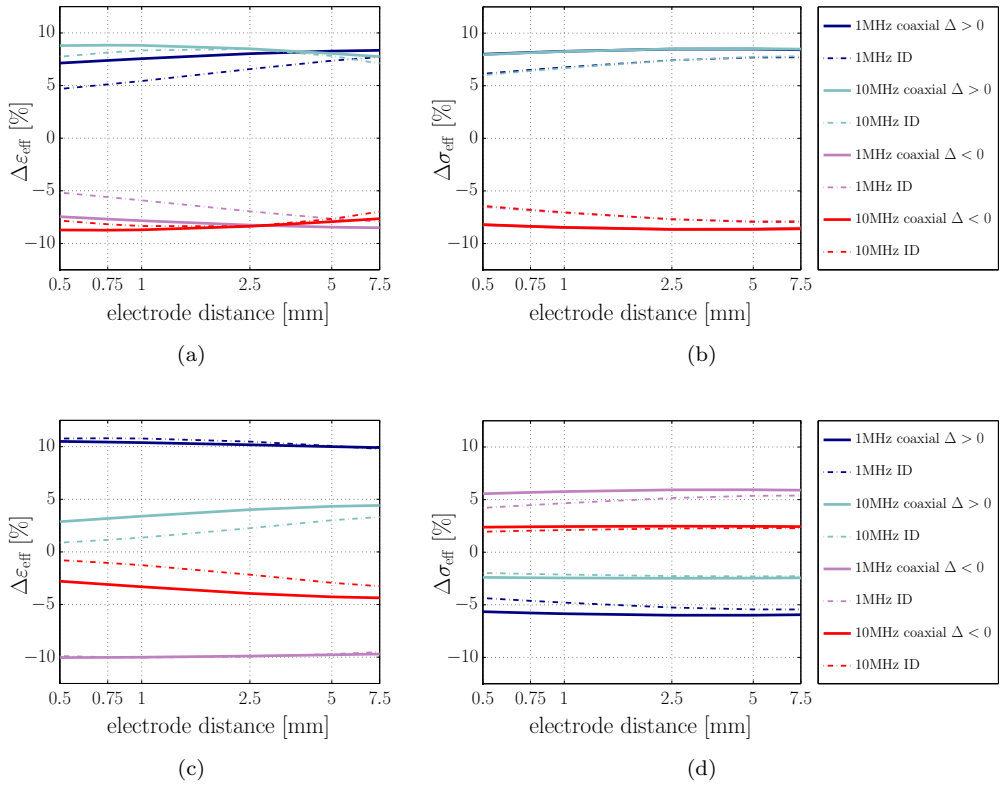


**Figure 6.20:** Comparison of relative changes in effective permittivity and conductivity of the dispersive three-layer system ($d_1 = 20$ $\mu$m, $d_2 = 1$ mm and $d_3 \to \infty$) under a coaxial probe and an 2D model of an interdigitated sensor (denoted as ID in the legend) as a function of the electrode distance. Variations ($\Delta = 0.1$) of the following parameters of the second layer: $\Delta\widetilde{\varepsilon}_{2,2} = \Delta\widetilde{\varepsilon}_{2,2}(1 \pm \Delta)$ and $\widetilde{\sigma}_{DC,2} = \sigma_{DC,2}(1 \pm \Delta)$ in (a) and (b), and $\Delta\widetilde{\varepsilon}_{2,2} = \Delta\widetilde{\varepsilon}_{2,2}(1 \pm \Delta)$ and $\widetilde{\sigma}_{DC,2} = \sigma_{DC,2}(1 \mp \Delta)$ in (c) and (d).

sensitivity depends on the system under test and is a matter of optimization.

### 6.5.6 Geometry simplifications

A 2D simulation of the multi-electrode sensor consumes approximately 8 % computer memory and 0.6 % CPU time of the corresponding 3D problem. The relative deviation with respect to a 3D reference simulation is shown in Figure 6.21. The largest relative error (with respect to the 3D model) of approximately 15 % exhibits electrode $\mathrm{E}_1$ due to the large curvatures at the electrode ends compared to the electrode length.
An additional simplification of the 2D cross-section can be performed by simulating each electrode as a 2D cross-section separately (see plots denoted by '$\mathrm{E}_i$ - single electrode' in

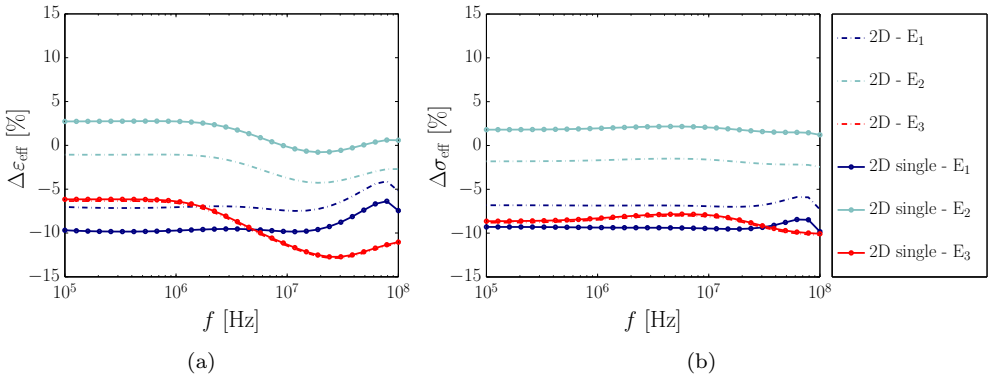


**Figure 6.21:** Relative deviations in effective permittivity $\Delta\varepsilon_{\text{eff}}$ (a) and conductivity $\Delta\sigma_{\text{eff}}$ (b) of the 2D model from the 3D simulation of a simplified three-layer skin model probed by the multi-electrode sensor shown in Figure 6.3.

Figure 6.3(c)). The driven electrode has the width $s_i$ and is again separated by $s_i$ on each side from the left and right ground electrode. The widths of the ground electrodes corrspond to half the sum of the grounded electrodes from the original 2D sensor cross-section.
Since 2D simulations are computationally very efficient, they can serve as a good approximation of the real structure yielding results which indicate the characteristics of the sensor. It has to be mentioned that, especially in the presented model with the very thin topmost layer, the electrode thickness of 40 $\mu$m of the sensor electrodes has to be included in the model. The difference between infinitely thin electrodes and electrodes with finite thickness of 40$\mu$m reaches up to 20% for the smallest electrode $E_3$. This has to be considered if the material under test is touching the substrate. Therefore, there is a large difference between sensing a solid, soft surface and a liquid.

## 6.6 Conclusion

The effective dielectric properties of a multilayer system probed by a coaxial probe were successfully calculated using an semi-analytical as well as a numerical method. The semi-analytical method served as a validation and was shown to be an alternative in case of very thin layers where the large aspect ration in numerical solution might lead to large errors.

In the framework of the sensitivity analysis the importance of using dispersive dielectric parameters for each layer of the skin model is demonstrated. The concept of a sensitivity and specificity analysis based on numerical simulations was successfully applied to different fringing-field electrode geometries probing a multi-layer system approximately representing human skin. It was found that the sensitivity strongly depends on fre-

quency, but is generally highest at the lower end of the frequency range from 100 kHz up to 100 MHz. Changes in the effective dielectric parameters can be uniquely assigned to specific changes in permittivity and conductivity within the second layer based on an analysis of the dielectric spectra. Changes in the thickness of the second layer also cause a change in the effective dielectric parameters but exhibit an almost constant shift in the spectrum. Overall it is shown that as much information about the spectral behaviour as possible is needed in order to increase the possibility to distinguish between different types of changes. The presented procedure not only can be used to determine mechanisms causing detectable changes in dielectric properties in a specific layer of a layered system, but also for the optimization of a specific sensor design. Moreover, the procedure is generally applicable to other kinds of multi-layer structures. In the specific case of human skin a sufficiently precise skin model could be used to calibrate out the influence of the skin upper layer allowing to monitor deeper-lying tissues.

# 7 Application to human skin

In Chapter 6 it was demonstrated in the macroscopic multilayer model that layers with constant parameters are insufficient for tissue modeling in the MHz region and the influence of the cell membrane has to be included. The aim of this chapter is to gather the findings from Chapters 4 to 6 and applying them in order to establish a dielectric model of human skin based on its morphology and material properties. The skin will be represented as a composite on multiple spatial scales.

To date no comprehensive (continuous) set of the dielectric properties of skin sublayers SC, epidermis, dermis and hypodermis is available in the frequency range between 1 MHz and 100 MHz. In [132] and [165] the dielectric properties of the uppermost layer, the SC have been assessed by *in vivo* measurements of skin with and without this top layer. Coaxial probes of different sizes were employed in order to distinguish the SC, epidermis/dermis and hypodermis (subcutaneous fat), providing permittivity estimations for these layers, however, only at single frequencies [132]. The dielectric properties of skin and subuctaneous fat on human abdomen were assessed in [166]. Powdered native SC was also measured with a coaxial probe using the time domain reflectometry (TDR) method in [130] including an identification and quantification of two relaxation processes in the microwave frequency range. *In vivo* skin measurements as well as measurements of blood, infiltrated and non-infiltrated fat were performed in [34], also providing Cole-Cole relaxation models for all measured materials. In [33] human skin was measured *in vivo*, also including a Cole-Cole fit. As observed in [167] the Cole-Cole fits are a popular and useful tool in order to describe dielectric spectra of tissue in general. However, as already pointed out in Chapter 2 an unambiguous physical and physiological interpretation of the obtained Cole-Cole parameters remains difficult, because the impact of the numerous morphological and dielectric parameters as well as their variations has only partially been assessed so far.
Alternative modeling methods of other tissues or tissue-like structures using mixing formulas in the context of the effective medium approach or numerical methods have been presented e.g. in [3], [88] or [168]. The modeling method in this work is a combination of those methods including a multi-scale approach introduced in [126] and [102].

In [169] it is claimend that in order to minimize the effect of anisotropy on measurements of electrical properties of tissues, it is necessary to use modeling techniques to decouple the sample geometry from the measured tissue resistivity. In this work the opposite approach is followed by establishing a numerical model which accounts for the anisotropy of tissue, no matter which probe geometry is used.

Depending on the probe geometry effective dielectric parameters of layered structures as

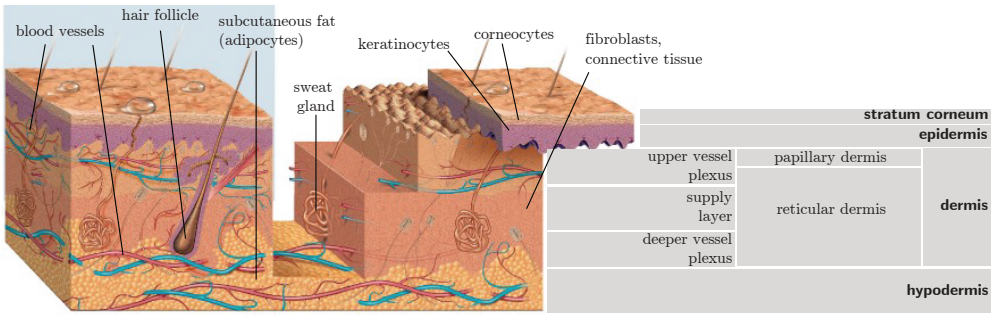


**Figure 7.1:** Structure of human skin adapted from [170].

the skin are usually a combination of the dielectric properties of the sublayers. In order to obtain the dielectric behaviour at different depths within the skin in this work a sensor with multiple planar electrodes is employed. The wider the distance from the driven to ground electrode the deeper the penetration of the electric field into the material.

## 7.1 Morphology of human skin

The human skin has a protective function. It regulates the body temperature and acts as a chemical and biochemical barrier. Also many physiological processes take place in the skin.

It was found in Chapters 3 and 4 that the cell shape has a significant influence on the effective dielectric properties at frequencies $< 10$ MHz. In order to be able to decide which features are likely to be included in an appropriate skin model detailed knowledge of the skin morphology is necessary. Therefore, a brief literature review on skin anatomy is given in the following. The review is similar to the one in Section 6.3 but contains more details.

### 7.1.1 Stratum corneum

The SC contains flat hexagonally shaped corneocytes embedded in a lipid matrix forming a so-called "brick-and-mortar" structure [171], [172] and [173]. The diameter of a corneocyte is 40 $\mu$m, the height 0.8 $\mu$m [174]. The intercellular distance is approx. 0.1 $\mu$m which provides a cellular volume fraction of $\varphi_{\text{corneocyte}} = 0.91$ [175]. The cytoplasm contains ceramides, free fatty acids, cholesterol, proteins (keratin) and water. In contrary to most other cells the corneocyte does not contain a nucleus. The extracellular matrix, the "mortar" mainly consists of lipids and proteins and very little bound water (less than a monolayer). The total water volume fraction in the SC is 0.15-0.25, while 90% of the water is contained in within corneocyte [176] and [177]. By definition the SC belongs to the epidermis, but due to the high lipid and protein and low water content it differs significantly from the lower-lying epidermal layers and is here therefore considered

separately. The SC thickness strongly depends on the body site but exhibits only little interindividual variations among healthy subjects. On the dorsal site of the upper arm the SC is approximately 20 $\mu$m thick [171], [172], [173] and [178].

### 7.1.2 Epidermis

The living epidermis (E) mainly consists of keratinocytes. The cuboidal to columnar epidermal cells are gap-connected and occupy a volume fraction of $\varphi_{\text{keratinocyte}} = 0.83$ [90]. The overall water volume fraction in the dermis of 0.7 is equally distributed among intra- and extracellular space [179]. The epidermis is approximately 0.1-0.2 mm [180] thick.

### 7.1.3 Dermo-epidermal junction

The transition zone between epidermis and dermis, the so-called dermo-epidermal junction is not planar but forms papillae with a depth of approximately 50 $\mu$m [181].

### 7.1.4 Dermis

The papillary dermis (PD) occupies the upper 10% of the dermis and consists of a dense collagen network [182] and blood ($\varphi_{\text{blood}} = 0.04$ [183]). The major part of the dermis, the reticular dermis (RD) consists of irregular connective tissue, lymphatic vessels, nerves, blood vessels, stromal cells such as fibroblasts and other cellular components, e.g. macrophages or plasma cells. The capillaries in the approx. 50 $\mu$m long dermal papillae are oriented more or less perpendicular to the skin surface, while the upper vessel plexus (UVP) is a dense vascular network parallel to the skin surface with a thickness of $d_{\text{UVP}} = 80\mu$m and blood content of $\varphi_{\text{blood,UVP}} = 0.3$. The sparsely distributed blood vessels of the supply layer (SL) ($d_{\text{SL}} = 1.3$ mm, $\varphi_{\text{blood,SL}} = 0.04$) are as well perpendicular to the skin surface. The lowest layer is again a dense vascular network parallel to the skin surface, the deeper vessel plexus (DVP) ($d_{\text{DVP}} = 100$ $\mu$m, $\varphi_{\text{blood,DVP}} = 0.1$) [183]. The cellular volume fraction in the dermis is much smaller than in epidermis [41]. The cellular components in the dermis are mainly stellar-shaped fibroblasts which form a continuous network making a determination of the cell limits rather difficult. According to [184] the "body" of the cell has an approximate diameter of 5 - 10 $\mu$m, the extensions called stellae (4-6 per cell) are approx. 70 $\mu$m long. The collagen fibers are aligned parallel to the skin surface. Collagen is a major component embedded in the dermal matrix ($\varphi_{\text{collagen,dry}} = 0.17$ [185]). A thick collagen bundle can reach 2 to 15 $\mu$m in diameter. Besides collagen and elastin the extracellular space is mainly composed of glycosaminoglycans, gelatin, and sugars embedded in water. Collagen comprises about 75% of the fat free dry weight and 18-30% of the volume of dermis.

### 7.1.5 Hypodermis

The subcutis or hypodermis (HYP) mainly consists of white fat cells, the adipocytes building the subcutaneous fat. White adipocytes are spherically shaped with a mean cell diameter of 82.6 $\mu$m [186] (88.5 $\mu$m in [187]). The intracellular fat forms a spherical

droplet pushing the cytoplasm including nucleus towards the cell membrane. The volume fraction of the lipid droplet within the cytoplasm is $\varphi_{\text{fat,intracellular}} = 0.9$ [188] the aqueous phase volume fraction is therefore only 0.1. The HYP thickness is subject to large intra- and interindividual variations.

### 7.1.6 Muscle

Finally, muscular tissue (M) consisting of tightly packed narrow cells is situated beneath the hypodermis. Muscle cells are oriented with their long axis parallel to long axis of the humerus (upper arm bone). Muscular tissue is highly anisotropic [189]. In [94] a cell radius of 50 $\mu$m and a minimum distance among cells of 1 $\mu$m is used for a simplified model of skeletal muscle in the transversal plane.

### 7.1.7 Other structures

Features such as hair follicles, sweat ducts and sebaceous glands cross the entire skin down to the hypodermis [190] are mentioned for completeness, but not considered for further modeling.

## 7.2 Skin models and scaling hierarchies

Due to the high computational cost to date it is currently not realistic to simultaneously model single cells and the presented fringing field sensor. The scale of a cell membrane is in the range of nanometers while the electrode distance is up to few millimeters. Therefore, alternatives for transferring structural information from micro- to macro-scale have to be found.
A first attempt to numerically model the effective dielectric parameters of the skin in the MHz frequency range is presented in Chapter 6. The skin is subdivided into three layers (SC, epidermis and dermis (E/D) and hypodermis (HYP)) according to the differing water contents of these tissue types. Then, Cole-Cole models from literature are assigned to each layer and in a FEM simulation the layered system is probed by a fringing field probes. However, as already mentioned Cole-Cole models are to be avoided in this work because of the difficult assignment of spectral features to the microstructure.
Here, the setup of a general dielectric tissue model for quasi-static electric fields presented in Chapter 5 is applied to the skin. The principal idea is to consider tissue as a quasi-periodic structure exposed to a homogeneous external electric field [102] and to perform multi-step homogenization procedure.
The first step in the application of the homogenization scheme to human skin consists again of a subdivison into macroscopic layers. As mentioned in Section 7.1.3 in come cases the interface between skin layers is not planar. However, in a first approximation all layer interfaces are assumed as planar. In course of a refinement step the non=planar transition region could be replaced by a layer with effective properties obtained according to the introduced homogenization procedure.
Then each layer is investigated with respect to quasi-periodic structures. Some skin layers only contain quasi-periodicity on the cellular scale (single biological cell composed

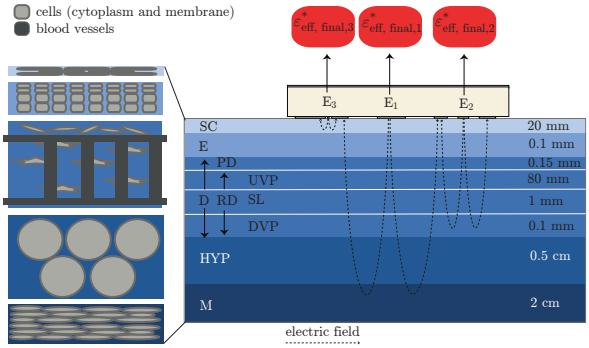


**Figure 7.2:** 2D cross-section sketch of the layered skin model consisting of stratum corneum (SC) , epidermis (E) , dermis (D) , hypodermis (HYP) and M . In the basic model denoted as MGW the epidermis and dermis are concatenated to one single layer denoted as epidermis and dermis (E/D). In the most refined model the dermis is subdivided into papillary dermis (PD) and reticular dermis (RD), whereas the latter contains the upper vessel plexus (UVP) , the supply layer (SL) and the deeper vessel plexus (DVP) . A sketch of the microstructure of the skin layers is given on the left.

of water and fatty, dry biological material), other skin layers suggest the use of a multi-step homogenization, as e.g. the dermis. For each layer $\bar{\varepsilon}^*_{\text{eff}}$ and its dispersive features are then analytically or numerically calculated and finally inserted into the numerical macroscopic model. The overall procedure for the model with the highest complexity is later depicted in Figure 7.3. Except for muscle tissue the skin is supposed to be isotropic in the $x$-$y$-plane with the $z$-axis of the coordinate system is perpendicular to the layer boundaries and the effective dielectric tensor reduces to

$$\bar{\varepsilon}^*_{\text{eff}} = \begin{pmatrix} \varepsilon_{xx,\text{eff}} & 0 \\ 0 & \varepsilon_{zz,\text{eff}} \end{pmatrix} \tag{7.1}$$

in the 2D model. The final skin models are experimentally validated. As the SC has a large influence on the effective dielectric properties its removal is used as an additional validation criterium.

As already mentioned the first macroscopic subdivision of skin happens according to the the water content of the layers. It was found in Chapter 6 that for the model of intact skin with SC a model down to the hypodermis is sufficient, i.e. the electric field does not penetrate beyond this layer. However, after removal of the rather insulating SC the penetration depth extends down to muscle tissue assuming a HYP thickness of 5 mm extracted from the MR image. Therefore, muscle is included in the model as well. After defining the macroscopic model the dielectric properties of each of the sublayers have to be defined. The complexity of the different models follows the subsequential inclusion of features that are likely to affect the dielectric spectrum. In the MHz region the $\beta$-dispersion, the short-circuiting of the cell membranes [27] is the dominant feature

and has therefore be reproduced by a valid model. Other dispersion mechanisms such as electrode polarization and $\alpha$-dispersion below 1 MHz and the relaxation of free water ($\gamma$-dispersion) in the low GHz region occur outside of the considered frequency range. Therefore, those mechanisms are said not to affect the spectrum in the MHz range and are not included in the model. The weak $\delta$-dispersion above 100 MHz caused by the relaxation of bound water and proteins might extend into the upper part of the frequency region of interest between 1 and 100 MHz, but is neglected here because of its weakness compared to the $\beta$-dispersion. From the structural point of view on the sub-cellular scale the simplification with the largest impact consists of not including organelles and cell nucleus in the models as shown in Chapters 3 and 4.
In the following the models for the effective properties of each layer are introduced. The model order follows a hierarchy given by the increasing degree of complexity in terms of number of layers as well as number of components and stages for the homogenization of the dielectric parameters.

Electrode surface roughness, the influence of a potentially occurring air or sweat layer, pressure variations and structural features crossing the entire skin (sweat ducts, hair follicles) are potential sources of error or variation, but were not included in the model.

### 7.2.1 Maxwell-Garnett water content model (MGW)

The first model consists of representing the skin layers as two-phase mixtures. Biological tissue in general mainly consists of an aqueous phase (extracellular liquid, cytoplasm) and a lipid phase (cell membrane, intra- and extracellular lipids) being distinct from a dielectric point of view. The aqueous phase basically consisting of water and electrolytes with the approximate dielectric parameters $\varepsilon_1^{(1)} = 78$ and $\sigma_{\mathrm{DC},1}^{(1)} = 1.2$ S/m. On the other hand the lipid phase approximated by oleic acid has a low permittivity $\varepsilon_2^{(1)} = 2.5$ and is practically non-conducting $\sigma_{\mathrm{DC},2}^{(1)} = 0$ S/m [191]. Since the water contents of the skin layers differ significantly ($\varphi_{\mathrm{water,SC}} = 0.2$ [177], $\varphi_{\mathrm{water,E}} = 0.7$, $\varphi_{\mathrm{water,D}} = 0.7$, $\varphi_{\mathrm{water,HYP}} = 0.25$ [183] and $\varphi_{\mathrm{water,M}} = 0.8$), the volume fractions of the aqueous and lipid phase, respectively, a simple two-phase model is set up in order to characterize each layer. The effective dielectric parameters $\varepsilon_{\mathrm{eff}}^{(1)}$ and $\sigma_{\mathrm{eff}}^{(1)}$ of the so-defined binary mixtures are calculated with the MG mixture formula [46] in Equation 7.2. Here, $j = 1$ and material 2 is embedded in material 1. Equation 7.2 provides the exact (first-order) solution for the effective permittivity of a spherical inclusion for volume fractions up to $\varphi = 0.1$, but since geometry is not considered in this model it actually has no significance. The dielectric parameters for this model are all scalar.

$$\frac{\varepsilon_{\mathrm{eff}}^{*,(j)} - \varepsilon_1^{*,(j)}}{2\varepsilon_{\mathrm{eff}}^{*,(j)} - \varepsilon_1^{*,(j)}} = \varphi_2^{(j)} \frac{\varepsilon_2^{*,(j)} - \varepsilon_1^{*,(j)}}{2\varepsilon_2^{*,(j)} - \varepsilon_1^{*,(j)}} \tag{7.2}$$

**Table 7.1:** Material and geometrical parameters for the models MGI, MGA, LOI and HBA. Each layer within a model provides a dielectric tensor $\bar{\varepsilon}^{*,(j)}$ which is inserted into the macroscopic model. Some phases at scale level $j$ are already mixtures with $\bar{\varepsilon}^{*,(j-1)}$ at a lower scale. ($^*$) The parameters for blood are frequency dependent.

| Skin layer | Sub-phase | Geometry | | | | Material parameters | | |
|---|---|---|---|---|---|---|---|---|
| | | | | | | Phase | Dielectric parameters | |
| | | Shape of inclusion | $\varphi_\mathrm{i}$ | $(d_x\ d_y\ d_z)$ [$\mu$m] | $d_\mathrm{shells}$ [nm] | | $\varepsilon_i^{(j)}$ | $\sigma_{\mathrm{DC},i}^{(j)}$ [S/m] |
| SC | SC extracellular | | | | | extracellular medium | 80 | 0.53 |
| | | sphere | 0.95 | | | dry biological material | 2.5 | 0 |
| | SC cytoplasm | | | | | extracellular medium | 80 | 0.53 |
| | | sphere | 0.8 | | | dry biological material | 2.5 | 0 |
| | | shelled ellipsoid | 0.91 | (20 20 0.8) | 7 | SC extracellular cell membrane SC cytoplasm | 9.04 | $10^{-6}$ |
| E | | shelled ellipsoid | 0.83 | (5.97 5.97 11.95) | 7 | extracellular medium cell membrane cytoplasm | 80 9.04 50 | 0.53 $10^{-6}$ 0.12 |
| D UVP | collagen | | | | | extracellular medium | 80 | 0.53 |
| | | cylinder | 0.17 | ($\infty$ 100 100) | | dry biological material | 2.5 | 0 |
| | dermis "matrix" | | | | | collagen ($xy$-isotropic) | | |
| | | shelled ellipsoid | 0.315 | (70 70 7) | 7 | cell membrane | 9.04 | $10^{-6}$ |
| | | | | | | cytoplasm | 50 | 0.12 |
| | | | | | | dermis "matrix" | | |
| | | cylinder ($xy$-isotropic) | 0.3 | ($\infty$ 50 50) | | blood$^*$ | [34] | [34] |
| SL | | | | | | dermis "matrix" | | |
| | | cylinder | 0.04 | (50 50 $\infty$) | | blood$^*$ | [34] | [34] |
| DVP | | | | | | dermis "matrix" | | |
| | | cylinder ($xy$-isotropic) | 0.1 | ($\infty$ 50 50) | | blood$^*$ | [34] | [34] |
| HYP | | double-shelled sphere $\varphi_\mathrm{fat} = 0.771$ | 0.8 | (45 45 45) | 7 $3.76{\cdot}10^3$ | extracellular medium cell membrane cytoplasm dry biological material | 80 9.04 50 2.5 | 0.53 $10^{-6}$ 0.12 0 |
| M | | shelled ellipsoid | 0.85 | (0.5 2 0.5) | 7 | extracellular medium cell membrane cytoplasm | 80 9.04 50 | 0.53 $10^{-6}$ 0.12 |

### 7.2.2 Maxwell-Garnett isotropic model (MGI)

For the following models, the initial subdivision of skin into three layers is refined. The layer thicknesses are the following: $d_{SC} = 20\mu$m, $d_E = 100\mu$m, $d_{D,PD} = 150\mu$m, $d_{D,UVP} = 80\mu$m, $d_{SL} = 1$mm, $d_{DVP} = 100\mu$m, $d_{HYP} = 5$mm. Finally, muscle tissue terminates the model ($d_M = 2$cm, $\infty$). The system consisting of sensor and layer structure is depicted in Figure 7.2.
A first attempt to truly incorporate microstructural information into a skin layer model is undertaken by approximating single tissue cells by shelled ellipsoids. This has already been performed in order to calculate dielectric parameters of e.g. suspensions of *E. coli* cells [58], red blood cells [87] or rat liver tissue [59]. Since the MG formula can be generalized for multi-shelled confocal ellipsoids [61] it is employed here in order to calculate the effective dielectric parameters of the skin layers modeled as a suspension of randomly oriented single-shelled ellipsoids. The cell dimensions, volume fractions and material compositions were estimated based on literature values given in Section 7.1. The dielectric parameters for extracellular medium, cell membrane and cytoplasm were set according to [192]. All geometrical and material parameters are given in Table 7.1. As the membrane thickness $d_{\mathrm{m}} = 7$ nm is much larger than the cell dimensions the concentric approximation of the shelled ellipsoid (see Figure 3.8) was considered as justified. Compared to the relatively straight-forward representations of SC and HYP the modeling of the epidermis and dermis imposes some challenges. Although the water content is similar in dermis and epidermis ($\varphi_{\mathrm{water}} = 0.7$) a unified morphological description of the two layers is rather difficult. The structural properties even suggest to subdivide at least the dermis into sublayers. The cellular volume in the dermis is so small that the influence of the cell shapes on the dielectric properties will probably be much smaller than the other features such as the collagen network or orientation of blood vessels. Therefore, the goal for the dermis model was first to directly or indirectly include single cells and second, to capture main anisotropy directions likely to be seen in dielectric spectra. Especially, the dermis anisotropy is not described in terms unit cells on a single cell level anymore, but at a larger scale the distribution of blood vessels embedded in a collagen network replaces this measure. Consequently, the E/D is partitioned into the joint layer consisting of epidermis and capillary layer of the papillary dermis (PD), the upper vessel plexus (UVP) the supply layer (SUP) and finally the deeper vessel plexus (DVP). The dimensions (scaling of the dermis thickness obtained by MRI) and parameters for blood volume fractions were set according to [183]. The PD was entirely approximated by densely simple cubic packed columnar keratinocytes ($\varphi_{\mathrm{keratinocyte}} = 0.83$, $d_x = d_y < d_z$) given in Figure 7.4(e). The deeper lying layers were analytically modeled using the Hanai-Bruggeman formula given by Equation 3.12 for aligned cylinders in an anisotropic collagen matrix. The cylinder material consisted of blood with parameters obtained from [34], the radius according to [193] for capillaries. The volume fractions of the cylinders and their orientation (perpendicular or parallel to the skin surface) were set as introduced in the previous subsection. The parameters for the collagen matrix itself were again calculated with the MG formula. The mixture consisted of collagen cylinders parallel to the skin surface, embedded in extracellular medium. The volume fraction and collagen fiber radius for collagen were taken from [194].

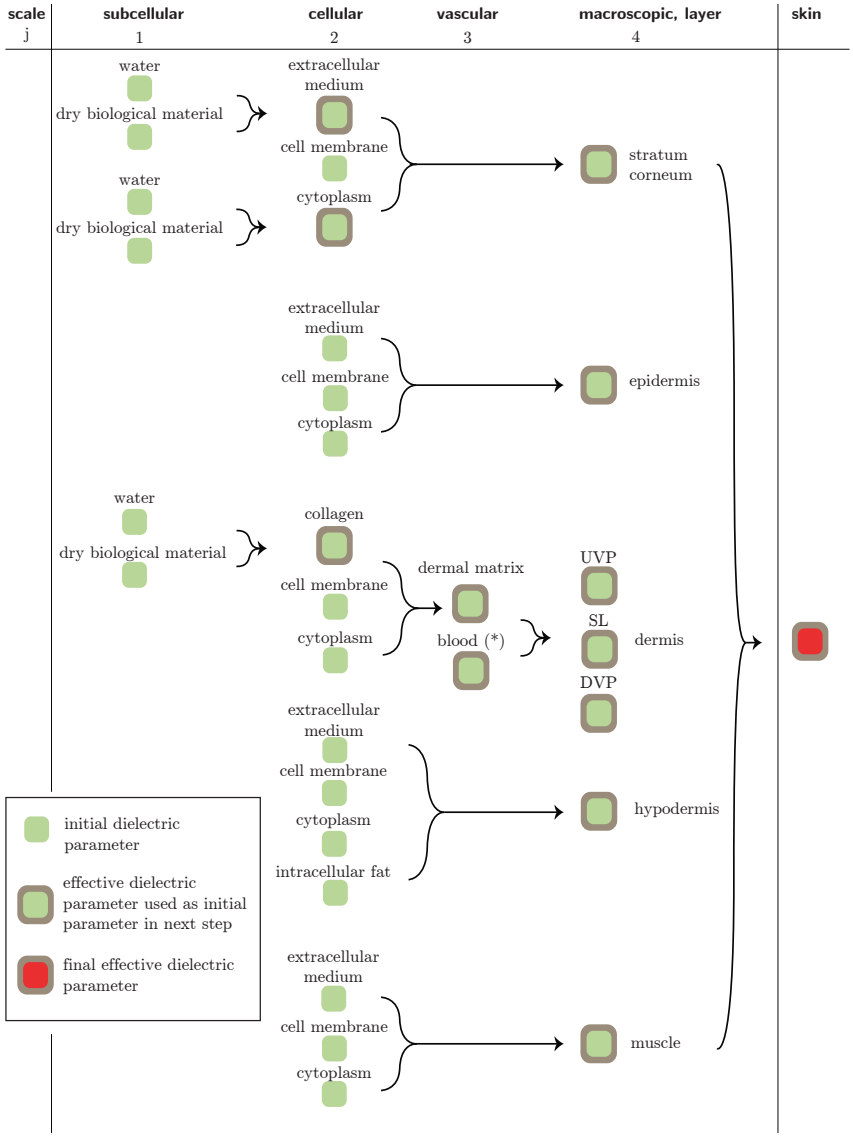


**Figure 7.3:** Complete mixing scheme for the final dielectric human skin model (NUM). (*) The effective parameters for blood were taken from [34]. Abbrevations for dermis subdivision: upper vessel plexus (UVP), supply layer (SL) and deeper vessel plexus (DVP).

In the case of the MGI model the particle orientations are averaged out and the effective material is isotropic.

### 7.2.3 Landau-Lifshitz-Looyenga isotropic model (LOI)

The Landau-Lifshitz-Looyenga isotropic model (LOI) model is set up in the same manner as the MGI model. The effective dielectric properties of the inclusion (material with index $i = 2$) are calculated using the MG formula, but the final step is calculated with the LLL formula in Equation 3.14 also leading to an averaging of particle orientation. Since the LLL formula averages the anisotropy and the mixing formula is symmetric, a major part of the geometrical information is not contained.

### 7.2.4 Maxwell-Garnett anisotropic model (MGA)

For aligned particles the $\bar{\varepsilon}^{*,(1)}_{\text{eff}}$ calculated with the MG formula does not reduce to a scalar and anisotropy can be accounted for. Accordingly, the MGA model corresponds to the MGI model, up to the fact that the cells are aligned. The parameters are given in Table 7.1. As mentioned, the MG formula is only valid for inclusion volume fractions $\varphi_{\text{inclusion}} < 0.1$ since interparticle interactions are neglected [46]. Above this volume fraction limit, also occuring in the case of all skin layers presented here the MG formula is only an approximation.

### 7.2.5 Hanai-Bruggeman anisotropic model (HBA)

In order to overcome the volume fraction restriction of the MG formula in the the HB formula (valid for volume fractions up to $\varphi_{\text{inclusion}} < 0.8$) given in Equation 3.12 is employed in the HBA model. In analogy to the MGA model, the HB solution for aligned single-shelled ellipsoidal particles provides the $\bar{\varepsilon}^{*}_{\text{eff}}$.

### 7.2.6 Model with numerically calculated dielectric parameters (NUM)

Both, MG as well as the HB formula impose a volume fraction limit due to interparticle interaction as well as due to the quasi-periodic structure and resulting simple cubic packing. The aim of the NUM model was to include features and aspects that are not part of the previous models but expected to affect the dielectric spectra up to the macroscale. In order to keep the computational effort reasonable the focus in the NUM model was put once again on the following features:

- Cellular volume fraction $\varphi$
- Approximate composition of extracellular medium and cytoplasm
- Intercellular interactions (cell shape, ordering)

Since the shape of biological cells usually differs from ellipsoidal and the volume fraction in tissue often exceeds even the densest possible packing of ellipsoids ($\varphi_{\text{inclusion}} = 0.7707$ [89]) a motivation for the refinement of the MGA/HBA models arises. In terms of a more flexible geometry the effective dielectric parameters of particles can be calculated analytically using the spectral density function approach [53], [68]. But as the expressions get very complicated with increasing shape complexity numerical simulations were used in the NUM model. The cell shapes were generated with the SF introduced in Section

4.3.1. Following the approach in [102] the cell is placed in a parallel plate capacitor filled with extracellular medium in order to generate the corresponding electric field background for the determination of the effective dielectric properties. Its dimensions are determined by the volume fraction of the cell and the maximal distances of the cell shape in $x$-, $y$- and $z$-direction. In order to obtain the diagonal dielectric tensor $\bar{\varepsilon}^*_{\text{eff}}$ (Equation 5.1) as for the MGA and HBA models the electric field is first applied in $x$-, then in $y$- and finally in $z$-direction with Neumann boundary conditions on boundaries perpendicular to the electrodes in each corresponding case. This geometric setup implies as already mentioned in conjunction with Equation 5.1 a periodic structure in the plane perpendicular to the applied electric field due to the mirror images.

**Table 7.2:** Supershape parameters for selected skin cells. Both corneocyte model are additionally scaled down in $z$-direction by a factor of 0.02. The corneocyte cubic, keratinocyte and adipocyte cubic models were employed in the numerical (NUM) model.

| Cell type | Skin layer | Supershape parameters | | | | | | | Figure 7.4 |
|---|---|---|---|---|---|---|---|---|---|
| | | $a$ | $b$ | $m$ | $n_1$ | $n_2$ | $n_3$ | $d$ | |
| Corneocyte | SC | 1 | 1 | 6 | 4 | 4 | 2 | 60 | (a) |
| Corneocyte $D_{4h}$ | SC | 1 | 1 | 4 | 8 | 8 | 8 | 60 | (b) |
| Keratinocyte 1 | E | 1 | 0.5 | 4 | 4 | 4 | 4 | 30 | (c) |
| Keratinocyte 2 | E | 1 | 1 | 4 | 4 | 4 | 4 | 30 | (d) |
| Keratinocyte 3 | E | 0.5 | 0.5 | 4 | 4 | 4 | 4 | 30 | (e) |
| Fibroblast | dermis (D) | 1 | 1 | 4 | 0.5 | 1 | 0.75 | 60 | (f) |
| Adipocyte | HYP | 1 | 1 | 4 | 4 | 4 | 4 | 40 | (g) |
| Muscle cell | M | 3 | 0.3 | 4 | 2 | 2 | 2 | 200 | (h) |

The application of supershapes (see 4.3.1) in dielectric modeling of cell suspensions and tissues has already successfully been performed in [102]. Diverse types of cell shapes occurring in the skin can be created using the SF and are given in Figure 7.4, for the corresponding shape parameters see Table 7.2. The three-dimensional ordering of the corneocytes, which can be approximated by flat hexagons ordered in a hexagonally close packed HCP unit cell. But since the presented procedure requires a unit cell with perpendicular walls two approximations were performed. The first approximation rendering the cell shape correctly is a BCC unit cell with hexagonal corneocytes. As it is not possible to reach the required volume fraction of $\varphi_{\text{corneocyte}} = 0.91$, the second approximation consists of flattened cubes instead of hexagons in a BCC unit cell, allowing to reach the required volume fraction. The keratinocytes of the epidermis are also modeled numerically in order to reach the desired volume fraction and to better render the shape. With increasing distance from the skin surface a smooth shape transition from corneocyte to the basal kerationcyte occurs. This transition can also be reproduced with the SF and is sketched in Figures 7.4 (a) to (e). However, for simplicity reasons the epidermis is entirely represented by cubic columnar cells in this model. Although the SF can describe even complicated shapes as fibroblast-like cells given in Figure 7.4(f) and approximate almost any cell type, the dermis structure on the cellular level is due to the large number of constituents so heterogeneous that the NUM model uses the same

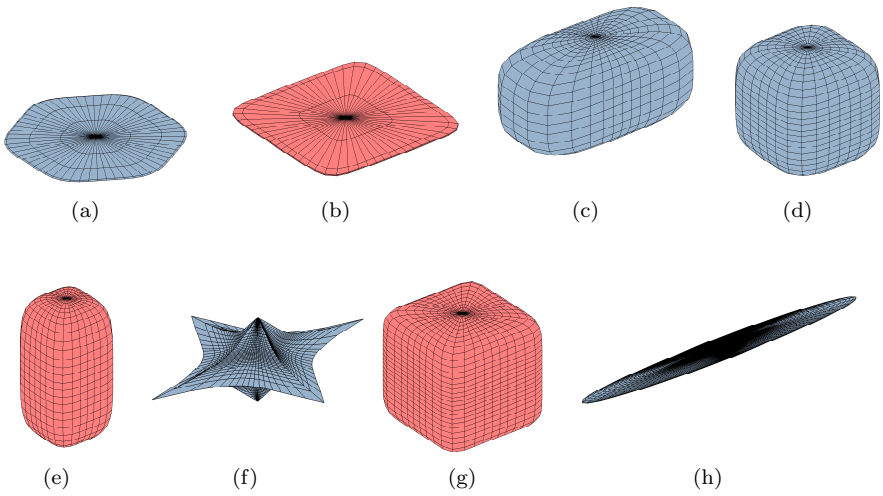


**Figure 7.4:** Estimated shapes of cells occurring in the skin parameterized with the Superformula. Only the red-coloured cell shapes ((b), (e) and (g)) were used in the NUM model. The more realistic corneocyte hexagonal shape in (a) was replaced by the $D_{4h}$-shape in (b) in order to model a realistic volume fraction and to be able to establish a BCC unit cell. The same holds for the adipocyte in (g). The corresponding shape parameters are given in Table 7.2.

model parameters for the dermis sublayers as the MGI, LOI, MGA and HBA models. The HYP is modeled using the same idea as for SC. However, the densest possible packing of spheres (lipid phase of the adipocyte interior) provides only a maximal volume fraction of $\varphi = 0.744$, obtained either with HCP or BCC unit cells. As the actual adipocyte volume fraction must be higher than this value again, cuboidal-shaped cells in a BCC unit cell are used in order to conform with the large cellular volume fraction.

## 7.3 Measurements

### 7.3.1 Dielectric measurements

Dielectric measurements were performed between 5 and 100 MHz using the multi-electrode sensor shown in Figure 6.3 connected to a HP8753ES vector network analyzer (VNA). The voltage between driven electrode and ground was 1V; the other two electrodes were set to ground, repeating the procedure for all three electrodes (denoted as $E_1$, $E_2$ and $E_3$ in Figure 6.3). The setup was calibrated with air and deionized water with known static conductivity. The left upper arm was chosen as measurement site because of its accessibility, relative homogeneity of tissue parallel to the sensor surface compared to other body parts (e.g. wrist) and ability to tightly attach the sensor on the skin. The sensor was placed on the upper arm with the longer axes of the electrodes ($y$-direction) being parallel to the long axis of the humerus and attached with rubber bands.

After measuring untreated, dry skin the SC was removed by consecutive stripping with adhesive tape [138] and [195]. After each stripping the admittance was measured. The stripping was terminated after 40 strippings [195] and the SC considered to be removed. All measurements were carried out at room temperature. The dielectric parameters were extracted according to the procedure described in Section 6.1. The removal of th SC in experiment (and model as well) was used as a **validation** criterion.

### 7.3.2 Skin layer thickness determination with MRI

Skin layer thicknesses exhibit significant intra- and inter-individual variations [196], [197] and should be carefully estimated. Literature values are provided in [132], [198], [199] and [132]. In the present work MRI scans of the site of dielectric measurement were recorded in order to determine skin layer thicknesses. The instrumentation consisted of a 1.5T Philips Achieva MRI scanner in connection with a Philips microscopy coil having an inner diameter of 23 mm and the following scan protocol: T1-weighted 3D fast field echo, TR 600; TE 14, flip angle 90°, FOV 25x25 mm, matrix 256x256, acquired resolution 0.06x0.9 mm, slice thickness 1.25 mm reconstructed to 0.4 mm, bandwidth 9.8Hz/pixel, 2 signal averages, 30 slices in the coronal plane.

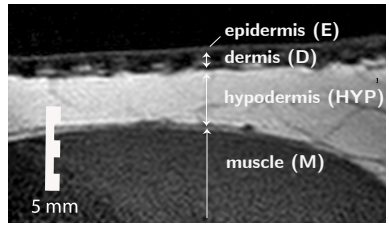


**Figure 7.5:** 1.5T MR image of the skin (dorsal upper left arm) used in determination of the skin layers on the site of the dielectric measurement. E, D, HYP and M can clearly be distinguished.

According to [153] the epidermis, dermis, subcutaneous fat and muscle can clearly be distinguished in Figure 7.5. The outer high-signal zone (0.2 mm) corresponds to the epidermis, the low-signal zone (1.3 mm) to the dermis. The image suggests significant compositional differences between E and D. The thick, approximately 5 mm high-signal zone is assigned to the hypodermis and the lower-lying low-signal zone under the hypodermis corresponds to muscle.
The thickness of the SC cannot be resolved with MRI and is different on different body sites. Nevertheless, it does not exhibit large variation among healthy individuals for a specific body site and therefore, the SC thickness for the upper arm, $d_{\mathrm{SC}} = 20\mu$m, is adapted from literature [171], [172] and [173].

## 7.4 Results and discussion

According to Figure 7.6 the measured data before stripping lies in the same range and exhibits a very similar characteristic as literature values obtained from measurements of dry skin with open-ended coaxial probes [34], [33]. The measurements show that above 200 MHz resonances connected to the electrical length of the electrode/sensor system occur. Therefore, above 200 MHz the quasi-static regime does not suffice anymore and a full-wave numerical model of the sensor and tissue multilayers would be required in order to correctly reproduce the measured data. In order to exclude effects due to electrode polarization, large measurement uncertainties of the VNA at low frequencies as well as the mentioned resonances the frequency region of interest was reduced to the range from 5 to 100 MHz.

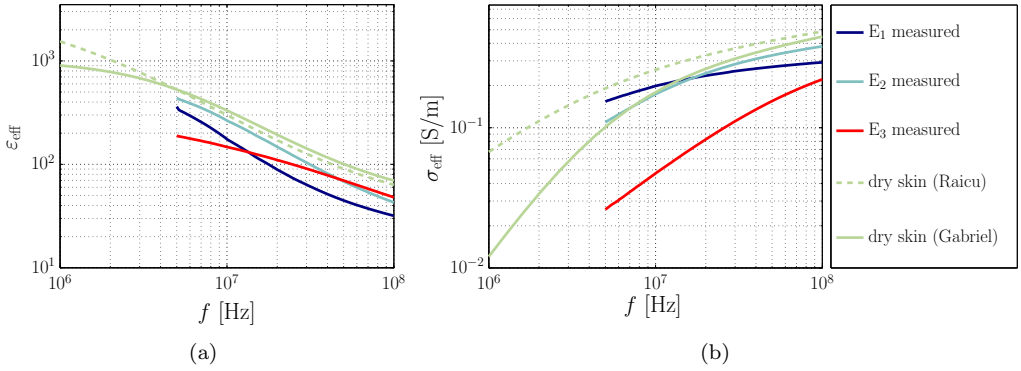


**Figure 7.6:** Comparison between effective permittivity (a) and conductivity (b) of dry skin measured with the multi-electrode sensor shown in Figure 6.3 and parameters obtained from measurements with coaxial probes of different sizes published in literature [33] and [34].

The dielectric parameters and thicknesses of SC, viable skin and hypodermis (also compared to the inter-electrode distance) are in a such relation that a layered model with each layer's water content as a characteristic parameter (model Maxwell-Garnett water content model (MGW)) generates a relaxation in the lower MHz region due to the thin, poorly conductive SC between electrode and viable skin. On the other hand measurements of skin also exhibit a strong dispersion in this region, the mentioned $\beta$-dispersion [34] caused by interfacial polarization at the cell membranes. In order to test the suitability of the models the SC was removed. Measurements show a prominent increase in both $\varepsilon_{\text{eff}}$ and $\sigma_{\text{eff}}$ for the $E_3$ and $E_2$ electrode and a decrease of $\varepsilon_{\text{eff}}$ and increase of $\sigma_{\text{eff}}$ for the $E_1$ electrode after removal of the SC. As expected the MGW model could not reproduce this behaviour. The contrast between viable skin and subcutaneous fat is too poor because the E/D is about 2 orders of magnitude thicker than the SC and has larger permittivity and especially conductivity. Therefore, the observed values will not be reconstructed by the model and the contribution of the layering to the total spatial

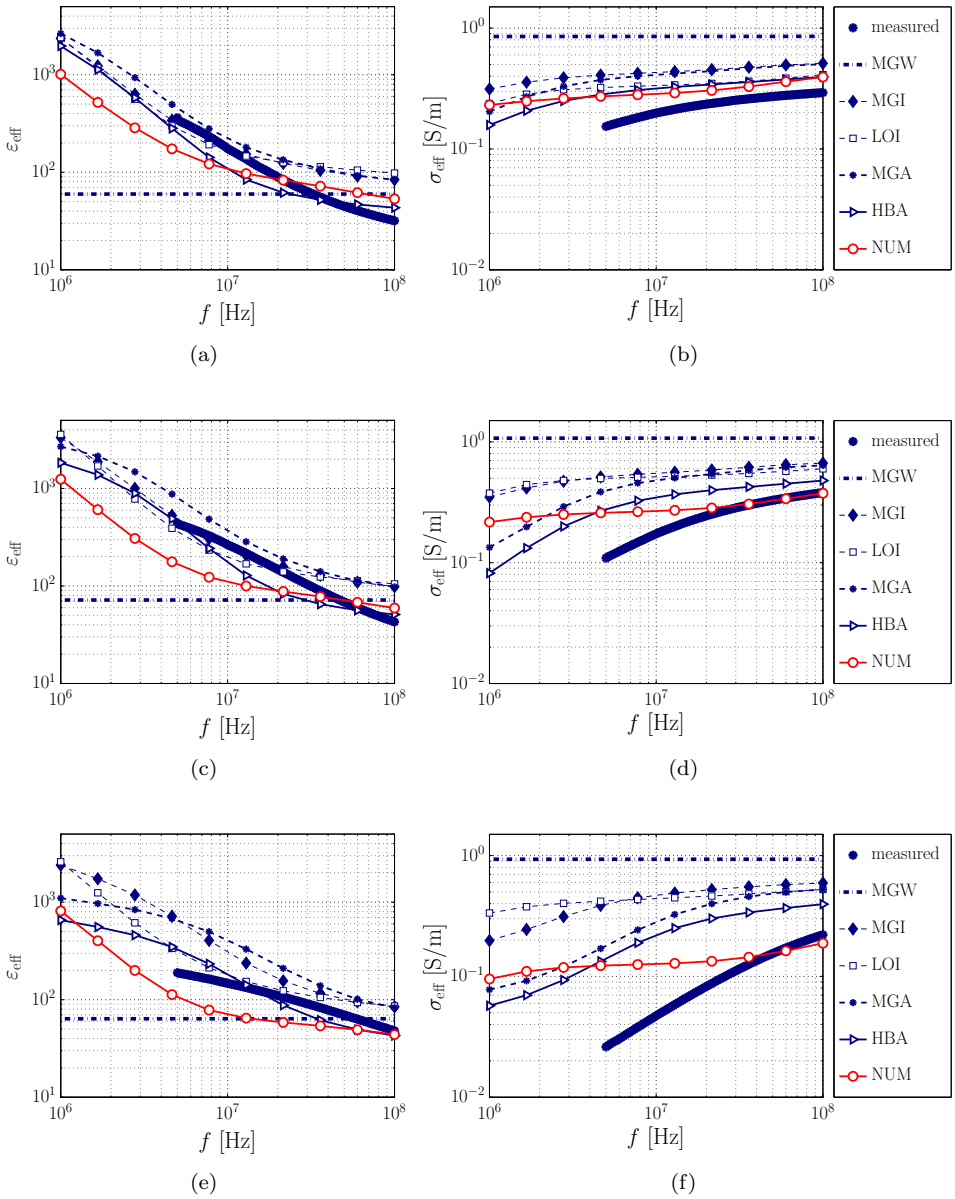


**Figure 7.7:** Effective permittivity ((a), (c) and (e)) and conductivity ((b), (d) and (f)) of intact skin probed by three different electrodes of the multi-electrode sensor from Figure 6.3. Measured data (mean value for all measurements of one subject) and models.

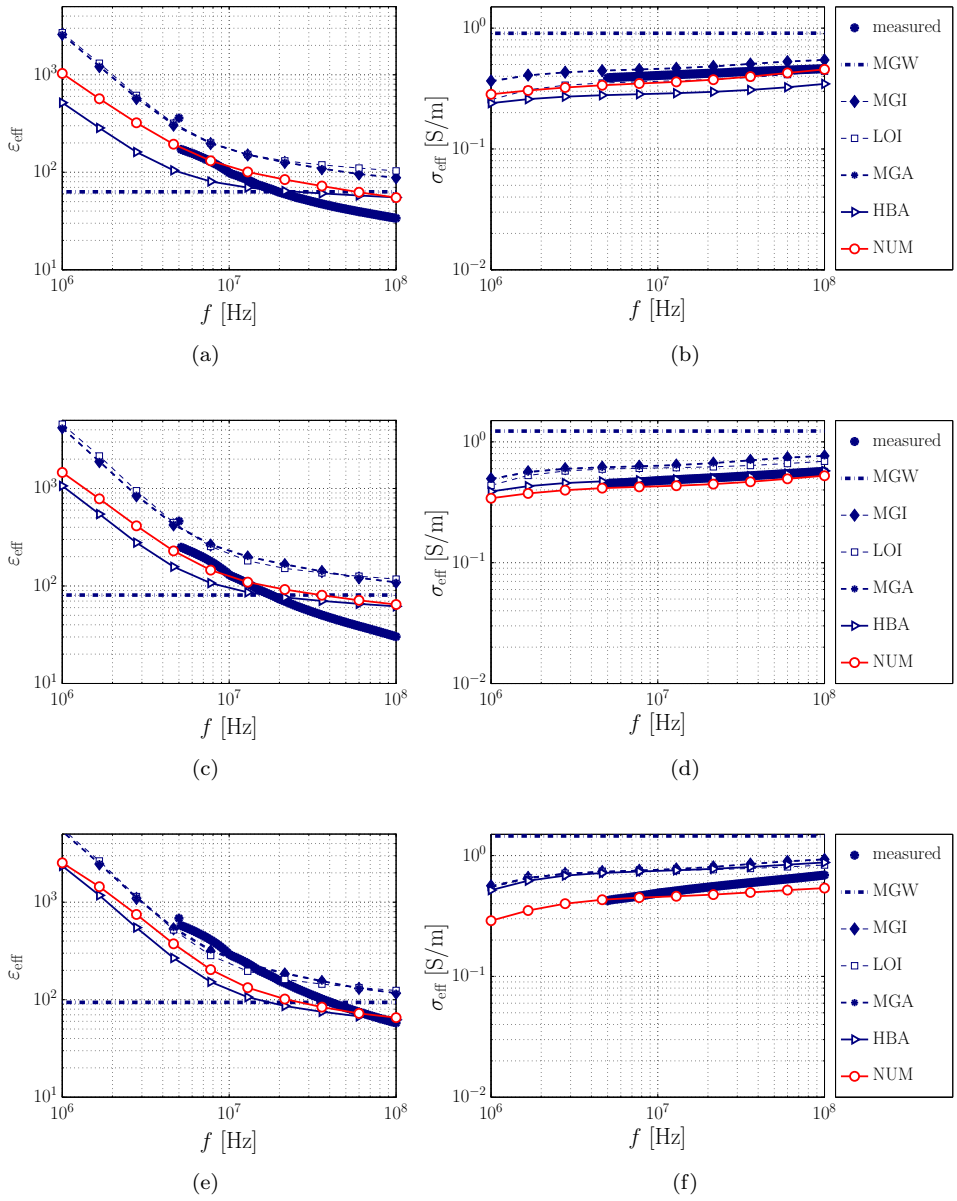


**Figure 7.8:** Effective permittivtiy ((a), (c) and (e)) and conductivity ((b), (d) and (f)) of skin without SC probed by three different electrodes of the multi-electrode sensor from Figure 6.3. Measured data (mean value for all measurements of one subject) and models.

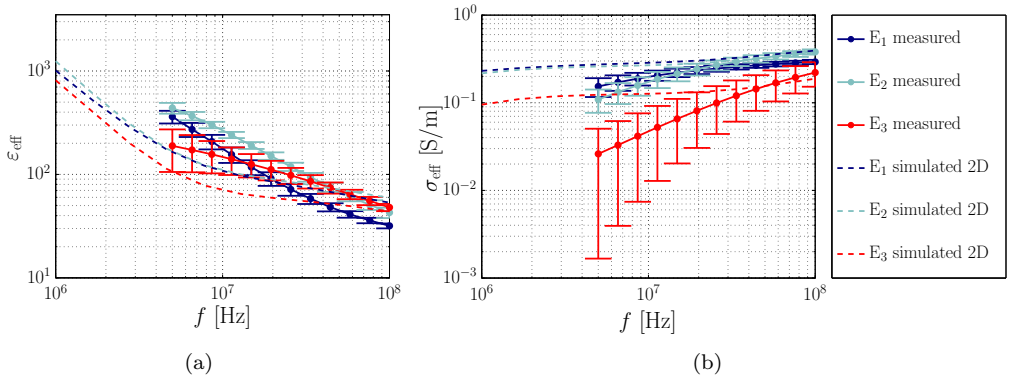


**Figure 7.9:** Effective permittivity (a) and conductivity (b) of measured (mean value of four measurements on one subject and corresponding standard deviation) and modeled (NUM model) intact skin.

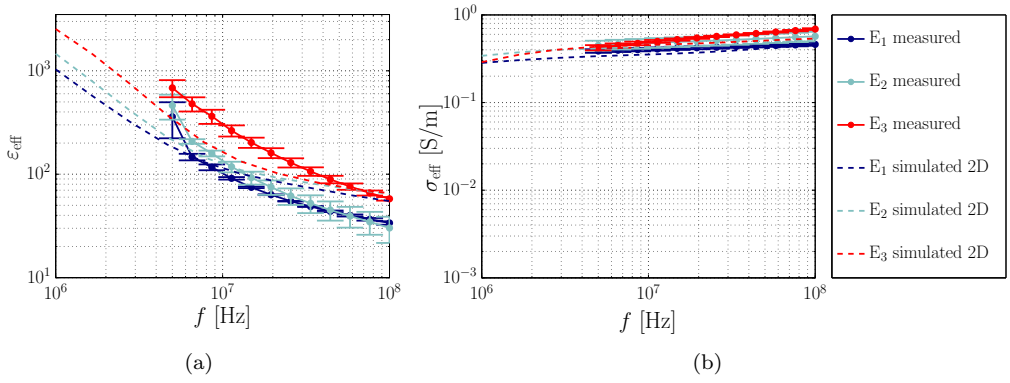


**Figure 7.10:** Effective permittivity (a) and conductivity (b) of measured (mean value of four measurements on one subject and corresponding standard deviation) and modeled (NUM model) skin without SC.

dispersion is very small. These results also indicate that the theory, where the SC is strongly contributing at lower frequencies and E/D dominating at higher frequencies (> 100 MHz) [138] might be wrong. The contribution can be equal but caused by other parameters such as by the water content for whose the contrast between layers is smaller. This could e.g. be assessed by evaluating the electric energy and resistive heating in the layers. An additional argument against a significant lacking of contribution of the SC is also provided in [27].
Furthermore, according to [34] the two-phase formulas are reliably applicable only at fre-

quencies above 400 MHz, which makes sense because in the lower MHz range $\beta$-dispersion dominates and masks the influence of free water.
Modeling the $\varepsilon$ and $\sigma$ of each layer as shelled particles embedded in a host medium is a good initial approach in order to reproduce trends based on morphological parameters and material composition on the cellular level, even though the initial presented MGI model is not accurate yet. With the LOI model a small improvement is achieved by averaging out the deviations from realistic cell shapes according to Figures 7.7 and 7.8. The comparison between the models MGI/LOI and the MGA model shows that the oriented ellipsoidal particles resulting in anisotropic dielectric parameters (especially for SC) also provide a better reproduction of the measured data than isotropic mixtures of randomly oriented particles. The MGA model qualitatively reproduces the observed frequency dispersions in the measurements after removal of the SC (rise of $\varepsilon_{\text{eff}}$ and $\sigma_{\text{eff}}$), at least for the $E_2$ and $E_3$ electrodes. For $E_1$, the decrease of $\varepsilon_{\text{eff}}$ could not be reproduced. But it has to be noted that the penetration depths of the electric fields of $E_2$ and $E_3$ are smaller than of $E_1$ and therefore the accumulated uncertainty due to assumptions on layer properties as well. Several aspects such as the constitution, anisotropic bound water shells [87] or the inclusion of organelles [47] can be accounted for already using an analytical or semi-analytical mixing rule. A comparison between the MGA and HBA models from Figures 7.7 and 7.8 shows an even better agreement of the HBA model with the measurement data due to the account for high cellular volume fractions.

While inspecting the dispersion spectra an overall comparison of all models suggests that the NUM model is most suitable for the reproduction of the dispersion characteristics of the skin and also has the largest potential for improvement due to the flexibility concerning cell shape. The NUM model without SC provides a good agreement with the measured data. However, the NUM model of intact skin suggests that the SC might be less conductive than modeled. It is very likely, that an adjustment of the conductivity of the water phase in the SC also moves the dispersion characteristics into the correct direction. The dependency of the dielectric parameters on the gap widths of the electrodes also indicated a similar direction of model improvement.

An additional advantage of the NUM model consist in the ability to model wet skin. In dry skin the volume fraction of extracellular water is very small. By wetting the skin this volume fraction increases, which can be easily incorporated into the model. It was shown previously e.g. in [189] and [33] that the permittivity and conductivity of wet skin is significantly larger than of dry skin. This can be explained with the increase of dielectric contrast between extracellular medium and cell membrane and also between cytoplasm and membrane. If exposed to water the corneocytes themselves start to absorb water, so the intracellular water volume fraction increases as well.

## 7.5 Conclusion

The presented results suggest the need for a complex model of human skin in the frequency range between 5 and 100 MHz. The model with the biphasic water mixtures fails

to reproduce the skin's dielectric properties after removal of the stratum corneum. The latter model type characterized only by the water content of each layer as the relevant parameter is only applicable above 400 MHz as reported previously. If the entire frequency region between 100 kHz and 1 GHz is considered at least the basic structure of tissue (cells) has to be taken into account in order to correctly reproduce trends in the spectra. MG- or HB-mixtures of shelled particles already provide correct trends. Comparing measurement and simulation the model containing dielectric parameters of numerically calculated cell-like structures with more realistic shapes resulting in anisotropic effective dielectric properties for each skin layer provides the best results. The removal of the stratum corneum as a validation criterion for the need for at least three-phase mixtures containing approximated cells was successfully proven. The presented results suggest a suitability for adaption of the concept for other tissues. Model improvement is expected to happen after incorporation of mass transport on the microscale. This would directly enable to assess the sensitivity of dielectric spectroscopy to physiological changes and processes.

# 8 Conclusion

A flexible framework for the modeling of dielectric parameters of biological tissue was successfuly established using mixing formuals and numerical models within a multiscale approach. The approach applied to modeling of human skin and was validated with measurements. Moreover, prosperously using the removal of the stratum corneum in model and experiment as an additional validation criterion substantiated the suggested modeling method.

To the author's best knowledge the presented model is the only one available which is entirely based on morphology and material composition information without any fitting of parameters to measured data.
Focusing on the microsctrucure it was shown that for frequecies up to few 100 MHz shape and volume fraction of cells strongly influence the dielectric spectra of biological bulk materials such as cell suspensions and tissues. Above 100 MHz shape and volume fraction lose their importance and the principal characteristic in effective properties is determined by the volume fractions of the different constituents only. In other words for dielectric modeling of biological tissue below 100 MHz cell shape and cellular volume fraction has to be well represented in the model. Mixing formulas can serve as a first approximation, but for more realistic scenarios only numerical simulations offer the required flexiblity and accuracy. A limitation is the actual shape generation in the employed software.
As some tissues exhibit a layered substructure on the macro- or submacroscopic scale the uniqueness of effective properties as well as the sensitivity in the latter to parameter changes was investigated. Generally, the reconstruction is an ill-posed problem. Only if the range of unknowns is sufficiently small one can potentially assign the origin of a certain change with respect to a reference scenario in the effective parameters to a parameter variation in a specific layer.

The multiscale concept was succesfully validated by measurements on human skin. However, further research is needed in order to to improve the accuracy of the model and to validate it for other tissues. Furthermore, the experimental setup for measurements on skin has to be re-designed focusing on reproducibility and capturing of effects on measured data due to environmental changes. This will especially be important for tracking of physiological parameters requiring high sensitivity.

# 9 Outlook

In the currently available form the presented framework can be employed for the assessement of the origin of observed changes in effective dielectric parameters as well as for optimization of sensor geometries for specific applications. However, it is suggested to refine the tissue model. Due to the modular structure of the framework this is assumed to need only limited effort, at least on the conceptional level.

In terms of material models a combination of the multiscale approach with the self-similar or fractal character of tissue, surfaces and cell membranes [60] could lead to improvements in efficiency. The fractal dimension is useful to describe irregularity and shape complexity in systems that appear to display scaling correlations (between structural units) over several orders of length or size [200]. Attempts to describe dielectric properties of tissue within the framework of fractal theory have been performed in [201] and [202].
Aiming for higher frequencies than few hundred MHz while using frininging-field sensors in the dimensions of centimeters the presented electroquasistatic approximation does not hold anymore because the probe starts to resonate, requiring a full-wave electrodynamic model. Also the incorporation of other physical processes and multiple time scales would improve material models of cells, tissues, nanocomposites and other structures in general. For example the comprehensive multiphysics multiscale model of the heart presented in [203] could serve as an example. It comprises soft tissue mechanics, reaction-diffusion equations governing current flow and Navier-Stokes equations solved for coronary blood flow as well as the transport of oxygen and metabolites, coupled to energy-dependent cellular processes.
Concerning both, the micro- and macroscopic model incorporating kinetics of charge carriers (Nernst-Planck equation) the electrode polarization which is reported to have a large impact at low frequences ($\alpha$-dispersion) could be included in order to better reproduce measured data. The coupling with thermodynamics would allow for a better understanding of electrothermal interactions between tissue and electromagnetic fields due to the more precise dielectric model.
On the microscopic scale model refinment could be achieved incorporating ion channels, macromolecules (proteins) and organelles as well as a more detailed model of bound water for modeling of the $\delta$-dispersion. Combining electromagnetic simulations with other physical processes the shape parametrization would also allow for the impact of cell deformation due to interactions such as mechanical stress, variations in ion concentrations or temperature as well as possibly cell differentiation on the dielectric spectra. Furthermore, an advanced model could help to answer the so far unanswered question if electromagnetic fields have non-thermal effects on biological material or if weak fields influence the temperature dependency of biochemical processes [204].

Focusing on the technical aspects the implementation of an own FEM code would be a benefit in order to be able to fully control the hand-over of geometry and mesh to the establishment of the matrices due to the critical aspect ratios and the involved numerical inaccuracies. With the presented framework also virtual cell [205], a software environment for computational cell biology enabling the establishment of a cell model based on the choice of different physical processes for a chosen geometry could be extended by electromagnetics.

The field of non-invasive monitoring of physiological parameters could be further explored. Since in appropriety set up models sensitivity analysis spectra provide specific information on the underlying parameter variations mechanisms leading to dielectric changes could possibly be identified, such as e.g. for the glucose level in blood. It was found [206] that when the glucose level rises and the effective parameters of skin are measured $\varepsilon_{\text{eff}}$ and $\sigma_{\text{eff}}$ both drop in the MHz range and vice versa. Yet, the mechanism for this phenomenon is still unknown. Possible explanations are an altered ion channel activity or a shift of interstitial water. The latter effect has e.g. been demonstrated with optical coherence tomography (OCT) measurements [207] and [208]. The transport through the involved cell types results in changes of transmembrane potential and ion channel activity, potentially observable in dielectric measurements.
Another effect suggests that the changes in osmotic pressure caused by the hydrophilic glucose molecule [209], which can lead to a so-called stress-generated potential (piezoelectric effect) in the epidermis and dermal collagen [210] and [211]. However, the question if a sensor pressed onto the skin contributes to the stress-generated potential and enhances the effect of osmotic pressure would have to be investigated as well. In a mentioned multiphysics model combining mass transport, tissue mechanics and electromagnetics this theory could be investigated.

In terms of measurement self-similar electrode arrays might be a solution in order to provide a variety of penetration depths of the electric field per available surface.

# Appendix A

# Surface triangulation

The presented general algorithm in this section is based on Delaunay and Voronoi triangulation, suitable for any kind of unbordered surface and based on the works of [113] and [117].
The principle is based on identification and separation of Voronoi vertices with respect to their relative position (inside or outside) to the 3D point cloud. Voronoi vertices approximating the medial axis/the surface normals are denoted as poles

1. Introduce a bounding box $B$ consisting of 8 vertices which is approximately 5 times larger than the tightest bounding box.
2. Compute the Delaunay and Voronoi diagram of $S \cup B$ including circumsphere radii (Voronoi balls) and quality factors of the tetrahedrons (Glassmeier parameter and Robert/Roux parameter [212]).
3. Filter out NaNs, Infs and bad quality tetrahedrons.
4. Identify outer convex poles $XP$ as outer poles of the points of $S$ belonging to the convex hull.
5. Identify poles for each sample point in $S$.
   - Let $p^+$ be the farthest vertex of the Voronoi cell of $s_i$.
   - Let $p^-$ be the farthest vertex of the Voronoi cell of $s_i$ with a negative dot product of $\overline{s_i p_i^+}$ and $\overline{s_i p_i^-}$.
6. Identify outer seed poles as the poles ($p^+$ or $p^-$) that are Voronoi vertices of tetrahedrons with at least one point from $B$. The corresponding inner seed pole is the other pole ($p^-$ or $p^+$) in the same Voronoi cell.
7. Label all poles as 'inner' or 'outer':
   - Push all $p^+$ and $p^-$ that are not seed poles into the 'unlabeled' queue.
   - Put seed poles into the 'labeled' queue. Label them as 'inner' or 'outer'.
   - Take a pole from the 'labeled' queue. This pole is the current pole.
   - All poles inside the current pole's Voronoi ball have the same label as the current pole. Mark the opposite poles belonging to the same $s_i$ with the opposite label as the current pole.
   - Remove the labeled poles out of the 'unlabeled' queue, push them into the 'labeled' queue.

- Remove the current pole from the 'labeled' queue.
- Return to step 3 and repeat procedure until all poles are labeled.

8. Extract outer concave poles $OCP$ as outer poles not belonging to $XP$.
9. Compute the Delaunay triangulation of $S \cup B \cup OCP$.
10. Tetrahedrons: Extract only those tetrahedrons with all vertices from $S$.
11. Triangles: Extract only those tetrahedrons with exactly one vertex from $B \cup OCP$ and three vertices from $S$. From the selected tetrahedrons extract only those triangles with all vertices from $S$.
12. Repair mesh if required.

In Step 5. the range-searching data structure $k$-D tree is employed in order to determine poles within the respective Voronoi ball. The corresponding MATLAB® files were downloaded from the file exchange [213].

This general algorithm is suitable for any kind of unbordered surfaces and could be extended to process bordered surfaces if necessary. It requires i) an initial Delaunay and Voronoi triangulation of $n + 8$ points and ii) a final Delaunay triangulation of $n + 8 + q$ points where $n$ is the number of points of $S$ and $q$ the number of $OCP$.
A detailed theoretical description is provided in [117] numerical issues such as the exclusion of bad quality tetrahedrons (mentioned in [113]) and points out that their presented algorithm does not need a heuristic which is not exactly true. Low-quality tetrahedrons always occur and cause problems. In this case false inner seed poles can be obtained from almost tangential very thin/flat tetrahedrons. The Voronoi vertices $p^-$ of these tetrahedrons have the required negative dot product and the largest distance from $s_i$ in the half-space/corresponding Voronoi cell but lie outside of the object. In other words the Voronoi cell extends beyond the object instead of being completely inside in this half-space.
Also the occurrence of holes or edges in undersampled regions is not addressed. In the case of supershapes undersampling is - although indirectly - an issue if the triangulation is used for geometry generation (in COMSOL Multiphysics® ): Although the sampling density can be almost arbitrarily high the distance and size of faces in the FEM software cannot be arbitrarily small for further processing. This fact has either to be taken into account if modeling complicated shapes or the number of points close to the critical $(0, 0, \pm z)$ points can be reduced. For a fixed $d$ the parameter $c$ denotes the number of removed $\theta$ discretization values directly following $-\pi/2$ and directly preceding $+\pi/2$.

# Appendix B

# Implementation

This appendix contains MATLAB® source codes of selected functions used in this work.

## B.1 Mixing formulas

The MG and HB formulas were implemented by setting up a recursive routine for the complex permittivity of the particle. The following features are available:

- Volume fractions of inclusion: $0 < \varphi < 1$ ($\varphi \neq 0, 1$)
- Axes: Arbitrary axes between 0 and '$\infty$' (The difference between smallest and largest axis should not exceed $10^{12}$. This is especially important in the case of cylinders, which require the choice of a high number in order to substitute $\infty$.)
- Shells: Arbitrary number of shells
- Orientation: Full, random in $xy$-direction and oriented in $z$-direction, random in $yz$-direction and oriented in $x$-direction, random in $xz$-direction and oriented in $y$-direction, random
- Full parametrization: Simultaneous or consecutive variation of an arbitrary number of all geometrical and material parameters

Although for the HB formula there are several analytical solutions for special cases, as e.g. shelled spheres [63] or randomly oriented shelled spheroids in [214], in this work it was implemented for arbitrary shapes (from sphere, ellipsoid to cylinder, disk or needle), meaning arbitrary values for the depolarization factors $L_k$. The numerical integration and solution of Equation 3.12 was performed with the `quad` and an initial guess for the numerical solution for high volume fractions of aligned particles:

$$\varepsilon_{\mathrm{eff},j} = \frac{\varepsilon_{\mathrm{i},j} - \varepsilon_{\mathrm{h},j}}{\varepsilon_{\mathrm{h},j} + (\varepsilon_{\mathrm{i},j} - \varepsilon_{\mathrm{h},j})L_j} \tag{B.1}$$

The initial guess for the numerical solution for randomly oriented particles is the mean value of the three $\varepsilon_{\mathrm{eff}}$-components for aligned particles.
The implementation of the LLL formula is straight-forward.

### B.1.1 Maxwell-Garnett formula

```
function cdata = calcMaxwellGarnett(params)
```

```
systemParams = params.systemParams;
geomParams = params.geomParams;
materialParams = params.materialParams;

fnames = fieldnames(geomParams);
for jj = 1:length(fnames)

    if iscell(geomParams.(fnames{jj}))
        geomParams.(fnames{jj}) = cell2mat(geomParams.(fnames{jj}));
    end
end

%-------------------------------------------------------------------------------------------
% systemParams.systemname:              system name
% systemParams.freq:                   frequency
% systemParams.locfile:                file for saving calculated dielectric properties
% geomParams.phi:                      volume fraction of particle
% geomParams.axesAbs:                  outermost axes (absolute values) of particle
% geomParams.shellsAbs:                shell thicknesses (absolute values)
%                                      confocal ellipsoids: size(shellsAbs,1) == 1
%                                      concentric ellipsoids approximation:
%                                      size(shellsAbs,1) == 3
% geomParams.shellsIndex:              reference axis for shell thickness for confocal
%                                      ellipsoids
%                                      (x = 1; y = 2; z = 3)
% materialParams.name:                 material names
% materialParams.loc:                  location of material parameters in results "data"
%                                      structure
%                                      if loc does not exist material
%                                      parameters are taken from database
%                                      function getDielectricData
% materialParams.locfile:              .mat-file where "data" structure is located
% materialParams.iso:                  indication if isotropic values are required
%                                      (fully isotropic: 'xyz'; 'xy'; 'xz'; 'yz')
% materialParams.particle:             get effective properties of
%                                      dispersed phase only
%-------------------------------------------------------------------------------------------

getcd = cd;
disp(strcat('Calculated system:',systemParams.systemname))
format long

eps0 = 8.8541878176e-12;

freq = systemParams.freq;
lf = length(freq);
omega = 2*pi*freq;
omegaVec = repmat(omega,3,1);
lm = length(materialParams.name);
mm = lm-1;

%-------------------------------------------------------------------------------------------
% Calculation of dielectric parameters for each phase
%-------------------------------------------------------------------------------------------
epsilon = zeros(3,lm,lf);
```

```
cd ..
cd('Dielectric data')
materialParams.cmplx = 1; % get complex epsilon
materialParams = getDielectricTensor(materialParams,freq); % Materials
epsilonTensor = materialParams.epsilonTensor;
for kk = 1:lm
    epskk(:,:,1) = epsilonTensor{kk};
    epsilon(:,kk,:) = permute(epskk,[1 3 2]);
end
cd(getcd)

%-------------------------------------------------------------------------------------------
% Calculation of absolute geometry (confocal ellipsoids in general)
%-------------------------------------------------------------------------------------------
if isfield(geomParams,'axesAbs')

    if size(geomParams.axesAbs,1) == 1
        % sphere
        axesAllAbs = repmat(geomParams.axesAbs,3,mm);

    elseif size(geomParams.axesAbs,1) == 3
        % ellipsoid
        axesAllAbs = repmat(geomParams.axesAbs,1,mm);
    else
        error('The number of rows of the "axesAbs"-vector must be either 1 or 3.')
    end

    if isfield(geomParams,'shellsAbs')

        if isfield(geomParams,'shellsIndex')

            % confocal ellipsoid
            xi = 2*geomParams.axesAbs(geomParams.shellsIndex)*geomParams.shellsAbs - ...
                 geomParams.shellsAbs.^2;
            xi = repmat(xi,3,1);
            axesAllAbs = (axesAllAbs.^2 - xi).^(1/2);
        else
            % shelled sphere
            axesAllAbs = axesAllAbs - repmat(geomParams.shellsAbs,3,1);
            if any(geomParams.axesAbs(1)~=geomParams.axesAbs) == 1
                % concentric ellipsoid
                disp(strcat('Inner ellipsoids are not confocal. The Maxwell-Garnett ...
                            solution is only an approximation.'))
            end
        end
    end
else
    % sphere, only defined by volume fraction
    axesAllAbs = repmat(((3/4*pi)*geomParams.phi).^(1/3),3,1);
end

%-------------------------------------------------------------------------------------------
% Relative values for all semiaxes
%-------------------------------------------------------------------------------------------
axf = ((geomParams.phi*3)/(4*pi*axesAllAbs(1,1)*axesAllAbs(2,1)*axesAllAbs(3,1)))^(1/3);
axesAll = axf*axesAllAbs;
```

```
%-------------------------------------------------------------------------------------------
% Depolarisation factors n; (shape factor u: %u(:,ii) = (1-n(:,ii))./n(:,ii);
% infThresh: axesAllAbs(j,:) > infThresh = Inf
% Calculation with initial absolute values for semiaxes
%-------------------------------------------------------------------------------------------
getDepolar = @(a,b,c) ((1/2)*(a.*b.*c).*...
              quad(@(s) (1./((s+a.^2).*((s+a.^2).*(s+b.^2).*(s+c.^2)).^(1/2))),0,1e9));
n = zeros(3,mm);

for ii = 1:mm
    nx = getDepolar(axesAll(1,ii),axesAll(2,ii),axesAll(3,ii));
    ny = getDepolar(axesAll(2,ii),axesAll(1,ii),axesAll(3,ii));
    nz = getDepolar(axesAll(3,ii),axesAll(1,ii),axesAll(2,ii));
    n(:,ii) = [nx; ny; nz];
end

n = repmat(n,[1 1 lf]);

%-------------------------------------------------------------------------------------------
% Actual calculation of the dielectric parameters
%-------------------------------------------------------------------------------------------
epsOut = epsilon(:,1,:);
e_high = epsilon(:,2:end,:);
e_low = epsilon(:,1:end-1,:);
vUp = e_high + n.*(e_low - e_high);
vDown = n.*(1-n).*(e_high - e_low);
mUp = e_high - e_low;
mDown =  e_low + n.*(e_high - e_low);

axesProduct = prod(axesAll);
indxAxes = 1;
for ii = 1:mm
    indxvecNew = zeros(1,2^(ii-1));
    indxvecNew(1:2:end) = indxAxes;
    indxvecNew(2:2:end) = ii;
    indxAxes = indxvecNew;
end

tUp = zeros(3,2^(mm-1),lf);
tDown = zeros(3,2^(mm-1),lf);

for ii = 1:mm
    jj = mm-ii+1;

    mUp_i = repmat(mUp(:,jj,:),[1 2^(jj-1) 1]);
    mDown_i = repmat(mDown(:,jj,:),[1 2^(jj-1) 1]);
    vUp_i = repmat(vUp(:,jj,:),[1 2^(jj-1) 1]);
    vDown_i = repmat(vDown(:,jj,:),[1 2^(jj-1) 1]);

    fQuot = axesProduct(indxAxes);
    fQuot = repmat(fQuot,[3 2 lf]);
    indxAxes = indxAxes(1:2:end);

    tUp_i = (fQuot(:,2:2:end,:)./fQuot(:,1:2:end,:)).*mUp_i + vUp_i.*tUp;
    tDown_i = mDown_i+ vDown_i.*tDown;
```

```
    tUpdate = tUp_i./tDown_i;
    tUp = tUpdate(:,1:2:end,:);
    tDown = tUpdate(:,2:2:end,:);
end

%-------------------------------------------------------------------------------------------
% Anisotropic
%-------------------------------------------------------------------------------------------
e = tUpdate;
epsEff = epsOut  + (geomParams.phi*epsOut .*e)./(1-geomParams.phi*n(:,1,:).*e);
% only particle
ov = ones(3,1,lf);
epsParticle = epsOut.*((e + ov - n(:,1,:).*e)./(ov - n(:,1,:).*e));

%-------------------------------------------------------------------------------------------
% Isotropic (random orientation)
%-------------------------------------------------------------------------------------------
sum1 = sum(e);
sum2 = sum(n(:,1,:).*e);
term3 = (geomParams.phi/3)*sum1./(1-(geomParams.phi/3)*sum2);
term3 = repmat(term3,[3 1 1]);
epsEffiso = sum(epsOut(:,:,:) + epsOut(:,:,:).*term3,1)/3;

% isotropic only in x-y-direction
sum1 = sum(e(1:2,:,:));
sum2 = sum(n(1:2,1,:).*e(1:2,:,:));
term3 = (geomParams.phi/2)*sum1./(1-(geomParams.phi/2)*sum2);
term3 = repmat(term3,[2 1 1]);
epsEffiso_i = sum(epsOut(1:2,:,:) + epsOut(1:2,:,:).*term3,1)/2;
epsEffisoXY = [epsEffiso_i;epsEffiso_i;epsEff(3,:,:)];

% isotropic only in x-z-direction
sum1 = sum([e(1,:,:);e(3,:,:)]);
sum2 = sum([n(1,1,:).*e(1,:,:);n(3,1,:).*e(3,:,:)]);
term3 = (geomParams.phi/2)*sum1./(1-(geomParams.phi/2)*sum2);
term3 = repmat(term3,[2 1 1]);
epsEffiso_i = sum([epsOut(1,:,:);epsOut(3,:,:)] + [epsOut(1,:,:);epsOut(3,:,:)].*term3,1)/2;
epsEffisoXZ = [epsEffiso_i;epsEff(2,:,:);epsEffiso_i];

% isotropic only in x-y-direction
sum1 = sum(e(2:3,:,:));
sum2 = sum(n(2:3,1,:).*e(2:3,:,:));
term3 = (geomParams.phi/2)*sum1./(1-(geomParams.phi/2)*sum2);
term3 = repmat(term3,[2 1 1]);
epsEffiso_i = sum(epsOut(2:3,:,:) + epsOut(2:3,:,:).*term3,1)/2;
epsEffisoYZ = [epsEff(1,:,:);epsEffiso_i;epsEffiso_i];

%-------------------------------------------------------------------------------------------
epsEff = squeeze(permute(epsEff,[1,3,2]));
epsEffisoXY = squeeze(permute(epsEffisoXY,[1,3,2]));
epsEffisoXZ = squeeze(permute(epsEffisoXZ,[1,3,2]));
epsEffisoYZ = squeeze(permute(epsEffisoYZ,[1,3,2]));
epsEffiso = squeeze(permute(epsEffiso,[1,3,2]));
epsParticle = squeeze(permute(epsParticle,[1,3,2]));

sigEff = 1i*epsEff.*omegaVec*eps0;
```

```
sigEffisoXY = 1i*epsEffisoXY.*omegaVec*eps0;
sigEffisoXZ = 1i*epsEffisoXZ.*omegaVec*eps0;
sigEffisoYZ = 1i*epsEffisoYZ.*omegaVec*eps0;
sigEffiso = 1i*epsEffiso.*omega*eps0;
sigParticle = 1i*epsParticle.*omegaVec*eps0;

% Save data
if exist('xi','var')
    cdata.geomParams.xi = xi(1,:);
end

cdata.systemParams = systemParams;
cdata.geomParams = geomParams;
cdata.materialParams = materialParams;
cdata.freq = freq;
cdata.epsEff = epsEff;
cdata.epsEffiso = epsEffiso;
cdata.epsEffisoXY = epsEffisoXY;
cdata.epsEffisoXZ = epsEffisoXZ;
cdata.epsEffisoYZ = epsEffisoYZ;
cdata.sigEff = sigEff;
cdata.sigEffiso = sigEffiso;
cdata.sigEffisoXY = sigEffisoXY;
cdata.sigEffisoXZ = sigEffisoXZ;
cdata.sigEffisoYZ = sigEffisoYZ;
if exist('epsParticle','var')
    cdata.epsParticle = epsParticle;
    cdata.sigParticle = sigParticle;
end
cdata.date = datestr(now);

cd(getcd)
end
```

### B.1.2 Hanai-Bruggeman formula

```
function cdata =  calcHanaiBrugg(params)
```

The first part of this function including the setup of the geometry corresponds to the one used in the previous subsection up to the paragraph 'Actual calculation of the dielectric parameters'.

```
%-------------------------------------------------------------------------------------------
% Anisotropic
%-------------------------------------------------------------------------------------------
epsOut = epsilon(:,1,:);
ax_high = axesAll(:,2:end);
ax_low = axesAll(:,1:end-1);
nu_i = prod(ax_high)./prod(ax_low);
nu = repmat(nu_i,[3 1 lf]);
ov = ones(3,1,lf);
epsParticle = epsilon(:,end,:);

for ii = 1:lm-2
    jj = lm-ii;
```

```
    epsShell = epsilon(:,jj,:);
    sum4 = epsParticle - epsShell;

    epsParticle = ...
        epsShell.*(ov + ((nu(:,jj-1,:).*sum4)./...
        (epsShell + n(:,jj,:).*sum4 - nu(:,jj-1,:).*n(:,jj-1,:).*sum4)));
end

%-------------------------------------------------------------------------------------------
% Extension to high volume fractions
%-------------------------------------------------------------------------------------------
phiterm = repmat(1-geomParams.phi,[3 1 lf]);
fa = @(q) ((((q - epsParticle)./...
                    (epsOut - epsParticle)).*((epsOut./q).^n(:,1,:)))-phiterm);

% Initial guesses for integration (solution of regular MGHB for small
% volume fractions)
epsGuess = geomParams.phi*((epsParticle - epsOut)./...
        (epsOut + n(:,1,:).*(epsParticle - epsOut))).*epsOut.*(1 - n(:,1,:)) + epsOut;

epsEffp = fsolve(fa,epsGuess);
epsEff = squeeze(permute(epsEffp,[1 3 2]));
sigEff = real(1i*epsEff.*omegaVec*eps0);
epsGuess = squeeze(permute(epsGuess,[1 3 2]));
sigGuess = real(1i*epsGuess.*omegaVec*eps0);

%-------------------------------------------------------------------------------------------
% Isotropic (random orientation)
%-------------------------------------------------------------------------------------------
epsEffiso = zeros(1,lf);
epsGuessiso = zeros(1,lf);

for ii = 1:lf

    n_i = squeeze(permute(n(:,1,ii),[1 3 2]));
    epsParticle_i = squeeze(permute(epsParticle(:,1,ii),[1 3 2]));
    epsOut_i = squeeze(permute(epsOut(1,:,ii),[1 3 2]));
    epsGuess_i = squeeze(permute(mean(epsEffp(:,1,ii)),[1 3 2]));
    epsGuessiso(1,ii) = epsGuess_i;
    epsEffiso(1,ii) = fsolve(@(q) calcHanaiBrugg_integrate...
                            (q,epsParticle_i,n_i,epsOut_i,geomParams.phi),epsGuess_i);
end

sigEffiso = 1j*epsEffiso.*omega*eps0;
sigGuessiso = 1j*epsGuessiso.*omega*eps0;


% Save data
if exist('xi','var')
    cdata.geomParams.xi = xi(1,:);
end

cdata.systemParams = systemParams;
cdata.geomParams = geomParams;
cdata.materialParams = materialParams;
```

```
cdata.freq = freq;
cdata.epsEff = epsEff;
cdata.sigEff = sigEff;
cdata.epsEffiso = epsEffiso;
cdata.sigEffiso = sigEffiso;
cdata.date = datestr(now);

cd(getcd)
end

%--------------------------------------------------------------------------------------------
%                                      SUBFUNCTIONS
%--------------------------------------------------------------------------------------------
function y = calcHanaiBrugg_integrate(qeps,qepsParticle,qn,qepsOut,qphi)

y = integrated(qeps,qepsParticle,qn,qepsOut)  - log(1 - qphi);

    function yy = integrated(qeps,qepsParticle,qn,qepsOut)

        yy =  quadv(@(qeps) integrand(qeps,qepsParticle,qn),qepsOut,qeps);

        function yyy = integrand(qeps,qepsParticle,qn)

            yyy = 3./(qeps.*(sum((qeps - qepsParticle)./(qeps + (qepsParticle -...
                qeps).*qn))));
        end
    end
end
```

## B.2 Transfer of the dielectric tensor

```
function materialParams = getDielectricTensor(materialParams,freq)

%--------------------------------------------------------------------------------------------
% Get diagonal dielectric tensor for all materials from the system to
% calculate
%--------------------------------------------------------------------------------------------

% INPUT
%--------------------------------------------------------------------------------------------
% materialParams.name:                  material names
% materialParams.loc:                   location of material parameters in results
%                                       "data" structure
%                                       if loc does not exist material
%                                       parameters are taken from database
%                                       function getDielectricData
% materialParams.locfile:               .mat-file where "data" structure is located
% materialParams.iso:                   indication if isotropic values
%                                       are required
%                                       (fully istoropic: 'xyz'; 'xy'; 'xz'; 'yz')
% materialParams.particle:              get effective properties of
%                                       dispersed phase only
% freq:                                 frequency
%--------------------------------------------------------------------------------------------
```

```
% OUTPUT
%-----------------------------------------------------------------------------------------
% materialParams.epsilonTensor(spatial component,material number,frequency point)
% materialParams.sigmaTensor(spatial component,material number,frequency point)
%-----------------------------------------------------------------------------------------
getcd = cd;
lm = length(materialParams.name);
epsilonTensor = cell(1,lm);
sigmaTensor = cell(1,lm);

for kk = 1:lm

    % Material in data structure as result
    if isfield(materialParams,'loc') && ~isempty(materialParams.loc{kk})

        mname = char(materialParams.name(kk));

        cd ..
        cd('Results')

        % Get file where data is located
        if isfield(materialParams,'locfile')

            if iscell(materialParams.locfile)

                load(materialParams.locfile{kk})
            else
                load(materialParams.locfile)
            end
        else
            load mydatabase
        end


        % Only particle parameters
        if isfield(materialParams,'particle') && ~isempty(materialParams.particle{kk})
            epsStr = 'epsParticle';
            % Isotropy in certain space directions?
        elseif ~isfield(materialParams,'iso') || isempty(materialParams.iso{kk})
            epsStr = 'epsEff';
        elseif isequal(materialParams.iso{kk},'xyz')
            epsStr = 'epsEffiso';
        elseif isequal(materialParams.iso{kk},'xy')
            epsStr = 'epsEffisoXY';
        elseif isequal(materialParams.iso{kk},'xz')
            epsStr = 'epsEffisoXZ';
        elseif isequal(materialParams.iso{kk},'yz')
            epsStr = 'epsEffisoYZ';
        end
        sigStr = strrep(epsStr,'eps','sig');

        matLocation = eval(strcat(materialParams.loc{kk},'.',mname));

        if iscell(matLocation)
            matLocation = matLocation{1};
        end
```

```
        epskk = matLocation.(epsStr);
        sigkk = matLocation.(sigStr);
        freqi =  matLocation.freq;

        % Interpolate in case of unequal frequency vectors
        if ~isequal(freq,freqi)
            epskk = interp1(freqi',epskk',freq',’nearest’,’extrap’)’;
            sigkk = interp1(freqi',sigkk',freq',’nearest’,’extrap’)’;
            disp(’Unequal frequency vectors. Dielectric parameters have been interpolated.’);
        end

    % Material in database
    else

        cd ..
        cd(’Dielectric data’)

        if ~isnumeric(materialParams.name{kk})

            mname = char(materialParams.name(kk));
        else
            mname = materialParams.name{kk};
        end

        if ~isfield(materialParams, ’conc’) || isempty(materialParams.conc{kk})
            [epsCmplx, sigCmplx] =  getDielectricData(mname,freq);
        else
            [epsCmplx, sigCmplx] =  getDielectricData(mname,freq,materialParams.conc{kk});
        end

        if ~isempty(epsCmplx)

            if ~isfield(materialParams,’cmplx’) || isequal(materialParams.cmplx,0)
                epskk = real(epsCmplx);
                sigkk = real(sigCmplx);
            else
                epskk = epsCmplx;
                sigkk = sigCmplx;
            end
        end

        cd(getcd);
    end

    % Extend to diagonal tensor if material isotropic
    if isequal(size(epskk,1),1)
        epsilonTensor{kk} = repmat(epskk,3,1);
        sigmaTensor{kk} = repmat(sigkk,3,1);
    else
        epsilonTensor{kk} = epskk;
        sigmaTensor{kk} = sigkk;
    end

    materialParams.epsilonTensor = epsilonTensor;
    materialParams.sigmaTensor = sigmaTensor;
```

```
end
```

## B.3 Effective dielectric parameters of a simple cubic unit cell

In COMSOL Multiphysics® version 3.5a the necessary steps in order to obtain a supershape geometry which can be used for further processing are as follows:

1. Remove poles
2. Create iso-$z$-curves with function `poly`
3. Coerce to faces with function `solid2`
4. Linear lofting with function `loft`
5. Embed into 3D geometry with function `embed`
6. Transform into a solid object with functions `geomcomp` and `geomcoerce`

It is crucial to ensure that points are connected linearly and not using spline interpolation. Due to the small distance between original and offset surface this leads to an overlap of the curves and surfaces and consequently, to an incorrect topology with additional domains.

The main function evaluating the admittance of a unit cell containing a supershape with arbitrary number of shells is given on the following.

Another technical issue concerns the appropriate choice of a solver. It was found that iterative solvers sometimes converge to the wrong solution (geometric multigrid, [215]) or are extremely slow (GMRES). Therefore, the solver of choice will be an direct one. The best experience was made with PARDISO although if the number of degrees of freedom exceeds a certain value (usually around 4 million) an internal error occurs.

```
function fem = comsolSupershape(params,structinfo)

% GET PARAMETERS
%-------------------------------------------------------------------------------------------
timeTotal = tic;
getcd = cd;
disp(['System: ',params.systemParams.systemname])
structinfo.systemname = params.systemParams.systemname;


% SOLVE (and sweep parameters if available)
%-------------------------------------------------------------------------------------------
if ~isfield(params.systemParams,'loopParams')

    simresults = comsolSolveFunction(params);
else

    loopParamsInfo = comsolGetParamsMulti(params);

    pnumstotal = loopParamsInfo.pnumstotal;
    pnums = loopParamsInfo.pnums;
    pinds = loopParamsInfo.pinds;
```

```
    ginds = [isequal(numel(pnums),1) pnums];
    simresults = cell(ginds(ginds > 0));

    for mm = 1:loopParamsInfo.pnumstotal

        disp(['Parameter step ', num2str(mm),' of ',num2str(pnumstotal)])
        disp('Parameter indices: ')
        disp(pinds(mm,:))

        [params,indcell] = comsolSetParamsMulti(params,loopParamsInfo,mm);

        simresultsi = comsolSolveFunction(params);
        simresults(indcell{:}) = {simresultsi};

    end
end

cd ..
cd('Results')
saveMyData(structinfo,simresults,systemParams.matfilename)
cd(getcd);

timeTotal = toc(timeTotal);
disp(['Total CPU time: ',num2str(timeTotal),' [s]'])

%-------------------------------------------------------------------------------------------
% SOLVE PROBLEM
%-------------------------------------------------------------------------------------------
    function cdata = comsolSolveFunction(params)

        geomParams = params.geomParams;
        meshParams = params.meshParams ;
        materialParams = params.materialParams;
        systemParams = params.systemParams;

        % DEFINE QUANTITIES, PREALLOCATE
        %-------------------------------------------------------------------------------
        eps0 = 8.8541878176e-12;

        freq = systemParams.freq;
        freqpts = length(freq);
        reY = zeros(1,freqpts);
        imY = zeros(1,freqpts);
        epsEff = zeros(3,freqpts);
        sigEff = zeros(3,freqpts);
        timeStep = zeros(1,freqpts);

        % GET MATERIAL DATA
        %-------------------------------------------------------------------------------
        cd ..
        cd('Dielectric data')
        materialParams = getDielectricTensor(materialParams,freq);
        cd(getcd);

        % GEOMETRY
        %-------------------------------------------------------------------------------
```

```
geomParams.numberOfMaterials = length(materialParams.name);
[fem,geomParams] = comsolGeometrySupershape(geomParams);

% BOUNDARY AND SUBDOMAIN IDENTIFICATION
%--------------------------------------------------------------------------------
idParams = comsolIdentifyBndsSubdomains(fem,geomParams);

% MESH
%--------------------------------------------------------------------------------
meshParams.geomdim = geominfo(fem.geom,'out',{'gd'});
fem = comsolMesh(meshParams,fem);

% APPLICATION VARIABLES
%--------------------------------------------------------------------------------
clear appl
appl.mode.class = 'QuasiStatics';
appl.name = 'emqvw';
appl.module = 'ACDC';
appl.shape = {'shlag(2,''lm1'')','shlag(2,''V'')'};
appl.gporder = {10,4};
appl.border = 'on';
appl.assignsuffix = '_emqvw';
clear prop
prop.elemdefault='Lag2';
prop.analysis='smallcurr';
clear weakconstr
weakconstr.value = 'on';
weakconstr.dim = {'lm1','tlmx','tlmy','tlmz','lm2'};
prop.weakconstr = weakconstr;
appl.prop = prop;

fem1 = fem;

vinp = {'1' '2' '3'}; % Switch electrodes

for jj = 1:length(vinp)

    bndParams.inp = vinp{jj};
    bndParams.id = idParams.forBnd;
    appl = comsolBndEllipsoid(appl,bndParams); % Boundaries

    % FREQUENCY SWEEP
    %----------------------------------------------------------------------------
    for ii = 1:freqpts

        time1 = tic;
        disp(['Frequency step: ',num2str(jj),' ',num2str(ii)])
        fem = fem1;
        appl = comsolMaterialEllipsoid(materialParams,freq,appl,ii,idParams);

        % MORE APPLICATION VARIABLES
        %------------------------------------------------------------------------

        fem.appl{1} = appl;
        fem.border = 1;
        clear units;
```

```
            units.basesystem = 'SI';
            fem.units = units;
            clear ode
            clear units;
            units.basesystem = 'SI';
            ode.units = units;
            fem.ode=ode;

            % SOLVING
            %--------------------------------------------------------------------------
            fem=multiphysics(fem);
            fem.xmesh=meshextend(fem);
            fem.sol=femstatic(fem, ...
                'solcomp',{'lm1','V'}, ...
                'outcomp',{'lm1','V'}, ...
                'blocksize','auto', ...
                'linsolver','pardiso');

            %femstruct{ii} = fem;

            % POST-EVALUATION
            %--------------------------------------------------------------------------

            rY = posteval(fem,'real(Y11_emqvw)');
            reY(jj,ii) = rY.d('u');
            iY = posteval(fem,'imag(Y11_emqvw)');
            imY(jj,ii) = iY.d('u');

            C = imY(jj,ii)./(2*pi*freq(ii));

            indx = [1 2 3];
            indxn = str2double(vinp{jj});

            unitCellDims.d = geomParams.unitCellDims(indxn);
            unitCellDims.A = geomParams.unitCellDims(indxn ~= indx);

            epsEff(jj,ii) = (C*unitCellDims.d)/(prod(unitCellDims.A)*eps0);
            sigEff(jj,ii) = reY(jj,ii)*unitCellDims.d/prod(unitCellDims.A);

            timeStep(jj,ii) = toc(time1);
            disp(['CPU time per frequency step: ',num2str(timeStep(jj,ii)),' [s]'])
        end
    end

    % SAVE DATA
    %-----------------------------------------------------------------------------
    cdata.date = datestr(now);
    cdata.systemParams = systemParams;
    cdata.geomParams = geomParams;
    cdata.meshParams = meshParams;
    cdata.materialParams = materialParams;
    cdata.timeStep = timeStep;
    cdata.freq = freq;
    cdata.reY = reY;
    cdata.imY = imY;
    cdata.epsEff = epsEff;
```

```
        cdata.sigEff = sigEff;
        %cdata.femstruct = femstruct;
    end
end

%-------------------------------------------------------------------------------------------
%                                      SUBFUNCTIONS
%-------------------------------------------------------------------------------------------

%-------------------------------------------------------------------------------------------
% GEOMETRY
%-------------------------------------------------------------------------------------------
function [fem,geomParams] = comsolGeometrySupershape(geomParams)


% Calculate geometry, offset surface for triangulation and shape volume
%-------------------------------------------------------------------------------------------
sfParams = geomParams.sfParams;

[x,y,z,nv,p,nvp,xcu,ycu,zcu] = superformula3D(sfParams.d,...
                                              sfParams.a,...
                                              sfParams.b,...
                                              sfParams.m,...
                                              sfParams.n1,...
                                              sfParams.n2,...
                                              sfParams.n3,...
                                              sfParams);
close gcf
close gcf

if ~isfield(sfParams,'fd') || isempty(sfParams.fd)
    fd = 10/sfParams.d;
else
    fd = params.fd;
end

p3 = p + fd*nvp;
[tri,tet,eu,em] = triangulateSimple(p,p3);
volumeRelative = sum(getTetVolume(p,tet));
surftri(tri,p,eu,em)
close gcf

% Scaling
%-------------------------------------------------------------------------------------------
shellsAbs = repmat(geomParams.shellsAbs,3,1);
axesRelative = [max(max(xcu)) - min(min(xcu));...
    max(max(ycu)) - min(min(ycu));...
    max(max(zcu)) - min(min(zcu))];
scl = geomParams.axesAbs/axesRelative(geomParams.axesIndex);
% disp(scl)
dmRelative = shellsAbs(1,2)/scl;
volumeAbs = scl^3*volumeRelative;
% disp(vol)
axesAll = scl*axesRelative;
qax = axesAll./geomParams.axesAbs;
```

```
% environment box
boxUnitVol = volumeAbs/geomParams.phi;
boxUnitLength = boxUnitVol^(1/3);
boxUnitValRef = boxUnitLength/(prod(qax))^(1/3);
boxUnitVal = qax*boxUnitValRef;
geomParams.unitCellDims = geomParams.array.*boxUnitVal;
boxDisplc = boxUnitVal.*(geomParams.array > 1);
midUnitVal = boxUnitVal/2;

axesAll = repmat(axesAll/2,[1 geomParams.numberOfMaterials-1]);
axesAll = axesAll - shellsAbs;

% Removal of overlapping points @ x = xmin for each z
%-------------------------------------------------------------------------------------------
% outer surface
xcr = xcu;
ycr = ycu;
zcr = zcu;
xyz = cat(3,xcr,ycr,zcr);
xyzr = permute(xyz,[2 3 1]);

% inner offset surface
nvOff = nv((3+sfParams.cut):end-(2+sfParams.cut),1:end-1,:);
xOff = xcu(:,1:end-1) - dmRelative*nvOff(:,:,1);
yOff = ycu(:,1:end-1) - dmRelative*nvOff(:,:,2);
zOff = zcu(:,1:end-1) - dmRelative*nvOff(:,:,3);
xyzOff = cat(3,xOff,yOff,zOff);
xyzrOff = permute(xyzOff,[2 3 1]);

% Curves || x-y-plane and loft
%-------------------------------------------------------------------------------------------
numslcs = size(xcr,1);
numslcsOff = size(xOff,1);
slcs = cell(1,numslcs);
eltoel = cell(1,numslcs);
slcsOff = cell(1,numslcsOff);
eltoelOff = cell(1,numslcsOff);
jj = 1;
jj2 = 1;

for ii = 1:numslcs

    crv = poly1(xyzr(:,1,ii),xyzr(:,2,ii));
    slcs{ii} = solid2(crv);
    slcs{ii} = crv;
    eltoel{ii} = 1;
    if isequal(ii,1) || isequal(ii,numslcs)
        slcsEnd{jj} = solid2(crv);
        planeCoo{jj} = [0 1 0;0 0 1;xyzr(1,3,ii) xyzr(1,3,ii) xyzr(1,3,ii)];
        jj = jj+1;
    end
    if ii <= numslcsOff
        crvOff = poly1(xyzrOff(:,1,ii),xyzrOff(:,2,ii));
        slcsOff{ii} = solid2(crvOff);
        slcsOff{ii} = crvOff;
        eltoelOff{ii} = 1;
```

```
        if isequal(ii,1) || isequal(ii,numslcsOff)
            slcsEndOff{jj2} = solid2(crvOff);
            planeCooOff{jj2} =...
            [0 1 0;0 0 1;xyzrOff(1,3,ii) xyzrOff(1,3,ii) xyzrOff(1,3,ii)];
            jj2 = jj2+1;
        end
    end
end

tiltrot = zeros(2,numslcs);
intrrot = zeros(1,numslcs);
zshift = [zeros(2,numslcs);zcr(:,1)'];
dvr = {zshift,tiltrot,intrrot};
g1 = loft(slcs,'loftEdge',eltoel,'loftSecPos',dvr,'loftMethod','linear');

q1 = slcsEnd{1};
q2 = slcsEnd{2};
q1 = embed(q1,'wrkpln',planeCoo{1});
q2 = embed(q2,'wrkpln',planeCoo{2});
g1a = geomcomp({g1 q1 q2});
g1 = geomcoerce('solid',g1a);

tiltrotOff = zeros(2,numslcsOff);
intrrotOff = zeros(1,numslcsOff);
zshiftOff = [zeros(2,numslcsOff);zOff(:,1)'];
dvrOff = {zshiftOff,tiltrotOff,intrrotOff};
g2 = loft(slcsOff,'loftEdge',eltoelOff,'loftSecPos',dvrOff,'loftMethod','linear');

q1Off = slcsEndOff{1};
q2Off = slcsEndOff{2};
q1Off = embed(q1Off,'wrkpln',planeCooOff{1});
q2Off = embed(q2Off,'wrkpln',planeCooOff{2});
g2aOff = geomcomp({g2 q1Off q2Off});
g2 = geomcoerce('solid',g2aOff);

% crv = geomspline(xyzr(:,1:2,ii)',...
%       'splinemethod','foley','closed','on');
% wghts = repmat(0.1,2,numslcs-1);
% wghtsOff = repmat(0.1,2,numslcsOff-1);
% g1 = loft(slcs,'loftEdge',eltoel,'loftSecPos',dvr,'loftWeights',wghts);
% g2 =
% loft(slcsOff,'loftEdge',eltoelOff,'loftSecPos',dvrOff,'loftWeights',wghtsOff);

% Scale and move supershape
%-------------------------------------------------------------------------------------
g1 = scale(g1,scl,scl,scl);
g2 = scale(g2,scl,scl,scl);
shp1 = move(g1,midUnitVal(1),midUnitVal(2),midUnitVal(3));
shp2 = move(g2,midUnitVal(1),midUnitVal(2),midUnitVal(3));
outerbox =block3(geomParams.unitCellDims(1),...
            geomParams.unitCellDims(2),...
            geomParams.unitCellDims(3),...
            'base','corner','pos',{'0','0','0'},'axis',{'0','0','1'},'rot','0');


% Assemble geometry
```

```
%-------------------------------------------------------------------------------------------
reptol = 1e-6;
particlesUnit=geomcomp({shp1 shp2},'ns','sf','face','none','edge','all','repairtol',reptol);
particlesCopy = geomarrayr(particlesUnit,boxDisplc(1),boxDisplc(2),boxDisplc(3),...
                           geomParams.array(1),geomParams.array(2),geomParams.array(3));

% If available: rotate each particle
%-------------------------------------------------------------------------------------------
if isfield(geomParams,'angl') && (all(geomParams.angl.theta) && all(geomParams.angl.phi))

    % check Matlab version
    vrsnm = version;
    vk = strfind(vrsnm,'.');
    vnum1 = str2double(vrsnm(1:vk(1)-1));
    vnum2 = str2double(vrsnm(vk(1)+1:vk(2)-1));
    if vnum1 > 7 || vnum2 > 9
        hdegtorad = @degtorad;
    else
        hdegtorad = @deg2rad;
    end

    particles = cell(1,prod(array));
    kk = 1;
    for iiz = 1:array(3)
        for iix = 1:array(1)
            for iiy = 1:array(2) % geomarrayr sweeps y before x!!

                iphi = hdegtorad(angl.phi(iix,iiy,iiz));
                itheta = hdegtorad(angl.theta(iix,iiy,iiz));

                rotax = [sin(iphi) -sin(itheta).*cos(iphi) 0];
                cntr = [(2*iix - 1) (2*iiy - 1) (2*iiz - 1)].*midUnitVal';
                if ~isequal(itheta,0)
                    particles{kk} = rotate(particlesCopy{kk},-itheta,rotax,cntr);
                else
                    particles{kk} = particlesCopy{kk};
                end
                kk = kk + 1;
            end
        end
    end
else
    particles = particlesCopy;
end

particles{end+1} = outerbox;
objsAll = particles;
clear s
s.objs=objsAll;
fem.draw=struct('s',s);
fem.geom=geomcsg(fem,'repairtol',reptol);

end

%-------------------------------------------------------------------------------------------
% GEOMETRY INFO
```

```
%-------------------------------------------------------------------------------------------
function idParams = comsolIdentifyBndsSubdomains(fem,geomParams)

numberOfMaterials = geomParams.numberOfMaterials;

% Orientation of faces relative to subdomains
%-------------------------------------------------------------------------------------------
adj = geominfo(fem.geom,'out',{'adj'},'odp',[2;3]);

[no,ud,nbs,rng] = geominfo(fem.geom,'out',{'no','ud','nbs','rng'},'od',[1 2 3]);
numSd = no(3);
vec = zeros(1,nbs);
subdomain = cell(numberOfMaterials,1);
subdomainBin = cell(numberOfMaterials,1);

% identify outer boundaries
[outerRow, outerCol] = find(ud == 0);
outerBin = vec;
outerBin(outerCol) = 1;
outerLog = logical(outerBin);
outerud = ud(:,outerLog);
subdomainBin{1}{1} = logical(outerBin);

% determine number of environment subdomain
[r,c,subdomEnv] = find(outerud);
subdomEnv = subdomEnv(1);
subdomain{1} = subdomEnv;

[firstRow, firstCol] = find(ud == subdomEnv);
firstBin = vec;
firstBin(firstCol) = 1;
firstLog = logical(firstBin) & ~outerLog;
firstud = ud(:,firstLog);
firstud(firstud == subdomEnv) = 0;
[r,c,subdomVec] = find(firstud);

%  Subdomain numbers for first layers
%-------------------------------------------------------------------------------------------
ii = 1;
while (any(subdomVec) == 1)
    [r c subdomVec] = find(subdomVec);
    subdomNmbr = subdomVec(1);
    subdomain{2}(ii) = subdomNmbr;
    subdomVec(subdomVec == subdomNmbr) = 0;

    % create binary vector for current subdomain number
    [rb cb] = find(ud == subdomNmbr);
    subdomBin = vec;
    subdomBin(cb) = 1;
    subdomainBin{2}{ii} = logical(subdomBin);
    ii = ii+1;
end
clear ii

%  Subdomain numbers for all other layers
%-------------------------------------------------------------------------------------------
```

```
for jj = 2:numberOfMaterials-1
    for kk = 1:length(subdomain{2})
        % number of previous subdomain
        subdomNmbrPv = subdomain{jj}(kk);
        % vector containing all el. with number of prev. subdomain
        subdomVecPv = ud(:,(subdomainBin{jj}{kk}));
        % exclude environment subdomain and previous neighbour subdomain
        subdomVec = subdomVecPv((subdomVecPv ~= subdomain{1}) &...
            (subdomVecPv ~= subdomNmbrPv));
        subdomNmbr = subdomVec(1);
        subdomain{jj+1}(kk) = subdomNmbr;

        % create binary vector for current subdomain number
        [rb cb] = find(ud == subdomNmbr);
        subdomBin = vec;
        subdomBin(cb) = 1;
        subdomainBin{jj+1}{kk} = logical(subdomBin);
    end
end
clear jj

idParams.sdParams.subdomainBin = subdomainBin;
idParams.sdParams.sdNumber     = numberOfMaterials;
idParams.sdParams.subdomain    = subdomain;

% Relative position of outer boundaries
%-------------------------------------------------------------------------------------------
% u-v-grid, only starting and end point required
[u,v] = meshgrid(0:1,0:1);
% prepare u-v-grid for one boundary
Sm(1,:,:) = deal([u(:) v(:)]);
% stack u-v-grid for all 6 outer boundaries
Sm = repmat(Sm,[6 1 1]);
% vector with numbers of outer boundaries
Bm = outerCol;

% get x,y,z coordinates for all 6 outer faces
xx = geominfo(fem.geom,'out',{'xx'},'par',{Bm Sm});

% compensate numerical error for 0-coordinates (if value is smaller than
% th*(shortest edge), set it to 0) as all block coordinates are >= 0 and
% no edge < thresheold*smallest outer edge
th = 1e-6;
xx(xx < th*min(geomParams.unitCellDims)) = 0;
xc = xx(:,:,1);
yc = xx(:,:,2);
zc = xx(:,:,3);

% bndid: boundary position identification vector
% bndid(1,2,3): face at x,y,z = 0
% bndid(4,5,6): face at xmax(bx),ymax(by),zmax(bz)
bndid(1) = find(~sum(xc,2));
bndid(2) = find(~sum(yc,2));
bndid(3) = find(~sum(zc,2));
bndid(4) = find((xc(:,1) & xc(:,2) & xc(:,3) & xc(:,4)));
bndid(5) = find((yc(:,1) & yc(:,2) & yc(:,3) & yc(:,4)));
```

```
bndid(6) = find((zc(:,1) & zc(:,2) & zc(:,3) & zc(:,4)));
bndid = bndid';
% assign boundary numbers to id vector
idParams.forBnd.bndIdNumber = outerCol(bndid);
idParams.forBnd.bndNumber = nbs;

end

%-------------------------------------------------------------------------------------------
% BOUNDARY SETTINGS
%-------------------------------------------------------------------------------------------
function appl = comsolBndEllipsoid(appl,bndParams)

clear bnd
bnd.inport = {0,0,1,0};
bnd.eltype = {'nJ0','V0','port','cont'};
bnd.magtype = {'A0','A0','A0','cont'};
bnd.wcshape = 1;
bnd.ind = 4*ones(1,bndParams.id.bndNumber);

switch bndParams.inp

    case('1')
        % set x = 0 boundary as inport
        bnd.ind(bndParams.id.bndIdNumber(1)) = 3;
        % set xmax boundary to ground
        bnd.ind(bndParams.id.bndIdNumber(4)) = 2;
        % set other to insulation
        bnd.ind(bndParams.id.bndIdNumber([2 3 5 6])) = 1;

    case('2')
        % set y = 0 boundary as inport
        bnd.ind(bndParams.id.bndIdNumber(2)) = 3;
        % set ymax boundary to ground
        bnd.ind(bndParams.id.bndIdNumber(5)) = 2;
        % set other to insulation
        bnd.ind(bndParams.id.bndIdNumber([1 3 4 6])) = 1;


    case('3')
        % set z = 0 boundary as inport
        bnd.ind(bndParams.id.bndIdNumber(3)) = 3;
        % set zmax boundary to ground
        bnd.ind(bndParams.id.bndIdNumber(6)) = 2;
        % set other to insulation
        bnd.ind(bndParams.id.bndIdNumber([1 2 4 5])) = 1;
end

appl.bnd = bnd;
end

%-------------------------------------------------------------------------------------------
% ASSIGN DIELECTRIC PARAMETERS TO SUBDOMAINS
%-------------------------------------------------------------------------------------------
function appl = comsolMaterialEllipsoid(materialParams,freq,appl,freqpoint,idParams)
```

```
clear equ
equ.gporder = 2;

equ.epsilonr = cell(1,idParams.sdParams.sdNumber);
equ.sigma = cell(1,idParams.sdParams.sdNumber);
for ii = 1:idParams.sdParams.sdNumber
    sdIndx = idParams.sdParams.subdomain{ii}(:);
    equ.epsilonr(1,ii) = {materialParams.epsilonTensor{ii}(freqpoint)};
    equ.sigma(1,ii) = {materialParams.sigmaTensor{ii}(freqpoint)};
    equ.ind(sdIndx) = ii;
end

equ.shape = 2;
appl.equ = equ;
appl.var = {'nu',freq(freqpoint)};

end
```

## B.4 Replacement of a geometrical domain by a boundary condition

In COMSOL Multiphysics® the introduction of a discontiunity of the solution variable, the potential $V$ is only possible if the geometry is composed of an assembly, so to each 'side' of a boundary denoted as 'source' and 'destination' different properties can be assigned, e.g. different types of mesh elements or in the case at hand different values of the solution variable. The discontinuity can be characterized in terms of thickness and material parameters. Although this option is not readily available in the user interface one can define the following boundary parameters on the in order to obtain the wanted solution. The following example holds for a boundary segment, the identitiy pair number 9, denoted as `ip9`.

- order of basis function on the boundary element: 1 `bnd.shape = 1`
- constraint forces: `bnd.constrf = test(-V)` and `bnd.constrf = test(V0port_emqvw-V)`
- constraints on elements: `bnd.constr = -V` and `V0port_emqvw-V`
- weak constraints: `bnd.weak = if(src2dst_ip9,(sigmaext_emqvw`
- `j*omega_emqvw*epsilon0_emqvw*epsilonrext_emqvw)*(src2dst_ip9(V)-V)*`
- `(dVolbnd_emqvw*V_test-src2dst_ip9(dVolbnd_emqvw)*`
- `test(src2dst_ip9(V)))/dbnd_emqvw,0)`

## B.5 Multilayer system under a coaxial probe

The semi-analytical calculation of $\varepsilon_{\text{eff}}$ of a layered structure under a coaxial probe was implemented in MATLAB® . The roots of the equation system consisting of equations are calculated using `fsolve` with the initial guess $p_{i,\text{guess}}$ $p_{i,\text{guess}} = p_i(1) + p_k$ and the integrals $P_{ij}$ with `quad` and the integration limits a = 0 and b = 50. `quad` is less likely to produce NaNs than `quadgk` which is actually tailored for oscillating integrands vanishing for $x \to \infty$. Unfortunately, the attempt to vectorize the procedure within a frequency band failed because `quadv` produced NaNs.

```
function calcCoaxVariational(params,structinfo)
%-------------------------------------------------------------------------------------------
% params.systemParams.name:             system name
% params.systemParams.freq:             frequency
% params.systemParams.locfile:          file for saving calculated dielectric properties
% params.systemParams.pguess:           initial guess for alpha, beta and p_i calculation
% params.systemParams.numterms:         number of TM0n modes
% params.geomParams.dzLayer:            vector with layer thicknesses
% params.geomParams.a:                  radius of inner conductor
% params.geomParms.b:                   radius of outer conductor
% params.materialParams.name:           material names
% params.materialParams.substrate:      material name of material between
%                                       conductors
% params.materialParams.loc:            location of material parameters in results "data"
%                                       structure
%                                       if loc does not exist material
%                                       parameters are taken from database
%                                       function getDielectricData
% params.materialParams.locfile:        .mat-file where "data" structure is
%                                       located
%-------------------------------------------------------------------------------------------

% GET PARAMETERS
%-------------------------------------------------------------------------------------------
timeTotal = tic;
getcd = cd;
disp(['System: ',params.systemParams.systemname])
structinfo.method = 'variational';
structinfo.systemname = params.systemParams.systemname;

% SOLVE (and sweep parameters if available)
%-------------------------------------------------------------------------------------------
if ~isfield(params.systemParams,'loopParams')

    simresults = coaxVariational(params);
else

    loopParamsInfo = comsolGetParams(params);

    pnumstotal = loopParamsInfo.pnumstotal;
    pnums = loopParamsInfo.pnums;
    pinds = loopParamsInfo.pinds;

    ginds = [isequal(numel(pnums),1) pnums];
    simresults = cell(ginds(ginds > 0));

    for mm = 1:loopParamsInfo.pnumstotal

        disp(['Parameter step ', num2str(mm),' of ',num2str(pnumstotal)])
        disp('Parameter indices: ')
        disp(pinds(mm,:))

        [params,indcell] = comsolSetParams(params,loopParamsInfo,mm);
        simresultsi = coaxVariational(params);

        % if probe geometry changes, cell constants have to be recalculated
```

```
        % each time
        if isfield(params.systemParams,'getconstants') && ...
           isequal(params.systemParams.getconstants.mode,'local')

            % keep original parameter settings
            %(changed in case of recalculation of cell constants)
            paramsprotect = params;

            disp('Cell constants are recalculated.')

            if isfield(params.materialParams,'loc')
                params.materialParams = rmfield(params.materialParams,'loc');
            end

            for pp = 1:length(params.materialParams.name)
                params.materialParams.name{pp} = 'air';
            end

            simresultsi.air = coaxVariational(params);

            for pp = 1:length(params.materialParams.name)
                params.materialParams.name{pp} = 'NaCl';
                params.materialParams.conc{pp} = 0.001;
            end

            simresultsi.NaCl0001 = coaxVariational(params);

            pms.structdirect = simresultsi;
            pms.matRef = params.systemParams.getconstants.matRef;
            pms.matMeasured = params.systemParams.getconstants.matMeasured;

            simresultsi = calcCellConstantsFinal(pms);
            params = paramsprotect;
        end

        simresults(indcell{:}) = {simresultsi};
    end
end

cd ..
cd('Results')
saveMyData(structinfo,simresults,systemParams.matfilename)
cd(getcd);

timeTotal = toc(timeTotal);
disp(['Total CPU time: ',num2str(timeTotal),' [s]'])

% SOLVE PROBLEM
%--------------------------------------------------------------------------------------
    function cdata = coaxVariational(params)

        systemParams = params.systemParams;
        geomParams = params.geomParams;
        materialParams = params.materialParams;

        % DEFINE QUANTITIES AND FUNCTIONS, PREALLOCATE
```

```
%-------------------------------------------------------------------------------
format long
eps0 = 8.8541878176e-12;
%
% % Add f = 1Hz for sigStat calculation
freq        = systemParams.freq;
numterms    = systemParams.numterms;
pguess      = systemParams.pguess;
ptol        = systemParams.ptol;
V           = systemParams.V;
scalefactor = systemParams.scalefactor;

fnames = fieldnames(geomParams);
for jj = 1:length(fnames)

    if iscell(geomParams.(fnames{jj}))
        geomParams.(fnames{jj}) = cell2mat(geomParams.(fnames{jj}));
    end
end
a           = geomParams.a/scalefactor;
b           = geomParams.b/scalefactor;
dzLayer     = geomParams.dzLayer/scalefactor;

lf          = length(freq);
lm          = length(materialParams.name);

epsilon     = zeros(3,lm,lf);
epsilonSubstrate = zeros(3,lf);

p_i         = zeros(1,numterms);
t_i         = zeros(1,numterms);
alpha_i     = zeros(1,numterms);
beta_i      = zeros(1,numterms);

C           = zeros(1,lf);
timeStep    = zeros(1,lf);

tfun        = @(alpha_,beta_,p_) ...
    (b.^2/2).*(alpha_.*besselj(1,b.*p_) + beta_.*bessely(1,b.*p_)).^2 - ...
    (a.^2/2).*(alpha_.*besselj(1,a.*p_) + beta_.*bessely(1,a.*p_)).^2;

% GET MATERIAL PARAMETERS
%-------------------------------------------------------------------------------
cd ..
cd('Dielectric data')

materialParams.cmplx = 1; % get complex epsilon
materialParams = getDielectricTensor(materialParams,freq); % Materials
epsilonTensor = materialParams.epsilonTensor;
for kk = 1:lm
    epskk(:,:,1) = epsilonTensor{kk};
    epsilon(:,kk,:) = permute(epskk,[1 3 2]);
end

materialParamsSubstrate.name = materialParams.substrate;
materialParamsSubstrate.cmplx = 1;
```

```
materialParamsSubstrate = getDielectricTensor(materialParamsSubstrate,freq);
epsilonSubstrate(:,:,1) = materialParamsSubstrate.epsilonTensor{1};

epsilon = epsilon(1,:,:);
epsilonSubstrate = epsilonSubstrate(1,:,:);

cd(getcd)

% CALCULATE P_i COEFFICIENTS AND NORMALIZATION CONSTANTS ALPHA AND BETA
%-------------------------------------------------------------------------------
pguess_i = pguess(1);
%fpguess = pguess(2);
options = optimset('TolX',ptol);

for ii = 1:numterms

    x0 = [pguess_i;0.5;0.5];
    pab = fsolve(@(x) calcCoaxVariational_AlphaBetaP(x,a,b),x0,options);

    p_k = pab(1);
    alpha_k = pab(2);
    beta_k = pab(3);

    t_i(ii) = tfun(alpha_k,beta_k,p_k);
    p_i(ii) = p_k;
    alpha_i(ii) = alpha_k;
    beta_i(ii) = beta_k;

    pguess_i = p_i(1)+p_k;
end

alpha_i = [0 alpha_i];
beta_i = [0 beta_i];
p_ii = [0 p_i];

for ff = 1:lf

    time1 = tic;
    disp(['Frequency step: ',num2str(ff)])

    epsMaterial  = squeeze(permute(epsilon(1,:,ff),[3 2 1]));
    epsSubstrate = epsilonSubstrate(1,ff);
    P_ij         = zeros(numterms+1);

    % Calculation of P_ij
    %---------------------------------------------------------------------------
    for jj = 1:(numterms + 1)
        for kk = jj:(numterms + 1)

            alpha_1 = alpha_i(jj);
            beta_1 =  beta_i(jj);
            p_1 =     p_ii(jj);

            alpha_2 = alpha_i(kk);
            beta_2 =  beta_i(kk);
            p_2 =     p_ii(kk);
```

```
                P_ij(jj,kk) = quad(@(x)...
                    calcCoaxVariational_Pij(x,a,b,V,alpha_1,alpha_2,beta_1,beta_2,...
                                            p_1,p_2,epsMaterial,dzLayer),...
                    0,25);
            end
        end

        % expand to full matrix
        P_ij = P_ij.' + triu(P_ij,1);

        Pzero = P_ij(1,2:end);
        Pnonzero = P_ij(2:end,2:end);

        % Pnonzero_diag*g = Pzero - > solve for g
        Pnonzero_diag = Pnonzero + diag((V.^2).*(epsSubstrate./epsMaterial(1)).*p_i.*t_i);
        g = Pnonzero_diag\(-Pzero.');

        P00 = P_ij(1,1);
        Pmat = [Pzero;Pnonzero];
        Pterm = P00 + [2 g.']*(Pmat*g);

        C(1,ff) = scalefactor*2*pi*eps0*(epsMaterial(1)*Pterm/(V^2) +...
                                         epsSubstrate(1).*sum((g.').^2.*p_i.*t_i));

        timeStep(1,ii) = toc(time1);
        disp(['CPU time per frequency step: ',num2str(timeStep(1,ii)),' [s]'])
    end

    reY = -2*pi*freq.*imag(C);
    imY = 2*pi*freq.*real(C);
    %-------------------------------------------------------------------------------------
    cdata.freq = freq;
    cdata.systemParams = systemParams;
    cdata.geomParams = geomParams;
    cdata.materialParams = materialParams;
    cdata.reY = reY;
    cdata.imY = imY;
    cdata.timeStep = timeStep;
    cdata.date = datestr(now);
end

cd(getcd)
end

%-------------------------------------------------------------------------------------
%                                    SUBFUNCTIONS
%-------------------------------------------------------------------------------------

%-------------------------------------------------------------------------------------
% Calculation of p_i
%-------------------------------------------------------------------------------------
function y = calcCoaxVariational_AlphaBetaP(x,a,b)

y =  [x(2,:).*besselj(0,x(1,:).*a) + x(3,:).*bessely(0,x(1,:).*a);
```

```
      x(2,:).*besselj(0,x(1,:).*b) + x(3,:).*bessely(0,x(1,:).*b);
      x(2,:).^2 + x(3,:).^2 - 1];
end

%-------------------------------------------------------------------------------------------
% Calculation of integrands
%-------------------------------------------------------------------------------------------
function P_arg = ...
calcCoaxVariational_Pij(x,a,b,V,alpha1,alpha2,beta1,beta2,p1,p2,epsMaterial,d)

% Calculation of dielectric contrast term
%-------------------------------------------------------------------------------------------
numlayers = length(epsMaterial);
Rterm = 1;

for ii = 1:numlayers-1

    nn = numlayers - ii;
    R = (epsMaterial(nn) - epsMaterial(nn+1))./(epsMaterial(nn) + epsMaterial(nn+1));
    Rterm = (R + Rterm.*exp(-2*x.*d(nn+1)))./(1 + R.*Rterm.*exp(-2*x.*d(nn+1)));
end

% Calculation of F_i and F_j (alpha, beta, p as (2x1)-vectors and for-loop
% from 1 to 2 doesn't work!!!)
%-------------------------------------------------------------------------------------------
if isequal([alpha1 beta1 p1],[0 0 0])

    F1 = (V./(log(b./a).^(1/2).*x)).*(besselj(0,b.*x) - besselj(0,a.*x));
else

    F1 = (((V.*x.*p1)./(p1.^2 - x.^2))).*...
        (b.*besselj(0,b.*x).*(alpha1.*besselj(1,b.*p1) +...
                              beta1.*bessely(1,b.*p1)) -...
         a.*besselj(0,a.*x).*(alpha1.*besselj(1,a.*p1) +...
                              beta1.*bessely(1,a.*p1)));
end

if isequal([alpha2 beta2 p2],[0 0 0])

    F2 = (V./(log(b./a).^(1/2).*x)).*(besselj(0,b.*x) - besselj(0,a.*x));
else

    F2 = (((V.*x.*p2)./(p2.^2 - x.^2))).*...
        (b.*besselj(0,b.*x).*(alpha2.*besselj(1,b.*p2) +...
                              beta2.*bessely(1,b.*p2)) -...
         a.*besselj(0,a.*x).*(alpha2.*besselj(1,a.*p2) +...
                              beta2.*bessely(1,a.*p2)));
end

P_arg = F1.*F2.*((1 - Rterm.*exp(-2.*x.*d(1)))./(1 + Rterm.*exp(-2.*x.*d(1))));
end
```

## B.6 Parametrization functions

The following functions allow to parametrize the problem in arbitrary dimensions. A simultaneous update of two or more parameters is also enabled.

### B.6.1 Get parameters

```
function loopParamsInfo = comsolGetParamsMulti(params)

geomParams = params.geomParams;
meshParams = params.meshParams;
materialParams = params.materialParams;
loopParams = params.systemParams.loopParams;

disp('Additional looped parameters:')
disp(loopParams.ptype)
disp(loopParams.pname)
if isfield(loopParams,'pindx')
    disp(loopParams.pindx)
end

ndims = length(loopParams.ptype);
pnums = zeros(1,ndims);
pvals = cell(1,ndims);
pmulti = zeros(1,ndims);

% GET PARAMETER VALUES
%--------------------------------------------------------------------------------------
for iiout = 1:ndims
    numPmulti = length(loopParams.ptype{iiout});

    for jj = 1:numPmulti
        ptype_i = eval(loopParams.ptype{iiout}{jj});

        if ~isfield(loopParams,'pindx') || isempty(loopParams.pindx{iiout}{jj})

            numP = length(ptype_i.(loopParams.pname{iiout}{jj}));
            pval = {ptype_i.(loopParams.pname{iiout}{jj})};
        else
            if isnumeric(ptype_i.(loopParams.pname{iiout}{jj})...
                                (loopParams.pindx{iiout}{jj}))

                numP = ...
                length(ptype_i.(loopParams.pname{iiout}{jj})...
                               (loopParams.pindx{iiout}{jj}));
            else
                numP = ...
                length(ptype_i.(loopParams.pname{iiout}{jj})...
                               {loopParams.pindx{iiout}{jj}});
            end
            pval = ptype_i.(loopParams.pname{iiout}{jj})(loopParams.pindx{iiout}{jj});
        end

        pvals{iiout}{jj} = pval;
```

```
    end

    pnums(1,iiout) = numP;
    pmulti(1,iiout) = numPmulti;
end

pnumstotal = prod(pnums);

% GET INDICES (different behaviour of ind2sub for different Matlab versions)
%-------------------------------------------------------------------------------------------
vrsnm = version;
vk = strfind(vrsnm,'.');
vnum1 = str2double(vrsnm(1:vk(1)-1));
vnum2 = str2double(vrsnm(vk(1)+1:vk(2)-1));

if vnum1 > 7 || vnum2 > 9 % everything ok

    inds = cell(1,ndims);
    [inds{:}] = ind2sub(pnums,linspace(1,pnumstotal,pnumstotal));
    inds = cell2mat(inds);
    inds = reshape(inds,[pnumstotal ndims]);

else
    % Matlab versions < 2010
    % replacement of ind2sub because number of parameters n for indices [i1,...in] unknown
    % ind2sub requires explicit array for indices
    % [varargout{1:nargout}] = ind2sub(pnums,pnumstotal) crashes...
    inds = zeros(pnumstotal,ndims);
    pold = 1;

    for iip = 1:ndims

        pnew = prod(pnums(1:iip));

        indsi = repmat(linspace(1,pnums(iip),pnums(iip))',[pnumstotal/pnew 1]);
        indsii = reshape(repmat(indsi',[pold 1]),pnumstotal,1);
        inds(:,iip) = indsii;

        pold = pnew;
    end
end

loopParamsInfo.ndims = ndims;
loopParamsInfo.pnumstotal = pnumstotal;
loopParamsInfo.pnums = pnums;
loopParamsInfo.pvals = pvals;
loopParamsInfo.pinds = inds;
loopParamsInfo.pmulti = pmulti;
end
```

### B.6.2 Set parameters

```
function [params,indcell] = comsolSetParamsMulti(params,loopParamsInfo,pnumCurrent)

geomParams = params.geomParams;
meshParams = params.meshParams ;
```

```
materialParams = params.materialParams;
loopParams = params.systemParams.loopParams;

ndims = loopParamsInfo.ndims;
pvals = loopParamsInfo.pvals;
pinds = loopParamsInfo.pinds;
pmulti = loopParamsInfo.pmulti;

indcell = cell(1,ndims);

for iip = 1:ndims
    for jj = 1:pmulti(1,iip)

        pvalCell = pvals{iip}{jj};
        pvalCell = pvalCell{1};
        pvalCurrent = pvalCell{pinds(pnumCurrent,iip)};

        if ~isfield(loopParams,'pindx') || isempty(loopParams.pindx{iip}{jj})

            structstr = strcat(loopParams.ptype{iip}{jj},'.',...
                loopParams.pname{iip}{jj});
        else

            structstr = strcat(loopParams.ptype{iip}{jj},'.',...
                loopParams.pname{iip}{jj},...
                '{',num2str(loopParams.pindx{iip}{jj}),'}');
        end

        if isnumeric(pvalCurrent)

            eval(strcat(structstr,'= pvalCurrent;'));
        else
            eval(strcat(structstr,'= char(pvalCurrent);'));
        end
        indcell{1,iip} = pinds(pnumCurrent,iip);
    end
end

params.geomParams = geomParams;
params.meshParams = meshParams;
params.materialParams = materialParams;

end
```

# Appendix C

# Multilayer system under a coaxial probe - semi-analytical solution

The effective dielectric properties of a layered material under a coaxial probe as a function of capacitance, admittance or $S$-parameters can be calculated with a variational method employed e.g. in [154], [157], [158], [159], [155], [160] and [156]. The procedure is outlined on the following.

The capacitance of an arbitrary structure where two conductors are at potentials zero and $V_0$ can be expressed as a functional of the potential function $V$

$$C = \frac{1}{V_0^2} \int_v \varepsilon (\Delta V)^2 dv \tag{C.1}$$

where $v$ is the volume of the capacitor. Using a cylindrical coordinate system $(r, \phi, z)$ and omitting the azimuthal dependence due to the cylindrical symmetry the potential $V$ can be expressed as

$$V_{\text{out}}(r, z) = \int_0^\infty f_0(\lambda) e^{-\lambda z} J_0(\lambda r) \lambda d\lambda, \qquad z \geq 0 \tag{C.2}$$

in the infinite half-space $z \geq 0$ with homogeneous dielectric and as

$$V_{\text{in}}(r, z) = V_0 \frac{\ln(r/b)}{\ln(a/b)} + V_0 \sum_{i=1}^{I} g_i T_i(r) e^{p_i z}, \qquad z \leq 0 \qquad \text{and} \qquad a \leq r \leq b \tag{C.3}$$

inside the probe, with the eigenfunctions

$$T_i = \alpha_i J_0(p_i r) + \beta_i Y_0(p_i r). \tag{C.4}$$

$J_0$ and $Y_0$ are Bessel functions of the first and second kind, defined in Equations C.5 and C.6.

$$J_p(x) = \sum_{m=0}^{\infty} \frac{(-1)^m (x/2)^{2m+p}}{m!(m+p)!} \tag{C.5}$$

$$Y_p(x) = \frac{J_p(x)\cos(p\pi) - J_{-p}(x)}{\sin(p\pi)} \tag{C.6}$$

The coefficients of the eigenfunctions $T_i(r)$ are numerically determined from the boundary condition $T_i(a) = T_i(b) = 0$ ($\mathbf{E}_t = \mathbf{E}_r = \vec{0}$ at the conductors) and the normalization condition (Bessel functions are orthogonal):

$$\alpha_i J_0(p_i a) + \beta_i Y_0(p_i a) = 0 \tag{C.7}$$

$$\alpha_i J_0(p_i b) + \beta_i Y_0(p_i b) = 0 \tag{C.8}$$

$$\alpha_i^2 + \beta_i^2 = 1 \tag{C.9}$$

The vector with all $p_i$ is given by

$$\mathbf{p} = \begin{pmatrix} p_1 \\ p_2 \\ ... \\ p_I \end{pmatrix}. \tag{C.10}$$

Setting $z = 0$ in C.2 and writing the inverse Hankel transform one gets

$$f_0 = \int_0^\infty V_1(0,r) J_0(\lambda r) r dr. \tag{C.11}$$

Since $V_1(0,r) = V_0$ as $r \leq a$, $V_1(0,r) = 0$ as $r \geq b$ and $V_1(0,r) = V_{\text{substrate}}(0,r)$ as $a \leq r \leq b$ Equation C.11 can be written as

$$f_0 = V_0 \int_0^a J_0(\lambda r) r dr + \int_a^b V_{\text{substrate}}(0,r) J_0(\lambda, r) r dr. \tag{C.12}$$

Substituting $V_{\text{substrate}}(0,r)$ from Equation C.3 the integrals can be expressed as the sum

$$f_0(\lambda) = F_0(\lambda) \sum_{i=1}^{I} g_i F_i(\lambda) \tag{C.13}$$

where

$$F_0(\lambda) = \frac{V_0}{\lambda\sqrt{\ln(a/b)}}[J_0(\lambda b) - J_0(\lambda a)] \tag{C.14}$$

$$F_i(\lambda) = \frac{V_0 \lambda p_i}{p_i^2 - \lambda^2}(bJ_0(\lambda b)[\alpha_i J_1(p_i b) + \beta_i Y_1(p_i b)] - aJ_0(\lambda a)[\alpha_i J_1(p_i a) + \beta_i Y_1(p_i a)]). \tag{C.15}$$

The unknown coefficients $g_i$ in Equation C.3 are determined by the continuity condition for the electric flux density over the substrate-medium interface at $z = 0$ and $a \leq r \leq b$.

$$\varepsilon_1 \frac{\partial V_1}{\partial z} = \varepsilon_1 \frac{\partial V_{\text{substrate}}}{\partial z} \tag{C.16}$$

In order to be able to use this condition even if the series in Equation C.3 is finite the eigenfunctions $T_i$ are used as weighting functions. The approximate solution is the

$$\int_a^b \varepsilon_1 \frac{\partial V_1}{\partial z} T_j(r) r dr = \int_a^b \varepsilon_{\text{substrate}} \frac{\partial V_{\text{substrate}}}{\partial z} T_j(r) r dr. \qquad j = 1...I \tag{C.17}$$

The orthogonality of the eigenfunctions $T_i$ provides

$$\int_a^b T_i(r) T_j(r) r dr = \delta_{ij} \tag{C.18}$$

with $\delta_{ij}$ the Kronecker delta.

$$R_k = \frac{r_k + R_{k-1} e^{-2\lambda d(m-k+1)}}{1 + r_k R_{k-1} e^{-2\lambda d(m-k+1)}} \tag{C.19}$$

with

$$r_k = \frac{\varepsilon^*_{m-k} - \varepsilon^*_{m-k+1}}{\varepsilon^*_{m-k} + \varepsilon^*_{m-k+1}} \tag{C.20}$$

$$P_{ij} = \int_0^\infty F_i(\lambda) F_j(\lambda) \tanh(\lambda d_1 R_{m-1}) d\lambda \tag{C.21}$$

$$t_i = \int_a^b T_i^2(r) dr = \frac{b^2}{2} \Big[\alpha_i J_1(p_i b) + \beta_i Y_1(p_i b)\Big]^2 - \frac{a^2}{2} \Big[\alpha_i J_1(p_i a) + \beta_i Y_1(p_i a)\Big]^2 \tag{C.22}$$

$$\mathbf{t} = \begin{pmatrix} t_1 \\ t_2 \\ ... \\ t_I \end{pmatrix} \tag{C.23}$$

$$\mathbf{P}_0 = \begin{pmatrix} P_{01} \\ P_{02} \\ ... \\ P_{0I} \end{pmatrix} \tag{C.24}$$

$$\mathbf{P}_k = \begin{pmatrix} P_{11} & P_{12} & ... & P_{1I} \\ P_{21} & P_{22} & ... & P_{2I} \\ \vdots & \vdots & \ddots & \vdots \\ P_{I1} & P_{I2} & ... & P_{II} \end{pmatrix} \tag{C.25}$$

The coefficients $g_i$ are components of the vector

$$\mathbf{G} = \begin{pmatrix} g_1 \\ g_2 \\ ... \\ g_I \end{pmatrix}. \tag{C.26}$$

In order to obtain $\mathbf{G}$ the system given by the matrix equation

$$(\mathbf{P}_k + V_0^2 \frac{\varepsilon^*_{\text{substrate}}}{\varepsilon^*_1} \delta_{ij} (\mathbf{p}\mathbf{t}^T) \cdot \mathbf{G} = \mathbf{P}_0 \tag{C.27}$$

has to be solved. The contribution of the exchange integrals can be written as

$$P = \mathbf{P}_{00} + 2\mathbf{G}^T \left( \begin{pmatrix} \mathbf{P}_0^T \\ \mathbf{P}_k \end{pmatrix} \mathbf{G} \right) \tag{C.28}$$

finally providing the total complex capacitance

$$C = \frac{2\pi\varepsilon_0}{V_0^2} \varepsilon^*_1 P + \varepsilon^*_{\text{substrate}} \sum_{i=1}^{I} g_i^2 p_i t_i. \tag{C.29}$$

The effective dielectric properties can be obtained by transformation of the complex capacitance $C$ into the admittance with $Y = -\omega \text{Im}\{C\} + j\omega \text{Re}\{C\}$ and with the calibration procedure described in Section 6.1. The accuracy of the semi-analytical solution will depend on the number of involved $\text{TM}_{0n}$ modes as well as on the numerical evaluation of the integrals.
In order to be able to calculate the effective dielectric properties for anisotropic sublayers one would have to be able to perform a coordinate transformation for cartesian $\bar{\varepsilon_{\text{eff}}}^*$ into cylindrical $\bar{\varepsilon_{\text{eff}}}^*$ coordinates.

# Bibliography


[1] X. Li, C. Kato, A. Zyuzin, and A. Mamishev, "Design of multi-channel fringing electric field sensors for imaging; Part I: General design priniciples," in *Conference Record of the 2004 IEEE International Symposium on Electrical Insulation, Indianapolis, USA*, 2004.

[2] P. Linderholm, J. Vannod, Y. Barrandon, and P. Renaud, "Bipolar resistivity profiling of 3D tissue culture," *Biosensors and Bioelectronics*, vol. 22, no. 6, pp. 789–796, 2007.

[3] D. C. Walker, B. H. Brown, R. H. Smallwood, D. R. Hose, and D. M. Jones, "Modelled current distribution in cervical squamous tissue," *Physiological Measurement*, vol. 23, pp. 159–168, 2002.

[4] P. Åberg, P. Geladi, I. Nicander, J. Hansson, U. Holmgren, and S. Ollmar, "Non-invasive and microinvasive electrical impedance spectra of skin cancer - a comparison between two techniques," *Skin Research and Technology*, vol. 11, pp. 281–286, 2005.

[5] D. M. Ferreira, C. S. Silva, and M. N. Souza, "Electrical impedance model for evaluation of skin irritation in rabbits and humans," *Skin Research and Technology*, vol. 13, pp. 259–267, 2007.

[6] M. S. Talary, F. Dewarrat, D. Huber, and A. Caduff, "In vivo life sign application of dielectric spectroscopy and non-invasive glucose monitoring," *Journal of Non-Crystalline Solids*, vol. 353, pp. 4515–4517, 2007.

[7] E. Marzec and W. Warchol, "Dielectric properties of a protein-water system in selected animal tissues," *Bioelectrochemistry*, vol. 65, no. 2, pp. 89–94, 2005.

[8] M. Miettinen, J. Mönkkönen, M. R. Lahtinen, J. Nuutinen, and T. Lahtinen, "Measurement of oedema in irritant-exposed skin by a dielectric technique," *Skin Research and Technology*, vol. 12, pp. 235–240, 2006.

[9] P.-O. Bagnaninchi, M. Dikeakos, T. Veres, and M. Tabrizian, "Complex permittivity measurement as a new noninvasive tool for monitoring in vitro tissue engineering and cell signature through the detection of cell proliferation, differentiation, and pretissue formation," *IEEE Transactions on Nanobioscience*, vol. 3, pp. 243–50, 2004.

[10] C. Skourou, A. Rohr, P. J. Hoopes, and K. D. Paulsen, "In vivo EIS characterization of tumour tissue properties is dominated by excess extracellular fluid," *Physics in Medicine and Biology*, vol. 52, pp. 347–363, 2007.

[11] M. Hakoda, T. Hachisu, Y. Wakizaka, S. Mii, and N. Kitajima, "Development of a method to analyze single cell activity by using dielectrophoretic levitation," *Biotechnology Progress*, vol. 21, no. 6, pp. 1748–1753, 2005.

[12] J. Yang, Y. Huang, X. Wang, X. Wang, F. Becker, and P. Gascoyne, "Dielectric properties of human leukocyte subpopulations determined by electrorotation as a cell separation criterion," *Biophysical journal*, vol. 76, no. 6, pp. 3307–3314, 1999.

[13] H. Morgan, T. Sun, D. Holmes, S. Gawad, and N. G. Green, "Single cell dielectric spectroscopy," *Journal of Physics D: Applied Physics*, vol. 40, pp. 61–70, 2007.

[14] D. Debuisson, A. Treizebré, T. Houssin, E. Leclerc, D. Bartès-Biesel, D. Legrand, J. Mazurier, S. Arscott, B. Bocquet, and V. Senez, "Nanoscale devices for online dielectric spectroscopy of biological cells," *Physiological Measurement*, vol. 29, pp. S213–S225, 2008.

[15] T. Sun, S. Gawad, N. G. Green, and H. Morgan, "Dielectric spectroscopy of single cells: Time domain analysis using Maxwell's mixture equation," *Journal of Applied Physics D: Applied Physics*, vol. 40, pp. 1–8, 2007.

[16] J. Gimsa, T. Müller, T. Schnelle, and G. Fuhr, "Dielectric spectroscopy of single human erythrocytes at physiological ionic strength: Dispersion of the cytoplasm," *Biophysical Journal*, vol. 71, pp. 495–506, 1996.

[17] F. Kremer and A. Schönhals, *Broadband Dielectric Spectroscopy.* Springer Berlin, 2003.

[18] D. Haarer and H. Spiess, *Spektroskopie amorpher und kristalliner Festkörper.* Springer, 1995.

[19] C. You, S. Shin, and S. Kim, "Modified effective-medium theory for magneto-optical spectra of magnetic materials," *Physical Review B*, vol. 55, no. 9, pp. 5953–5958, 1997.

[20] [Online]. Available: http://www.psrc.usm.edu/mauritz/dilect.html

[21] H. Schwan, "Electrical properties of tissue and cell suspensions." *Advances in biological and medical physics*, vol. 5, p. 147, 1957.

[22] T. Yamamoto and Y. Yamamoto, "Non-linear electrical properties of skin in the low frequency range," *Medical and Biological Engineering and Computing*, vol. 19, no. 3, pp. 302–310, 1981.

[23] M. O'Connor and R. Bentall, *Emerging Electromagnetic Medicine.* Springer, 1990.

[24] J. Songer, "Tissue ischemia monitoring using impedance spectroscopy: Clinical evaluation," Ph.D. dissertation, Worcester Polytechnic Institute, 2001.

[25] C. H. Riedel, "Planare induktive Impedanzmessverfahren in der Medizintechnik," Ph.D. dissertation, Universität Fridericiana Karlsruhe, 2004.

[26] A. Peyman, "Mechanisms of interaction of electromagnetic radiation with biological tissues," Ph.D. dissertation, King's College, University of London, 2002.

[27] C. Gabriel, *Handbook of Biological Effects of Electromagnetic Fields.* Taylor & Francis, 2006, ch. Dielectric Properties of Biological Materials, pp. 52–94.

[28] R. Pethig, "Dielectric properties of body tissues," *Clinical Physics and Physiological Measurement*, vol. 8, p. 5, 1987.

[29] C. Gabriel and A. Peyman, "Dielectric measurement: Error analysis and assessment of uncertainty," *Physics in Medicine and Biology*, vol. 51, p. 6033, 2006.

[30] N. Axelrod, E. Axelrod, A. Gutina, A. Puzenko, P. Ishai, and Y. Feldman, "Dielectric spectroscopy data treatment: I. Frequency domain," *Measurement Science and Technology*, vol. 15, p. 755, 2004.

[31] V. Kolehmainen, M. Vauhkonen, P. Karjalainen, and J. Kaipio, "Assessment of errors in static electrical impedance tomography with adjacent and trigonometric current patterns," *Physiological Measurement*, vol. 18, p. 289, 1997.

[32] F. Bordi, C. Cametti, and T. Gili, "Reduction of the contribution of electrode polarization effects in the radiowave dielectric measurements of highly conductive biological cell suspensions," *Bioelectrochemistry*, vol. 54, no. 1, pp. 53–61, 2001.

[33] V. Raicu, N. Kitagawa, and A. Irimajiri, "A quantitative approach to the dielectric properties of the skin," *Physics in Medicine and Biology*, vol. 45, pp. L1–L4, 2000.

[34] S. Gabriel, R. W. Lau, and C. Gabriel, "The dielectric properties of biological tissues: III. Parametric models for the dielectric spectrum of tissues," *Physics in Medicine and Biology*, vol. 41, pp. 2271–2293, 1996.

[35] K. Foster, J. Bidinger, and D. Carpenter, "The electrical resistivity of cytoplasm," *Biophysical Journal*, vol. 16, no. 9, pp. 991–1001, 1976.

[36] R. Hoffman and W. Britt, "Flow-system measurement of cell impedance properties," *Journal of Histochemistry and Cytochemistry*, vol. 27, no. 1, p. 234, 1979.

[37] J. Bao, C. Davis, and R. Schmukler, "Frequency domain impedance measurements of erythrocytes. Constant phase angle impedance characteristics and a phase transition," *Biophysical journal*, vol. 61, no. 5, pp. 1427–1434, 1992.

[38] P. Ellappan and R. Sundararajan, "A simulation study of the electrical model of a biological cell," *Journal of Electrostatics*, vol. 63, pp. 297–307, 2005.

[39] A. English, J. Squire, J. Bodmer, and A. Moy, "Endothelial cell electrical impedance parameter artifacts produced by a gold electrode and phase sensitive detection," *Biomedical Engineering, IEEE Transactions on*, vol. 54, no. 5, pp. 863–873, 2007.

[40] E. Krommenhoek, J. Gardeniers, J. Bomer, A. Van den Berg, X. Li, M. Ottens, L. Van Der Wielen, G. Van Dedem, M. Van Leeuwen, W. Van Gulik, *et al.*, "Monitoring of yeast cell concentration using a micromachined impedance sensor," *Sensors and Actuators B: Chemical*, vol. 115, no. 1, pp. 384–389, 2006.

[41] T. Tamura, M. Tenhunen, T. Lahtinen, T. Repo, and H. P. Schwan, "Modeling of the dielectric properties of normal and irradiated skin," *Physics in Medicine and Biology*, vol. 39, pp. 927–936, 1994.

[42] S. Morita, H. Umakoshi, and R. Kuboi, "Dielectric response of cells and liposomes and its utilization for evaluation of cell membrane-protein interaction," *Journal of Bioscience and Bioengineering*, vol. 90, no. 2, pp. 157–162, 2000.

[43] M. Stuchly and W. Xi, "Modelling induced currents in biological cells exposed to low-frequency magnetic fields," *Physics in Medicine and Biology*, vol. 39, p. 1319, 1994.

[44] [Online]. Available: http://www.agedefyingbody.com/Border.html

[45] G. Milton, *The Theory of Composites*. Cambridge University Press, 2002.

[46] A. Sihvola, *Electromagnetic Mixing Formulas and Applications*. Inspec/Iee, 1999.

[47] K. Asami, "Characterization of heterogeneous systems by dielectric spectroscopy," *Progress in Polymer Science*, vol. 27, pp. 1617–1659, 2002.

[48] M. Simeononva and J. Gimsa, "Dielectric anisotropy, volume potential anomalies and the persistent Maxwellian equivalent body," *Journal of Physics: Condensed Matter*, vol. 17, pp. 7817–7831, 2005.

[49] T. Kotnik and D. Miklavčič, "Theoretical evaluation of the distributed power dissipation in biological cells exposed to electric fields," *Bioelectromagnetics*, vol. 21, pp. 385–394, 2000.

[50] T. Sun, S. Gawad, V. Baernabini, N. G. Green, and H. Morgan, "Broadband single cell impedance spectroscopy using maximum length sequences: Theoretical analysis and practical considerations," *Measurement Science and Technology*, vol. 18, pp. 2859–2868, 2007.

[51] K. Asami, "Characterization of biological cells by dielectric spectroscopy," *Journal of Non-Crystalline Solids*, vol. 305, no. 1-3, pp. 268–277, 2002.

[52] E. C. Fear and M. A. Stuchly, "Modeling assemblies of biological cells exposed to electric fields," *IEEE Transactions on Biomedical Engineering*, vol. 45, pp. 1259–1271, 1998.

[53] E. Gheorghiu, C. Balut, and M. Gheorghiu, "Dielectric behaviour of gap junction connected cells: A microscopic approach," *Physics in Medicine and Biology*, vol. 47, pp. 341–348, 2002.

[54] I. Ermolina, Y. Poleyava, and Y. Feldman, "Analysis of dielectric spectra of eukaryotic cells by computer modeling," *Biophysics Letters*, vol. 29, pp. 141–145, 2000.

[55] J. Fan, G. Yu, J. Tan, and S. Tan, "Modeling and analysis of biological cells in dram implementation," in *Behavioral Modeling and Simulation Workshop, 2007. BMAS 2007. IEEE International*. IEEE, 2007, pp. 90–93.

[56] L. Liu and S. Cleary, "Absorbed energy distribution from radiofrequency electromagnetic radiation in a mammalian cell model: Effect of membrane-bound water," *Bioelectromagnetics*, vol. 16, no. 3, pp. 160–171, 1995.

[57] K. Asami, T. Hanai, and N. Koizumi, "Dielectric analysis of escherichia coli suspensions in the light of the theory of interfacial polarization," *Biophysical Journal*, vol. 31, no. 2, pp. 215–228, 1980.

[58] W. Bai, K. S. Zhao, and K. Asami, "Dielectric properties of *E. coli* cell as simulated by the three-shell spheroidal model," *Biophysical Chemistry*, vol. 122, pp. 136–142, 2006.

[59] V. Raicu, T. Saibara, H. Enzan, and A. Irimaijiri, "Dielectric properties of rat liver in vivo: Analysis by modeling hepatocytes in the tissue architecture," *Bioelectrochemistry and Bioenergetics*, vol. 47, pp. 333–342, 1998.

[60] F. Bordi, C. Cametti, A. Rosi, and A. Calcabrini, "Frequency domain electrical conductivity measurements of the passive electrical properties of human lymphocytes," *Biochimica et Biophysica Acta (BBA)-Biomembranes*, vol. 1153, no. 1, pp. 77–88, 1993.

[61] A. Sihvola and I. Lindell, "Polarizability and effective permittivity of layered and continuously inhomogeneous dielectric ellipsoids," *Journal of Electromagnetic Waves and Applications*, vol. 4, no. 1, pp. 1–26, 1990.

[62] D. A. G. Bruggeman, "Berechnung verschiedener physikalischer Konstanten von heterogenen Substanzen. III. Die elastischen Konstanten der quasiisotropen mischkörper aus isotropen substanzen," *Annalen der Physik*, vol. 421, no. 2, pp. 160–178, 1937.

[63] T. Hanai, "Theory of the dielectric dispersion due to the interfacial polarization and its application to emulsions," *Colloid & Polymer Science*, vol. 171, no. 1, pp. 23–31, 1960.

[64] L. D. Landau, E. M. Lifshitz, and L. P. Pitaevskii, "Electrodynamics of continuous media, vol. 8," *Course of theoretical physics*, vol. 38, p. 46, 1960.

[65] H. Looyenga, "Dielectric constants of heterogeneous mixtures," *Physica*, vol. 31, no. 3, pp. 401–406, 1965.

[66] D. Dube, "Study of Landau-Lifshitz-Looyenga's formula for dielectric correlation between powder and bulk," *Journal of Physics D: Applied Physics*, vol. 3, p. 1648, 1970.

[67] E. Tuncer, "Geometrical description in binary composites and spectral density representation," *Materials*, vol. 3, pp. 585–613, 2010.

[68] J. Lei, J. T. K. Wan, K. W. Yu, and H. Sun, "First-principle approach to dielectric behaviour of nonspherical cell suspensions," *Physical Review E*, vol. 64, pp. 012 903–1–012 903–4, 2001.

[69] A. V. Goncharenko and Y.-C. Chang, "Effective dielectric properties of biological cells: Generalization of the spectral density function approach," *Journal of Physical Chemistry B*, vol. 113, pp. 9924–9931, 2009.

[70] E. Tuncer, "Extracting the spectral density function of a binary composite without a priori assumptions," *Physical Review B*, vol. 71, no. 1, p. 12101, 2005.

[71] C. Prodan and E. Prodan, "The dielectric behaviour of living cell suspensions," *Journal of Physics D: Applied Physics*, vol. 32, p. 335, 1999.

[72] E. Tuncer, "The Landau-Lifshitz/Looyenga dielectric mixture expression and its self-similar fractal nature," *Arxiv preprint cond-mat/0503750*, vol. x, p. x, 2005.

[73] A. Goncharenko, "Spectral density function approach to homogenization of binary mixtures," *Chemical Physics Letters*, vol. 400, no. 4-6, pp. 462–468, 2004.

[74] C. Engström, "Effective properties of heterogeneous materials with applications in electromagnetics," Ph.D. dissertation, Lund, 2006.

[75] M. Nakamura and M. Mizuno, "Two-dimensional site percolation and conduction," *Journal of Physics C: Solid State Physics*, vol. 15, p. 5979, 1982.

[76] E. Kira, E. J. Neves, and R. H. Schonmann, "Percolation in a Voronoi competition-growth model," *Journal of Statistical Physics*, vol. 92, no. 5, pp. 755–764, 1998.

[77] S. W. Smye, C. J. Evans, M. P. Robinson, and B. D. Sleeman, "Modelling the electrical properties as a porous medium," *Physics in Medicine and Biology*, vol. 52, pp. 7007–7022, 2007.

[78] S. Newman, G. Forgacs, B. Hinner, C. Maier, and E. Sackmann, "Phase transformations in a model mesenchymal tissue," *Physical Biology*, vol. 1, p. 100, 2004.

[79] R. Merks, S. Newman, and J. Glazier, "Cell-oriented modeling of in vitro capillary development," *Cellular Automata*, vol. xx, pp. 425–434, 2004.

[80] S. Capuani, T. Gili, C. Cametti, B. Maraviglia, M. Colasanti, M. Muolo, and G. Venturini, "Radiowave dielectric investigation of boron compounds distribution in cultured tumour cells: Relevance to boron neutron capture therapy," *Chemical Physics Letters*, vol. 360, no. 1-2, pp. 79–84, 2002.

[81] M. Simeonova and J. Gimsa, "The influence of the molecular structure of lipid membranes on the electric field distribution and energy absorption," *Bioelectromagnetics*, vol. 27, no. 8, pp. 652–666, 2006.

[82] F. Bordi, C. Cametti, and T. Gili, "Dielectric spectroscopy of erythrocyte cell suspensions. A comparison between Looyenga and Maxwell-Wagner-Hanai effective medium theory formulations," *Journal of Non-Crystalline Solids*, vol. 305, pp. 278–284, 2002.

[83] E. Rey and D. Jongmans, "A 2D numerical study of the effect of particle shape and orientation on resistivity in shallow formations," *Geophysics*, vol. 72, no. 1, pp. F9–F17, 2007. [Online]. Available: http://link.aip.org/link/?GPY/72/F9/1

[84] A. Di Biasio and C. Cametti, "Effect of shape on the dielectric properties of biological cell suspensions," *Bioelectrochemistry*, vol. 71, pp. 149–156, 2007.

[85] A. Di Biasio, L. Abmbrosone, and C. Cametti, "Numerical simulation of dielectric spectra of aqueous suspensions of non-spheroidal differently shaped biological cells," *Journal of Physics D: Applied Physics*, vol. 42, pp. 1–9, 2009.

[86] J. L. Sebastián, S. Muñoz, M. Sancho, and J. M. Miranda, "Analysis of the influence of the cell geometry, orientation and cell proximity effects on the electric field distribution from direct RF exposure," *Physics in Medicine and Biology*, vol. 46, pp. 213–225, 2001.

[87] J. L. Sebastián, S. Muñoz, M. Sancho, G. Álvarez, and J. M. Miranda, "Electric field distribution and energy absorption in anisotropic and dispersive red blood cells," *Physics in Medicine and Biology*, vol. 52, pp. 6831–6847, 2007.

[88] M.-A. Golombeck, C. Riedel, and O. Dössel, "Calculation of the dielectric properties of biological tissue using simple models of cell patches," *Biomedical Technology*, vol. 47, pp. 253–256, 2002.

[89] A. Donev, I. Cisse, D. Sachs, E. A. Variano, F. H. Stillinger, R. Connelly, S. Torquato, and P. M. Chaikin, "Improving the Density of Jammed Disordered Packings Using Ellipsoids," *Science*, vol. 303, pp. 990–993, 2004.

[90] A. J. P. Klein-Szanto, "Clear and dark basal keratinocytes in human epidermis," *Journal of Cutaneous Pathology*, vol. 4, pp. 275–280, 1977.

[91] Y. Katsumoto, Y. Hayashi, I. Oshige, S. Omori, N. Kishii, A. Yasuda, and K. Asami, "Dielectric Cytometry with Three-Dimensional Cellular Modeling," *Biophysical Journal*, vol. 95, pp. 3043–3047, 2008.

[92] K. Asami, "Dielectric dispersion in biological cells of complex geometry simulated by the three-dimensional finite difference method," *Journal of Physics D: Applied Physics*, vol. 39, pp. 492–499, 2006.

[93] S. Muñoz San Martín, J. L. Sebastián, M. Sancho, and G. Álvarez, "Modeling normal and altered human erythrocyte shapes by a new parametric equation: Application to the calculation of induced transmembrane potentials," *Bioelectromagnetics*, vol. 27, pp. 521–527, 2006.

[94] D. O. H. Suzuki, A. Ramos, and J. L. B. Marques, "Modeling environment for numerical simulation of applied electric fields on biological cells," *Electromagnetic Biology and Medicine*, vol. 26, pp. 239–250, 2007.

[95] E. Tuncer, S. M. Gubanski, and B. Nettelblad, "Dielectric relaxation in dielectric mixtures: Application of the finite element method and its comparison with dielectric mixture formulas," *Journal of Applied Physics*, vol. 89(12), pp. 8092–8100, 2001.

[96] I. Krakovskỳ and V. Myroshnychenko, "Modeling dielectric properties of composites by finite-element method," *Journal of Applied Physics*, vol. 92, p. 6743, 2002.

[97] V. N. Kaliakin, *Introduction to Approximate Solution Techniques, Numerical Modeling and Finite Element Methods*. Marcel Dekker, Inc., 2002.

[98] M. Frehner, S. M. Schmalholz, E. H. Saenger, and H. Steeb, "Comparison of finite difference and finite element methods for simulating two-dimensional scattering of elastic waves," *Physics of the Earth and Planetary Interiors*, vol. 171, pp. 112–121, 2008.

[99] M. Micic, N. Klymyshyn, Y. Suh, and H. Lu, "Finite element method simulation of the field distribution for AFM tip-enhanced surface-enhanced Raman scanning microscopy," *Journal of Physical Chemistry B*, vol. 107, no. 7, pp. 1574–1584, 2003.

[100] T. Grosges, A. Vial, and D. Barchiesi, "Models of near-field spectroscopic studies: comparison between finite-element and finite-difference methods," *Optics Express*, vol. 13, pp. 8483–8497, 2005.

[101] B. Van de Wiele, A. Manzin, L. Dupré, F. Olyslager, O. Bottauscio, and M. Chiampi, "Comparison of finite-difference and finite-element schemes for magnetization processes in 3-D Particles," *IEEE Transactions on Magnetics*, vol. 45, pp. 1614–161, 2009.

[102] S. Huclova, D. Erni, and J. Fröhlich, "Modelling effective dielectric properties of materials containing diverse types of biological cells," *Journal of Physics D: Applied Physics*, vol. 43, p. 365405, 2010.

[103] K. Khairy, J. Foo, and J. Howard, "Shapes of Red Blood Cells: Comparison of 3D Confocal Images with the Bilayer-Couple Model," *Cellular and Molecular Bioengineering*, vol. 1, pp. 173–181, 2008.

[104] K. Khairy and J. Howard, "Spherical harmonics-based parametric deconvolution of 3D surface images using bending energy minimization," *Medical Image Ananlysis*, vol. 12, pp. 217–227, 2008.

[105] J. Gielis, "A generic geometric transformation that unifies a wide range of natural and abstract shapes," *American Journal of Botany*, vol. 90(3), pp. 333–338, 2003.

[106] J. Gielis, B. Beirinckx, and E. Bastiaens, "Superquadrics with Rational and Irrational Symmetry," in *SM'03*, 2003.

[107] [Online]. Available: http://pathology.mc.duke.edu/research/Histo_course/whitefat.jpg

[108] [Online]. Available: http://www.technion.ac.il/~mdcourse/274203/lect2.html

[109] [Online]. Available: http://www.canyons.edu/Departments/BIO/107Pig/histology.html

[110] [Online]. Available: http://www.mhhe.com/biosci/ap/histology_mh/neurons.jpg

[111] G. H. W. Lim, M. Wortis, and R. Mukhopadhyay, "Stomatocyte-discocyte-echinocyte sequence of the human red blood cell: Evidence for the bilayer-couple hypothesis from membrane mechanics," *PNAS*, vol. 99(26), pp. 16 766–16 769, 2002.

[112] [Online]. Available: http://history.nasa.gov/SP-368/s3ch3.htm

[113] N. Amenta, S. Choi, and R. K. Kolluri, "The Power Crust," in *6th ACM Symposium on Solid Modeling*, 2001.

[114] *COMSOL Matlab Interface Guide, Version 3.5a*, 2008.

[115] L. Zhang, H. Tan, and Z. Liu, "Rational approximation of offset surfaces by using bivariante s-power basis," *Second workshop on digital media and its application in Museum & Heritage*, vol. -, pp. 152–157, 2007.

[116] N. Amenta, M. Bern, and M. Kamvysselis, "A New Voronoi-Based Surface Reconstruction Algorithm," in *Siggraph '98*, 1998.

[117] C.-C. Kuo and H.-T. Yau, "Reconstruction of Virtual Parts from Unorganized Scanned Data for Automated Dimensional Inspection," *Transactions of the ASME*, vol. 3, pp. 76–86, 2003.

[118] A. Rodríguez, J. M. Espadero, D. López, and L. Pastor, "Delaunay Surface Reconstruction from Scattered Points," *Lecture notes in computer science*, vol. 1953, pp. 272–283, 2000.

[119] H. Enderling, A. Anderson, M. Chaplain, and G. Rowe, "Visualisation of the numerical solution of partial differential equation systems in three space dimensions and its importance for mathematical models in biology," *Mathematical Biosciences and Engineering*, vol. 3, no. 4, p. 571, 2006.

[120] E. Haber and S. Heldmann, "An octree multigrid method for quasi-static Maxwell's equations with highly discontinuous coefficients," *Journal of Computational Physics*, vol. 223, no. 2, pp. 783–796, 2007.

[121] W. Liu, Y. Liu, D. Farrell, L. Zhang, X. Wang, Y. Fukui, N. Patankar, Y. Zhang, C. Bajaj, J. Lee, *et al.*, "Immersed finite element method and its applications to biological systems," *Computer Methods in Applied Mechanics and Engineering*, vol. 195, no. 13-16, pp. 1722–1749, 2006.

[122] V. Sukhorukov, G. Meedt, M. Kürschner, and U. Zimmermann, "A single-shell model for biological cells extended to account for the dielectric anisotropy of the plasma membrane," *Journal of Electrostatics*, vol. 50, no. 3, pp. 191–204, 2001.

[123] H. Mebatsion, P. Verboven, Q. Ho, B. Verlinden, and B. Nicolaī, "Modelling fruit (micro) structures, why and how?" *Trends in Food Science & Technology*, vol. 19, no. 2, pp. 59–66, 2008.

[124] P. Ghysels, G. Samaey, B. Tijskens, P. Van Liedekerke, H. Ramon, and D. Roose, "Multi-scale simulation of plant tissue deformation using a model for individual cell mechanics," *Physical Biology*, vol. 6, p. 016009, 2009.

[125] H. Banks, "A probabilistic multiscale approach to hysteresis in shear wave propagation in biotissue," DTIC Document, Tech. Rep., 2004.

[126] M. J. Peters, M. Hendriks, and J. G. Stinstra, "The passive dc conductivity of human tissues described by cells in solution," *Bioelectrochemistry*, vol. 53, no. 2, pp. 155 – 160, 2001.

[127] S. Huclova, J. Fröhlich, L. Falco, F. Dewarrat, M. S. Talary, and R. Vahldieck, "Validation of skin models in the MHz region," in *IEEE Engineering in Medicine and Biology Society Conference, Minneapolis*, 2009.

[128] M. Lazebnik, D. Popovic, L. McCartney, C. Watkins, M. Lindstrom, J. Harter, S. Sewall, T. Ogilvie, A. Magliocco, T. Breslin, *et al.*, "A large-scale study of the ultrawideband microwave dielectric properties of normal, benign and malignant breast tissues obtained from cancer surgeries," *Physics in Medicine and Biology*, vol. 52, p. 6093, 2007.

[129] L. Hagströmer, N. Kuzmina, J. Lapins, T. Talme, and L. Emtestam, "Biophysical assessment of atopic dermatitis skin and effects of a moisturizer," *Clinical and experimental dermatology*, vol. 31, no. 2, pp. 272–277, 2006.

[130] S. Naito, M. Hoshi, and S. Yagihara, "Microwave dielectric analysis of human stratum corneum in vivo," *Biochimica et Biophysica Acta*, vol. 1381, pp. 293–304, 1998.

[131] Ø. Martinsen, S. Grimnes, and E. Haug, "Measuring depth depends on frequency in electrical skin impedance measurements," *Skin Research and Technology*, vol. 5, pp. 179–181, 1999.

[132] E. Alanen, T. Lahtinen, and J. Nuutinen, "Measurement of dielectric properties of subcutaneous fat with open-ended coaxial probes," *Physics in Medicine and Biology*, vol. 43, pp. 475–485, 1999.

[133] H. Benjamin, S. Bhansali, S. Hoath, W. Pickens, and R. Smallwood, "A planar micro-sensor for bio-impedance measurements," *Sensors and Actuators B: Chemical*, vol. 111, pp. 430–435, 2005.

[134] E. Somersalo, M. Cheney, D. Isaacson, and E. Isaacson, "Layer stripping: A direct numerical method for impedance imaging," *Inverse Problems*, vol. 7, pp. 899–926, 1991.

[135] H. Banks and N. Gibson, "Electromagnetic inverse problems involving distributions of dielectric mechanisms and parameters, crsctr05-29, august, 2005," *Quarterly of Applied Mathematics*, vol. 64, pp. 749–795, 2006.

[136] R. Irastorza, M. Mayosky, and F. Vericat, "Noninvasive measurement of dielectric properties in layered structure: A system identification approach," *Measurement*, vol. 42, no. 2, pp. 214–224, 2009.

[137] T. Lahtinen, J. Nuutinen, and E. Alanen, "Dielectric properties of the skin," *Physics in Medicine and Biology*, vol. 42, p. 1471, 1997.

[138] E. Alanen, T. Lahtinen, and J. Nuutinen, "Penetration of electromagnetic fields of an open-ended coaxial probe between 1 MHz and 1 GHz in dielectric skin measurements," *Physics in Medicine and Biology*, vol. 44, pp. N169–N176, 1999.

[139] I. Shay and M. Zahn, "Cylindrical geometry electroquasistatic dielectrometry sensors," in *Annual Report Conference on Electrical Insulation and Dielectric Phenomena*, 2002.

[140] P. von Guggenberg and M. Zaretsky, "Estimation of one-dimensional complex-permittivity profiles: A feasibility study," *Journal of Electrostatics*, vol. 34, pp. 263–277, 1995.

[141] Y. Sheiretov and M. Zahn, "Modeling of spatially periodic dielectric sensors in the presence of a top ground plane bounding the test dielectric," *IEEE Transactions on Dielectric and Electrical Insulation*, vol. 12, pp. 993–1004, 2005.

[142] A. Mamishev, K. Sundara-Rajan, F. Yang, Y. Du, and M. Zahn, "Interdigital sensors and transducers," *Proceedings of the IEEE*, vol. 92, pp. 808–845, 2004.

[143] N. Kidner, Z. Homrighaus, T. Mason, and E. Garboczi, "Modeling interdigital electrode structures for the dielectric characterization of electroceramic thin films," *Thin Solid Films*, vol. 496, no. 2, pp. 539–545, 2006.

[144] A. Mamishev, B. Lesieutre, and M. Zahn, "Optimization of multi-wavelength interdigital dielectrometry instrumentation," *IEEE Transactions on Dielectrics and Electrical Insulation*, vol. 5, pp. 408–420, 1998.

[145] S. Mukhopadhyay, "A novel planar mesh-type microelectromagnetic sensor. Part I. Model formulation," *IEEE Sensors Journal*, vol. 4, no. 3, pp. 301–307, 2004.

[146] ——, "A novel planar mesh-type microelectromagnetic sensor. Part II. Estimation of system properties," *IEEE Sensors Journal*, vol. 4, no. 3, pp. 308–312, 2004.

[147] B. R. Midmore, R. J. Hunter, and R. W. O'Brien, "The Dielectric Response of Concentrated Lattices," *Journal of Colloid and Interface Science*, vol. 120(1), pp. 210–217, 1987.

[148] C. Gabriel, E. Grant, and I. Young, "Use of time domain spectroscopy for measuring dielectric properties with a coaxial probe," *Journal of Physics E: Scientific Instruments*, vol. 19, p. 843, 1986.

[149] E. Alanen, T. Lahtinen, and J. Nuutinen, "Variational formulation of open-ended coaxial line in contact with layered biological medium," *IEEE Transactions on Biomedical Engineering*, vol. 45, pp. 1241–1248, 1998.

[150] [Online]. Available: http://www.cheme.cmu.edu/people/faculty/jbmiller.htm

[151] R. Igreja and C. Dias, "Analytical evaluation of the interdigital electrodes capacitance for a multi-layered structure," *Sensors and Actuators A: Physical*, vol. 112, no. 2-3, pp. 291–301, 2004.

[152] F. Dewarrat, L. Falco, A. Caduff, M. Talary, Y. Feldman, and A. Puzenko, "Measurement and simulation of conductive dielectric two-layer materials with a multiple electrodes sensor," *Dielectrics and Electrical Insulation, IEEE Transactions on*, vol. 15, no. 5, pp. 1406–1414, 2008.

[153] J. Mäurer, H. Requardt, B. Sander, F. D. Knollmann, A.-J. Lemke, T. J. Vogl, and R. Felix, "Applications of specialized coils for high-resolution MRI on a whole-body scanner," *Magnetic Resonance Materials in Physics, Biology and Medicine*, vol. 4, pp. 27–33, 1996.

[154] L. Li, N. Ismail, L. Taylor, and C. Davis, "Flanged coaxial microwave probes for measuring thin moisture layers," *Biomedical Engineering, IEEE Transactions on*, vol. 39, no. 1, pp. 49–57, 2002.

[155] P. De Langhe, K. Blomme, L. Martens, and D. De Zutter, "Measurement of low-permittivity materials based on a spectral-domain analysis for the open-ended coaxial probe," *Instrumentation and Measurement, IEEE Transactions on*, vol. 42, no. 5, pp. 879–886, 1993.

[156] C. Gabriel, T. Y. A. Chan, and E. H. Grant, "Admittance models for open ended coaxial probes and their place in dielectric spectroscopy," *Physics in Medicine and Biology*, vol. 39, pp. 2271–2293, 1994.

[157] D. Hagl, D. Popovic, S. Hagness, J. Booske, and M. Okoniewski, "Sensing volume of open-ended coaxial probes for dielectric characterization of breast tissue at microwave frequencies," *Microwave Theory and Techniques, IEEE Transactions on*, vol. 51, no. 4, pp. 1194–1206, 2003.

[158] G. Panariello, L. Verolino, and G. Vitolo, "Efficient and accurate full-wave analysis of the open-ended coaxial cable," *Microwave Theory and Techniques, IEEE Transactions on*, vol. 49, no. 7, pp. 1304–1309, 2002.

[159] N. Stevens and L. Martens, "Dimensioning of open-ended coaxial probes for the dielectric characterization of thin-layered materials," in *Instrumentation and Measurement Technology Conference, 2001. IMTC 2001. Proceedings of the 18th IEEE*, vol. 2. IEEE, 2002, pp. 1288–1290.

[160] J. Baker-Jarvis, M. Janezic, P. Domich, and R. Geyer, "Analysis of an open-ended coaxial probe with lift-off for nondestructive testing," *Instrumentation and Measurement, IEEE Transactions on*, vol. 43, no. 5, pp. 711–718, 2002.

[161] D. K. Misra, "A quasi-static analysis of open-ended coaxial lines," *Microwave Theory and Techniques, IEEE Transactions on*, vol. 35, no. 10, pp. 925–928, 1987.

[162] H. Levine and C. Papas, "Theory of the circular diffraction antenna," *Journal of Applied Physics*, vol. 22, no. 1, pp. 29–43, 1951.

[163] J. Grant, R. N. Clarke, G. T. Symm, and N. M. Spyrou, "A critical study of the open-ended coaxial line sensor technique for rf and microwave complex permittivity measurements," *Journal of Physics E: Scientific Instruments*, vol. 22, p. 757, 1989.

[164] B. Xiaobei, S. Larson, A. Zyuzin, and A. Mamishev, "Design principles for multichannel fringing electric field sensors," *IEEE Sensors Journal*, vol. 6, pp. 434–440, 2006.

[165] Ø. G. Martinsen, S. Grimnes, and O. Sveen, "Dielectric properties of some keratinised tissues. Part 1: Stratum corneum and nail in situ," *Medical & Biological Engineering & Computing*, vol. 35, pp. 172–176, 1997.

[166] L. Petäjä, J. Nuutinen, A. Uusaro, T. Lahtinen, and E. Ruokonen, "Dielectric constant of skin and subcutaneous fat to assess fluid changes after cardiac surgery," *Physiological measurement*, vol. 24, p. 383, 2003.

[167] T. Tatara and K. Tsuzaki, "Derivation of extracellular fluid volume fraction and equivalent dielectric constant of the cell membrane from dielectric properties of the human body. Part 2: A preliminary study for tracking the progression of surgical tissue injury," *Medical & Biological Engineering & Computing*, vol. 38, no. 4, pp. 384–389, 2000.

[168] V. Raicu, T. Saibara, and A. Irimaijiri, "Dielectric properties of rat liver in vivo: A nonivasive approach using an open-ended coaxial probe at audio/radio frequencies," *Bioelectrochemistry and Bioenergetics*, vol. 47, pp. 325–332, 1998.

[169] S. Kun and R. Peura, "Effects of sample geometry and electrode configuration on measured electrical resistivity of skeletal muscle," *IEEE Transactions Biomedical Engineering*, vol. 47, no. 2, pp. 163–169, 2002.

[170] [Online]. Available: http://adhesivos-industriales.com/SID-597D1971-64F57F1B/innovation/the-structure-of-human-skin-21742.htm

[171] L. Chrit, P. Bastien, G. Sockalingum, D. Batisse, F. Leroy, M. Manfait, and C. Hadjur, "An *in vivo* randomized study of human skin moisturization by a new confocal Raman fiber-optic microprobe: Assessment of a glycerol-based hydration cream," *Skin Pharmacology and Physiology*, vol. 19, no. 4, pp. 207–215, 2006.

[172] P. Wertz, "Stratum corneum lipids and water," *Exogenous Dermatology*, vol. 3, no. 2, pp. 53–56, 2005.

[173] L. Chen, G. Lian, and L. Han, "Use of bricks and mortar model to predict transdermal permeation: Model development and initial validation," *Industrial & Engineering Chemistry Research*, vol. 47, no. 17, pp. 6465–6472, 2008.

[174] N. Kashibuchi, Y. Hirai, K. O'Goshi, and H. Tagami, "Three-dimensional analyses of individual corneocytes with atomic force microscope; Morphological changes related to age, location and to the pathologic skin conditions," *Skin Research and Technology*, vol. 8, pp. 203–211, 2002.

[175] H. Frasch and A. Barbero, "Steady-state flux and lag time in the stratum corneum lipid pathway: Results from finite element models," *Journal of pharmaceutical sciences*, vol. 92, no. 11, pp. 2196–2207, 2003.

[176] R. Potts and M. Francoeur, "The influence of stratum corneum morphology on water permeability," *Journal of Investigative Dermatology*, vol. 96, no. 4, pp. 495–499, 1991.

[177] J. Bouwstra, A. de Graaff, G. Gooris, J. Nijsse, J. Wiechers, and A. van Aelst, "Water distribution and related morphology in human stratum corneum at different hydration levels," *Journal of Investigative Dermatology*, vol. 120, no. 5, pp. 750–758, 2003.

[178] N. Nakagawa, S. Sakai, M. Matsumoto, K. Yamada, M. Nagano, T. Yuki, Y. Sumida, and H. Uchiwa, "Relationship between NMF (lactate and potassium) content and the physical properties of the stratum corneum in healthy subjects," *Journal of Investigative Dermatology*, vol. 122, no. 3, pp. 755–763, 2004.

[179] A. Lee, J. King, and T. Rogers, "A multiple-pathway model for the diffusion of drugs in skin," *Mathematical Medicine and Biology*, vol. 13, no. 2, p. 127, 1996.

[180] M. Mogensen, H. Morsy, L. Thrane, and G. Jemec, "Morphology and epidermal thickness of normal skin imaged by optical coherence tomography," *Dermatology*, vol. 217, no. 1, pp. 14–20, 2008.

[181] S. Nouveau-Richard, M. Monot, P. Bastien, and O. De Lacharriere, "In vivo epidermal thickness measurement: ultrasound vs. confocal imaging," *Skin Research and Technology*, vol. 10, no. 2, pp. 136–140, 2004.

[182] R. Prum and R. Torres, "Structural colouration of mammalian skin: Convergent evolution of coherently scattering dermal collagen arrays," *Journal of Experimental Biology*, vol. 207, no. 12, p. 2157, 2004.

[183] I. V. Meglinski and S. J. Matcher, "Quantitative assessment of skin layers absorption and skin reflectance spectra simulation in the visible and near-infrared spectral regions," *Physiological Measurement*, vol. 23, pp. 741–753, 2002.

[184] G. Novotny and C. Gnoth, "Variability of fibroblast morphology in vivo: A silver impregnation study on human digital dermis and subcutis." *Journal of Anatomy*, vol. 177, p. 195, 1991.

[185] F. Silver, J. Freeman, and D. DeVore, "Viscoelastic properties of human skin and processed dermis," *Skin Research and Technology*, vol. 7, no. 1, pp. 18–23, 2001.

[186] J. Després, R. Savard, A. Tremblay, and C. Bouchard, "Adipocyte diameter and lipolytic activity in marathon runners: Relationship with body fatness," *European Journal of Applied Physiology and Occupational Physiology*, vol. 51, no. 2, pp. 223–230, 1983.

[187] A. Albright and J. Stern, "Adipose tissue," *Encyclopedia of Sports Medicine and Science, TD Fahey (Editor). Internet Society for Sport Science: http://sprtsci.org*, vol. 7, p. x, 1998.

[188] C. Gomillion and K. Burg, "Stem cells and adipose tissue engineering," *Biomaterials*, vol. 27, no. 36, pp. 6052–6063, 2006.

[189] C. Gabriel, S. Gabriel, and E. Corhout, "The dielectric properties of biological tissues: I. Literature survey," *Physics in Medicine and Biology*, vol. 39, pp. 2231–2249, 1996.

[190] M. Abdel-Naser, M. Abdallah, H. de Almeida Jr, and U. Wollina, "Human skin cell culture and its impact on dermatology," *Egyptian Dermatology Online Journal*, vol. 1, no. 2, p. 2, 2005.

[191] S. R. Smith and K. R. Foster, "Dielectric properties of low-water-content tissues," *Physics in Medicine and Biology*, vol. 30(9), pp. 965–973, 1985.

[192] M. Simeononva, D. Wachner, and J. Gimsa, "Cellular absorption of electric field energy: Influence of molecular properties of the cytoplasm," *Bioelectrochemistry*, vol. 56, pp. 215–218, 2002.

[193] K. Kretsos and G. Kasting, "A geometrical model of dermal capillary clearance," *Mathematical Biosciences*, vol. 208, no. 2, pp. 430–453, 2007.

[194] L. Vitellarq-Zuccarello, K. Dyne, and G. Cetta, "Biochemical, Morphological and Stereological Study of the Dermis in Three Members of A Large Family with Type Iv Ehlers-Danlos Syndrome," *Connective Tissue Research*, vol. 23, no. 1, pp. 1–17, 1989.

[195] J. A. Cowen, R. E. Imhof, and P. Xiao, "Opto-thermal measurement of stratum corneum renewal time," *Analytical Sciences*, vol. 17, pp. 353–356, 2001.

[196] M. Egawa, T. Hirao, and M. Takahashi, "In vivo estimation of stratum corneum thickness from water concentration profiles obtained with raman spectroscopy," *Acta Dermato-Venerologica*, vol. 87, pp. 4–8, 2007.

[197] T. L. Moore, M. Lunt, B. McManus, M. E. Anderson, and A. L. Herrick, "Seventeen-point dermal ultrasound scoring system - a reliable measure of skin thickness in patients with systemic sclerosis," *Rheumatology*, vol. 42, pp. 1559–1563, 2003.

[198] D. Miklavčič, N. Pavšelj, and F. X. Hart, *Wiley Encyclopedia of Biomedical Engineering*. John Wiley & Sons, Inc., 2006, ch. Electric Properties of Tissues, pp. 1–12.

[199] T. Yamamoto and Y. Yamamoto, "Electrical properties of the epidermal stratum corneum," *Medical & Biological Engineering*, vol. 14(2), pp. 151–158, 1976.

[200] C. Jones, "Image analysis of fungal biostructure by fractal and wavelet techniques," Ph.D. dissertation, Swinburne University of Technology, 1997.

[201] V. Raicu, T. Sato, and G. Raicu, "Non-Debye dielectric relaxation in biological structures arises from their fractal nature," *Physical Review E*, vol. 64, pp. 021 916–1–021 916–10, 2001.

[202] L. A. Dissado, "A fractal interpretation of the dielectric response of animal tissues," *Physics in Medicine and Biology*, vol. 35, pp. 1487–1503, 1990.

[203] N. P. Smith, D. P. Nickerson, E. J. Crampin, and P. J. Hunter, "Multiscale computational modelling of the heart," *Acta Numerica*, vol. 13, pp. 371–431, 2004.

[204] J. Weaver, T. Vaughan, and G. Martin, "Biological effects due to weak electric and magnetic fields: the temperature variation threshold," *Biophysical journal*, vol. 76, no. 6, pp. 3026–3030, 1999.

[205] L. Loew and J. Schaff, "The virtual cell: A software environment for computational cell biology," *Trends in Biotechnology*, vol. 19, no. 10, pp. 401–406, 2001.

[206] A. Caduff, E. Hirt, Y. Feldman, Z. Ali, and L. Heinemann, "First human experiments with a novel non-invasive, non-optical continuous glucose monitoring system," *Biosensors & Bioelectronics*, vol. 19, pp. 209–217, 2003.

[207] K. Larin, M. Motamedi, T. Ashitkov, and R. Esenaliev, "Specificity of noninvasive blood glucose sensing using optical coherence tomography technique: A pilot study," *Physics in Medicine and Biology*, vol. 48, p. 1371, 2003.

[208] R. Kuranov, V. Sapozhnikova, D. Prough, I. Cicenaite, and R. Esenaliev, "In vivo study of glucose-induced changes in skin properties assessed with optical coherence tomography," *Physics in Medicine and Biology*, vol. 51, p. 3885, 2006.

[209] W. Groenendaal, K. Schmidt, G. von Basum, N. van Riel, and P. Hilbers, "Modeling glucose and water dynamics in human skin," *Diabetes Technology & Therapeutics*, vol. 10, no. 4, pp. 283–293, 2008.

[210] H. Athenstaedt, H. Claussen, and D. Schaper, "Epidermis of human skin: pyroelectric and piezoelectric sensor layer," *Science*, vol. 216, no. 4549, p. 1018, 1982.

[211] D. De Rossi, C. Domenici, and P. Pastacaldi, "Piezoelectric properties of dry human skin," *Electrical Insulation, IEEE Transactions on*, vol. -, no. 3, pp. 511–517, 1986.

[212] J. J. Guzmán and C. Schiff, "A preliminary study for a tetrahedron formation: Quality factors and visualization," American Institute of Aeronautics and Astronautics, Tech. Rep., 2000.

[213] [Online]. Available: http://www.mathworks.com/matlabcentral/fileexchange/21512-kd-tree-for-matlab

[214] C. Boned and J. Peyrelasse, "Some comments on the complex permittivity of ellipsoids dispersed in continuum media," *Journal of Physics D: Applied Physics*, vol. 16, p. 1777, 1983.

[215] K. Hollaus, B. Weiss, C. Magele, and H. Hutten, "Geometric multigrid to accelerate the solution of the quasi-static electric field problem by tetrahedral finite elements," *Physiological Measurement*, vol. 25, p. 169, 2004.

# Acknowledgments

The financial means for this thesis were provided by the Comission for Technology and Innovation (KTI/CTI), Bern, Solianis Monitoring AG, Zurich and the ETH Zurich. However, the realization of the presented work would not have been possible without the assistance of many people.

My deepest thank goes to first and foremost to my supervisor Jürg Fröhlich for his guidance and encouragement. Being a gifted scientist he imparted knowledge while as a great open-minded character he provided me with invaluable advice on a personal level. I doubt whether I would have finished my degree without his support.
Second, I want to express my sincere appreciation for Daniel Erni from the University of Duisburg−Essen, Germany, for co-examinating this thesis. In particular I would like to thank for the fruitful collaboration, which was a great pleasure. He substantially improved the quality of my work with his sharp-minded and critical comments.
Third, I extend my thanks to Rüdiger Vahldieck and Christian Hafner who gave me the necessary institutional support and freedom. In addition, I would like to acknowledge Christian Hafner for overtaking the examination.
As computational resources were indispensable for this work I would like to thank Aldo Rossi, Ray Ballisti and Patrick Leidenberger for maintaining the IT infrastructure. Likewise, I thank Hansruedi Benedickter for his valuable assistance with measurements.
My colleagues of Christian Hafner's group have significantly contributed to my professional and personal time at the Laboratory for Electromagnetic Fields and Microwave Electronics. I am particularly grateful having met Dirk Baumann and Christoph Böcklin. They enriched this work with intellectual input as with active participation in my experiments. I was also fortunate to share enjoyable moments beyond office doors with them − be it on bicycles, rowing machines or during lively discussions on whatsoever topics.
Furthermore, I could not have imagined having more agreeable office mates than Andreas Alt and Haifeng Sun from the Millimeter-Wave Electronics group. In particular, Andreas has been a major support during the past years. Endlessly patient, he provided advice in seemingly hopeless situations while always(!) spreading a positive attitude.
Another important person for me was Gregor Dürrenberger from the "Forschungsstiftung Mobilkommunikation" next door, sharing his experience of life and wine.
Special thanks also go to Christian Kreienbühl for performing a thorough layout check of the thesis, greatly improving its readability.

In the end, I owe my deepest gratitude to those who supported me during the past five years in any sense. Only thanks to their friendship, love and time my thesis did not remain unfinished. I am not taking this for granted.

# List of Publications

## Publications related to this thesis

### Journal papers

**P1** S. Huclova, D. Erni and J. Fröhlich, "Modeling effective dielectric properties of materials containing diverse types of biological cells" *Journal of Physics D: Applied Physics*, vol. 43, 365405, 2010.

**P2** S. Huclova, D. Baumann, M. S. Talary and J. Fröhlich, "Sensitivity and specificity analysis of fringing-field dielectric spectroscopy applied to a multi-layer system modeling human skin" *Physics in Medicine and Biology*, accepted for publication, October 2011.

**P3** S. Huclova, D. Erni and J. Fröhlich, "Modeling and validation of dielectric properties of human skin in the MHz region focusing on skin layer morphology and material composition" submitted to *Journal of Physics D: Applied Physics*, accepted for publication, November 2011.

### Conference papers

**P4** S. Huclova, J. Fröhlich, L. Falco, F. Dewarrat, M. S. Talary and R. Vahldieck, "Validation of skin models in the MHz region", in the 31st Annual International *IEEE EMBC* Conference, Minneapolis, Minnesota, USA, September 2009.

**P5** S. Huclova and J. Fröhlich, "Simulation of bulk dielectric parameters of cell suspensions", in the Bioelectromagnetics Society (*BEMS*) 32nd Annual Meeting, Seoul Eduction Cultural Center, Seoul, South Korea, June 2010.

**P6** S. Huclova and J. Fröhlich, "Towards a realistic dielectric tissue model: A multiscale approach", in the 32nd Annual International *IEEE EMBC* Conference, Buenos Aires, Argentina, September 2010.